Isolated photon production in p-Pb collisions at $\sqrt{(s\_NN)} = 5.02$ TeV with the ALICE experiment at the LHC

Lucile Ronflette

UNIVERSITE BRETAGNE LOIRE

UNIVERSITÉ DE NANTES

Thèse de Doctorat

Lucile RONFLETTE

Mémoire présenté en vue de l'obtention du
grade de Docteur de l'Université de Nantes
sous le sceau de l'Université Bretagne Loire

École doctorale : *3MPL – Molécules, Matières et Matériaux en Pays de la Loire*

Discipline : *Constituants élémentaires et physique théorique*
Spécialité :
Unité de recherche : *Laboratoire SUBATECH - UMR 6457*

Soutenue le *23 novembre 2016*
Thèse N° :

Isolated photon production in p-Pb collisions at $\sqrt{s_{NN}}$ = 5.02 TeV with the ALICE experiment at the LHC

JURY

Rapporteurs :	**Christophe FURGET**, Professeur, LPSC - Université de Grenoble **Raphaël GRANIER DE CASSAGNAC**, Directeur de Recherche, LLR
Examinateurs :	**Philippe CROCHET,** Directeur de Recherche, LPC Clermont-Ferrand **Klaus WERNER**, Professeur, SUBATECH - Université de Nantes - Président du jury
Directeur de Thèse :	**Barbara ERAZMUS**, Directeur de Recherche, SUBATECH
Co-directeur de Thèse :	**Marie GERMAIN**, Chargé de Recherche, SUBATECH

Abstract

Title: Isolated photon production in p-Pb collisions at $\sqrt{s_{NN}}$ = 5.02 TeV with the ALICE experiment at the LHC

Quantum ChromoDynamics is the theory associated to the strong interaction in the standard model. It predicts that partons (quarks and gluons) are confined into hadrons at standard thermodynamic conditions. A state of deconfined hadronic matter, the Quark Gluon plasma (QGP), is predicted for a high energy density and should have existed in the early state of the Universe. ALICE (A Large Ion Collider Experiment) at CERN-LHC (Large Hadron Collider) is dedicated to the study of QCD matter in p-p, p-Pb (Pb-p) and in Pb-Pb collisions where QGP formation is expected. Photons produced by different mechanisms (hard processes, fragmentation, decay), sensitive or not to the medium, are especially interesting to probe the matter.

In this thesis, we will present the study of photons coming directly from parton-parton hard scatterings, the prompt photons. Their production cross-section is calculable in perturbative Quantum ChromoDynamics theory. Such a measurement in p-Pb collisions enables the study of cold nuclear matter effects whose knowledge is crucial to distinguish key signatures of the QGP from nuclear effects in Pb-Pb collisions. Experimentally, the prompt photon can be discriminated using the isolation analysis method. In this thesis, the measurement of the isolated photon cross-section in p-Pb collisions at $\sqrt{s_{NN}}$ = 5.02 TeV with the EMCal calorimeter of the ALICE experiment, is presented. The results are consistent, within the uncertainties, with theoretical calculations using different models of nuclear parton distribution functions. The comparison with the cross-section measurement from pp data at $\sqrt{s}$ = 7 TeV is performed via the determination of the nuclear modification factor R_{pA}. The last one is compatible with unity and does not clearly indicate modification of the prompt photon production due to nuclear effects in p-Pb collisions.

Key words

Isolated photons, direct photons, pQCD, p-Pb collisions, Electromagnetic calorimeter, ALICE, LHC, QGP

Acknowledgements

Avant tout je souhaiterais présenter mes excuses auprès des personnes que j'aurais pu oublier dans ces remerciements. Ceux-ci ne pouvant qu'être partiels, la liste des personnes ayant contribuer à l'aboutissement de ces nombreuses années d'étude, d'une manière ou d'une autre, par une parole ou une simple précense, étant impossible à énumerer ici.

En premier lieu, je tiens à remercier mes encadrantes de thèse, Marie Germain et Barbara Erazmus, sans qui ces trois ans de thèse n'auraient pas été pareils, et qui ont su m'accompagner jusqu'au bout et même au delà. J'ai pu apprécier au fil de ces années leurs conseils, implication et soutien.

Merci à l'ensemble des membres de mon jury, Christophe Furget, Raphaël Granier de Cassagnac, Philippe Crochet et Klaus Werner, d'avoir accepté d'évaluer ce travail et pour la pertinence de leurs remarques.

Ce travail a été réalisé au sein de la collaboration ALICE et je tiens à présenter mes remerciements aux personnes qui ont rendu possible, de bien des façons, la réalisation de l'analyse présentée ici.

Je remercie l'ensemble des membres du laboratoire Subatech, qui m'ont permis de passer de bons moments, et plus particulièrement l'ensemble des membres du groupe Plasma que j'ai pu cotoyer au fil des années: Guillaume, Ginez, Laurent, Philippe, Diego, Astrid, Audrey, Benjamin et Erwann. Bien entendu cette thèse n'aurait pas eu la même saveur sans la présence des autres thésards du laboratoire. Il est difficile de nommer tout le monde sans en oublier certains. Je tiens à remercier plus particulièrement Javier, Lucia, Charlotte, Florian, Alexandre, Fanny, Loïck, Roland et ceux que j'aurais immanquablement oublié, soyez sûr dus sentiement de culpabilité qui m'animera lorsque je m'en rendrai compte.

Il y aussi ceux qui, malgré les années passant, sont toujours là, pour mon plus grand bonheur, Anaïs, Harmony, Camille, qui auront poussé leur bienveillance jusqu'à ne pas s'endormir lors de ma soutenance de thèse, Leïla, Yohann et Golmote. La sobriété des ces remerciements ne reflète pas l'étendue des sentiments qui m'animentà votre égard.

Je tiens aussi à remercier mes grand-parents, mes parents et mes frères Benoît et Romain, pour leur soutien constant.

Résumé de la thèse

La chromodynamique quantique est la théorie associée à l'interaction forte dans le modèle standard. Elle prédit le confinement des partons (quarks et gluons) à l'intérieur des hadrons dans des conditions thermodynamiques standard. Lorsque de hautes densités d'énergie sont mises en jeu, un état de déconfinement de la matière hadronique, le plasma de quarks et gluons (PQG), est prédit par la théorie. Cet état aurait existé aux premiers instants de l'Univers. L 'expérience ALICE (A Large Ion Collider Experiment) au LHC (Large Hadron Collider) basé au CERN (Centre européen pour la recherche nucléaire) est dédiée à l'étude de la matière hadronique dans les collisions pp, p-Pb et dans les collisions Pb-Pb où la formation d'un PQG est attendue. Les photons, produits suivant différents mécanismes (processus de haute énergie, fragmentation, décroissance) sensibles ou non au milieu traversé, sont particulièrement intéressants pour sonder la matière.

Dans cette thèse, l'étude des photons issus des interactions dures entre partons est présentée. Leur section efficace de production est calculable dans le cadre de la chromodynamique quantique perturbative (QCD). Une telle mesure, effectuée dans les collisions p-Pb, permet d'étudier les effets nucléaires froids. La connaissance de ces derniers est cruciale pour pouvoir mesurer les signatures du PQG dans les collisions Pb-Pb. Expérimentalement, les photons prompts sont mesurés en utilisant la méthode de l'isolement. La mesure de la section efficace des photons isolés dans les collisions p-Pb à $\sqrt{s_{NN}}$ = 5.02 TeV avec le calorimètre EMCal de l'expérience ALICE est présentée dans cette thèse.

Le premier chapitre de la thèse est consacré à la description de la matière hadronique dans le modèle standard. La théorie associée, la ChromoDynamique quantique prédit l'existence d'un état de déconfinement des partons à l'intérieur des hadrons pour de grandes densités d'énergie. Expérimentalement, cet état de la matière est accessible grâce aux collisions d'ions lourds telles que les collisions Pb-Pb réalisées au Large Hadron Collider. Lors de ces collisions, des signatures de la formation d'un PQG ont été observées, telles qu'une modification de la production de certaines particules ou une observation d'effets collectifs dans le milieu. Afin d' effectuer ce type de mesure, il est essentiel de pouvoir distinguer les signatures d'un plasma de quarks et de gluons, des effets de la matière nucléaire froide liés aux interactions induites par la présence de noyau. L'étude de la matière hadronique dans le cadre des collisions p-Pb, où la formation d'un plasma de quarks et de gluons n'est pas attendue, permet une meilleure connaissance des effets nucléaires. Cependant, les premières mesures effectuées au LHC, ont montré l'existence de phénomènes non prédits par la théorie. Ainsi, des comportements collectifs ont été observés. En revanche, la mesure de certaines

observables, tels que les jets, indique une absence de modification dans leur production, contrairement à ce qui est observé lorsque que la matière hadronique est déconfinée.

Dans le chapitre 2, les mécanismes de production des photons prompts, c'est-à-dire les photons directs et les photons issus de la fragmentation d'un parton, sont présentés. Ces photons, et plus particulièrement les photons directs, constituent des sondes intéressantes de la matière hadronique. En effet la production de photons directs, émis lors des collisions partoniques, ne devrait pas être affectée par le milieu hadronique traversé, ce qui en fait des candidats naturels pour l'étude de corrélations avec les autres produits de l'interaction dont ils sont issus. De plus, leur section efficace est calculable dans le cadre de la chromodynamique quantique perturbative à l'aide de fonctions de distribution partonique ou de fonctions de distribution partonique nucléaire modélisant la distribution des partons dans les hadrons collisionnant. La mesure de leur section efficace, permet alors de tester, et parfois de contraindre, les modèles théoriques. Les photons directs ont des propriétés cinématiques similaires à celles des photons issus de la fragmentation d'un parton, il n'est donc pas possible de les discriminer dans la mesure. La méthode mise en œuvre consiste alors à s'appuyer sur une proriété des photons de fragmentation : ils sont émis à l'intérieur d'un jet de particules et sont donc, de fait, entourés d'un flot de particules énergétiques. Les photons directs qui sont au contraire émis à l'azimuth d'un parton qui fragmente, sont, a priori, isolés de l'environnement hadronique. Il est ainsi possible de définir un cône autour d'un photon d'intéret et de mesurer l'énergie qui l'entoure. Si cette énergie est inférieure à un seul discriminant, le photon peut être considéré comme isolé et assimilé à un photon direct. La part des photons de fragmentation dans la mesure de la section efficace est ainsi réduite de l'ordre de 75 % et devient négligeable par rapport à la part de photons directs. De telles mesures, ont déjà été effectuées dans différents systèmes, à différentes énergies et ont montré des résultats compatibles avec les calculs théoriques. La première mesure de la section efficace de production des photons isolés dans les collisions p-Pb au LHC constitue ce travail de thèse.

Le troisième chapitre est consacré à la présentation du LHC (Large Hadron Collider) et de l'expérience ALICE (A Large Ion Collider Experiment). Le LHC permet d'accélérer et de délivrer des faisceaux de protons ou de noyaux de plomb qui collisionnent en différents points d'interaction. Autour de chacun des ces points d'interaction sont installées des expériences dont les expériences CMS (Compact Muon Solenoid) et ATLAS (A Thoroidal LHC ApparatuS) principalement dédiées à la découverte du Boson de Higgs et d'une éventuelle physique nouvelle, au-delà du modèle standard. Chacune de ces expériences possède un calorimètre électromagnétique avec lequel des mesures de sections efficaces de photons isolés ont été réalisées. En effet, la voie préférentielle pour l'étude du boson de Higgs étant sa décroissance en 2 γ, les photons prompts constituent une source de bruit de fond et leur contribution doit être évaluée. L'expérience ALICE a, quant à elle, été construite afin de réaliser l'étude de la matière hadronique et notamment de sa phase de déconfinement. Elle est composée d'un ensemble de détecteurs qui permettent la détection du vertex d'interaction, la mesure (et l'identification) des particules chargées, des particules électromagnétiques et des muons. Ils permettent d'obtenir un jeu de mesures donnant une image globale du comportement de la matière hadronique. Les données brutes enregistrées sont reconstruites suivant différentes étapes. Une première calibration des détecteurs est effectuée sur un petit volume de données puis l'ensemble des

données prises est reconstruite. Ces reconstructions permettent d'obtenir des objets utilisables pour la mesure de différentes observables. Les principes de reconstruction des données, ainsi que leur analyse en vue de la détermination de leur qualité, sont également présentés dans ce chapitre.

La description du calorimètre électromagnétique EMCal, qui constitue le principal détecteur impliqué dans cette analyse, fait l'objet du chapitre 4. EMCal permet la mesure des particules électromagnétiques. En effet, ces dernières (électrons, photons) perdent leur énergie dans le détecteur, constitué de couches successives de plomb et de scintillateur, via une combinaison de création de paire et de rayonnement Bremsstrahlung. Une gerbe électromagnétique est ainsi formée. L'ensemble de l'énergie émise est collecté par des cellules élémentaires. Des algorithmes permettent la reconstruction des agrégats correspondant au dépôt d'énergie d'une particule dans le calorimètre. Une pré-calibration du détecteur a été effectuée lors des tests sous faisceaux mais une partie de la calibration, notamment en temps et en énergie du calorimètre, est réalisée avec les données reconstruites. Les performances du calorimètre, la résolution en énergie, position et la linéarité de la réponse du détecteur, sont présentées. L'analyse de la qualité des données reconstruites pour le calorimètre de l'expérience ALICE est décrite. Elle permet, en plus de valider les données utilisables pour les analyses effectuées dans le calorimètre, de réaliser les cartes de canaux défectueux.

Les chapitres suivants font l'objet de l'analyse à proprement parler. Le chapitre 5 présente les méthodes utilisées pour la sélection des photons pour l'analyse des photons isolés dans le calorimètre. Les photons prompts étant des photons de hautes énergies dont la section efficace de production associée est faible, les données permettant une telle analyse ont été enregistrées à l'aide d'un système de déclenchement spécifique dont le seuil est élevé. La sélection des données à utiliser pour l'analyse a été effectuée après une étude de la qualité des données. Des simulations Monte-Carlo, basées sur ces données, ont par ailleurs été produites pour modéliser le signal et le bruit de fond. Les agrégats de cellules sélectionnés pour l'isolement ont été formés afin de rejeter les agrégats issus de bruit de fond électronique et de collisions satellites, autres que celles considérées pour l'évènement. De plus, il est nécessaire de rejeter les agrégats issus de particules chargées. Pour ce faire, les traces de la chambre à projection temporelle sont prolongées jusqu'à la surface du calorimètre si celles-ci sont proches d'un agrégat de cellules, ces derniers sont considérés comme chargés et rejetés dans l'analyse. Par ailleurs, il est nécessaire de discriminer les agrégats provenant des photons prompts des agrégats issus de la décroissance en 2 γ des mésons neutres, principalement π^0 et η, qui sont produits en grande quantité dans les collisions hadroniques en raison de leur faible masse. L'angle entre les gerbes életromagnétiques des deux photons de décroissance de ces mésons étant inversement proportionnel à leur énergie, il est relativement faible dans la gamme d'énergie considérée. Il y a donc un recouvrement de ces gerbes qui produisent des agrégats de cellules dont la forme est elliptique. La sélection des agrégats se fait donc sur leur forme, par le biais d'une coupure sur la valeur du grand axe associé à leur extension dans le plan transverse. Seuls les agrégats ayant une forme circulaire sont sélectionnés. Ils correspondent principalement aux dépôts d'énergie issus de photons prompts. Le code utilisé pour la réalisation de cette analyse a été testé sur les données des collisions pp, et des comparaisons avec les mesures précédentes de la section efficace de production des photons isolés ont été effectuées. Cette étude qui a constitué une part importante du travail de thèse, a permis de converger vers des résultats similaires sur la mesure de la section efficace. Il a

par ailleurs servi à évaluer les erreurs systématiques liées au choix de la méthode de rejet des agrégats issus de particules chargées, dans la mesure des photons isolés dans les collisions pp. De plus, la procédure d'analyse a été validée par cette comparaison ce qui permet d'être confiant dans les résultats obtenus pour la mesure de la section efficace dans les collisions p-Pb.

Le chapitre qui suit est consacré à la détermination d'un critère d'isolement discrimant, pour l'étude des photons isolés. En effet, lors des collisions, des particules sont produites dans tout l'espace suite à des interactions secondaires autres que les processus durs. Ces particules constituent l'évènement sous-jacent. Leur contribution énergétique est plus importante dans le cadre des collisions d'ions lourds et doit donc être prise en compte pour l'étude des photons isolés dans les collisions p-Pb. Elle doit être soustraite de l'énergie dans le cône d'isolement afin d'appliquer un seuil discriminant sur l'énergie issue de l'activité hadronique dans le cône. Pour se faire, une étude de la contribution des évènements sous-jacents a été réalisée dans des espaces ou aucune contribution issue du processus dur n'est attendue. Le choix a été fait de soustraire cet évènement sous-jacent évènement par évènement afin d'éviter d'être trop sensible aux fluctuations. La contribution énergétique de ces évènements sous-jacents a été évaluée dans des bandes en pseudo-rapidité dans l'acceptance du calorimètre afin de pouvoir soustraire la contribution issues des particules chargées et des particules neutres. Une bande similaire, mais dans l'acceptance de la chambre à projection temporelle, est utilisée afin de réaliser une étude de l'isolement des photons en utilisant seulement la contribution des particules chargées. Cette procédure présente l'avantage de pouvoir augmenter l'acceptance du détecteur accessible. Les spectres bruts de photons isolés ont ainsi pu être obtenus en utilisant deux déclencheurs de seuil différents afin de pouvoir mesurer les photons dans la même gamme d'énergie que pour la mesure des photons isolés en pp, c'est-à-dire dans la gamme $[10-60]$ GeV.

Le chapitre 7 de cette thèse est consacré à l'extraction du signal. La contamination du bruit de fond restant dans le spectre brut doit être évaluée. Pour cela, l'hypothèse est faite que la probabilité d'isolement du bruit de fond est la même dans la région où l'on mesure le signal, c'est-à-dire où les agrégats de cellules sont circulaires, que dans le région où on s'attend à trouver du bruit de fond, c'est-à-dire la région où les agrégats de cellules ont une forme elliptique. Cette hypothèse est biaisée. Le principal biais apparaît pour les photons de plus basse énergie. En effet, dans ce cas les photons issus de la décroissance des mesons neutres qui se trouvent dans le région du signal ont une probabilité plus importante de ne pas être isolés. La probabilité que le photon partenaire se trouve dans le cône d'isolement est importante et diminue la probabilité que ce photon soit isolé. Ce n'est pas le cas lorsque les deux gerbes électromagnétiques sont associées pour former un agrégat de forme elliptique. Une correction basée sur des similations Monte-Carlo gamma-jet pour simuler le signal et jet-jet pour simuler le bruit de fond permet de corriger cet effet ainsi que ceux issus de la présence de signal dans la région du bruit de fond. Le spectre obtenu doit être corrigé de l'efficacité de reconstruction des agrégats. Ceci est réalisé à l'aide de simulations reproduisant le signal. Les erreurs induites par les choix effectués dans les coupures de rejet ou d'acceptation des évènements et des agrégats ont été estimées. Enfin, la détermination de la section efficace de production des photons isolés est effectuée à l'aide de la section efficace de biais minimum connue utilisée comme référence.

Le dernier chapitre de cette thèse présente la comparaison des résultats obtenus avec les calculs théoriques et la section efficace de production des photons isolés lors des collisions pp. Afin de réaliser ces comparaisons, la section efficace des photons isolés dans les collisions p-Pb équivalente à celle en pp à été déterminée. Les calculs théoriques de chromodynamique perturbative ont été effectués à l'aide de JetPHOX en utilisant différents modèles de fonction de distribution partonique nucléaire. Ils ont été corrigés par un facteur qui prend en compte le fait que l'isolement des photons dans la mesure se fait au niveau des particules et non au niveau partonique. Les résultats de la mesure sont compatibles avec les prédictions théoriques. La comparaison avec la section efficace mesurée dans les collisions p-p a été réalisée via la détermination du facteur de modification nucléaire, R_{pA}. La section efficace des photons isolés dans les collisions pp n'étant pas disponible pour une énergie dans le centre de masse de $\sqrt{s_{NN}}$ = 5.02 TeV, les valeurs correspondant aux collisions pp à $\sqrt{s_{NN}}$ = 7 TeV ont été extrapolées. Les résultats du R_{pA} sont compatibles avec l'unité mais tendent à être inférieurs. Cependant, il est difficile de conclure de façon définitive compte tenu des erreurs importantes associées à la mesure qui sont particulièrement importantes.

Table of Contents

List of Tables

List of Figures

Acronyms

ACORDE ALICE COsmics Ray DEtector.

ALICE A Large Ion Collider Experiment.

ATLAS A Toroidal LHC ApparatuS.

CERN Centre européen pour la recherche nucléaire.

CMS Compact Muon Solenoid.

CNM Cold Nuclear Matter.

DCal Di-jet Calorimeter.

EMCal ElectroMagnetic Calorimeter.

FF Fragmentation Function.

FMD Forward Multiplicity Detector.

HMPID High Momentum Particle Identification.

ITS Inner Tracking system.

LEP Large Electron-Positron collider.

LHC Large Hadron Collider.

LHCb Large Hadron Collider beauty experiment.

LHCf Large Hadron Collider forward.

NLO Next-to-Leading-Order.

nPDF nuclear Parton Distribution Function.

nPDFs nuclear Parton Distribution Functions.

PDF Parton Distribution Function.

PDFs Parton Distribution Functions.

PHOS PHOton Spectrometer.

PMD Photon Multiplicity Detector.

pQCD perturbative Quantum ChromoDynamics.

PS Proton Synchrotron.

QCD Quantum ChromoDynamics.

QGP Quark Gluon plasma.

RHIC Relativistic Heavy Ion Collider.

SPS Super Proton Synchrotron.

T0 TZero.

TOF Time Of Flight.

TOTEM TOTal cross-section, Elastic scattering and diffraction Measurement.

TPC Time Projection Chamber.

TRD Transition Radiation Detector.

V0 VZero.

ZDC Zero Degree Calorimeter.

General introduction

The ALICE experiment (A Large Ion Collider Experiment) at the LHC (Large Hadron Collider) is devoted to study the hadronic matter under extreme conditions. In the standard model, Quantum ChromoDynamics (QCD) associated to the strong interaction, describes the interactions of quarks and gluons, which constitute partons. The theory predicts the confinement of this elementary constituants into structures called hadrons. This property of confinement allows the consistency of the nuclear matter. When submitted to high energy densities, a deconfinement of quarks and gluons into a medium, the so-called Quark-Gluon plasma, is predicted by the theory. This state of the matter should have existed at the beginning of our Universe, just after the Big-Bang. The study of such medium, as well as of the phase transition, allows a better understanding of the nuclear matter.

Experimentally, the way to produce a QGP is to reach high energy density via heavy ion collisions. At the LHC, this is performed using lead ions. To efficiently study this medium, one has to be able to distinguish the effects related to the nucleus structure of the colliding ions, the cold nuclear matter effects, and the ones linked to a QGP formation. Such studies are performed analysing data from p-Pb collisions where no QGP formation is expected. The present thesis work has been realised in this context.

The photons produced in parton-parton interactions, called direct photons, are particulary interesting. They witness primary collisions and their production is not affected by the traversed medium. Thus, they are interesting references in correlation studies to measure parton energy loss in the medium. They also allow to test and to constrain theoretical models. In particular, their production cross-section calculations in the pertubative QCD theory are related to the used parton distribution functions (PDF) or nuclear parton distribution functions (nPDF) in the case of ion collisions. In this thesis, we present the first measurement of the isolated photon cross-section in p-Pb collisions at the LHC which enables to test the nuclear parton distribution function models.

The first chapter of the thesis is devoted to a brief description of the strong interaction in the standard model. Some measurements, performed in heavy ion collisions where a QGP formation is expected, are introduced. The last part of the chapter deals with measurements performed in p-Pb collisions at the LHC. Some surprising and unexpected results are highlighted.

The chapter 2 introduces the prompt photon production in the high energy parton-parton interaction and their pertinence as probe of the hadronic matter. In order to select the direct photons and reject photons coming from parton fragmentation, the isolation method is used. The isolated photon measurements are presented focusing on the results performed at the LHC.

The analysis has been realised in the ALICE experiment facility based at an interaction point of the LHC. The chapter 3 is dedicated to the description of the LHC. Then, the presentation is focused on the ALICE detectors and the data taking framework associated to this experiment.

The EMCal (ElectroMagnetic Calorimeter) characteristics are shown in the fourth chapter. This detector is the one involved to study electromagnetic clusters in the isolated photon analysis of this thesis work.

The chapter 5 is devoted to the description of the applied methods to select the events of interest in the data as well as the clusters, the energy deposits associated to particles in the calorimeter, candidates for isolation. The analysis has been tuned with the isolated photon analysis in pp collisions at $\sqrt{s}$ = 7 TeV.

The chapter 6 presents the study of a new discriminant isolation criteria for p-Pb collisions. Indeed, one has to notice that in p-Pb collisions the contribution coming from events other than hadron one is not negligeable and has to be evaluated in order to choose an isolation criteria on purpose. The used procedures are detailed.

The chapter 7 is dedicated to the signal extraction from the spectra already measured. The remaining contamination of background photons is evaluated. The results are corrected for the detector reconstruction efficiency via Monte-Carlo simulations. The cross-section of isolated photons in p-Pb collisions at $\sqrt{s_{NN}}$ = 5.02 TeV is measured.

The last chapter is dedicated to the comparison of the obtained results with the theoretical calculations in perturbative Quantum ChromoDynamics.The nuclear modification factor, R_{pA}, is computed to perform a comparison with an extrapolation from the isolated photon cross-section results in pp collisions at $\sqrt{s}$ = 7 TeV.

Part I

Prompt photons in the hadronic matter

CHAPTER 1

From the standard model to experimental hadronic physics

Contents

In this first chapter, we will introduce the main characteristics of the strong interaction in the standard model. The associated particles, quarks and gluons, are confined into structures called hadrons. The theory predicts the existence of a de-confined state of hadronic matter, the Quark Gluon plasma, for high temperature or high hadronic matter density as it should have existed during the first moment of the Universe in the Big Bang theory. The phase transition of the hadronic matter is described. Experimentally, such a state is reachable in collider via heavy ion collisions. Some selected experimental results will be highlighted. The last part of the chapter is dedicated to cold nuclear matter effects, due to the nature of the nucleus, and studied in p-Pb collisions where the QGP formation is not expected.

1.1 Fundamental interactions in the standard model

In particle physics, the standard model enables to describe the fundamental interactions, the electromagnetic, the weak and the strong ones, and their associated particle behaviour. Bosons (integer spin) are the mediators of the interaction while fermions (semi-integer spin) are the elementary particles involved. The fermions can be divided into 2 groups:

- leptons: electron (e^-), muon (μ^-), tau (τ^-), the corresponding neutrinos, ν_e, ν_μ and ν_τ and their associated anti-particles, e^+, μ^+ and τ^+. They are only sensitive to the electromagnetic and to the weak interactions.

- quarks: up, down and strange (u, d and s) and charm, bottom and top (c, b and t). They are sensitive to the electromagnetic, the weak and the strong interactions.

The mediators of the interactions are gauge bosons: photons, W and Z bosons and gluons. Photons carry out the electromagnetic interaction, W and Z bosons the weak interaction and gluons the strong one.The particles of the standard model and their interaction are illustrated in the Figure 1.1. The standard model fails to include gravitation and cannot explain, in its widely spread form, some recent results such like the neutrino flavour change [1] [2] [3]. This leads to the existence and the development of models beyond the standard model like supersymetry ones.

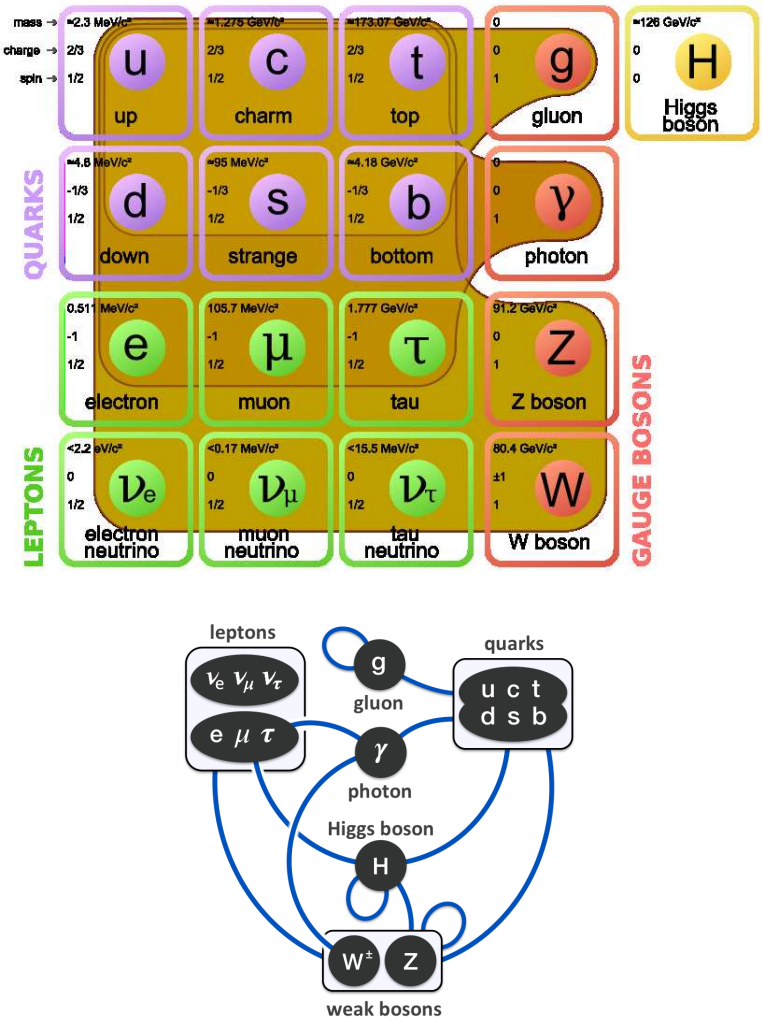

Figure 1.1: Up: standard model of the particle physics which describes the fundamental interactions and particles behaviour. Bottom: representative scheme of the allowed interactions between particles and mediators of the interaction in the standard model.

The standard model is a relativistic quantum field theory associated to the symmetry groups $SU(3)_c \otimes SU(2)_L \otimes U(1)_Y$. The breaking in the gauge symmetry [4] leads to a scalar field apparition associated to the existence of the Higgs Boson [5] [6] [7], which is responsible for particle masses and

has been observed in the ATLAS (A Toroidal LHC ApparatuS) and CMS (Compact Muon Solenoid) experiments at the LHC (Large Hadron Collider) [8] in 2012 [9] [10] [11]. While the electromagnetic and weak interactions are unified in the electroweak theory [12] [13] [14] associated to the symmetry group $SU(2)_L \otimes U(1)_Y$, the strong interaction is described by the QCD (Quantum ChromoDynamics) [15] associated to the symmetry group $SU(3)_c$. It allows the confinement into hadrons [16] of quarks and gluons, called partons. Hadrons are classified in two categories, mesons composed of a pair of quark-antiquark and baryons composed of three quarks. Quarks carry a colour charge, red (r), blue (b) or green (g), and antiquarks an anti-colour one, $\overline{r}$, $\overline{b}$ or $\overline{g}$, like an electric charge can be carried. Gluons carry a colour and an anti-colour. These allow them to interact with each other. Note that hadrons have a colourless structure.

Eight different gluons exist according to the carried colour charges. The next paragraph is focused on the description of the QCD and its main predictions.

1.2 The Quantum ChromoDynamics to describe strong interaction

The Quantum Chromodynamics is the quantum field theory associated to the strong interaction. In this section, we will present its properties leading to the existence of the QGP (Quark Gluon plasma).

1.2.1 Formalism

In the quantum field theory the interaction can be described by the Lagrangian which is equivalent to the density of the field in the space. The Lagrangian associated to the QCD can be written as:

$$L_{QCD} = \sum_n \overline{\psi_n}(i \not{D} - m_n)\psi_n - \frac{1}{4} G^a_{\mu\nu} G^{\mu\nu}_a \tag{1.1}$$

$\not{D}$ is the covariant derivative, defined as:

$$\not{D} = \gamma^\mu \mathrm{D}_\mu = \gamma^\mu (\partial_\mu + i\sqrt{4\pi\alpha_s} G_\mu) \tag{1.2}$$

with:

- γ^μ being the Dirac matrices and
- α_s being the QCD coupling constant.
- ψ_n is the quark spinor, n representing the flavour of the considered quark and $\overline{\psi_n}(i\not{D} - m_n)\psi_n$ describes the quark field.
- $\frac{1}{4} G^a_{\mu\nu} G^{\mu\nu}_a$ describes the scalar field from bosons, gluons where a represents the summation index of the gluon flavour.

As already mentioned, quarks and also gluons carry out a colour charge, red, green or blue. It rules out gluons interacting among themselves. This behaviour results in the quark and gluon con-

finement into colourless [1] hadronic structures at low energy, whereas the de-confinement is allowed at higher energy densities.

The Quantum ChromoDynamics theory cannot be solved literally due to the infinite number of possible interactions allowed by gluons. Different approaches have been elaborated for numerical applications like Feynman's parton model [17] and its improvement, the pQCD (perturbative Quantum ChromoDynamics) [18] or lattice QCD. While lattice QCD enables to predict the Quark Gluon plasma formation [19], the perturbative QCD is used for hard probes produced in high energy parton interactions.

1.2.2 Asymptotic freedom

The strength of a force is characterized by its coupling constant. In the case of strong interaction, the constant coupling α_s can be expressed at the leading order in perturbative theory as:

$$\alpha_s(Q^2) = \frac{4\pi}{(11 - \frac{2}{3}N_f)ln(\frac{Q^2}{\Lambda^2_{QCD}})} \tag{1.3}$$

where:

- N_f is the number of flavour,
- Q^2 is the energy involved in the interaction momentum transfer,
- Λ^2_{QCD} is a threshold which defines the perturbative QCD scale.

The coupling constant α_s increases toward infinity when:
$ln(\frac{Q^2}{\Lambda^2_{QCD}})$ is decreasing and $\frac{Q^2}{\Lambda^2_{QCD}} \to 0$ meaning than $Q^2 \ll \Lambda^2_{QCD}$.
On the contrary, at high Q^2 ($Q^2 \gg \Lambda^2_{QCD}$), the coupling constant becomes low enough to allow perturbative calculation. The QCD can be expressed as a development in α_s series corresponding to the possible interaction vertices [20]. The α_s evolution with Q^2 can be seen in the Figure 1.2[2].

This behaviour of the coupling constant in QCD suggests the confinement of quarks and gluons into hadrons at standard thermodynamic conditions. The asymptotic freedom allows the deconfinement of partons. In these asymptotic states partons can be in a new state of matter well described by ideal fluid, the QGP. The pQCD is used in the case of high energy interactions where the coupling constant α_s is low and enables to determine interaction cross section.

Experimentally, the QCD scale Λ^2_{QCD} can be determined through the expression of hard process cross section in term of α_s [22]. The value is of the order of 200 MeV.

[1] Colourless has to be understood as with additive colour, as a "white" structure. The colourless structure can also be due to an association of a colour charge and of the corresponding anti-colour one.

[2] One can notice that the coupling constant of the electromagnetic interaction, α_e, has an opposite behaviour, it tends to infinity when the energy involved increases.

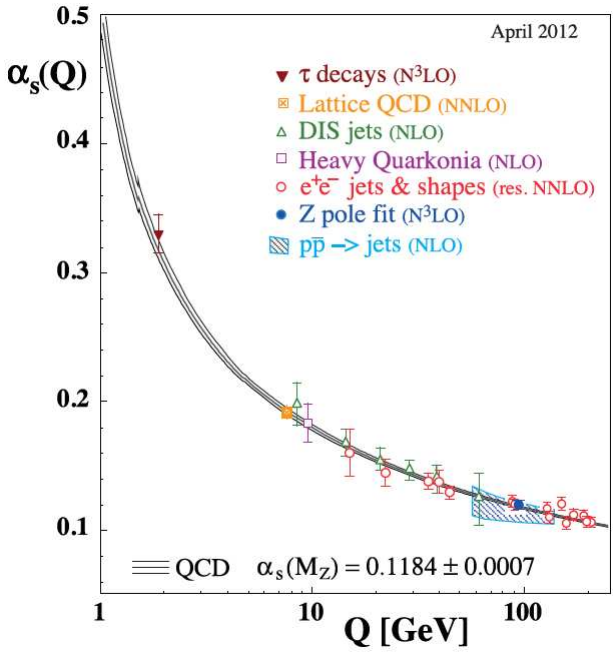

Figure 1.2: Different measurements of the QCD coupling constant [21].

1.3 The Quark Gluon Plasma, a de-confined state of hadronic matter

1.3.1 Predictions

The pQCD is not relevant to describe the hadronic matter at $Q^2 << \Lambda^2_{QCD}$. In this domain only effective theory are usable, like lattice QCD. This last has predicted the phase transition between a confined and a de-confined state of the quark and gluon matter.

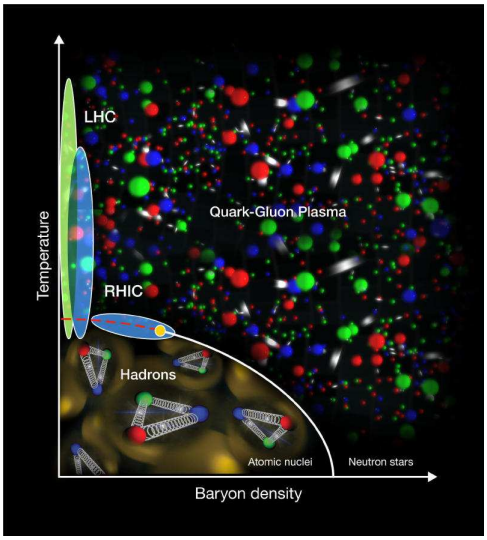

Figure 1.3: Phase diagram of hadronic matter.

This de-confined state of the matter where quarks and gluons are expected to be released from the strong interaction, is expected at high temperature or at high densities, as illustrated on the transition phase diagram of the hadronic matter presented in the Figure 1.3. At high densities, in cold matter, the neutron stars should be observed [23]. The lattice QCD has predicted a phase transition temperature around 175 MeV. The study of such a phase transition is crucial for the comprehension of the strong interaction, still not well known whereas it maintains the matter cohesion.

Experimentally, the QGP state of matter is reached involving high temperature via heavy ion collisions. Some measurements indicate that the phase transition has already been crossed in heavy ion experiments at SPS, RHIC and the LHC [24].

1.3.2 Experimental probes

The lifetime of the Quark Gluon plasma is predicted to be of the order of $10^{-23}s$ [25]. Therefore, it is not possible to directly measure this state of the matter. Only the final state observables of the medium are measurable. The Figure 1.4 describes the time-evolution of heavy ion collisions as assumed by the Bjorken scenario [26].

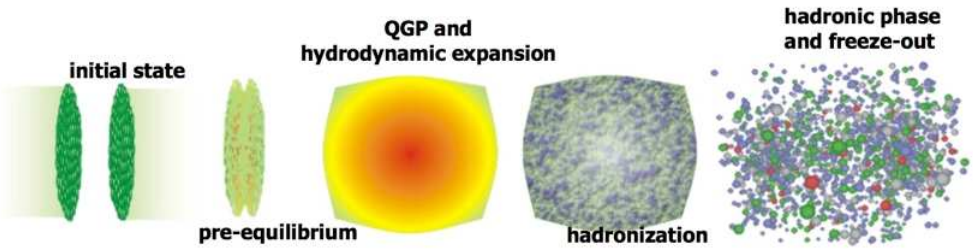

Figure 1.4: Evolution of an heavy ion collision from the initial state to the freeze-out.

- **Pre-equilibrium** ($0 < \tau < 1$ **fm/c**). $\tau = 0$ represents the time at which the nuclei collide. Right after, multiple parton-parton interactions occur. This produces a pre-equilibrium state leading to a thermalization of the medium.
- **QGP formation and hydrodynamic expansion** (1 **fm/c** $< \tau < 10$ **fm/c**). When the evolved energy in the collision is high enough, partons produced in the pre-equilibrium stage of the collisions are de-confined and a QGP is formed. The medium expands. This expansion can be described by hydrodynamical models.
- **Hadronization** ($\tau < 20$ **fm/c**). During the expansion phase, the medium cools. When the temperature tends to the critical transition phase value, quarks and gluons start to reconfine into hadrons.
- **Hadronic phase and freeze-out** ($\tau < 20$ **fm/c**). When temperature of the transition phase is reached, all the partons are confined into hadrons and the medium becomes a hadron gas

in expansion. The composition of the system is determined at the chemical freeze-out which occurs when the inelastic hadron-hadron interactions stop. The kinematic freeze-out occurs when the mean free path of hadrons is high enough that elastic hadron collisions cease.

Signals are measured only after the freeze-out. This leads to probe the deconfined hadronic matter through many indirect observables. The comparison of their production in heavy ion (A-A) collisions and in proton-proton (pp) collisions, where no QGP creation is expected, allows to characterize the produced medium. Different observables can be produced at different time scales in the collision and their production can be affected or not by the crossed medium. This leads to a set of observables useful to probe the hadronic matter.

We will only present two representative types of measurements.

The nuclear effects are mainly quantified via the nuclear modification factor described in the equation (1.4). The multiple interactions of nucleons in Pb-Pb collisions are measured using a Glauber Model calculation for high energy nuclear collisions [27]. The comparison of the results obtained in heavy ion collisions to the ones from p-p collisions is realised taking into account the geometry of the collision and the number of its participants in the A-A collisions.

$$R_{AA} = \frac{d^2N_{AA}/dp_T dy}{< T_{AA} > d\sigma^2_{pp}/dp_T dy} \tag{1.4}$$

where:

- $d^2N_{AA}/dp_T dy$ is the yield of the considered particles in A-A collisions.
- $d^2\sigma_{pp}/dp_T dy$ is the differential cross section of the considered process in p-p collisions.
- y is the rapidity which in particle physics is defined relatively to the particle beam axis, as $y = \frac{1}{2} ln(\frac{E+p_z}{E-p_z})$ where:
  - z is the beam axis,
  - $p_z \equiv p_L$, the longitudinal momentum.
    $p_T = \sqrt{p_x^2 + p_y^2}$ represents the transverse momentum, the particle momentum in the transverse plan.
- $< T_{AA} >$ is the nuclear overlap function where:
  - $< T_{AA} >= \frac{< N_{coll} >}{\sigma^{pp}_{inel}}$ with $< N_{coll} >$ the average number of inelastic nucleon-nucleon collisions,
  - σ^{pp}_{inel}, the inelastic cross section associated to pp collisions.

It means that the ratio $\frac{d^2N_{AA}/dp_T dy}{< T_{AA} >}$ represents the p-p equivalent cross-section associated to heavy ions collisions.

$R_{AA} = 1$ corresponds to the absence of medium or nuclear effects. When $R_{AA} > 1$, an enhancement is observed in A-A collisions compared to p-p ones. $R_{AA} < 1$ indicates a suppression due to nuclear effects from initial or final stage of the collisions.

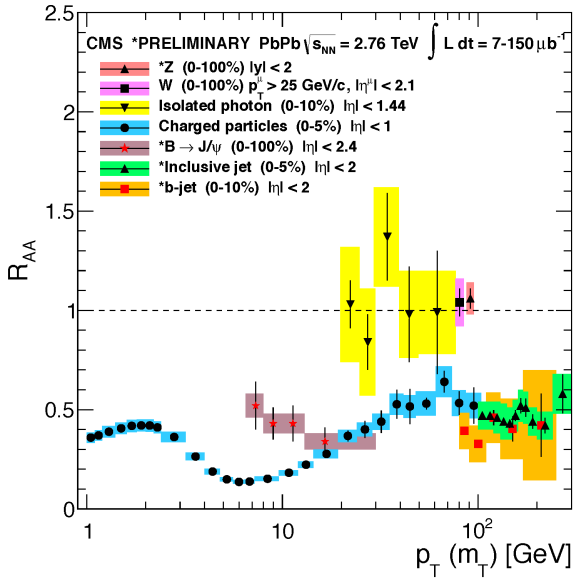

Figure 1.5: Nuclear modification factor of isolated photons [28], charged particles [29], Z [30] and W boson [31], J/ψ [32] and jet production [33] performed with the CMS experiment using the Pb-Pb data at $\sqrt{s_{NN}} = 2.76$ TeV [34].

In the Figure 1.5, one can see CMS results for R_{AA} of different observables in Pb-Pb collisions. The isolated photon [28] and Z^0 [30] and $W^{\pm}$ [31] bosons measurements are compatible with unity as expected from models. Indeed, these particles are not sensitive to the strong interaction and are produced in the earliest stages of the collision in parton-parton interaction. A suppression is observed in charged particles [29] and J/ψ [32] production. Jet production modification [33] is also observed due to parton energy loss [35] in the medium. It attests of an existence of medium effects related to the hot hadronic matter created in heavy ion collisions.

Another key probe of the QGP is the measurement of the collective motion in the particle production. Indeed the Quark Gluon plasma is expected to have a behaviour similar to a fluid and to be well described by hydrodynamics models. As a matter of fact, a spatial anisotropy in the flow of particles which are sensitive to the created medium is expected due to the pressure gradient induced by the collision geometry in non-central[3] collisions [36]. When the impact parameter is low so the number of participants is high, the collisions are more central. These anisotropy measurements are performed via the determination of the coefficients of the expansion in Fourier series of the azimuthal distribution of particles (v_2, elliptic flow, v_3, triangular flow and v_4, quadrangular flow).

[3]The centrality is defined in heavy ions via the geometry of the collision through the number of participants.

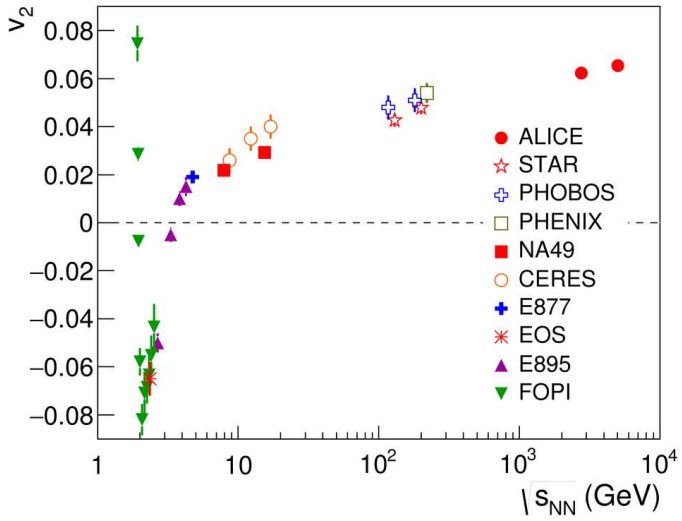

Figure 1.6: Integrated elliptic flow of charged particles measured in ALICE compared with lower center-of-mass energy results. The measurements have been performed with data from Pb-Pb collisions at $\sqrt{s_{NN}}$ = 2.76 TeV and at $\sqrt{s_{NN}}$ = 5.02 TeV in the 20-30% centrality class [37] [38].

In the Figure 1.6, is presented the elliptic flow measurement of charged particles in different experiments and center-of-mass energies, including the ALICE (A Large Ion Collider Experiment) measurement at $\sqrt{s_{NN}}$ = 5.02 TeV [38] and at $\sqrt{s_{NN}}$ = 2.76 TeV [37]. The increase of the elliptic flow with the center-of-mass energy is mainly attributed to an increase of the average transverse momentum with the energy involved in the collisions. The results shown are compatible with calculations of hydrodynamic models with a QGP formation [37].

1.4 Cold nuclear matter effects

To be able to distinguish final state effects (related to a QGP medium) from initial state effects (due to the nucleon interactions) one has to study observables produced in the cold hadronic matter in p-A collisions. In such collisions a QGP formation is not expected. These CNM (Cold Nuclear Matter) effects have different origin:

- **shadowing:** the parton density is lower in nucleons embedded in nuclear matter than in free nucleons, at low x, where x is the momentum fraction carried by the parton with respect to the total momentum of the nucleon.
- **anti-shadowing:** parton density higher in nucleons in nuclear matter than in free nucleons, at highest x,
- **EMC effects [39]:** modification of quark and gluon distributions,
- **Fermi motion:** nucleon bound states motion in the nucleus.

The impact of these effects on the nuclear modification factor as a function of particle momentum fraction is shown in the Figure 1.7. The study of such effects can particularly enable to constrain

the nPDFs (nuclear Parton Distribution Functions), which are used to describe the behaviour of partons in the nucleus. Another known CNM effect is the Cronin effect [40], a shift toward the hardest value in the transverse momentum spectrum in p-A with respect to the spectrum in pp collisions, which leads to hadron production suppression at small transverse momentum in p-Pb collisions with respect to pp ones and an enhancement in the production for intermediate p_T.

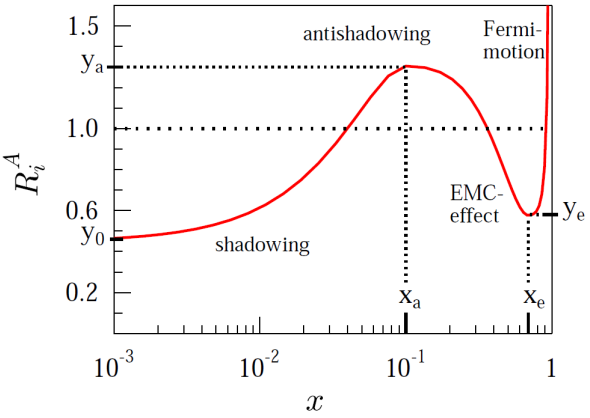

Figure 1.7: Illustration of the R_{pA} sensitivity to the nuclear effects depending on the kinematic characteristics of the particles [41].

Similarly to what is defined in Pb-Pb collisions, a nuclear modification factor, R_{pPb}, can be defined to quantify the cold nuclear matter effects in p-Pb collisions.

$$R_{pA} = \frac{d^2N_{pA}/dp_T dy}{< T_{pA} > d\sigma^2_{pp}/dp_T dy} \tag{1.5}$$

The equation (1.5) terms is similar to the one of the equation (1.4) except that it is defined for p-A collisions instead of A-A.

In p-Pb collisions, the number of participants is drastically lower than in Pb-Pb collisions what leads to larger multiplicity fluctuations in the considered pseudo-rapidity ranges. As the centrality and $< N_{coll} >$ (or $< T_{pA} >$) are determined through the multiplicity, biases are expected. In order to take into account these existing biases, a nuclear modification factor for centrality-dependant studies, has been defined, $Q_{pPb}(p_T, cent)$ [42].

$$Q_{pPb} = \frac{d^2N^{cent}_{pPb}/dp_T}{< T^{cent}_{pA} > d\sigma^2_{pp}/dp_T} \tag{1.6}$$

The Q_{pPb} definition is similar to the one of R_{pPb} but a $Q_{pPb} \neq 1$ would not necessarily mean that a nuclear effect is measured. The Q_{pPb} has been introduced in the literature related to p-Pb studies at the LHC. One has to notice that in the present thesis work, no centrality dependent measurement is presented and the choice has been made not to show a Q_{pPb} distribution here.

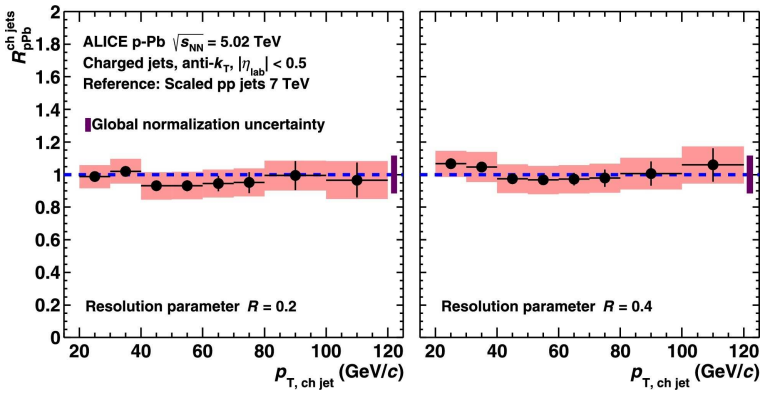

Figure 1.8: Charged jet, with $R = 0.2$ and $R = 0.4$, R_{pA} at $\sqrt{s} = 5.02$ TeV in p-Pb collisions as a function of transverse momentum [43]. The measurement has been performed with the ALICE experiment.

In this section, some representative results obtained with the p-Pb data at $\sqrt{s} = 5.02$ TeV at the LHC are presented. In the Figure 1.8, the R_{pA} measurement of the charged jet production with the ALICE experiment is shown. Its values are compatible with unity. The results are also compatible with pQCD calculations [43]. This measurement seems to indicate an absence of strong nuclear effects on the jet production in p-Pb collisions [43].

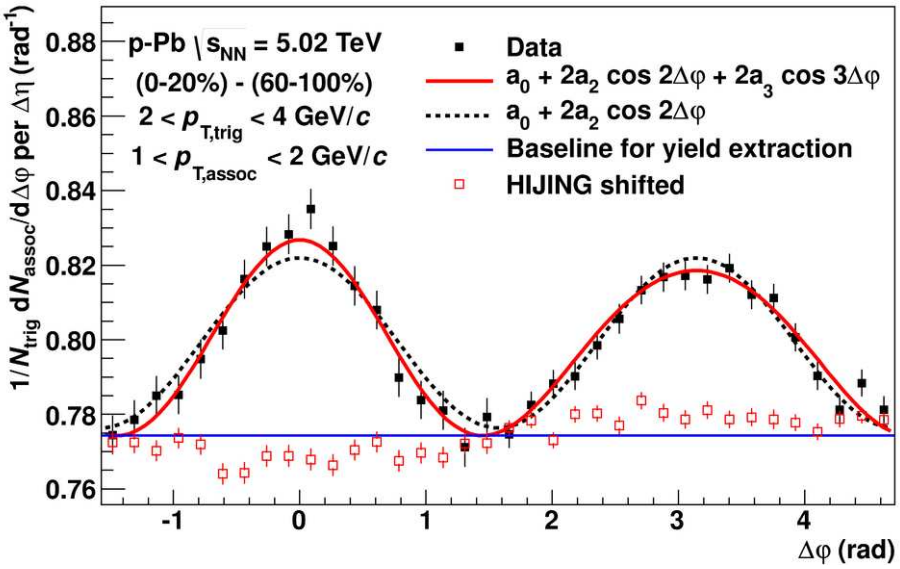

Figure 1.9: Projection on $\Delta\varphi$ of the associated yield to a trigger particle for pairs of charged particles for the most central collisions after subtraction of the considered yield in 60 – 100% centrality class measured with the ALICE experiment. The result has been fitted by a development in Fourier series. The Hijing simulation results are plotted [44].

In the Figure 1.9, one can see the projection in φ of the associated yield to a trigger particle. One can observe a structure in the yield, compatible with a Fourier series fit associated to a collective phenomena. The Hijing model, including nuclear effects, is not able to reproduce any flow-like ef-

fect [44].

Unexpected results have been obtained with some observables in the p-Pb data analysis, as collective phenomena [44] or the $\psi(2S)$ suppression [45] compatible with models including an energy loss in the medium. Whereas no strong nuclear effects are observed in the jet or in the hadrons production, these observations have already permited to develop new models and changed the theoretical perception of the created medium in p-Pb collisions and by extension in Pb-Pb collisions.

The description of the strong interaction in the standard model, allowed one to introduce the existence of a deconfinement state of the hadronic matter, the QGP. This state would have existed at the first moment of the Universe just after the Big-Bang. The study of such a transition phase enables a better knowledge of the nuclear matter. Experimentally, a QGP formation is expected in heavy ion collisions and an overview of some measurements, which indicate this medium creation, has been presented. The study of the cold nuclear matter effects in p-A collisions, where no QGP formation should occur, provides essential information on initial state effects. Some observable studies have already shown unexpected results at the LHC. Few selected measurements have been presented in this chapter.

CHAPTER 2

Prompt photon production in heavy ion collisions

Contents

This chapter is devoted to the description of the production of the observables in high energy partonic interaction, the prompt photons. Direct and fragmentation photons constitute the prompt photons. Direct photons are particularly interesting for their properties in the hadronic matter. To perform the measurement of these photons, the isolation method is applied and presented here. The last part of the chapter is dedicated to the state-of-the art of the isolated photon cross-section measurement, particulary at the Large Hadron Collider.

2.1 Prompt photon production mechanisms

Prompt photons are high energy photons produced during the earliest stages of the collision. These photons are of two types: the direct ones (section 2.1.1), which are produced in parton-parton hard scattering, and the fragmentation ones (section 2.1.2), which are issued from a parton fragmentation and consequently, their production can be affected by the crossed medium via the parton energy loss [46] [47]. In this paragraph, we will introduce different mechanisms of the prompt photon production and the associated cross-sections.

Direct and fragmentation photons are produced in hard processes occurring in proton and heavy ion collisions with large momentum transfer. In this domain (see chapter 1), the pQCD (perturbative Quantum ChromoDynamics), based on the Feynman's parton model [48] can be applied. This implies that hadron collisions can be considered as interactions of point-like constituents of nucleons namely quarks and gluons.

2.1.1 Direct photons

Direct photons are directly issued from parton-parton interactions via Compton scattering as one can see in the left Feynman's diagram of the Figure 2.1, similar to the Compton process in electromagnetism. To a lesser extend, at LHC energies, direct photons can also be produced via annihilation process [49], shown on the right Feynman's diagram of the Figure 2.1.

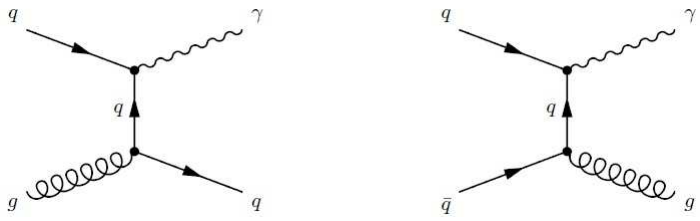

Figure 2.1: Feynman's diagrams for the direct photon production via Compton scattering (left plot) and annihilation (right plot)

The differential cross-section associated to the direct photon production, $\frac{d^2\sigma^{A+B\to\gamma+X}}{dp_T d\eta}$, can be expressed, following the factorization theorem [50], and the pQCD [18] as:

$$\frac{d^2\sigma^{A+B\to\gamma+X}}{dp_T d\eta} = \sum_{i,j=q,\bar{q},g} \int dx_1 dx_2 F_{i/h_1}(x_1,M) F_{j/h_2}(x_2,M) \frac{d^2\sigma^{i+j\to\gamma+X\prime}}{dp_T d\eta} \tag{2.1}$$

where:

- x_1 and x_2 represent the momentum fractions taken away by the interacting partons
- $F_{i/h_1}(x_1,M)$ and $F_{j/h_2}(x_2,M)$ are respectively the PDFs (Parton Distribution Functions) of the hadrons 1 and 2 involved in the collision. In the case of nucleus collision, $F_{i/h}(x,M)$ is the nuclear Parton Distribution Function (nPDF). These models are not specific to pQCD, they are universal.
- M represents the scales μ_R, μ_f et μ_F, respectively re-normalisation, factorisation and fragmentation scale, coming from the perturbative development of the QCD (Quantum Chromo-Dynamics) theory to determine cross-sections [18].
- $\frac{d\sigma^{i+j\to\gamma+X\prime}}{dp_T d\eta}$ is the differential cross-section, as a function of the transverse momentum and the pseudo-rapidity η, of the direct photon production in parton-parton interactions. This cross-section can be calculated in pQCD to a given order.
- η is the pseudo-rapidity defined in particle physics as $\eta = -ln(\frac{tan\theta}{2})$, where θ is the angle between the beam axis and the particle momentum; $\eta \to 0$ for particles carrying out mainly a transverse momentum whereas $\eta \to \infty$ for particle carrying out longitudinal momentum.

As mentioned in the introduction, this thesis work is dedicated to study direct photons in p-Pb collisions, and the differential cross section of their production is, in this particular case, expressed as:

$$\frac{d^2\sigma^{p+Pb\to\gamma+X}}{dp_T d\eta} = \sum_{i,j=q,\bar{q},g} \int dx_1 dx_2 F_{i/p}(x_1,M) F_{j/Pb}(x_2,M) \frac{d^2\sigma^{i+j\to\gamma+X\prime}}{dp_T d\eta} \tag{2.2}$$

where:

$F_{i/p}(x_1,M)$ represents the PDF of the proton and $F_{j/Pb}(x_2,M)$, the nPDF of the lead ion.

2.1.2 Fragmentation photons

At the first order, the parton-parton interaction is followed by fragmentation of an outgoing parton, which can produce photons and partons of lower energies before hadronisation. The associated Feynman's diagram is presented on the Figure 2.2.

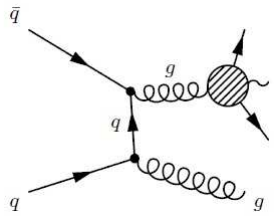

Figure 2.2: Feynman's diagram associated to the fragmentation photon production in the QCD theory

Like the direct photon production, the differential cross-section of the fragmentation photon production, $\frac{d^2\sigma^{A+B\to\gamma+X}}{dp_T d\eta}$, can be expressed through factorization theorem [50] with perturbative parts described by pQCD and non perturbative parts (PDFs, fragmentation function). It is defined as:

$$\frac{d^2\sigma^{A+B\to\gamma+X}}{dp_T d\eta} = \sum_{i,j,k=q,\bar{q},g} \int dx_1 dx_2 \frac{dz}{z^2} F_{i/h_1}(x_1,M) F_{j/h_2}(x_2,M) D_{\gamma/k}(z,Q^2) \frac{d^2\sigma^{i+j\to k+X\prime}}{dp_T d\eta} \tag{2.3}$$

As in the direct photon production equation (Eq.2.1):

- x_1 and x_2 represent the fractions of momentum taken away by the interacting partons and
- $F_{i/h_1}(x_1,M)$ and $F_{j/h_2}(x_2,M)$ are respectively the PDFs or the nPDFs of hadrons or nucleus involved in the collisions.
- M features the scales of the pQCD as in the equation 2.1.
- $D_{\gamma/k}$ is the parton-to-photon FF (Fragmentation Function) which is not in the perturbative regime.
- z is the momentum fraction taken by the photon during the fragmentation.

The fragmentation photon production can be expressed, in the particular case of p-Pb collisions, as:

$$\frac{d^2\sigma^{p+Pb\to\gamma+X}}{dp_T d\eta} = \sum_{i,j,k=q,\bar{q},g} \int dx_1 dx_2 \frac{dz}{z^2} F_{i/p}(x_1, M) F_{j/Pb}(x_2, M) D_{\gamma/k}(z, Q^2) \frac{d\sigma^{i+j\to k+X}}{dp_T d\eta} \tag{2.4}$$

The calculation requires the introduction of the nuclear parton distribution function associated to the lead nucleus. One can notice that the fragmentation function is independent of the considered collision system but relies on the energy involved in the collision.

2.1.3 Prompt photons as probes of the hadronic matter

Direct and fragmentation photons are produced in hard processes. We have seen that their cross-section production in proton or heavy ion collisions, can be calculated, via the pQCD, at a given order. Nevertheless, direct photons are issued from parton-parton interactions at the primary stage of the collision and, since photons are not sensitive to the hadronic medium, they are witness of this primary collision. Their energies are unchanged by crossing the medium. On the other hand, fragmentation photons are produced at a later stage of the collision following partonic interactions in the medium. This makes the production of fragmentation photons sensitive to the crossed medium and particularly to the QGP (Quark Gluon plasma) formation and its properties. One can also notice that direct photons are also interesting candidates for correlation study to determine parton energy loss in a medium of de-confined hadronic matter [51] [52] and especially enable to probe hadron suppression or jet quenching expected in the QGP.

Another key point is the dependence of the direct photon production cross-section (Eq.2.1) only on the theoretical models of the PDFs or nPDFs. Whereas, the fragmentation photon production cross-section (Eq.2.3) is also dependent on the fragmentation function and the momentum fraction carried by the photon. This makes the production of the direct photon cross-section measurement in heavy ion collisions a tool to constrain the PDFs or nPDFs models. Particularly, in the case of proton-proton collisions, the cross-section calculation only relies on the proton PDFs. A comparison with experimental measurements directly constrains theoretical requirements. In the case of p-Pb collisions which concern this thesis work, the cross-section depends on the PDF of the proton as well as the nPDF of the lead ions. This makes the cross-section associated to the direct photon production, the perfect tool for better understanding of the nPDFs (nuclear Parton Distribution Functions) of the lead ions, via the comparison with theoretical models and the determination of the nuclear modification factor, R_{pPb}. The latter enables to extract crucial information on cold nuclear matter effects which are still not fully understood [53] [54] [55].

Experimentally, the main challenge of this kind of study is to distinguish high energy direct photons from fragmentation ones. They have the same kinematic properties and their cross-sections, especially at the LHC's energies are of the same order of magnitude, as one can notice on the left plot of the Figure 2.3 where the proportion of fragmentation and direct photon contributions in the prompt photon production is presented as a function of the photon energy. The analyses use iso-

lation method to discriminate between direct and fragmentation photons as discussed in the next paragraph. We will also see that this method allows to reject a part of the background contamination due to photon from neutral meson decay which are produced in large quantities in proton and heavy ion collisions.

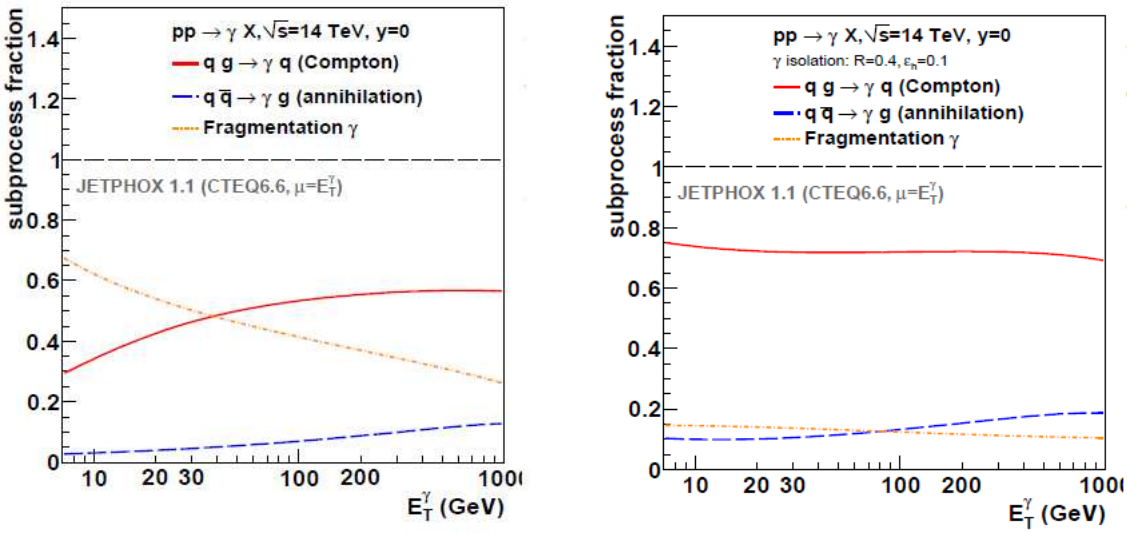

Figure 2.3: Contribution of inclusive prompt photon production (left plot) and isolated prompt photon (right plot) production depending on the considered sub-process, Compton, annihilation or fragmentation. Calculations have been performed in p-p collisions at $\sqrt{s_{NN}} = 14 TeV$ with JetPHOX [56] [57].

2.2 Isolation, a selective analysis method

2.2.1 Definition of the method

Figure 2.1 shows that the direct photons are emitted in the opposite direction of a parton, which will essentially fragment at the considered energies. On the contrary fragmentation photons are emitted into a jet particles and consequently they are surrounded by particles which will deposit their energy in detectors. The isolation method is based on this characteristic feature. The scheme in the Figure 2.4 illustrates the prompt photon production in parton-parton collisions.

One can define a cone around the photon in which the energy contribution is studied. The cone radius is defined as:

$$R = \sqrt{(\eta - \eta_\gamma)^2 + (\varphi - \varphi_\gamma)^2} \tag{2.5}$$

with:

- η_γ the pseudo-rapidity
- φ_γ the azimuthal angle of the photon as schematically shown in the Figure 2.5.

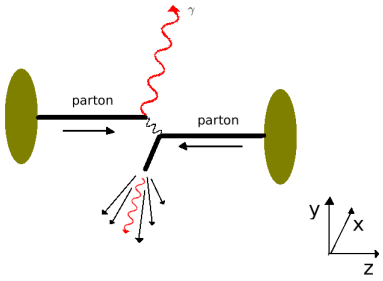

Figure 2.4: Scheme of a prompt photon production in parton-parton collision. The axis z is the beam axis. The plane (x,y) is the transverse plane which contains the transverse energy carried off by the photon. $E_T = \sqrt{E_x^2 + E_y^2}$ is the corresponding transverse energy.

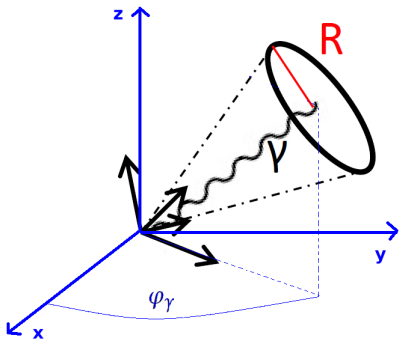

Figure 2.5: Scheme of isolation cone defined around a photon

The photon is considered as isolated when the energy inside the isolation cone is lower than an energy threshold E_T^{max}. The latter can be defined as an absolute threshold or as a threshold depending on the considered photon energy, $E_{T\gamma}$.

(2.6) $$\sum_i E_{T,i} < \epsilon E_{T\gamma} = E_T^{max}$$

where E_T^{max} is proportional to photon energy (ϵ fixed),
or

(2.7) $$\sum_i E_{T,i} = E_T^{iso} < E_T^{max}$$

where E_T^{max} is fixed.
This isolation definition can also be applied on the contribution of the particles momentum:

(2.8) $$\sum_i p_{T,i} = p_T^{iso} < p_T^{max}$$

which will be prefered when the isolation is performed by measuring also the charged particle energy contributions in the isolation cone.

This method allows to drastically decrease the contribution of fragmentation photons in the measurement, as it is shown in the Figure 2.3 (right plot). On the left figure, the contributions of the different sub-processes in the prompt photon production in pp collisions have been calculated with JetPHOX [56]. The fragmentation contribution is dominant at the lowest transverse energies and remains significant while increasing energies. On the right plot, the same calculation has been performed applying an isolation cut of $R = 0.4$ and $E_T^{max} = 0.1 E_T^{\gamma}$ to select the photon. The fragmentation contribution strongly decreases to about 10%. The expected behaviour in p-Pb collisions is expected to be the same. The cross-section would only be modified by nuclear effects as one will see in chapter 8.

The calculations of the contribution of direct and fragmentation photons in the photon production, using different isolation criteria, have been performed and are summarized in the Table 2.1. Comparing the results obtained with a fixed cone and different absolute thresholds with the results obtained with a fixed threshold and different isolation cone sizes, one can notice that the energy criteria is the most discriminant one. The selectivity of isolation criteria increases when the energy threshold decreases, as it could be expected. The isolation criteria based on threshold depending on photon energy enables to select around 85% of direct photons in the measurement and its selectivity is stable increasing photon transverse momentum, contrary to the case of fixed threshold criteria. Nevertheless this definition of the energy threshold will not be used in the analysis. Its common use in the theoretical calculations motivated its presentation in this thesis.

	Isolation cone					
	R<0.4			$\sum_i E_{T,i} < 5$ **GeV/**c		**R<0.4**
E_T^{γ}	$\sum_i E_{T,i} < 2$ **GeV/**c	$\sum_i E_{T,i} < 5$ **GeV/**c	$\sum_i E_{T,i} < 10$ **GeV/**c	**R<0.3**	**R<0.5**	$\epsilon = 0.1$
10-12	79%	66%	54%	66%	66%	85%
12-14	80%	67%	56%	67%	67%	85%
14-17	82%	70%	59%	70%	70%	85%
17-20	85%	73%	64%	73%	73%	86%
20-25	87%	76%	56%	76%	76%	86%
25-30	89%	79%	70%	79%	79%	86%
30-40	91%	82%	73%	82%	82%	86%
40-50	93%	86%	78%	86%	86%	87%
50-70	95%	89%	81%	89%	89%	87%

Table 2.1: Contribution in % of the direct photon process in the prompt photon production cross-section for different isolation criteria. Calculations have been performed with JetPHOX [56], the PDF CTEQ6.6 [58] and the FF BFGII [59] for a center of mass energy $\sqrt{s} = 7$ TeV in pp collisions.

2.2.2 Impact on background photon rejection

The main experimental source of background in the isolated photon analysis is the photon production from neutral meson decays. Neutral mesons like η (m = 548 MeV/c^2 [22]) and π^0 (m = 135 MeV/c^2 [22]) are produced in abundance in pp, p-Pb and Pb-Pb collisions. They both decay into photons. The π^0 decays via the channel $\pi^0 \rightarrow \gamma + \gamma$ with a branching ratio of almost 99%. The η decays to photons with a branching ratio of 72%, mainly via the channel $\eta \rightarrow \gamma + \gamma$ at 39% and $\eta \rightarrow \pi^0 + \pi^0 + \pi^0$ at 33%.

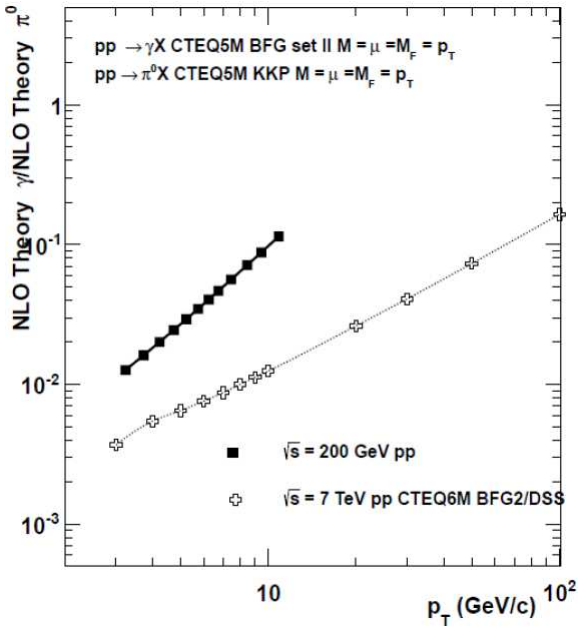

Figure 2.6: Ratio of the NLO pQCD calculations with INCNLO [60] for the direct photon production cross-section to the π^0 one depending on photon or π^0 transverse momentum.

In the Figure 2.6, the ratio of the direct photon cross-section to the π^0 one, from the pQCD calculations with INCNLO [60], is around 10^{-2} and decreases when the involved center-of-mass energy $\sqrt{s}$ increases. These photons from neutral meson decay constitute our main source of contamination in the measurement, mainly at low transverse momentum. However, they are mostly produced into jets and consequently they are not isolated from the energy deposit from hadrons. The isolation cut, enables to reduce its contribution. Moreover, the topology of the decay of the neutral mesons, associated to the calorimeter properties, allows to reject such clusters. The remaining contamination is estimated via the determination of the purity which will be more detailed and discussed in the chapters 5 and 7.

The choice of the isolation criteria to be used in the analysis is mainly constrained by the experimental conditions. Indeed, looking at the Table 2.1, one could choose to apply an energy isolation criterion with the highest selectivity, as an energy threshold depending on the photon energy ($\sum_i E_{T,i} < \epsilon E_{T\gamma} = E_T^{max}$ or $\sum_i p_{T,i} < \epsilon p_{T\gamma} = p_T^{max}$) but such tight criterion could lead to reject some direct photons of low cross-section production in the measurement. In the present analysis, the iso-

lation criteria are $R < 0.4$ and $\sum_i p_{T,i} < 2$ GeV/c which represent a good compromise between the direct photon selectivity and the measurement efficiency. This will also enable a direct comparison between the isolated photon measurement in pp and in p-Pb collisions with the ALICE experiment. The process which has led to choose this criteria is detailed in chapter 6.

2.3 State-of-the-art of the isolated photon measurement

In this section, we will present some main results of isolated photon measurements to illustrate the present knowledge and what it can bring.

One has to notice that many isolated photon measurements have been performed as part of the Higgs boson analysis at LHC [5] [6] [7]. Indeed, one of the preferred channels for this study is the invariant mass determination via the channel $H^0 \rightarrow \gamma + \gamma$ [22].Its associated cross-section implies that the background in the measurement has to be very carefully studied. Direct photons, due to their kinematics properties, constitute one of these background sources.

LHC				
Experiment	$\sqrt{s}$	**Luminosity**	E_T **range**	η **range**
pp collisions				
CMS [28]	2.76 TeV	231 nb^{-1}	20 GeV/c< E_T< 80 GeV/c	$\|\eta\| < 1.44$
[61]	7 TeV	2.9 pb^{-1}	21 GeV/c< E_T< 300 GeV/c	$\|\eta\| < 1.45$
[62]		36 pb^{-1}	25 GeV/c< E_T < 400 GeV/c	$\|\eta\| < 2.5$
ATLAS [63]	7 TeV	880 nb^{-1}	15 GeV/c< E_T<100 GeV/c	$\|\eta\| < 1.37$ $1.52 \leq \|\eta\| \leq 1.81$
[64]		35 pb^{-1}	45 GeV/c≤ E_T< 400 GeV/c	$\|\eta\| < 1.37$ $1.52 \leq \|\eta\| < 2.37$
[65]		4.6 fb^{-1}	100 GeV/c≤ E_T ≤1000 GeV/c	$\|\eta\| < 1.37$ $1.52 \leq \|\eta\| \leq 2.37$
[66]	8 TeV	20.2 fb^{-1}	25 GeV/c< E_T<1500 GeV/c	$\|\eta\| < 1.37$ $1.56 \leq \|\eta\| \leq 2.37$
ALICE [67]	7 TeV	35 pb^{-1}	10 GeV/c< E_T<60 GeV/c	$\|\eta\| < 0.27$
Pb-Pb collisions				
CMS [28]	2.76 TeV	6.8 μb^{-1}	20 GeV/c< E_T< 80 GeV/c	$\|\eta\| < 1.44$
ATLAS [68]	2.76 TeV	0.14 nb^{-1}	22 GeV/c≤ E_T< 280 GeV/c	$\|\eta\| < 1.37$ $1.52\|\eta\| < 2.37$

Table 2.2: Isolated photon measurements performed at the LHC at different center of mass energy and with the different experiments.

An extensive summary of the isolated photon measurements, already performed at Tevatron, RHIC (Relativistic Heavy Ion Collider) and SPS (Super Proton Synchrotron) can be found in [49]. These results [69] [70] [71] [72] [73] [74] [75] [76] [77] [78] [79] have shown a good agreement with the pQCD calculation at the next-to-leading-order for all the considered center-of-mass energies ranging from $\sqrt{s}$ = 200 GeV to $\sqrt{s}$ = 1.96 TeV, except for the experiment E706 at Tevatron [80] [81] [82]. Indeed, in this last one, which is an experiment on fixed target, in p-p and p-Be collisions,

the measured direct photon cross-section was significantly higher than the theoretical predictions. These observations, not supported by any other experiment neither theoretical predictions, are not taken into account to constrain the models and seem to come from experimental problems which have led to underestimate the associated uncertainties [49].

The isolated photon production cross-section increases with the considered center-of-mass energy. The contribution to the direct photon production from the annihilation process becomes negligible and the production of decay photons increases.

In the Table 2.2, the isolated photon measurements, performed at the LHC have been summarized. The isolation criteria have not been reported since the choice is to a large extent dependent on the detector properties. One has to notice that no isolated photon measurement in heavy ion collisions, or proton-heavy ion collisions, has been performed before the LHC start up. The first published results from CMS and ATLAS in pp collisions at $\sqrt{s}$ = 7 TeV have already allowed to constrain the PDFs [49].

The ALICE measurement in pp collisions [67] will be described in detail in Part III, *Isolated photon study in p-Pb collisions*. As one can see in the Figure 2.7, the results are consistent with the theoretical calculations performed with JetPHOX [56]. The measurement in p-Pb collisions constitutes this thesis work.

The latest results from CMS at $\sqrt{s}$ = 2.76 TeV in pp and Pb-Pb collisions have been highlighted in the Figure 2.8. The CMS results from the pp and Pb-Pb collisions at $\sqrt{s}$ = 2.76 TeV [28] are shown, as well as the corresponding R_{AA}. Both measurements are in a good agreement with the pQCD calculation at NLO (Next-to-Leading-Order). The R_{AA} results are compatible with unity, as expected, leading to a validation of the nuclear overlap function used to scale the cross-section measured in heavy ion collisions. Its values as a function of the considered photon p_T are compatible with the calculated values using different PDF and nPDF models.

The results of isolated photon cross-section from the ATLAS experiment in pp collisions at $\sqrt{s}$ = 8 TeV [66] are presented for different rapidity ranges in the Figure 2.9. The comparison with theoretical calculations from pQCD at NLO, performed with JetPHOX and PETER [84] with the CT10 [83] PDF show a good agreement within the error bars.

All the performed measurements have already allowed to refine the PDF. The ALICE experiment at LHC will enable to complete the scanned p_T range by going to lower values. The p-Pb measurement is the first one in such collision system and will probe the nuclear effects. These measurements, and especially the p-Pb one, will be described in detail in the next parts.

In this chapter we have presented the prompt photon, direct and fragmentation, production mechanisms in high energy parton interactions. We are particulary interesting by direct photons which are not affected by the crossed hadronic medium. The cross-section associated to their production, directly related to the models of PDF or nPDF, is a tool to test or to constrain theoretical predictions. In heavy ion collisions or proton collisions at high energies, the kinematic properties of prompt photons are

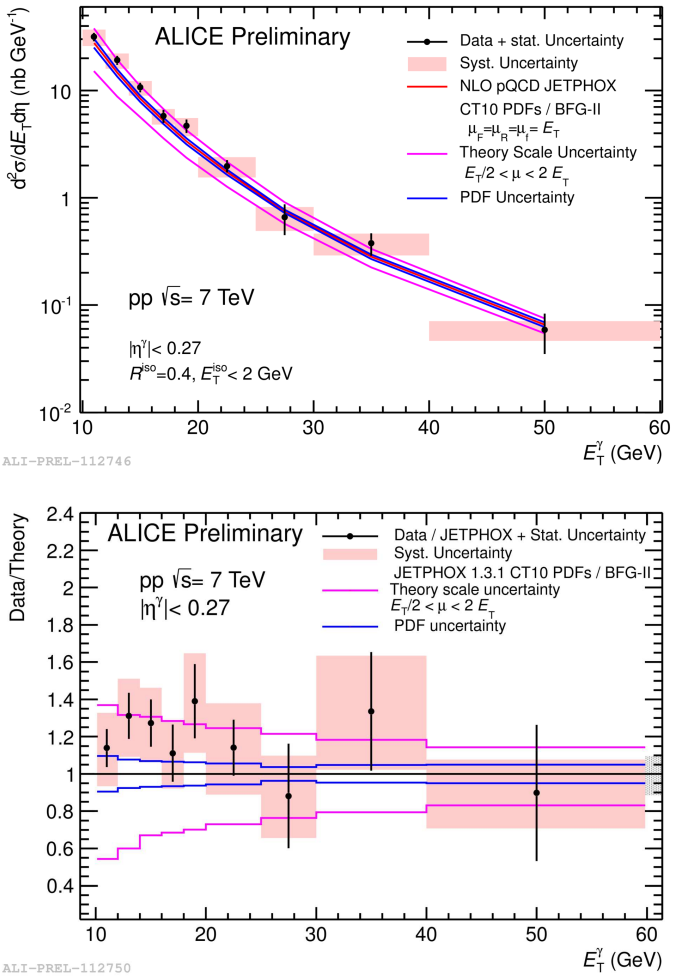

Figure 2.7: On the top plot, the differential isolated photon cross-section measured in pp collisions at $\sqrt{s}$ = 7 TeV with the ALICE experiment [67]. The theoretical calculation from JetPHOX are shown. On the bottom plot, the ratio of the cross-section results to the calculations performed with JetPHOX.

identical. In order to reject fragmentation photons, which are believed to be emitted in a jet of particles, the isolation method is used. Photons whose energy in a cone is above an energy threshold are removed from the measurement. This allows to drastically decrease the fragmentation photon yield and to reject the main part of the background issued from neutral meson decays. The already performed measurements of isolated photons have shown an agreement between experimental cross-sections and theoretical predictions. The isolated photon measurement in p-Pb collisions we will present here, is the first one at the LHC.

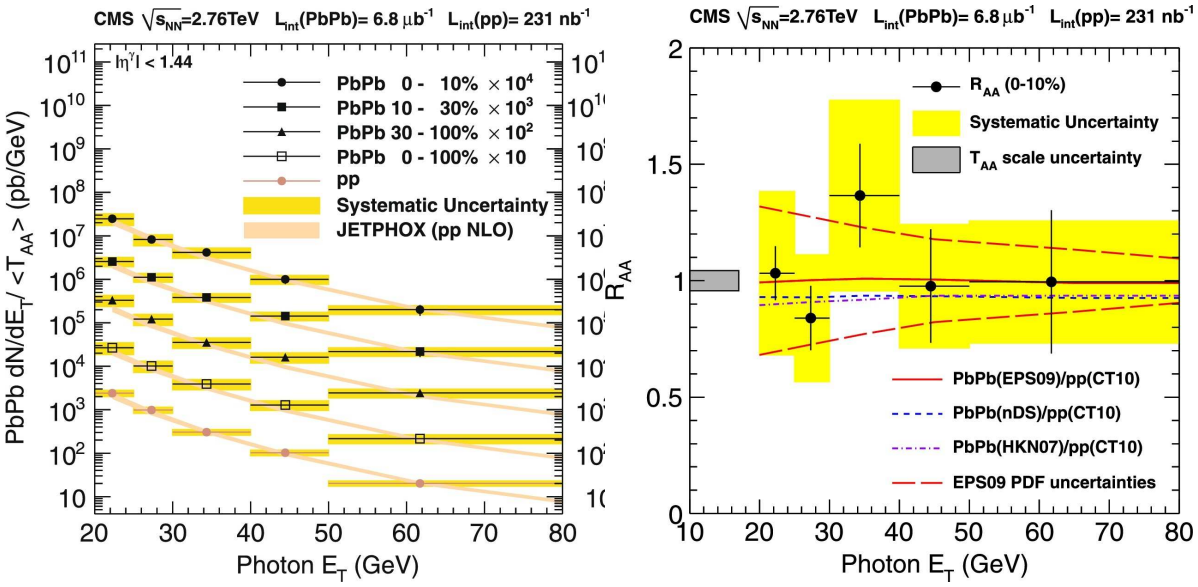

Figure 2.8: On the left, the differential isolated photon cross-section measured in pp and Pb-Pb collisions at $\sqrt{s} = 2.76$ TeV with the CMS experiment. The theoretical calculation from JetPHOX are shown. On the right plot, the corresponding R_{AA} is plotted as well as the expected values of the ratio of the calculations performed with JetPHOX for Pb-Pb and pp collisions [28].

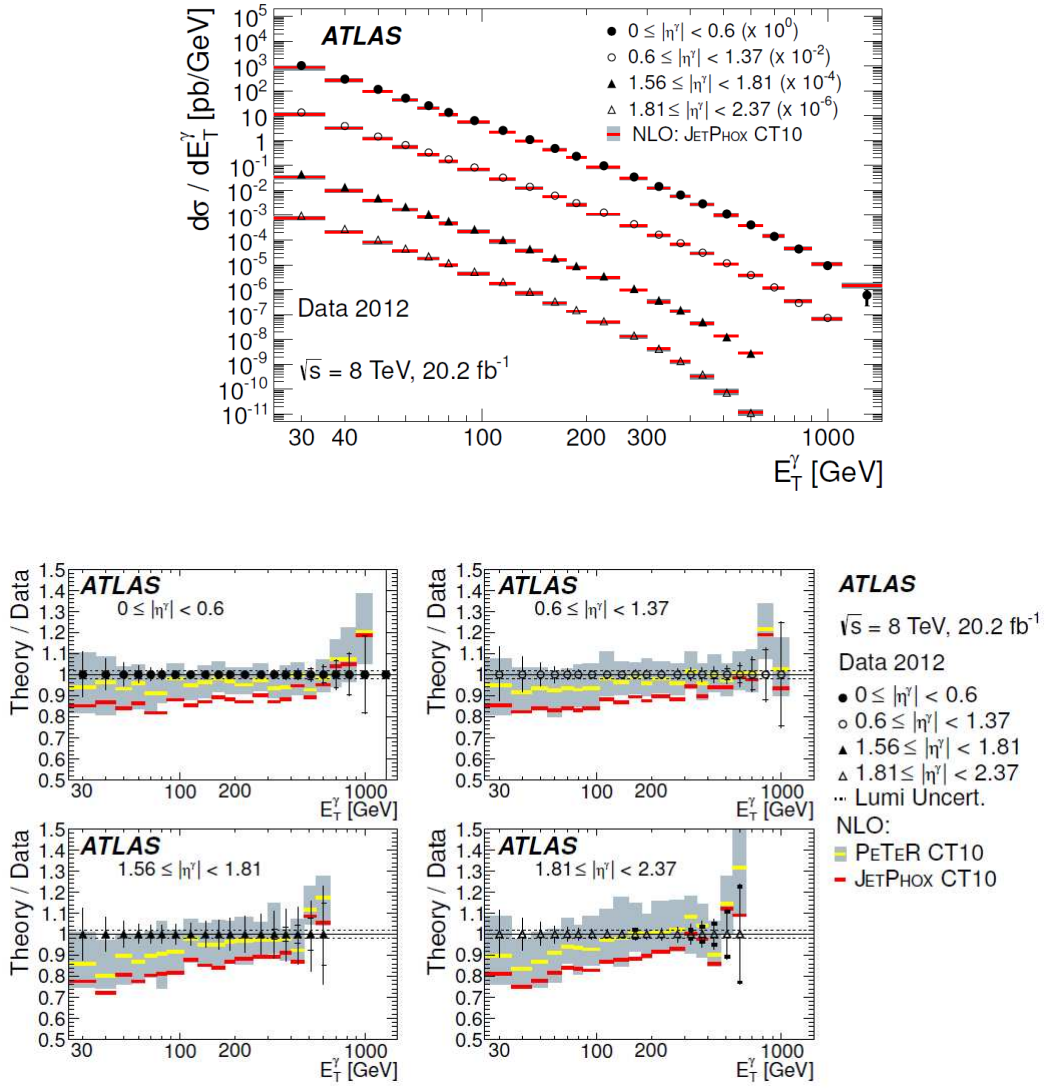

Figure 2.9: On the top plot, the differential cross-section measurement in pp collisions at $\sqrt{s} = 8$ TeV for different rapidity ranges is presented [66]. On the bottom plot, the ratio of the theory over the data is plotted. The theoretical calculations have been performed with JetPHOX and PeTeR and the PDF CT10 [83].

Part II

Experimental context

CHAPTER 3

A Large Ion Collider Experiment at the LHC

Contents

In this chapter, we present the Large Hadron Collider where protons or heavy ions collide after being accelerated. The main experiments situated at the interaction points are described by focusing on their specifities with respect to isolated photon measurements using electromagnetic calorimeters. A focus is made on the ALICE experiment. The properties of the detectors involved in the isolated photon analysis are highlighted. The data taking and reconstruction procedures are briefly described.

3.1 The Large Hadron Collider

3.1.1 Brief introduction

The LHC (Large Hadron Collider) [8], located at the French-Swiss border near Geneva and hosted by CERN (Centre européen pour la recherche nucléaire), is the most powerful particle accelerator existing in the world with its 27 km circumference. It enables to reach energies of the order of ten TeV.

The timeline below, summarizes the long history of the collider at CERN which has led to the construction of the LHC facility. The first collider, the Synchrocyclotron, reached an energy of 600 MeV while the LHC is designed to collide hadrons to an energy in the center-of-mass up to 14 TeV. The SC represents the SynchroCyclotron, PS the Proton Synchrotron, SPS the Super Proton Synchrotron and LEP the Large Electron-Positron collider.

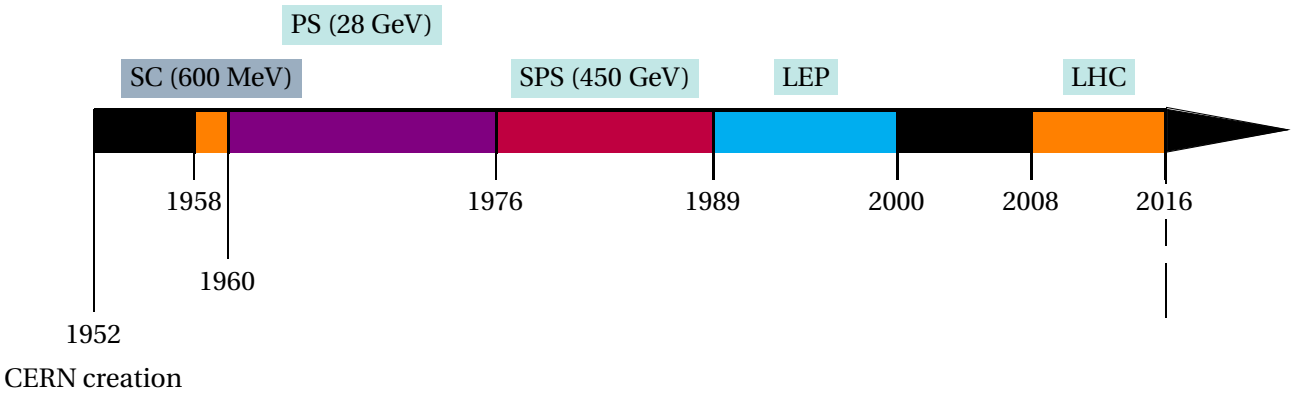

The LHC was mainly devoted to the Higgs boson physics at its beginning, leading to a collision program dedicated to p-p collisions. This collider also provides lead beams to study the nuclear matter in extreme thermodynamic conditions with the aim to provide a better knowledge of the hadronic medium and of the strong interaction.

The LHC was turned on in 2008. After an incident, it has been stopped and restarted in 2009 to reach the energy $\sqrt{s}$ = 7 TeV in 2010. The first data taking, called RunI, by the different experiments has started and lasted until 2013. It has been followed by the first long shutdown period (LS1) which enabled to upgrade the dectectors to perform with an increased delivered luminosity and with an increased center-of-mass collision energy. The second period of data taking, RunII, has started in 2015 and should stop in 2018 for LS2.

During the RunI data taking period, pp collisions were achieved with $\sqrt{s}$ = 2.76 TeV, 7 TeV and 8 TeV, while Pb-Pb collisions with $\sqrt{s}$ =2.76 TeV and p-Pb ones with $\sqrt{s}$ = 5.02 TeV. After two years of shut-down at the LHC, the Run2 data taking has started with $\sqrt{s}$ = 13 TeV in p-p collisions and $\sqrt{s}$ = 5 TeV in Pb-Pb collisions while in a second run of p-Pb collisions, at $\sqrt{s}$ values of 8 TeV and 5 TeV is expected for the end of 2016.

In the next subsection, we briefly describe the proton and lead beam generation before their injection in the LHC.

3.1.2 LHC beam production

Before the beam injection in the LHC, different steps are necessary to reach an energy of the TeV order. Protons come from a hydrogen source where an electric field allows to extract electrons. In Linac 2 (Linear accelerator 2), an alternating positive and negative conductors enable to accelerate protons while quadrupoles focus the produced beam. Linac 2 will be replaced by the upgraded Linac 4 after 2020 to increase the reachable beam energy. Afterwards the proton beam is injected in the PS (Proton Synchrotron) booster to be accelerated until 1.4 GeV due to 4 superposed synchrotron rings.

The ions $^{208}_{82}Pb^{+82}$ are produced by evaporation of a pure lead solid source. The lead gas is ionized in order to create a plasma from which the produced lead ions are extracted. After their extraction, they go through Linac 3 (Linear accelerator 3) where they are accelerated by alternately positively and negatively charged conductors. Superconductor magnets enable to focus the created

beam. Then the beam passes through the LEIR (Low Energy Ion Ring) where it is transformed into bunches at 72 MeV to be injected in the LHC.

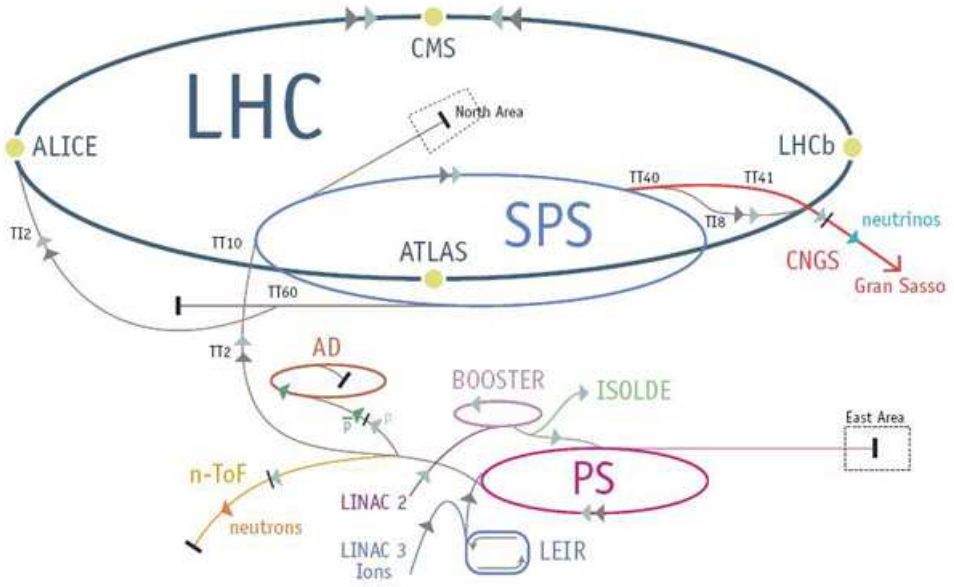

Figure 3.1: Detailed view of the Large Hadron Collider beam acceleration chain.

After these specific first steps, the path taken by the proton and the lead beams are similar. They are injected in the PS ring composed of 277 magnets. This enables to accelerate the beams up to 25 GeV. The next step, the last one before the LHC, is the injection in the SPS (Super Proton Synchrotron). The SPS, with its nearly 7 km circumference, composed of thousands of magnets allows the beam acceleration up to 450 GeV and the injection in the LHC ring. The LHC ring is composed of 2 pipes where the beams circulate in the opposite direction, with crossing pipe at the interaction points corresponding to the place where the LHC experiments are installed. The ultra-high vacuum is maintained in the beam pipes and thousands of supra-conducting magnets, at a temperature value near 0 K, are used to create a strong magnetic field to guide and to accelerate the beam. Some magnets are used near the interaction point in order to focus the beams and enable them to collide. The Figure 3.1 illustrates the acceleration chain of the LHC beams.

3.1.3 Luminosity delivered by the LHC

The collider performance can be quantified via the luminosity that it can deliver, i.e. the number of collisions produced per cm^2 and per second. It depends on the beam parameters, its energy as well as its geometry.

The luminosity can be expressed as [8]:

$$L = \frac{N_p N_{Pb} k_b f_{rev} \gamma F}{4\pi \epsilon_n \beta^{ast}} \tag{3.1}$$

where:

- N_p and N_{Pb} are respectively the number of proton/lead per bunches,
- k_b the number of bunches per beam,
- f_{rev} the revolution frequency,
- $\gamma = E/(m_0c^2)$ the Lorentz factor,
- ε_n the emittance,
- β^* the beta function at the collision point and
- F is a corrective factor which depends on the crossing angle at the interaction point.

The luminosity is not constant during a run of data taking, which leads to a loss in the intensity and the emittance of the beams and constrains the beam lifetime. In the Table 3.1, the RunI colliding systems, the reached energies and the corresponding luminosities are summarized.

Colliding system	Year	Energy	Integrated luminosity
p-p	2009	$\sqrt{s_{NN}}$ = 0.9 TeV	$L^{int} = 19.6\mu b^{-1}$
		$\sqrt{s_{NN}}$ = 2.36 TeV	$L^{int} = 0.87\mu b^{-1}$
	2010	$\sqrt{s_{NN}}$ = 0.9 TeV	$L^{int} = 0.31nb^{-1}$
		$\sqrt{s_{NN}}$ = 7 TeV	$L^{int} = 0.5pb^{-1}$
	2011	$\sqrt{s_{NN}}$ = 2.76 TeV	$L^{int} = 46nb^{-1}$
		$\sqrt{s_{NN}}$ = 7 TeV	$L^{int} = 4.9pb^{-1}$
	2012	$\sqrt{s_{NN}}$ = 8 TeV	$L^{int} = 9.7pb^{-1}$
	2013	$\sqrt{s_{NN}}$ = 2.76 TeV	$L^{int} = 129nb^{-1}$
Pb-Pb	2010	$\sqrt{s_{NN}}$ = 2.76 TeV	$L^{int} = 9\mu b^{-1}$
	2011	$\sqrt{s_{NN}}$ = 0.9 TeV	$L^{int} = 146\mu b^{-1}$
p-Pb	2013	$\sqrt{s_{NN}}$ = 5.02 TeV	$L^{int} = 14.9nb^{-1}$
Pb-p	2013	$\sqrt{s_{NN}}$ = 5.02 TeV	$L^{int} = 17.1nb^{-1}$

Table 3.1: Summary of the different colliding beams delivered by the LHC depending on the year during RunI [85]. The corresponding energy in the center-of-mass as well as the delivered luminosity are provided. One has to notice that during the pp and the minimum bias data taking in p-Pb collisions ($L^{int} = 0.891nb^{-1}$), the ALICE luminosity was reduced to enable detectors to safely operate.

It should be stressed that the luminosity delivered by the LHC is higher than what can be effectively registered by the ALICE experiment. In the section 3.2.2, we will explain how the luminosity is experimentally determined in the ALICE detector.

3.1.4 LHC experiments

The LHC provides colliding particle beams for different experiments. The main ones are CMS (Compact Muon Solenoid) [86], ATLAS (A Toroidal LHC ApparatuS) [87], LHCb (Large Hadron Collider

beauty experiment) [88] and ALICE [89]. One has to notice that two smaller experiments are also located on the LHC ring, LHCf (Large Hadron Collider forward) [90] and TOTEM (TOTal cross-section, Elastic scattering and diffraction Measurement) [91]. The next section is dedicated to the ALICE experiment, which has provided the data used in this thesis work. In the following description of the experiments and their characteristics, we will more focus on the properties with respect to the isolated photon measurements with electromagnetic calorimeters.

- **CMS (Compact Muon Solenoid)** (Figure 3.2) is one of the two general purpose LHC experiments. It is mainly dedicated to the Higgs boson physics and the physics beyond the standard models. Heavy ion program is also included. The main particularity of CMS is the supraconductor solenoid which enables to reach 3.8 T in order to have a precise measurement of the track momentum.

  The electromagnetic calorimeter, ECAL [92], is made of lead tungsten crystal (PbWO4). It is divided in two parts. The one in the central barrel enables to access the most central pseudorapidity, $|\eta| < 1.48$ whereas two other parts are located at forward and backward pseudorapidity ranges, $1.48 < |\eta| < 3$. In order to discriminate the two photons coming from the π^0 decay, two sampling calorimeters, constituted of one layer of lead and a layer of silicon tracking sensor have been added at forward and backward angles ($1.65 < |\eta| < 2.6$) in front of the calorimeter. The granularity associated to ECAL is $\Delta\eta \times \Delta\Phi = 0.0174 \times 0.0174$. These properties and the luminosity of the order of pb^{-1} enable the CMS electromagnetic calorimeter to perform high energy photon measurement, from 20 to 300 GeV/c (see chapter 4).

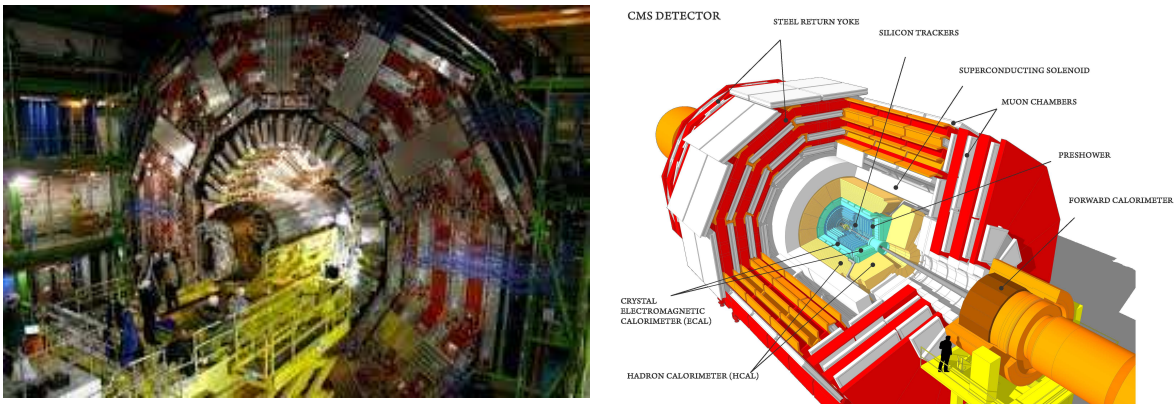

Figure 3.2: On the left: photography of CMS experiment. CERN©. On the right: detailed view of the CMS detector.

- **ATLAS (A Thoroidal LHC ApparatuS)** (Figure 3.3) detector is the largest one on the LHC ring. It is the oter general purpose LHC experiment mainly dedicated to the Higgs boson physics and the physics beyond the standard model. Heavy ion collision program is also performed.

  Its electromagnetic calorimeter, the Liquid Argon Calorimeter (Lar) [93], is a sampling calorimeter constituted of layers of liquid argon and layers of lead which cover the $|\eta| < 3.2$ pseudo-

rapidity domain divided into two parts, one in the central barrel, in the pseudo-rapidity $|\eta| < 1.5$ and two end-caps in the range $1.4 < |\eta| < 3.2$. The azimuthal coverage is maximal. The calorimeter is made of three layers and a pre-sampler. The granularity depends on the considered layer and the pseudo-rapidity range, from $\Delta\eta \times \Delta\Phi = 0.1 \times 0.1$ in $2.5 < |\eta| < 3.2$ for the second layer to $\Delta\eta \times \Delta\Phi = 0.025 \times 0.025$ in $|\eta| < 1.40$. This detector design, associated to a high luminosity of the order of tenths of pb^{-1}, allows to perform photon measurements until energies of 400 GeV/c.

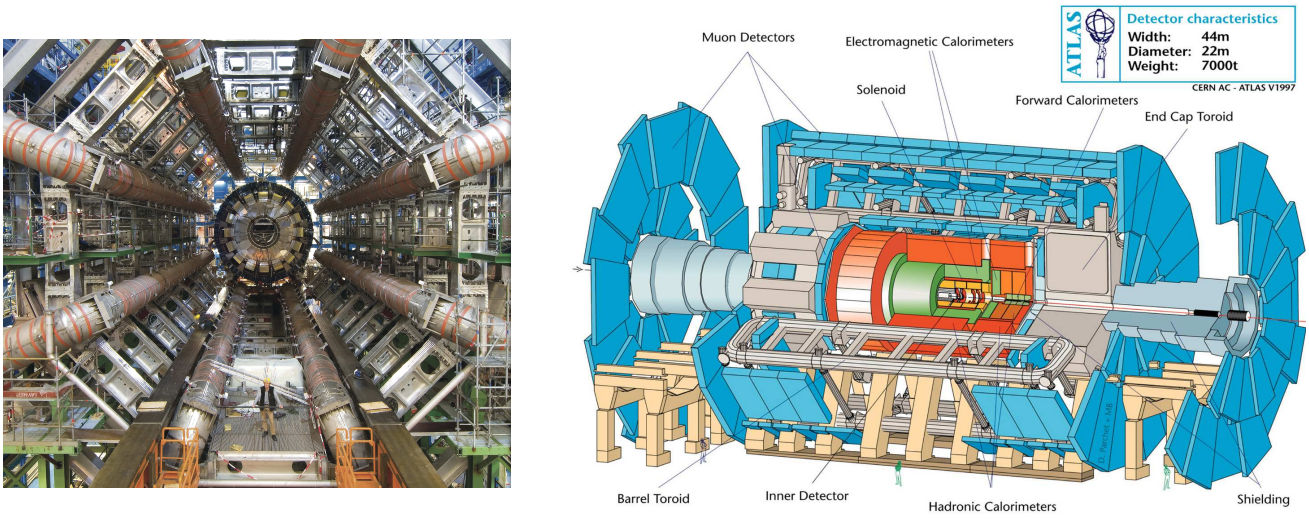

Figure 3.3: On the left: photography of ATLAS detector. CERN©. On the right: detailed view of the ATLAS detector.

- **LHCb (Large Hadron Collider beauty experiment)** (Figure 3.4) is dedicated to the CP violation study using the b quark production properties and also includes a heavy ion program since RunII data taking. Contrary to ATLAS, CMS (and the central barrel of ALICE, see section 3.2), the LHCb detector is not located around the interaction point. It is designed to measure particles with small angles with respect to the beam at the forward region and enables a high precision vertex measurement. An electromagnetic calorimeter (ECAL) [94] is composed of scintillating tiles and lead plates. Its acceptance is $0.025 < \Theta_x < 0.3$ and $0.025 < \Theta_y < 0.25$.

The characteristics of the CMS and the ATLAS calorimeters, which have already performed isolated photon measurements at the LHC, are summarized in the Table 3.2. These calorimeters have been mainly designed to perform the analysis of the Higgs boson via its decay to high energy photons. For this purpose, they allow a good discrimination of background and prompt photons. However their energy resolution does not allow measurements at an energy range as low as in the ALICE experiment (see next chapter).

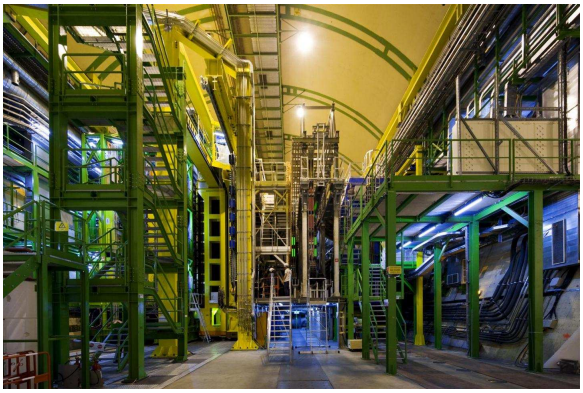

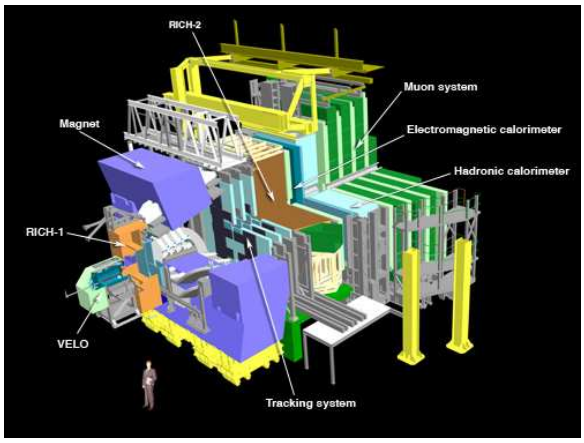

Figure 3.4: On the left: photography of the LHCb detector. CERN©. On the right: detailed view of the LHCb experiment and its sub-detectors.

Experiment	**Calorimeter**	**Type**	**Rapidity**	**Granularity** $\Delta\eta \times \Delta\varphi$
CMS	ECAL	$PbWO4$	$\lvert\eta\rvert < 1.48$ $1.48 < \lvert\eta\rvert < 3$	0.0174×0.0174
	Sampling calorimeter	layer of lead and silicon tracking sensor	$1.65 < \lvert\eta\rvert < 2.6$	
ATLAS	Lar	sampling calorimeter layers of liquid Argon pre-sampler	$\lvert\eta\rvert < 1.5$ $1.4 < \lvert\eta\rvert < 3.2$	depend on layer and rapidity from 0.1×0.1 in $2.5 < \lvert\eta\rvert < 3.2$ to 0.025×0.025 in $\lvert\eta\rvert < 1.40$

Table 3.2: Summary of characteristics of the CMS and the ATLAS calorimeters

3.2 A Large Ion Collider Experiment

The study of the QGP has motivated the heavy ion physicist community to elaborate a project at the LHC, ALICE (A Large Ion Collider Experiment). ALICE is dedicated to hadronic matter study under extreme conditions where the formation of the QGP is expected. This state is experimentally reachable via heavy ion collisions. In such collisions, the particle multiplicities are very large.

ALICE was designed to measure high multiplicity of charged particles, up to 8000 [95] [96]. This led to specific constrains for the detector systems. The first proposal was presented in 1993. The experiment was officially approved on February 14^{th}, 1997. The detector was built re-using the L3 magnet from the LEP (Large Electron-Positron collider). Its properties allow ALICE to measure soft as well as hard probes of the QGP (Quark Gluon plasma), with the order of magnitude of energy ranging from tenths of MeV/c to hundreds of GeV/c. The ALICE experiment took its first data in 2009. The collaboration associated to the experiment is currently constituted from more than 1600 members from 159 institutes in 43 countries.

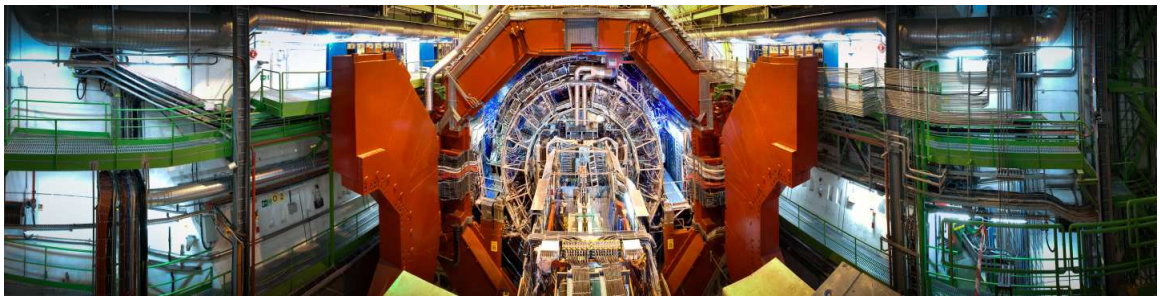

Figure 3.5: Photography of the ALICE detector in the cavern. CERN©

3.2.1 The ALICE sub-detectors

The ALICE detector is composed of different sub-detectors, as shown in the Figure 3.6, which can be divided in different categories depending on whether they are placed in the ALICE central barrel or at higher rapidities. One has to notice that the side of the ALICE detector, located at forward rapidities, is called A side whereas the opposite one, at backward rapidities is called C side. The ALICE central barrel is surrounded by a solenoid which enables to maintain a weak electromagnetic field of 0.5T.

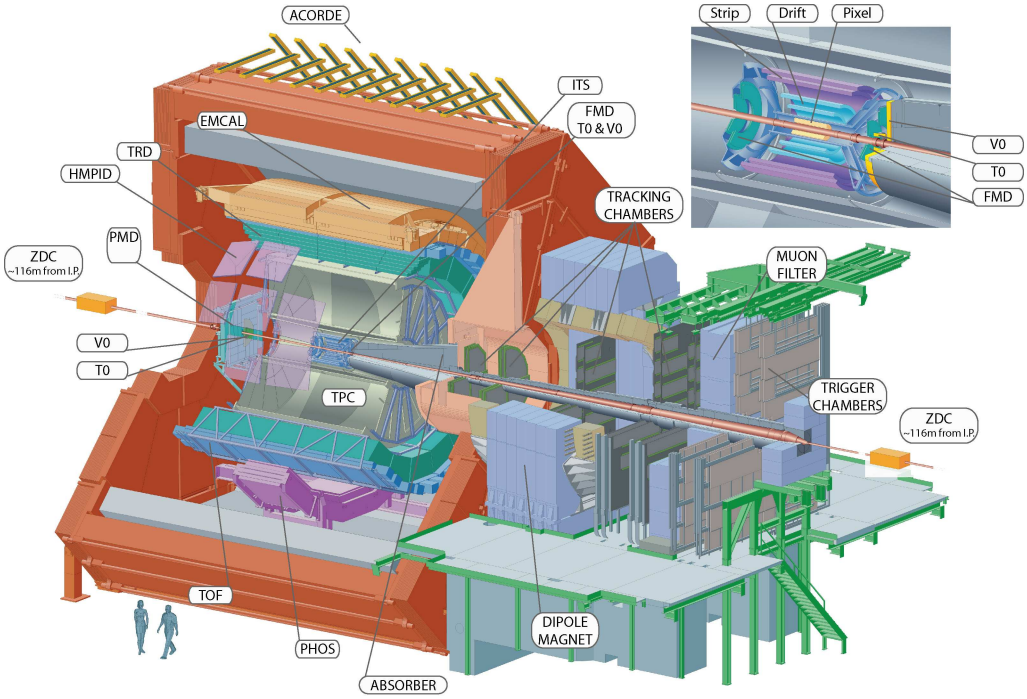

Figure 3.6: Detailed view of the ALICE detector

In this section, we will more focus on discussing the properties of the detectors which are used in the isolated photon analysis presented in this thesis. The next chapter 4 will be dedicated to the electromagnetic calorimeter (EMCAL) which is the key detector of the analysis.

- **Central barrel detectors**

  - ***ITS (Inner Tracking system)*** [97]. It is composed of six layers, two layers of SPD (Silicon Pixel Dectector) at $|\eta| < 2.0$ and $|\eta| < 1.4$, two of the SDD (Silicon Drift Detector) at $|\eta| < 0.9$ and two of the SSD (Silicon Strip Detector) at $|\eta| < 1$. The two innermost layers (SPD), enable to determine the primary vertex interaction point from which the most of tracklets are derived. The energy loss (dE/dx) in the silicon layer detectors enables to perform the charged particle tracking as well as the particle identification. The characteristic energy loss of the particles in the ITS is plotted in the Figure 3.7 (left plot).

  - ***TPC (Time Projection Chamber)*** [98]. It allows the particle tracking and identification via the trajectory and the characteristic energy loss dE/dx, as shown in Figure 3.7 (right plot). It is filled with a gas mixture Ne+CO_2 in RunI and Ar+CO_2 in RunII, and composed of a central cathode at -100 kV and multi-wire proportional chambers. It is the main detector of the ALICE central barrel with its particle identification and tracking performance which is efficient from 0.1 GeV/c to 100 GeV/c. The TPC covers the pseudo-rapidity range $|\eta| < 0.9$.

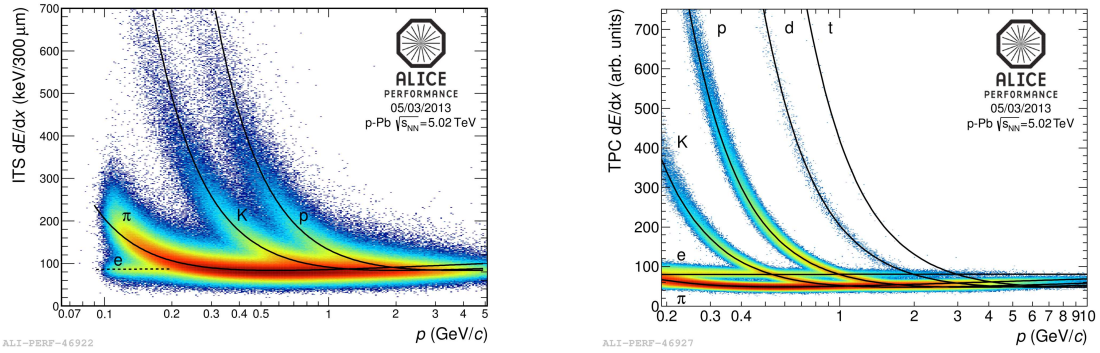

Figure 3.7: Characteristic energy loss, dE/dx in the ITS (left plot) and in the TPC (right plot) versus the particle momentum p in p-Pb collisions at $\sqrt{s_{NN}}$ = 5.02 TeV. The expected values for pions, electrons, kaons and protons are represented by the black lines.

  - **HMPID (High Momentum Particle Identification)** [99]. This detector is a ring imaging cherenkov detector which enables to identify hadrons at intermediate momenta using C_6F_{14} as liquid radiator and CsI photocathode. Its acceptance is $|\eta| < 0.6$ in pseudo-rapidity and $1° < \Phi < 59°$ in azimuthal angle.

  - **TOF (Time Of Flight)** [100]. Such a detector measures the arrival time of particles, in association with T0 as trigger system, in order to identify hadrons at intermediate momenta using Multi-gap Resistive Plate Chamber. It covers the pseudo-rapidity range $|\eta| < 0.9$.

  - **TRD (Transition Radiation Detector)** [101]. It allows electron identification with $p_T > 1$ GeV/c in association with TPC and ITS. It is mainly composed of a radiator where transition photons are emitted by electrons and absorbed by a gas mixture ($Xe + CO_2$) and

drifts chambers enabling the tracking of charged particles. It covers the pseudo-rapidity range $|\eta| < 0.8$.

- **PHOS (PHOton Spectrometer)** [102]. A high resolution photon spectrometer composed of lead-tungsten $PbWO_4$ crystals covering a pseudo-rapidity range $|\eta| < 0.12$ and azimuthal angles $260° < \Phi < 320°$. It is particularly designed to study neutral mesons, π^0 and η at low and intermediate p_T as well as thermal photons (low p_T photons).
- ***EMCal (ElectroMagnetic Calorimeter)*** [103] [104]. This detector is constituted of layers of lead and scintillator in which the electromagnetic particles lose their energy via a combination of bremsstrahlung radiation and pair creation. It covers a pseudo-rapidity range $|\eta| < 0.7$ and azimuthal angle $80° < \Phi < 187°$. This electromagnetic calorimeter has been completed by the DCal (Di-jet Calorimeter), at the opposite in the beam pipe, during the long shut-down before the RunII. Located around PHOS and covering an acceptance $260° < \Phi < 327°$ and $|\eta| < 0.7$ (including PHOS η acceptance), it will enable to study di-jet events and photon/π^0-jet events. The next chapter (4) is dedicated to EMCal which is the main detector involved in the isolated photon analysis.
- **ACORDE (ALICE COsmics Ray DEtector)** [105]. This scintillator based detector is located on top of the magnet in order to trigger on cosmic ray events. It covers an acceptance $|\eta| < 1.3$ and $30° < \Phi < 150°$. This particular detector is usually not used to take data during beam collisions (except in 2012 during p-p collisions, some cosmic ray events have been recorded in parallel to collisions events).

- **Forward detectors**

  - **ZDC (Zero Degree Calorimeter)** [106] allows to determine the centrality of heavy ion collisions via the measurement of the spectator nucleons. In order to count the number of neutron and proton spectators, two tungsten quartz neutron calorimeters and two brass quartz proton calorimeters are located symmetrically with respect to the interaction point. A lead quartz electromagnetic calorimeter, composed of two modules placed symmetrically in azimuth angle, is used to distinguish the most central collisions, with few spectators, and the most peripheral ones, with most of the nucleons bound in nuclear fragments. The neutron calorimeters cover the pseudo-rapidity range $|\eta| > 8.8$, the proton calorimeter acceptance is $6.5 < |\eta| < 7.5$ and $10° < \Phi < 10°$ and the electromagnetic calorimeter covers the acceptance $4.8 < \eta < 5.7$ and $|2\Phi| < 32°$.
  - **PMD (Photon Multiplicity Detector)** [107] is composed of gas counters which enable to detect photons after passing through a converter initiating an electromagnetic shower. Its acceptance is $2.3 < \eta < 3.9$.
  - **FMD (Forward Multiplicity Detector)** [108]. The detector allows charged particles measurement due to silicon strips covering the acceptance $3.6 < \eta < 5.$ and $1.7 < \eta < 3.7$ and $-3.4 < \eta < -1.7$.
  - ***V0 (VZero)*** [108]. Two rings of plastic scintillators are located on each side of the interaction point, V0A at $2.8 < \eta < 5.1$ and V0C at $-3.7 < \eta < -1.7$. The coincidences in the

deposit energy in the V0A and V0C detectors are used as minimum bias trigger for collision events in the ALICE experiment. The centrality of heavy ion collisions can also be determined due to the charged particle multiplicities measured in the V0 detector. In the next section we will explain how this detector can be used to determine the luminosity via van der Meer scan analysis.

– **T0 (TZero)** [108] is composed of two arrays of quartz cherenkov detectors measuring the vertex position via the coincidence between T0A, $4.6 < \eta < 4.9$, and T0C $-3.3 < \eta < -3$. Due to its fast response it is used as a trigger for the measurement of the particle time of arrival in TOF.

- **Muon spectrometer** [109] consists of a hadron absorber in front of 5 tracking stations with two pad chambers and 2 trigger stations. A dipole magnet produces an electromagnetic field of 0.3 mT in order to discriminate positively and negatively charged muons. It is mainly dedicated to quarkonium measurements in a pseudo-rapidity range $-4 < \eta < -2.5$. Its trigger system is also used as a trigger for the ALICE experiment for the data taking in association with the V0, T0 and the two calorimeters.

3.2.2 Data taking

In order to register the data of interest at high luminosity, a trigger system is needed. Otherwise, the detector would mainly register background and would most probably miss collision events. The system is divided in different levels of decisions from the lowest one, the minimum bias, to the highest one, the rare triggers with dedicated threshold used to register rare events.

The data acquisition is triggered by the timing coincidence of signals in both side of the V0 detector. This corresponds to the main minimum bias trigger of ALICE which can provide the luminosity measurement. One has to notice that for the p-Pb data taking in 2013, the luminosity was also measurable due to the T0 minimum bias trigger, based on the coincidence between T0A and T0B, with an additional requirement on the vertex position with respect to the interaction point in ALICE. This method allows to reject background events from beam-gas events. The associated cross-section can be determined using van der Meer scan [110]. This measurement of the cross-section of reference is crucial to determine the integrated luminosity for all the cross-section measurements performed in the ALICE experiment. In p-Pb collisions at $\sqrt{s_{NN}} = 5.02$ TeV, collected during the first data taking period in 2013, the interaction rate was of 200 kHz for rare triggers. It corresponds to a luminosity measured by ALICE of about 10^{29} cm^{-2}s^{-1} [85].

In order to determine the inelastic cross-section for the considered process (V0A and V0C coincidence, here) one can define $\sigma = \frac{R}{L}$,

with:

- R, the process rate and
- L, the associated luminosity.

The rate is known but the associated luminosity directly depends on the beam frequency of revolution as well as of the beam intensities and also on the beam shape, which is unknown. To

solve this problem, special runs for Van der Meer scans are performed for each of the data taking period. Assuming that the two beam shapes are the same, the beams are displaced from each other in the two transverse directions and the associated rate is measured depending on beam shifting. By comparison with the head-on rate, when beams are not displaced, the effective beam width can be measured. This enables to define the luminosity associated to the minimum bias trigger as well as the cross-section. During 2013 data taking, the results of the V0 minimum bias cross section were:

- $\sigma(\text{V0}) = 2.08b \pm 3.4\%(\text{sys})$ in p-Pb collisions and
- $\sigma(\text{V0}) = 2.12b \pm 3.2\%(\text{sys})$ in Pb-p collisions [110].

In the analysis of isolated photons in p-Pb and Pb-p collisions at $\sqrt{s_{NN}}$, which is presented here, this reference cross-section enables to recover the isolated photon cross section from the raw spectra (see chapter 8).

In the ALICE experiment, in order to perform the data acquisition, different levels of triggers are used and managed by the CTP (Central Trigger Process) [111] depending on the defined configuration. Different levels of trigger exist, L0, L1 (both used in this analysis), L2 and the HLT (High Level Trigger) [112]. L0 is the first step to trigger the data acquisition with the ALICE detector. Theses inputs can come from V0, T0, EMCal, PHOS or the muon spectrometer. Then the accepted events are evaluated by the L1 triggers, TRD, EMCal, ZDC. L2 trigger decision time corresponds to the TPC drift time (100 μs to compare with 300 ns for L0 and L1 triggers). This trigger enables the migration of the raw data to the DAQ (Data AcQuisition) [113] and the sending to the HLT for compression, which will allow the event building.

In this analysis, the minimum bias trigger used is the one from V0. EMCal is used as L0 and as L1 trigger in order to measure the prompt photon spectra. The EMCal trigger decision will be described in more details in the next chapter 4.

3.2.3 Data reconstruction

Data taking sequences are stored into runs. In order to get usable data for the analysis, one has to perform the reconstruction of these runs. In the first stage we need to store all the parameters of the run data taking in OCDB (Offline Conditions DataBase) which will be updated later with the off-line calibration information. This allows to perform the different passes of reconstruction and to obtain the particle tracks and clusters. The Figure 3.8 shows the stage of the raw data after the data taking. In Monte-Carlo simulations, the corresponding step is the digit one.

In the first pass, cpass0, the reconstruction is performed on events sample. It enables to have input for some detector calibration, TPC, TRD, TOF and T0 as well as for the centrality. Then the calibration is applied to the events during the calibration pass. A first data analysis of quality assurance is performed on the events to verify the calibration accuracy. This pass also allows the improvement of the calibration of the detectors such as SDD, TPC and EMCal. This latter is applied in order to verify the calibration accuracy of the detectors. The first passes of the calibration are only applied on

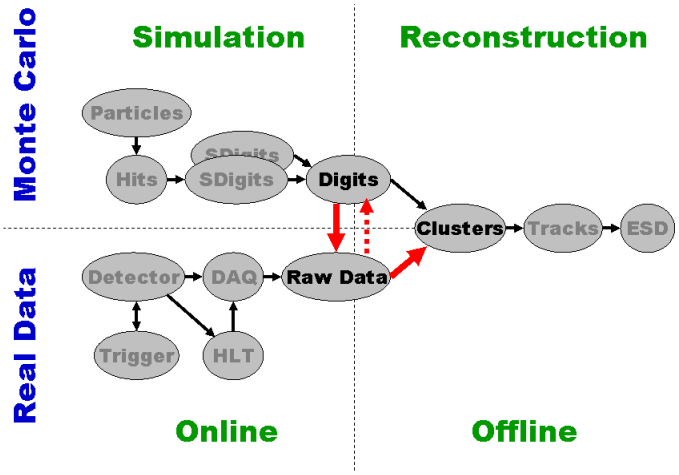

Figure 3.8: Scheme illustrating the different steps from the data taking to the reconstructed data for the analysis. It also presents the case of the Monte-Carlo simulation.

data samples. Afterwards, all the events are reconstructed during the physics pass, called ppass. The clusters and tracks corresponding to the particle energy deposit in the detectors are reconstructed. A data quality assurance (QA) analysis is performed for each detector to check the reconstruction and the validity of the data taking. The pass can be redone several times to improve the quality of the reconstructed events for the analysis. These events are stored in ESDs (Event Summary Data) objects. The ESDs can be filtered in order to produce AODs (Analysis Object Data). These last objects are lighter and can be specific to somes detectors or analysis or general ones. They are the preferred objects for the data analysis. In the specific case of the EMCal calorimeter, in general purpose AODs no additional filters are applied on clusters with respect to ESDs.

In this chapter, we have presented the LHC which provides colliding beams of protons or lead ions. The characteristics of the electromagnetic calorimeters of the CMS and ATLAS experiments already allowed to measure isolated photons at high energies, up to 400 GeV/c (CMS) and up to 1000 GeV/c (ATLAS). The ALICE experiment can provide, due to its apparatus, the measurement of various kind of observables to allow the study of hadronic matter. A trigger system is used to register events of interest. The data taken are finally stored in analyzable objects after different passes of calibration and reconstruction.

CHAPTER 4

EMCal calorimeter: Acquisition, reconstruction and quality assurance

Contents

In this chapter, we present the characteristics of the EMCal calorimeter of the ALICE experiment after a brief introduction on calorimetry in high energy particle physics. Then the acquisition and reconstruction process of the detector is described. The calorimeter calibration method is detailed. The last parts are dedicated to the EMCal performance and to the presentation of the data quality assurance.

4.1 The ElectroMagnetic Calorimeter

4.1.1 The calorimetry of electromagnetic particles

A calorimeter, in particle physics, enables destructive energy measurement. The particles lose their energy in the detector by a combination of different processes. This energy is then collected. The choice of the used materials and the detector geometry determines the type of particles measured. In our case, the calorimeter is designed to detect photons and electrons. For this purpose, it is composed of layers of high atomic number Z, where the particles lose their energy by interaction, and layers of scintillators which enable the energy measurement of electromagnetic particles.

Three types of particle-matter interaction can be considered for photons depending on the atomic number Z of the calorimeter material and the considered type of particles and their energy. The pair creation, the Compton diffusion, as well as the photoelectric effect, can occur. At high energies (> GeV), the dominant effect is the pair creation $\gamma \rightarrow e^+e^-$ as one can notice in the Figure 4.1.

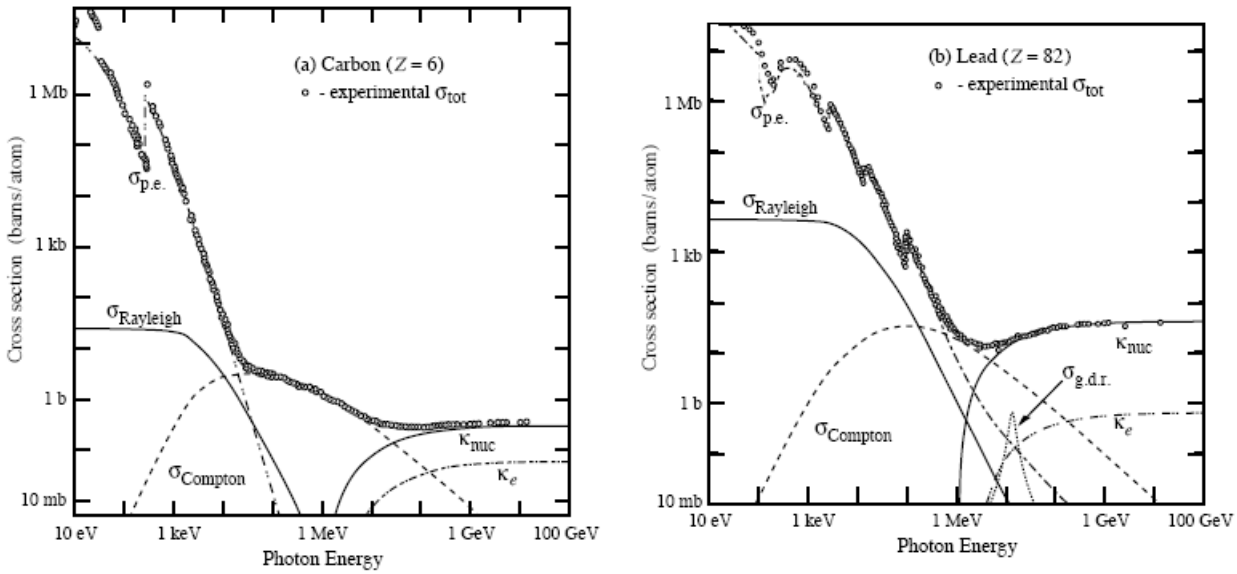

Figure 4.1: Photon interaction in the matter depending on considered energy, on the left plot, in the carbon case and, on the right plot, in the lead case.

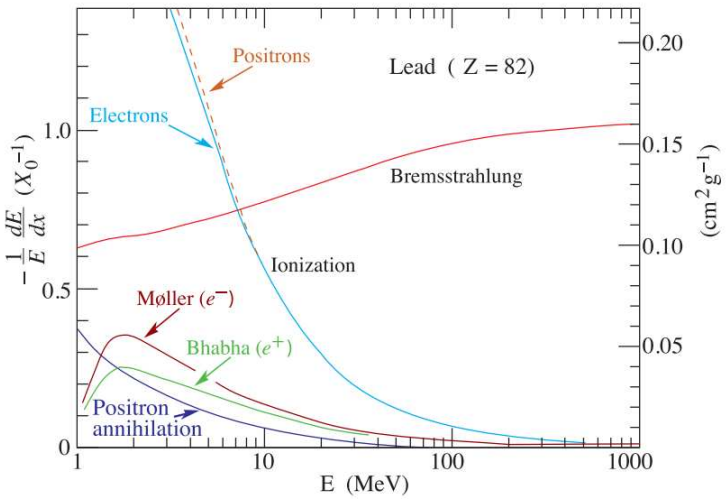

Figure 4.2: Probability of electron interaction per process in the lead matter as a function of the electron energy.

At high energies, the electron mainly interacts via Bremsstrahlung radiation. Indeed, when the electron interacts with ions which compose the matter, a breaking radiation is emitted as a photon.

The probability of an electron interaction per process in the lead matter depending on its energy is shown in the Figure 4.2.

The combination of the pair creation (an electron and a positron are emitted), when a photon crosses the matter, and of the photon emission via Bremsstrahlung radiation, passing through the material, leads to create an electromagnetic shower. The development of the latter is schematically represented in the Figure 4.3. It is characterized by its longitudinal and radial expansion.

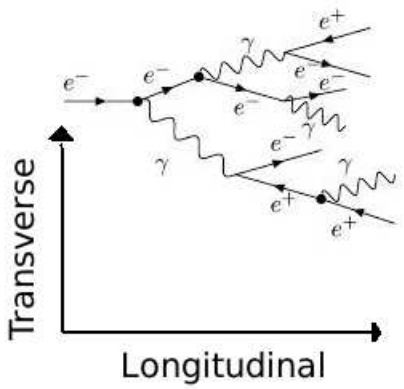

Figure 4.3: Scheme of the development of an eletromagnetic shower. The directions of the shower expansion, transverse and longitudinal, are shown.

Firstly, we focus on the longitudinal expansion and in a second time we will describe the shower shape in the transverse plane.

Longitudinal expansion

The radiation length X_0 characterizes the stopping power of the calorimeter [114]. It is defined as the length needed for the initial electron with an energy E_0 to reach an energy E_0/e. Indeed, the energy loss in the medium via breaking radiation, is described by an exponential function,

$$E = E_0 e^{-\frac{x}{X_0}} \tag{4.1}$$

where:

- X_0 depends on the material as:

$$X_0(\text{cm}) \approx \frac{716.4A}{Z(Z+1)ln(287/\sqrt{Z})} \times \frac{1}{\rho} \tag{4.2}$$

where:

- Z is the atomic number and
- ρ the material density.

This value directly depends on the considered material and its density. Higher is the atomic number and the density, and lower will be the radiation length. EMCal (ElectroMagnetic Calorimeter) is designed to study electrons until hundreds of GeV, so X_0 needs to be low enough to let electrons loose all their energy in the calorimeter. It needs to be compact enough. For that reason, lead material have been used ($\rho_{Pb_{82}} = 12$ g.cm^{-3}).

Radial expansion

In a calorimeter, the shape of the electromagnetic shower in the transverse plane, associated to the cells size, determines the energy resolution. If the radial expansion of the electromagnetic shower of particles is too large, the showers of 2 incident particles will be merged. The discrimination between the two different particles electromagnetic shower will not be directly possible.

This radial expansion is described by the Moliere radius, is the radius which corresponds to an cone where the incident electron has lost 90% of its energy. The Moliere radius [114] R_M is approximatively expressed as:

$$R_M \approx \frac{E_S}{E_C} X_0 \tag{4.3}$$

where:

- $E_S = m_e c^2 \sqrt{4\pi/\alpha} \approx 21 MeV$
- E_c is the critical energy of the considered medium for which the energy loss via ionisation becomes equivalent to the energy loss via pair creation. Then, the electromagnetic cascade is stopped.

With respect to the formula 4.3, the Moliere radius R_M increases with the radiation length X_0. Therefore, a good calorimeter resolution is achieved for reasonably low stopping power.

In the next paragraph, we will describe different characteristics of the EMCal calorimeter.

4.1.2 Characteristics of the EMCal

The EMCal [103] is the main ALICE experiment calorimeter, considering its acceptance coverage. This detector is composed of 76 layers (1.44 mm) of lead (Z=82) alternatively built up with 77 layers (1.76mm) of plastic scintillators. The stack is maintained by a pressure of $\sim 1.1 kg/cm^2$. This corresponds to 20.1 radiation length, X_0, of 12.3 mm. The corresponding Moliere radius is 3.20 cm.

The calorimeter is divided into 11,520 towers (+ 768 towers not included in the read-out for RunI) of $\Delta\eta \times \Delta\Phi \sim 0.014 \times 0.014$ composed of stacks of different layers. Optic fibres collect the scintillation light along them. The collected light yield is proportional to the photon energies. A group of 4 towers forms a module. The 2880 modules (+ 192) are assembled in supermodules. In 2013, during the p-Pb data taking, the calorimeter was formed of ten supermodules and two-third of supermodules were installed but not implemented in the detector readout. The two supermodules are distributed

Parameters	EMCAL
Layers	76 layers of Pb (1.44 mm) 77 layers of scintillators (1.76 mm)
X_0	12.3 mm
Number of X_0	20.1
R_M	3.20 cm
Density	$\sim 5.68\ g.cm^{-3}$
Granularity	$\Delta\eta \times \Delta\Phi \sim 0.014 \times 0.014$
Towers	11 520+768
Modules	2880+192
SuperModules	$10 + 2/3$
Size	$80° < \Phi < 187°$ $\lvert\eta\rvert < 0.7$

Table 4.1: Effective parameters of the EMCal calorimeter of the ALICE experiment

in two columns symmetrical with respect to the $\eta = 0$ axis. Schemes illustrating the calorimeter design are shown in the Figure 4.4.

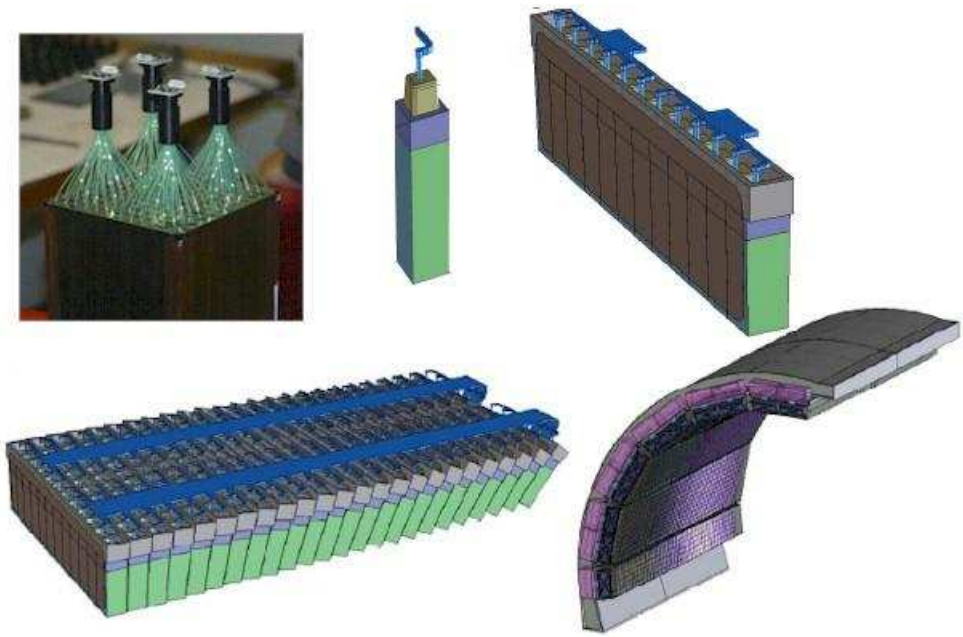

Figure 4.4: Detailed view of the composition of the EMCal calorimeter.

All the calorimeter characteristics are summarized in the Table 4.1.

4.2 Acquisition and reconstruction

4.2.1 Acquisition

As explained in the previous paragraph, the scintillation light, emitted in the scintillators by the particles of the electromagnetic shower, is collected by optic fibres which route the light till APD (Avalanche PhotoDiode). The last one converts the photonic signal into electrical signal via the photo-electric effect. The APDs are connected to pre-amplifiers.

A module constitutes one unit of the calorimeter in terms of electronics. A FEE (Front End Electronics) is connected to each module. It allows the digitalisation of the signal. After conversion of the light signal to the electric one, the Charge Sensitive Pre-amplifier (CSP) converts the signal to pulse. Then, Analog to Digital Converters (ADCs) allow the digitalisation of the signal which is transferred to the FEE modules. A Trigger Region Unit card (TRU) is coupled to a module to enable a fast level 0 trigger. A Summary Trigger Unit (STU) takes input from TRU modules to perform the energy sum. It provides a level 1 trigger "without dead time". 9 FEE modules are brought together and read by the GTL buses of the ALICE system under control of a RCU (Readout Control unit) card [115]. The schematic view of the EMCal electronics is presented in the Figure 4.5. One has to notice that the read-out electronics of the EMCal is similar to the one used in the PHOS calorimeter of ALICE.

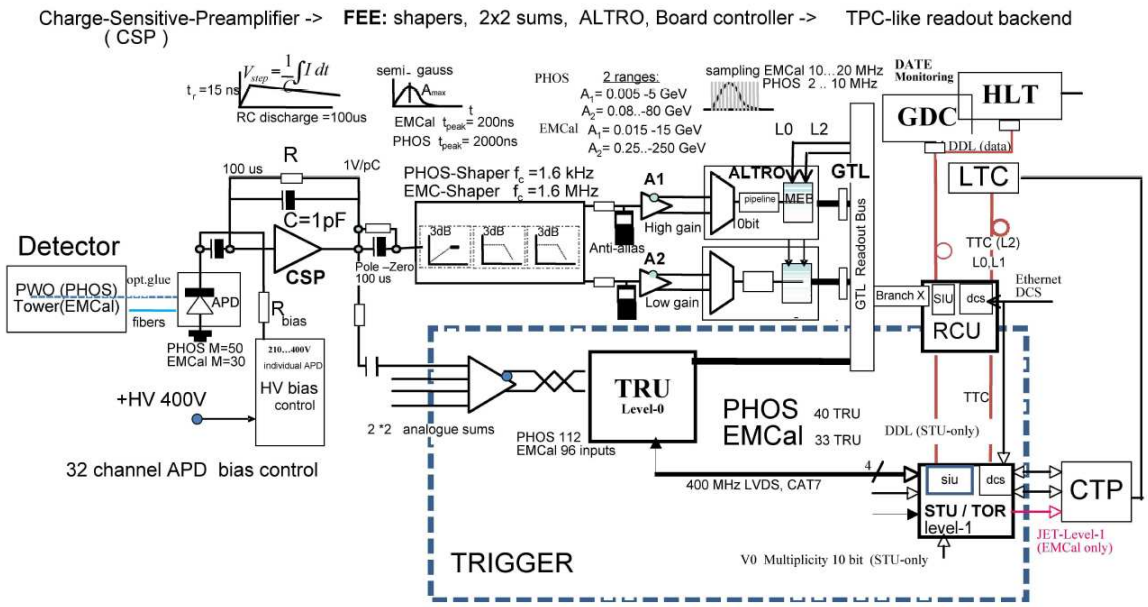

Figure 4.5: Scheme of the EMCal front end electronics

The EMCal different level triggers provide the measurement of photons and jets ranging from MeV to GeV. Three different triggers exist in the EMCal. The level 0 trigger corresponds to an energy threshold evaluated in a TRU (so with 2×2 tower patch), as previously mentioned. When the L0 is triggered in the EMCal, the two types of L1 trigger are evaluated. One L1 EMCal trigger is dedicated to photon measurement, whereas the other one to jet measurements. The specificity of the

L1 gamma trigger with respect to L0, is that the energy measured by different TRU is summed up using a scanning of the EMCal surface. The L1 jet trigger evaluation is similar, except that the energy deposit in the calorimeter is scanned using a bigger window (16×16 towers) to take into account the jet size.

The response of the triggers are sent to the CTP (Central Trigger Process) of the ALICE experiment (see chapter 3).

4.2.2 Reconstruction

The ADC signals are digitalized in time sample. It can be described by a Γ-function which depends on the time t as [115]:

$$ADC(t) = Pedestal + A \cdot x^{\gamma} \cdot e^{\gamma(1-\gamma)} \tag{4.4}$$

$$x = \frac{(t - t_0 + \tau)}{\tau} \tag{4.5}$$

where t_0 is the characteristic time of the peak function, τ the decay constant, $\gamma = 2$ is the power of the Γ-function and A is the amplitude of the response functions. Because ADC value is directly proportionnal to the energy deposit, each channel need to be carefully calibrated (see next section).

In order to recover the particle energy, which has initiated the electromagnetic shower, algorithms are used to associate the energy measured in the neighbouring towers/cells. The clusterization is realized. At the analysis level, one has to deal with this cluster. Different algorithms are used according to the measurement goal and the biases that have to be avoided. These algorithms are presented below:

- clusterizer V1: The energy in the cells is measured. If the energy of a cell is higher than a determined threshold depending on the collision type (often at 300 MeV, as in the thesis analysis), it will constitute a seed for the clusterization. The cell energy around the seed cell is studied and if it is above a threshold (typically 50 MeV), the cell will be added to the cluster. The clusterization stops when no more neighbouring cells can fulfill the energy threshold condition. Using this algorithm, the clusters are large and the clusters from different electromagnetic showers, typically from decay photons, are merged. The advantage of this method is that the determination of the energy deposit is unbiased. This algorithm is the one used in the photon analysis to allow the π^0 identification by merged cluster (see chapter 5). It also limits the bias of the photon energy measurement.

- clusterizer V2: As with the previous algorithm, the energy deposit in the cells is measured and if it is above a threshold it will constitute a seed cell for the clusterization. The neighbouring cell energy is measured. Contrary to the previous case, the cell is added to the cluster only if its energy is smaller than the seed energy but higher than the surrounding ones. The cells

are added to the cluster until the cell energy condition is not fulfilled anymore. This clusterizer enables to separate the clusters with respect to their particle energy deposit. The disadvantage is the bias induced in the energy determination due to the energy deposit in a cell which can be shared by two different clusters. This clusterizer is preferred for the invariant mass and jet analysis.

- clusterizer NxN: The cells in a NxN window and the seed cell are added to the clusters. Typically this is a 3x3 window. At high energy it can lead to an energy bias removing cells of interest outside of the 3x3 window.

- clusterizer V1+unfolding: The algorithm is similar to the one used for the clusterizer V1. In addition, the V1 cluster local maxima are determined and the clusters are split regarding to the energy cells around this maxima. The advantages and disadvantages are similar to the clusterizer V2.

4.3 Calibration

In order to perform high energy particle measurements, the calorimeter needs to have a precise energy and time calibration. Electron beam tests have been achieved before its installation in the ALICE cavern.

We have seen in the previous paragraph, that the energy deposit in the cell is directly proportional to the APD gains. It is essential to perform a calibration of these gains tower by tower. Moreover, this calibration is particularly essential for the measurement of high energy particles with a sufficient energy calibration (1%). It also allows a pertinent trigger decision.

Before the EMCal implementation in the ALICE cavern, the different APD gains of the towers have been studied. Their behaviour under different high voltage and temperature conditions, as it can be in the ALICE experiment, has been characterized. The APD have been pre-calibrated.

After the tower assembly in supermodules, the APD have been calibrated with cosmic-ray muons which are minimum ionizing particles (MIP). Thus, the expected muon energy deposit in a single tower is known. The calibration is performed measuring the response of the APD to the energy deposit of muons in a tower. This procedure provides an initial energy calibration with a precision of around 5% [115].

After its installation in the ALICE experiment, the EMCal performs during stand-alone operations or data-taking for calibration with LED. A light pulse coming from the LED is sent to each tower in order to perform an APD gain calibration.

The last calibration was performed after the first p-p data-taking using π^0. Indeed, the invariant mass of π^0 is precisely known $M_{\gamma\gamma} = 134.9766 \pm 0.0006$ MeV/c^2. An iterative method is applied in order to calibrate each tower and to obtain the π^0 peak at the expected energy [115].

One has to notice that a time calibration is performed for the data taken with EMCal calorimeter of ALICE. Indeed, the mean cell timing is not centered on the time of the event. This enables to reject noisy cells or cells from pile-up events.

All the calibration coefficients are stored in an object from the ALICE analysis software in order to perform a proper reconstruction and analysis.

4.4 EMCal performances

4.4.1 Energy resolution

The energy resolution of the calorimeter can be expressed as:

$$\frac{\sigma}{E} = a \oplus \frac{b}{\sqrt{\sigma}} \oplus \frac{c}{E} \tag{4.6}$$

where:

- E is the energy of the electromagnetic shower,
- a, b and c are characteristic parameters of the calorimeter.
  - a represents stochastic fluctuations due to detector effects,
  - b systematic effects and
  - c the electronic noise.

The measurement of the resolution was performed during the beam test [115].

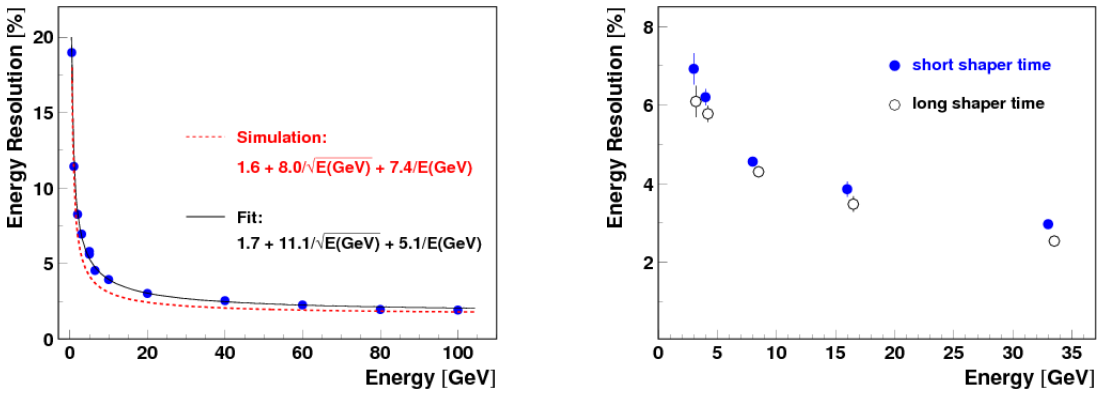

Figure 4.6: Energy resolution of the EMCal as a function of the incident particle energy.

Monte-Carlo simulation using GEANT 3 and the combined beam test at the SPS and PS enable to determine the coefficients of the equation 4.6 in an energy range [0.5−200] GeV via the simulation and a fit of the beam test results.

The results from the beam test and Monte Carlo simulation using GEANT 3 show similar results. The energy resolution is lower than 5% for an energy higher than 10 GeV. The results are presented in the Figure 4.6.

4.4.2 Position resolution

The position coordinates are determined via a logarithmic weighting of the energy deposit of the tower electromagnetic shower [115]. The resolution of the energy distribution in the cluster is better than the tower size, and similar in the x and y directions.

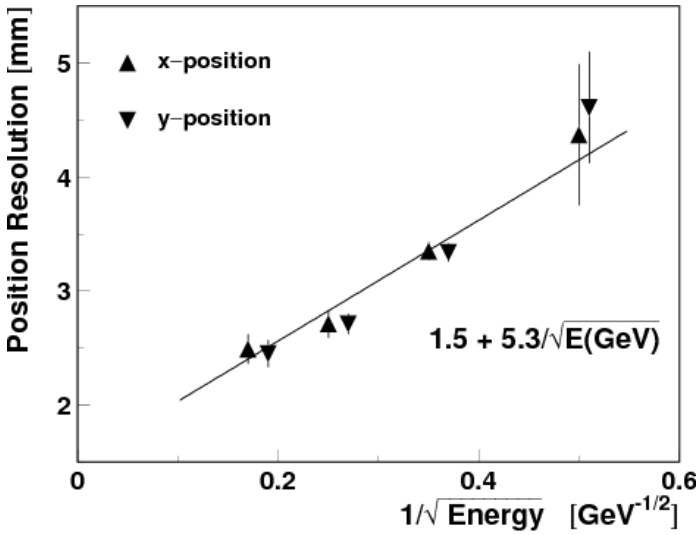

Figure 4.7: Position resolution of the particle (in millimeter) depending on its energy [115].

The beam test results are presented in the Figure 4.7. The position resolution of the electromagnetic shower is equal $1.5 \oplus 5.3\sqrt{E(GeV)}$ mm.

4.4.3 Linearity of the EMCal response

The linearity of the energy response of the EMCal has also been studied [115]. For an energy higher than 20 GeV, the linearity of the response is better than 1%. For lower values, it drastically decreases and is around 10% at 5 GeV. The linearity response of the detector is plotted in the Figure 4.8. The non-linearity effects can be modelled by a cubic function and corrected at the analysis level.

4.5 Quality assurance

During the data taking, and after the different passes of the data reconstruction, a quality assurance detector team is in charge of the verification of the quality of the data. Indeed, it enables to verify the reconstruction and to check the validity of the data taking. This action allows the next step of reconstruction and provides usable list of runs for analysis as well as for the calibration. This work is also done to validate the official Monte-Carlo production, based on detector calibration and reconstruction setups from the data.

The quality assurance for the EMCal calorimeter consists in monitoring different observables: the number of cells per cluster, the EMCal clusters-tracks multiplicity correlations, the time, the

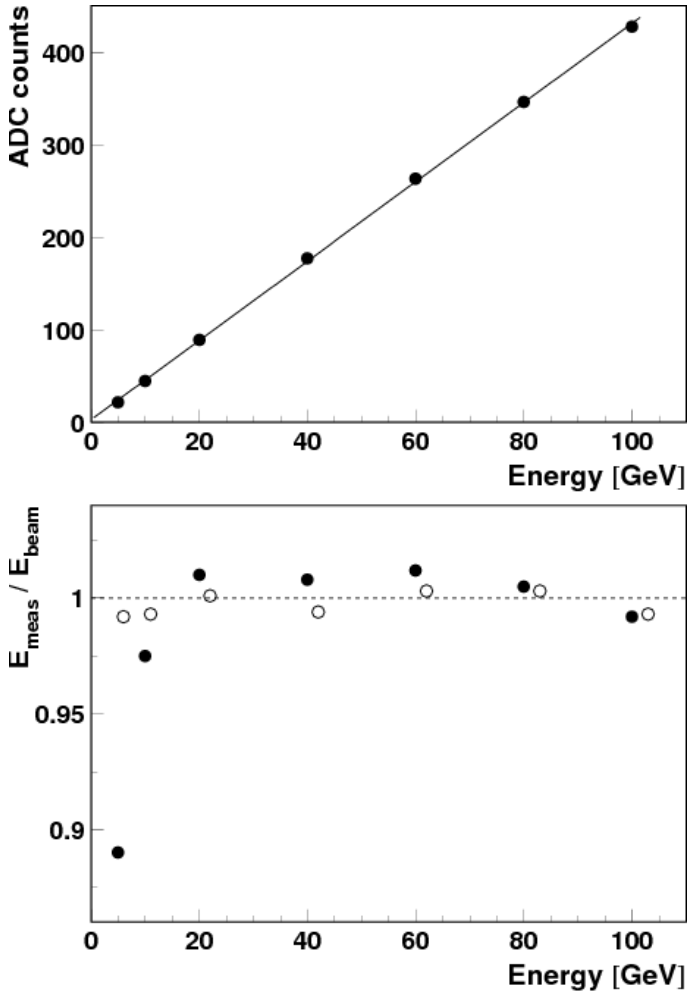

Figure 4.8: On the upper plot, linearity of the analogic signal reponse of the detector as a function the incident particle energy fitted by a linear function [115]. On the bottom plot, the ratio between the linear fit and the data (full circles) and a cubic fit and the data (open circles).

cluster multiplicities, the number of clusters and cells of clusters per event, clusters and cells occupancy maps, the π^0 invariant mass as well as the evolution of the number of clusters per event, the number of cells per clusters per event and the number of π^0 per event.

Such studies moreover enable to produce run lists of good quality data providing bad channel maps and performing the time and energy calibration with the π^0 invariant mass. The bad channel maps are stored in the OCDB (Offline Conditions DataBase). The bad channels, as well as the warm channels, if needed, are masked in the analysis.

In the Figures 4.9 and 4.10, one can see two trending distributions from the EMCal quality asssurance analysis. In the plot 4.9, the average number of clusters per event in each SuperModule and in each run of the data taking period are presented. One can notice that the distributions are flat. No differences are observed between the different SuperModules. The flat distribution indicates that

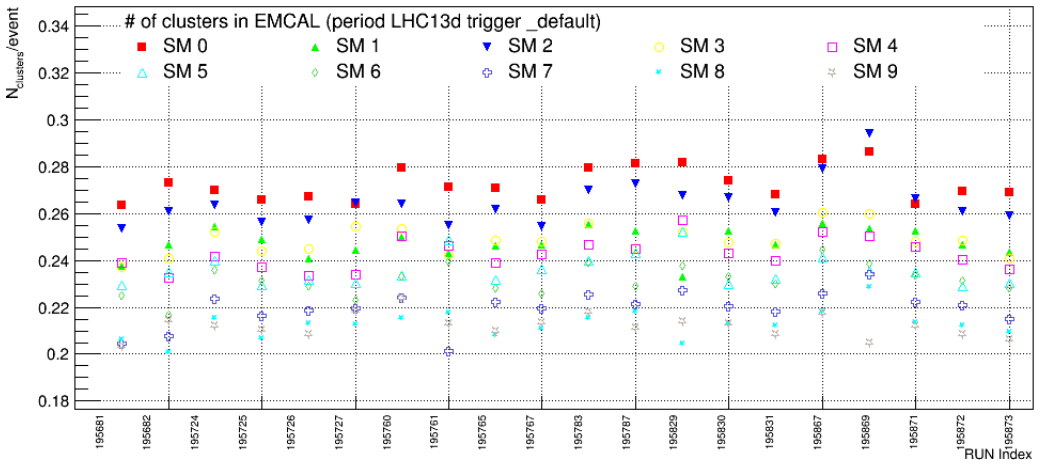

Figure 4.9: Example distribution of number of clusters per event in each SuperModule in a data taking period, LHC13d in the quality assurance analysis.

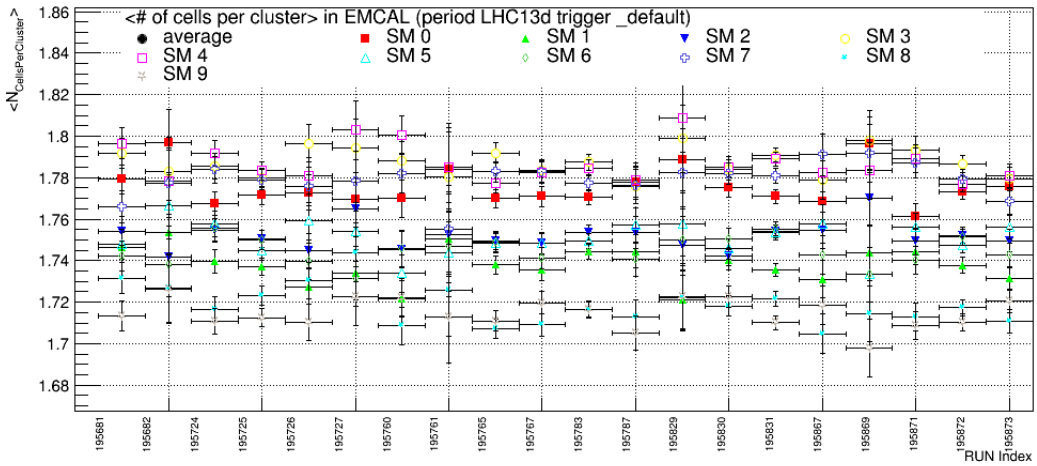

Figure 4.10: Example distribution of the average number of cells per cluster in each SuperModule in the LHC13d data taking period.

the readout acceptance of the detector is similar in all the runs. In the plot 4.10, the average number of cells per cluster in the different SuperModules, and depending on the runs, is shown. As in the previous case, the distribution is flat and no significant discrepancy is observed between the different SuperModule results.

Some example plots of the analysis of the run quality assurance are presented in the Figures 4.11 and 4.12. The plot 4.11 represents the sum of the cluster energy deposit in the EMCal acceptance. Such kind of maps enables to point out some warm or missing zones in the detector. No significantly noisy zones are seen in this plot. Here the plot does not correspond to the first pass of

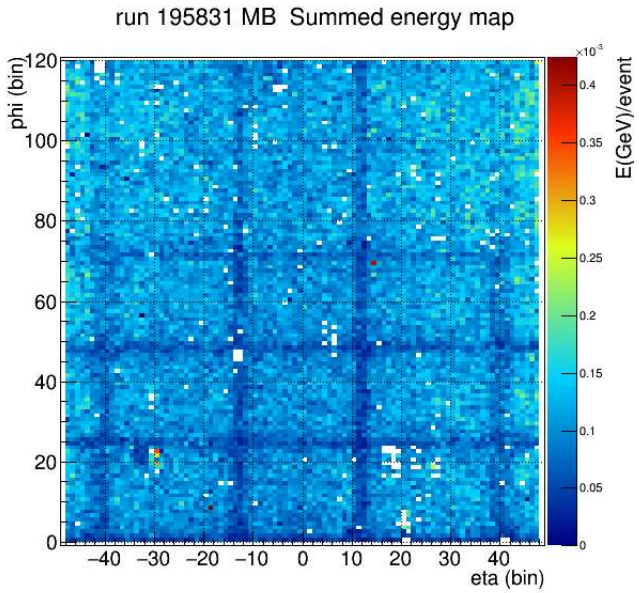

Figure 4.11: Example of energy map for a run of the data taking period LHC13d

reconstruction. The noisy channels are already masked. In the plot 4.12, is shown the π^0 invariant mass distribution in each SuperModule of a run from the data taking period LHC13d. Such a plot enables to check the energy calibration. Moreover, it gives insight of the remaining noise and of the quality of the provided bad channel map. In some case where the noise is too high, the invariant mass peak cannot be observed.

We have presented the characteristics of the EMCal calorimeter, measuring electrons and photons, which is the main detector involved in the isolated photon analysis presented here. It allows the measurement of high energy photons and jets via the dedicated triggers. The calibration of the detector, as well as its performance in terms of linearity of the response, energy resolution and linearity have been presented. The choice of the cluterizer algorithm induces a bias of the particle associated energy or of the discrimination between the energy deposit of the particle. During the thesis work, a part of the time was dedicated to the quality assurance analysis of the EMCal for the processed production and the production of bad channel maps for the first data taking of Run II.

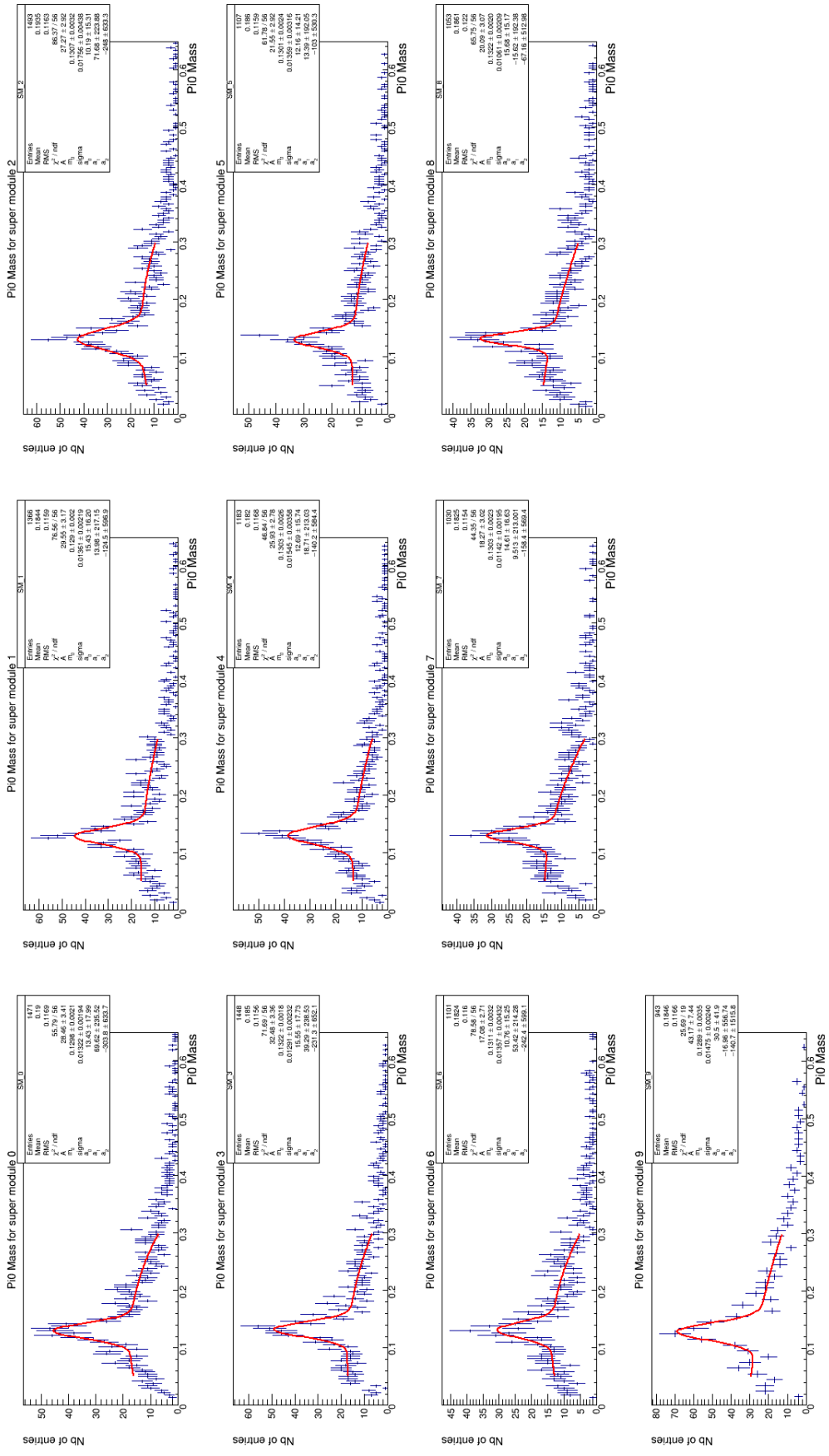

Figure 4.12: Example of π^0 invariant mass distribution in the different SuperModules for a run of the data taking period LHC13d

Part III

Isolated photon study in p-Pb collisions

CHAPTER 5

Data selection and photon identification

Contents

This chapter is dedicated to the description of methods used for selection of events and clusters of interest to perform the isolated photon analysis in p-Pb collisions at $\sqrt{s_{NN}}$ = 5.02 TeV. The analysis codes and the procedure have been calibrated with the analysis of the isolated photon in pp collisions at $\sqrt{s}$ = 7 TeV.

5.1 Data selection

5.1.1 Data sample and event selection

We are interested in the data taken in 2013 for p-Pb collisions and Pb-p collisions. In the ALICE experiment, these data are grouped into four different sets for p-Pb collisions:

- LHC13b, LHC13c, LHC13d and LHC13e

and in one set for Pb-p collisions:

- LHC13f.

LHC13b and LHC13c data sets were dedicated to record minimum bias events.

As we have seen in the chapter 2, the goal of this thesis work is to measure the direct photon production in p-Pb collisions by reducing the fragmentation contribution using the isolation method, which is based on the deposit energy by charged and neutral particles in a cone centered around the photon candidate. It implies that the reconstructed data have to be not only of a good quality for the resolution of the vertex interaction reconstruction and of the calorimeter cluster but also

for the charged particles tracks in the ITS (Inner Tracking system) and in the TPC (Time Projection Chamber). To select the runs[1] for the isolated photon analysis, an EMCal Quality Assurance (see previous chapter) has been performed. We have checked the Quality Assurance of the TPC and ITS and selected the runs with good performances for these detectors. Some selected plots are presented in the annex A.

We need to select, in the EMCal calorimeter, neutral clusters, which could be attributed to high energy photons. As prompt photons are rare events with a small cross section, a high level trigger is needed. For this reason, LHC13c and LHC13b data sets are not used in this analysis. Finally, the last requirement for the runs to be selected was the presence of the level 1 EMCal photon trigger, EMCEGA. For the considered periods, the last one had two thresholds, EMCEGA1, called EG1 for convenience, at 11 GeV and EMCEGA2, called EG2, at 7 GeV.

It enabled to select the run lists below:

LHC13d: 195724 195760 195767 195783 195787 195826 195827 195829 195867 195872 (10 runs)

LHC13e: 195935 195954 195955 195958 196085 196089 196090 196091 196185 196187 196194 196197 196199 196200 196201 196208 196214 196308 196309 196310 (20 runs)

LHC13f: 196475 196477 196535 196608 196648 196701 196702 196706 196721 196722 196869 196870 196965 196972 196973 196974 197003 197011 197012 197015 197031 197089 197090 197091 197092 197138 197139 197142 197184 197247 197254 197255 197256 197258 197260 197296 197297 197298 197299 197300 197302 197341 197342 197348 197351 197386 197387 197388 (48 runs)

The quality of the triggers EG1 and EG2 have been evaluated by looking at the stability of the number of clusters per event in the period, selected by each trigger. In the Figures 5.1 and 5.2, these distributions are represented depending on the considered run in different data sets. In blue, the points correspond to the distribution for EG1 trigger whereas the red points are associated to the EG2 results. One can notice that the number of clusters per event is stable for all of these considered runs, triggers and data sets. In the analysis, EG2 will be used to reach lowest p_T (from 10 GeV) whereas EG1 will be used to go up to 60 GeV. This energy range will allow to perform a comparison with isolated photon analysis in pp collisions at 7 TeV [67].

After the selection of the runs, one has to single out the events to be analysed. A cut on the quality of the vertex in the beam direction, has been applied. The vertex interaction point displaced by less than 10 cm compared to the nominal one has been kept, $|v_z| < 10$ cm. This distribution is represented in the Figure 5.3.

It enabled to select 542 146 events for the lower trigger threshold (EG2) whereas the higher trigger threshold (EG1) reached 1 131 910 events. In a detailed view, with EG2 trigger, there were 56986 selected events in LHC13d, 185916 in LHC13e and 299254 in LHC13f; with EG1 trigger, there were 181966 selected events in LHC13d, 325435 in LHC13e and 624510 in LHC13f. The number of se-

[1] A data sample in the ALICE experiment is called a run. In general in these p-Pb collision data, it corresponds to few hours of consecutive data taking

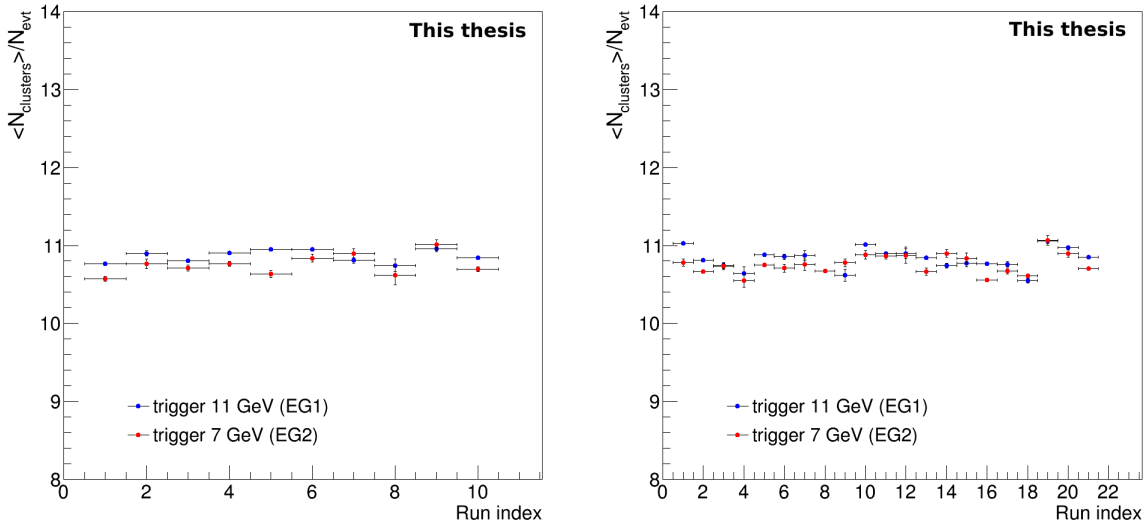

Figure 5.1: Number of clusters per event selected with the EG1 trigger (blue) and EG2 trigger (red) depending on the run index in LHC13d (left plot) and LHC13e (right plot) analysed runs

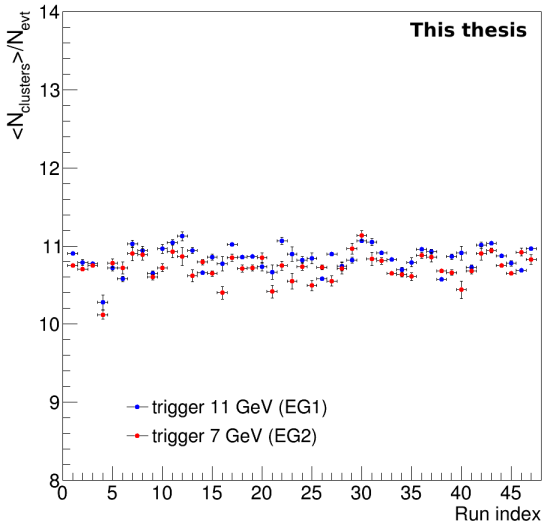

Figure 5.2: Number of clusters per event selected with the EG1 (blue) and EG2 (red) depending on the run index in LHC13f analysed runs

lected events in the different periods with the two trigger are summarized in the Table 5.1.

5.1.2 High level trigger rejection factor

As already mentioned, for the periods of interest, there were two high level triggers for photons in the EMCal: EG1 with a threshold at 11 GeV and EG2 with a threshold at 7 GeV. In order to recover the

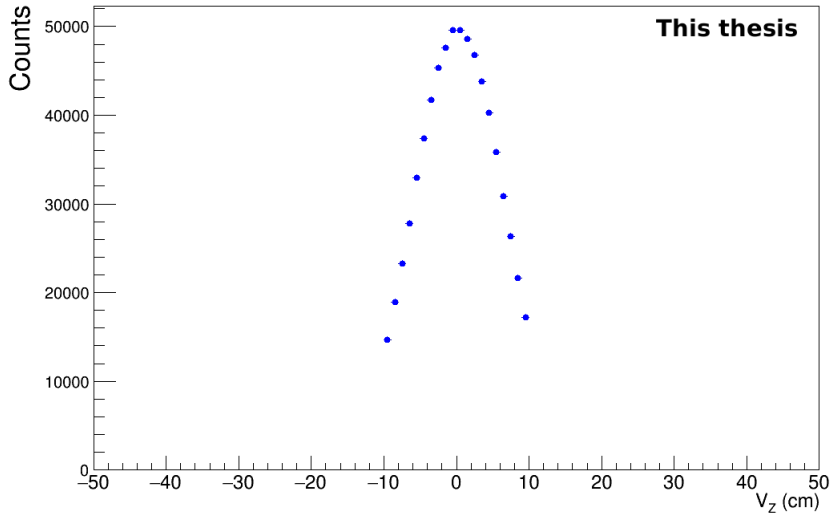

Figure 5.3: Vertex distribution along z axis after the cut at $|v_z| < 10$ cm

	Period	EG1	EG2
p-Pb	**d**	181966	56986
	e	325435	185916
Pb-p	**f**	624610	299254

Table 5.1: Summary of the number selected events in the periods, LHC13d,e and f with the triggers EG1 and EG2.

isolated photon cross-section, we need a cross-section of reference. Only the minimum bias trigger (corresponding to T0 and V0 triggers) cross section is already known and has been calculated using van der Meer scans [110] (see chapter 3). As the EMCal level 1 gamma trigger is a sub-sample of the V0 trigger, we will use the V0 minimum bias cross-sections as references. To make the link between the number of minimum bias events and the corresponding EG1 or EG2 events, we need to know the EMCEGA trigger rejection factors defined as:

$$RF^{EG1/2} = \left(\frac{dN^{EG1/2}_{clusters}}{dp_T N^{EG1/2}_{evt}}\right) / \left(\frac{dN^{INT7}_{clusters}}{dp_T N^{INT7}_{evt}}\right) \tag{5.1}$$

where:

- $\frac{dN^{EG1/2}_{clusters}}{dp_T N^{EG1/2}_{evt}}$ is the EG1/2 triggered cluster momentum distribution normalized per the number of considered events.
- $\frac{dN^{INT7}_{clusters}}{dp_T N^{INT7}_{evt}}$ is the minimum bias cluster momentum distribution normalized per the number of considered events.

The considered data-sets LHC13d, LHC13e and LHC13f mainly correspond to the triggered data. The minimum bias events registered is too low to recover the rejection factor of such high trigger. The LHC13c period, where essentially minimum bias data have been registered, is used as minimum bias reference. The LHC13b data set contains very few events, therefore it is not analyzed here. Only runs flagged as good with respect to the QA analysis in LHC13c data set, have been used which corresponds to the following list:

LHC13c: 195677 195675 195673 195644 195635 195633 195596 195593 195592 195568 195567 195566 195531 195529

The V0 minimum bias trigger allows the selection of 20 260 800 events.

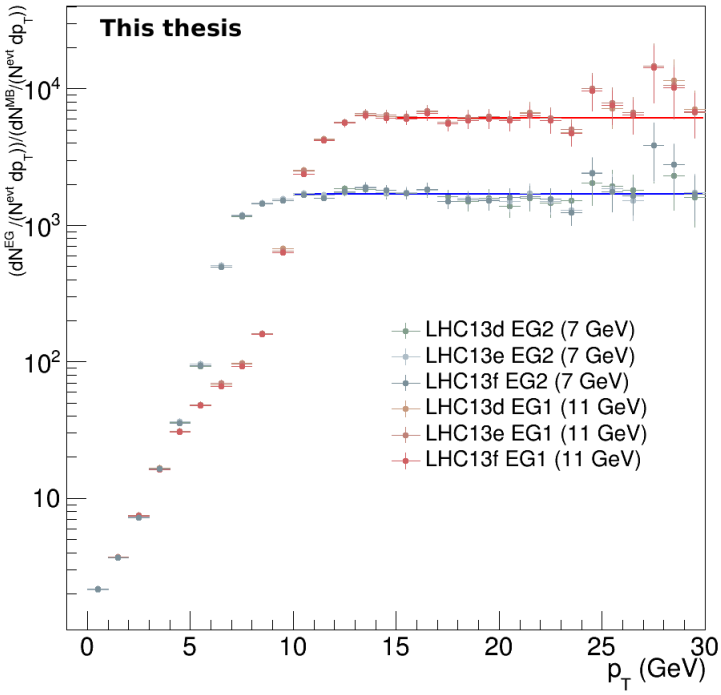

Figure 5.4: Ratio between the normalised clusters p_T distribution obtained with EG1/2 triggers and minimum bias trigger. The values obtained for the different data sets have been plotted for each trigger threshold. After the plateau is reached, the ratios have been fitted with a constant equation.

In the Figure 5.4, the trigger rejection factors of the two triggers are plotted, RF^{EG1} and RF^{EG2}, as function of the transverse momentum, for LHC13d, LHC13e and LHC13f. We can notice that the values, extracted with a linear fit, are totally consistent for each data set used in this analysis. It corresponds to the highest trigger threshold at 11 GeV (EG1):

$$RF^{EG1} = 6082 \pm 255 \tag{5.2}$$

and to the lower trigger threshold at 7 GeV, (EG2):

(5.3) $$RF^{EG2} = 1681 \pm 38$$

It means that, respectively, 6082 and 1681 minimum bias events would be necessary to obtain an EG1 and an EG2 event. The values of the trigger rejection factor will be used to compare the spectra obtained with the two level triggers in order to check if they are consistent and could be both used in the analysis. These results also permit the determination of the integrated luminosity associated to the measurement. This calculation is presented in the subsection 7.4.1.

5.1.3 Monte-Carlo simulation

To determine the detector reconstruction efficiency one needs to use Monte-Carlo simulations. This is also compulsory to perform the signal extraction by evaluating the remaining contamination from photon decay of neutral mesons. These simulations are anchored to the p-Pb and Pb-p data. It means that the data taking conditions are reproduced by using the corresponding calibration of the detectors. The simulations are based on Pythia 6 [116] for the particle generation in high energy events. Two types of simulations have been used in this analysis: one to reproduce the signal and one for the background. The corresponding signal comes from the partonic interaction producing a direct photon and a jet, called gamma-jet process. The simulation of the background has been realised using the generation of partonic events producing two jets. To reproduce the amount of high momentum π^0 in the data, the Monte-Carlo simulations have been enriched using a trigger on the energy of π^0 produced in the EMCal acceptance. We have performed two different simulations of background triggered by π^0: one with the π^0 energy above 3.5 GeV and one with π^0 above 7 GeV. The configuration of the particle generation takes into account the difference of the boost in the laboratory frame between p-Pb and Pb-p collisions. The underlying events are simulated using multiple particle interaction scenarios. The parton distribution function used is CTEQ5L [117]. The detector response is simulated with Geant 3 [118]. The simulations require important calculation resources. To be able to reach sufficient number of events, they are centrally processed. The simulations based on p-Pb collisions are anchored to the runs 195872, 195831, 195724 of LHC13d data set and the runs 196085 196187 196310 of LHC13e data set. For Pb-p collisions the simulations are anchored to the runs 195535, 197298 197138 196972 197348, of LHC13f. The specificity and the name of the simulation in the ALICE data set notation system are summarized in the Table 5.2. In this analysis the jet-jet low threshold simulation will be used to obtain the results in the three first energy bins [10 − 16] GeV/c whereas the jet-jet simulation with the high threshold will be used for the 6 highest energy bins [16 − 60] GeV/c.

In order to produce a complete cluster momentum spectra until 100 GeV/c, Pythia events are generated in different hard process p_T bins, called p_T hard bins, which are then renormalised to be associated. The total spectra cannot be obtained by simply merging the different p_T hard bin results but by applying a scaling factor taking into account the cross section associated to the event generation (gamma-jet or jet-jet, here), and the number of trials necessary to generate an event of

	p-Pb collisions	Pb-p collisions
Anchored data runs	LHC13d:195872 195831 195724 LHC13e:196085 196187 196310	LHC13f:195535, 197298 197138 196972, 197348
Type	**Name of the simulation data set**	
Gamma-Jet	LHC16c3c	LHC16c3c2
Jet-Jet low threshold	LHC16c3a	LHC16c3a2
Jet-Jet high threshold	LHC16c3b	LHC16c3b2

Table 5.2: Summary of the characteristics of the different Pythia simulations used in this analysis.

Gamma-Jet simulations	**Scaling factor (mb)**	
p_T **hard bin (GeV/c)**	**LHC16c3c**	**LHC16c3c2**
0-5	1.517909e-03	1.518477e-03
5-11	1.005272e-04	1.004067e-04
11-21	1.276945e-05	1.278024e-05
21-36	1.824329e-06	1.822928e-06
36-57	3.084067e-07	3.085716e-07
57-84	5.998380e-08	5.995454e-08
>84	1.882579e-08	1.883427e-08

Table 5.3: Scaling factor of the different p_T hard bins of the Pythia gamma-jet simulations

interest. This scaling factor corresponds to the initial cross-section divided per number of trials per event and per generated event. The scaling factors have been computed for different p_T hard bins of the simulation data sets. They are presented in the Table 5.3 for the gamma-jet simulation and in the Tables 5.4 and 5.5 for the two different jet-jet simulations. The jet-jet low threshold simulations will be used to compute the lowest p_T cluster, $[10-18]$ GeV/c, bins whereas the high threshold jet-jet simulations will be used for the highest p_T cluster bins, $[18-60]$ GeV/c.

Jet-Jet low threshold simulations	**Scaling factor (mb)**	
p_T **hard bin (GeV/c)**	**LHC16c3a**	**LHC16c3a2**
7-9	6.731200e-03	6.731246e-03
9-12	7.995602e-03	8.001738e-03
12-16	6.778717e-03	6.780539e-03
16-21	4.643571e-03	4.640654e-03
>21	6.014497e-03	6.013518e-03

Table 5.4: Scaling factor of the different p_T hard bins of the low threshold jet-jet simulations

The EMCal level 1 trigger decisions are not properly described by in the simulation and their use would have induced a bias in the obtained spectrum. This effect has been avoided by introducing a trigger smearing on the minimum bias events sample. It is performed by applying the known trigger threshold, and the associated dispersion. The effective trigger threshold depends on the efficiency of the fast reconstruction algorithm of cluster as it can be observed on the trigger rejection plots

Jet-Jet high threshold simulations	Scaling factor (mb)	
p_T hard bin (GeV/c)	LHC16c3b	LHC16c3b2
14-19	6.071458e-03	6.075249e-03
19-26	3.941701e-03	3.940758e-03
26-35	2.001984e-03	2.002858e-03
35-48	9.862765e-04	9.852572e-04
48-66	3.893911e-04	3.892609e-04
>66	1.865924e-04	1.865456e-04

Table 5.5: Scaling factor of the different p_T hard bins of the high threshold jet-jet simulations

in the section 5.1.2, where the turn on curve has a certain energy width, σ, whose value has been determined in coherence with other EMCal triggered analysis. To further improve the analysis, one could quantify the uncertainty associated to the energy width parameter. The effective values of the trigger can then be modelled by a gaussian function centered on the trigger threshold whose spread depends on the size of the turn on curve of the trigger, as described in the equation (5.4).

$$\text{effective threshold} = \frac{1}{\sigma\sqrt{2\pi}} e^{-(\frac{p_T - \text{threshold}}{\sqrt{2}\sigma})^2} \tag{5.4}$$

The effective value of the trigger threshold is then taken randomly in the generated values. The event can be considered as a triggered event and is kept if at least one of its cluster is higher than the effective trigger threshold. The results obtained in the different scaled hard bins of the simulation and the resulting spectra for the two EMCal triggers used can be seen in the Figure 5.5. The ones from the jet-jet high threshold simulation are plotted in the Figure 5.6.

5.2 Charged particle contribution

Charged particles are measured via the tracks they left in the TPC and in the different layers of the ITS. In the isolated photon analysis, the charged particle contribution in the isolation cone has to be estimated. The track distribution in the ITS is not uniform in the azimuthal direction of the detector acceptance, mainly due to missing zones in the SPD, as it is shown in the Figure 5.7. In order to obtain a smooth and complete spatial track distribution, an approach of hybrid tracks has been used. They are composed of two sets of reconstructed tracks: the tracks which have a hit in the SPD and the tracks without any hits in the SPD but which have been constrained to the primary vertex to have a sufficient tracking resolution. This method allows an uniform φ distribution of tracks. These tracks have been used to estimate the charged hadronic contribution in the defined isolation cone.

We should notice that only tracks coming from the TPC have been used to apply the charged particle veto presented in the next section.

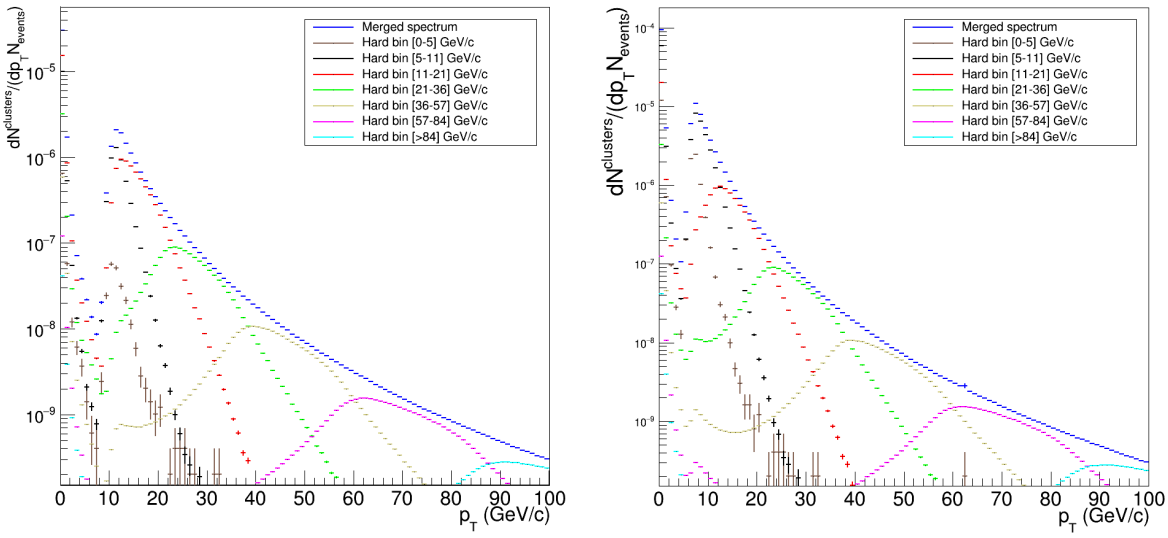

Figure 5.5: Clusters p_T distribution normalised to the scaling factor in the different p_T hard bins of the Pythia gamma-jet simulation anchored to the p-Pb data. The resulting merged spectrum depending on the cluster momentum is also presented. On the left plot, the used trigger smearing is the one for the trigger threshold at 11 GeV. On the right plot, the used trigger smearing corresponds to the trigger threshold at 7 GeV.

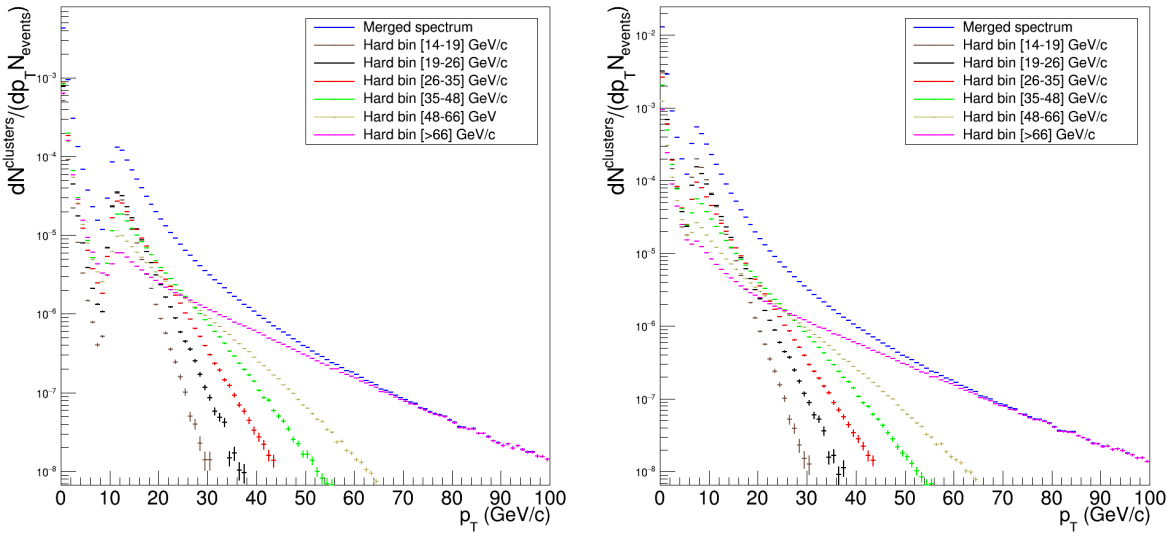

Figure 5.6: Clusters p_T distribution normalised to the scaling factor in the different p_T hard bins of the Pythia jet-jet high threshold simulation anchored to the p-Pb data. The resulting merged spectrum depending on the cluster momentum is also presented. On the left plot, the used trigger smearing is the one for the trigger threshold at 11 GeV. On the right plot, the used trigger smearing corresponds to the trigger threshold at 7 GeV.

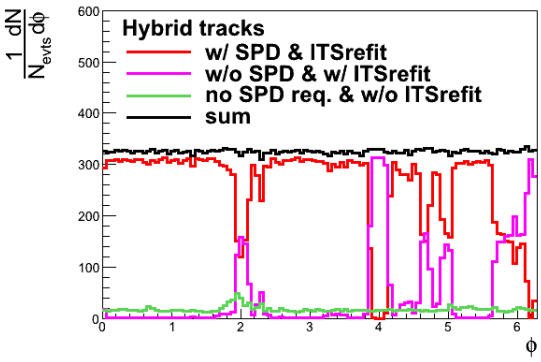

Figure 5.7: Illustrating plot of the azimuthal distribution of hybrid tracks versus SPD and TPC tracks

5.3 Photon identification

5.3.1 Neutral cluster selection

During the periods considered in this analysis, the EMCal was composed of 10 supermodules leading to an acceptance in pseudo-rapidity $|\eta| < 0.7$ and in azimuth $1.4 < \varphi < 3.3$. The clusterizer v1, described in the chapter 4, has been used as algorithm to reconstruct the clusters with a seed threshold of 50 MeV. The topology of the merged π^0 photon clusters is used to distinguish them from the prompt photon ones. The method will be described in the next paragrah 5.3.2.

In order to select cluster of interest, the following cuts have been applied on cells and clusters.

- $N_{cells} \geq 2$: the clusters need to be composed of at least two cells. It enables to remove the remaining noisy channels and to select clusters coming from electromagnetic particle showers.

- $E_{cluster} > 300$ MeV: the clusters have an energy of at least 300 MeV to avoid region where the calorimeter response is non linear and the cluster energy resolution is bad (see chapter 4).

- $d_{\text{bad channel}} \geq 2$ cells: the minimum distance to a bad channel is of 2 cells. This cut avoids the bias in the cluster energy if a masked bad channel is taken into account in the clusterization.

- NLM ≤ 2: the electromagnetic showers from close particles in the calorimeter can be merged. The used clusterization algorithm does not allow to separate into different clusters the merged electromagnetic showers. In order to remove the clusters that could be issued from multiple particle contributions the number of local maxima in the cluster is limited to 2. The case of 2 local maxima mainly corresponds to merged π^0 photon clusters and will be discussed in the next section.

- $1 - E_{cross}/E_{max} > 0.97$ (E_{cross} is the energy deposit in the cells in a cross contained in the cluster and centered on the cell with the maximum energy) and $\lambda_0^2 < 0.1$: the particle shower energy deposit should not be contained in a single cell. These clusters, called exotic clusters, are removed via cuts on the energy distribution in the clusters.

- The clusters coming from different bunch crossing are removed via the timing cut on the clusters, $|t^{cluster}| < 30$ ns corresponding to the bunch spacing. It rejects about 6% of the clusters.

The cluster p_T spectra after each cut and the associated selectivity are presented in the annex B.

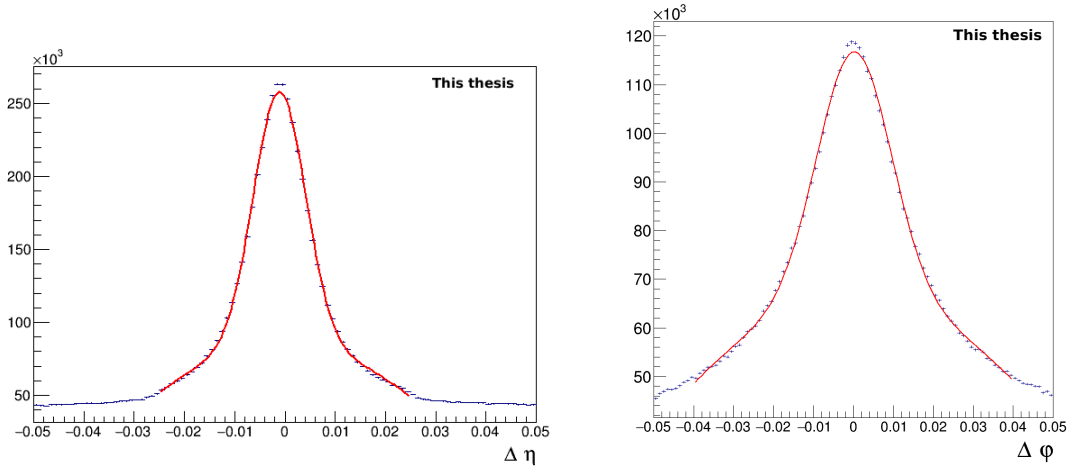

Figure 5.8: On the left plot: $\Delta\eta$ (distance between a track to clusters in pseudo rapidity) distribution fitted by a gaussian and a polynomial functions, $\sigma = 0.009$. On the right plot: $\Delta\varphi$ (distance between a track to clusters in azimuth) distribution fitted by a gaussian and a polynomial functions, $\sigma = 0.005$. LHC13d,e and f data have been used.

EMCal clusters, can be associated to charged particles, called charged clusters, as well as clusters associated to photons, called neutral clusters on which we focus in the presented analysis. Charged clusters, mainly from electrons, have been rejected applying a track-cluster matching cut (also called charged particle veto). This is based on the fact that charged particles also produce tracks in the central barrel, and especially in the TPC, contrary to photons. The tracks from the TPC are propagated to the EMCal surface checking the distance to the closest clusters in azimuth $\Delta\varphi = |\varphi_{track} - \varphi_{cluster}|$ and in pseudo-rapidity $\Delta\eta = |\eta_{track} - \eta_{cluster}|$. If the track is close to a cluster, both can be considered as issued from the same charged particle. This charged cluster is then rejected. In order to determine the proper cut value, a cut at 3 σ is applied on the $\Delta\varphi$ and $\Delta\eta$ distribution. As one can see in the Figure 5.8, the cuts are $\Delta\varphi < 0.03$ and $\Delta\eta < 0.02$, similar to the ones used in the p-p analysis [67]. No significant difference could be expected.

Applying this charged particle veto enabled to select neutral cluster.

5.3.2 Prompt photon cluster candidate

The background in our analysis is mainly coming from π^0, and to a less extent from η, which are produced in large quantities in heavy ion collisions. π^0 decays into two photons with a branching ratio of 97%, as explained in the chapter 2. The kinematics of the π^0 decay indicates that the angle θ between the two emitted photons is inversely proportional to the considered π^0 energy, as described by the equation 5.5.

$$sin^2\theta = \frac{m^2_{\pi^0/\eta}}{E^2_{\pi^0/\eta}} \tag{5.5}$$

Due to the granularity of the calorimeter and the small decay angle, the electromagnetic showers issued from the two decay photons are partially merged for $E_{\pi^0} > 10$ GeV/c and mainly totally merged for $E_{\pi^0} > 10$Gev/c. The used clusterization algorithm will produce only one cluster corresponding to these two showers. It does not allow to discriminate between the two merged showers. For these reasons, among the measured neutral clusters there are many remaining contamination clusters coming from the decay of neutral mesons. In order to remove them from our cluster candidates, the topology of the electromagnetic shower in the calorimeter EMCal will be used. Indeed, decay photon showers are merged into one shower whose transverse expansion has an elliptical shape like the corresponding cluster.

The parameters of the shower shape associated to a cluster, λ_0^2 and λ_1^2, can be defined as in the equations 5.6 and 5.7. They represent an elliptic shower parametrization in the cluster barycentric coordinates and enable to take into acount the weight of each cluster cell and its dispersion.

$$\lambda_0^2 = \frac{d_{\varphi\varphi} + d_{\eta\eta}}{2} + \sqrt{(\frac{d_{\varphi\varphi} - d_{\eta\eta}}{2})^2 + (d_{\varphi\eta})^2} \tag{5.6}$$

$$\lambda_1^2 = \frac{d_{\varphi\varphi} - d_{\eta\eta}}{2} + \sqrt{(\frac{d_{\varphi\varphi} - d_{\eta\eta}}{2})^2 + (d_{\varphi\eta})^2} \tag{5.7}$$

where $d_{\varphi\varphi}$,$d_{\eta\eta}$ and $d_{\varphi\eta}$ represent the dispersion according to η and φ as:

$$d_{AB} = \frac{\sum_i w_i A_i B_i}{\sum_i w_i} - \frac{(\sum_i w_i A_i)(\sum_i w_i B_i)}{(\sum_i w_i)^2} \tag{5.8}$$

A_i and B_i are the cells coordinate

w_i is their associated weight in the cluster:

$$w_i = 4.5 - log(\frac{E_i}{E_{cluster}}) \tag{5.9}$$

λ_0^2 can be considered as equivalent to the long axis of the cluster on the EMCal surface. It will be used as a discriminant parameter in order to reject photons from π^0. A high λ_0^2 corresponds to a cluster with an elliptic shape. Only circular shape clusters are selected to constitute our signal. In the Figure 5.9, one can see the λ_0^2 distribution depending on the transverse energy of the considered cluster. The signal region, with only circular shape clusters, is located between the two black lines. A sliding cut has been introduced in the pp collision analysis, presented in the Table 5.6, to reduce the bias induced by the discrepancy between the shower shape in the data and Monte-Carlo simulations, due to the bad reproduction of the shower shape in simulations, as one can notice on the Figure 5.10 in each energy bin.

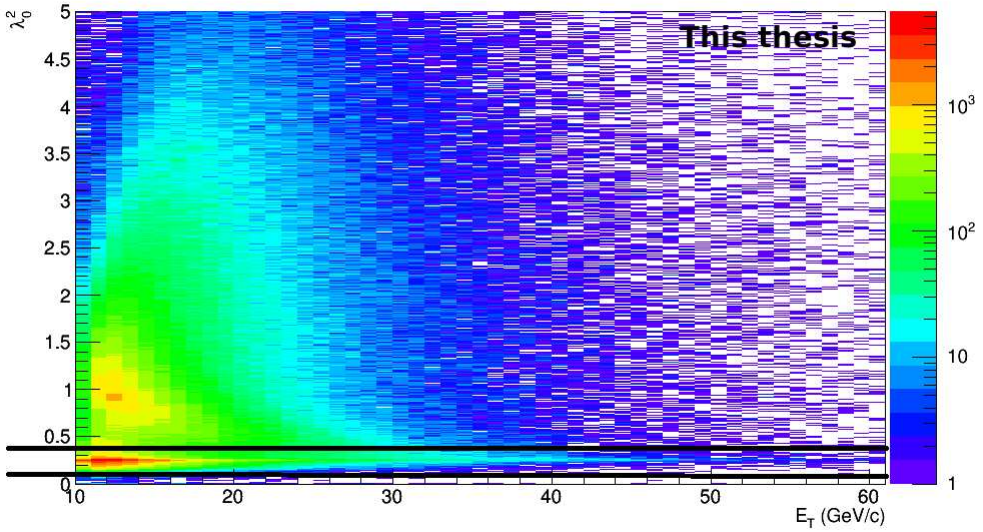

Figure 5.9: λ_0^2 distribution depending on the cluster p_T in the LHC13d/e/f data set. The region corresponds to clusters issued from the prompt photon electromagnetic shower located between the two black lines.

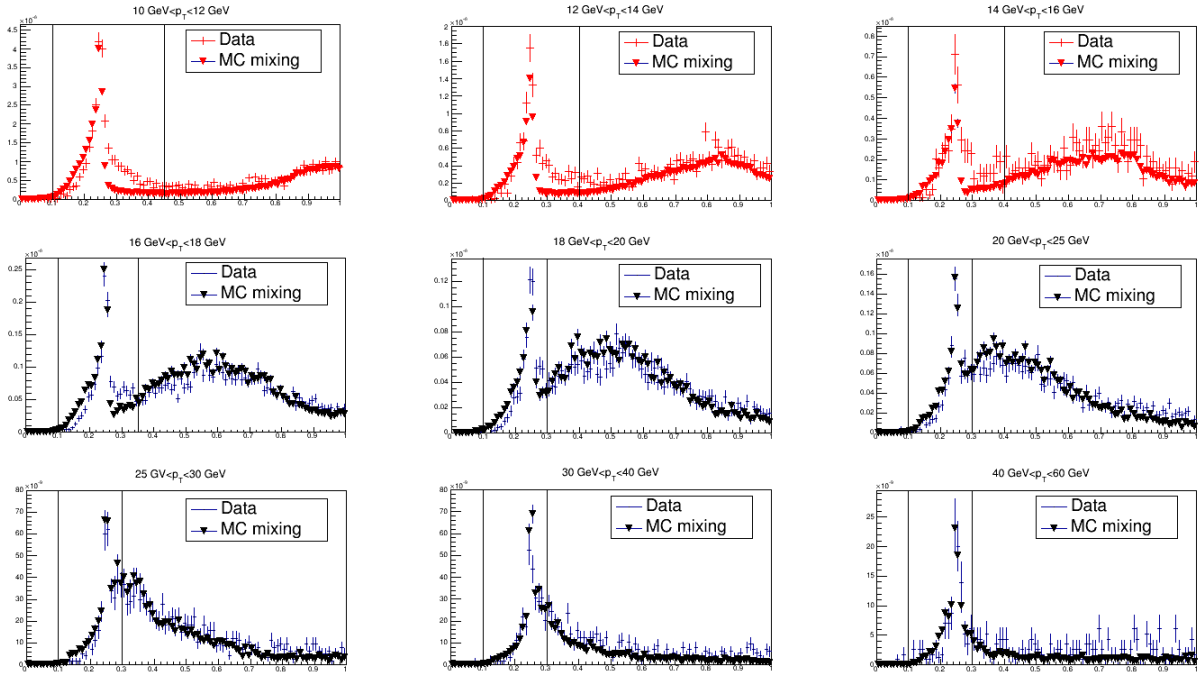

Figure 5.10: λ_0^2 distribution in each p_T bin in LHC13f data and a Monte-Carlo mix of LHC16c3c2 gamma-jet simulation and LHC16c3b2 jet-jet simulation (LHC16c3a2 for the three first bins). The pic around 0.27 corresponds to clusters with a circular shape. The black lines corresponds to cuts applied on λ_0^2 (tab.5.6)

E_T	Signal range
10-12 GeV	$0.1 < \lambda_0^2 < 0.45$
12-16 GeV	$0.1 < \lambda_0^2 < 0.4$
16-18 GeV	$0.1 < \lambda_0^2 < 0.35$
18-60 GeV	$0.1 < \lambda_0^2 < 0.3$

Table 5.6: Shower shape cut applied for the different energy ranges

The cut on λ_0^2 enabled to reject the main part of the π^0 contamination. Another part will be eliminated applying the isolation cut. Finally, the remaining contamination will be evaluated in the chapter 7.

After selecting the neutral clusters of interest, we need to apply discriminant isolation criteria. The isolation cone radius is taken as R=0.4. In order to determine a discriminant energy threshold on the hadronic energy contribution inside the isolation cone, another energy contribution needs to be evaluated. Indeed, in addition to the cluster energy which will not be taken into account in the cone energy, there is, in p-Pb and Pb-p collisons, a significant contribution from underlying events. A careful study of underlying events has to be performed using different methods depending on the neutral, charged or both contributions. This study will be presented in the next chapter.

5.4 Analysis calibrated with the pp data

The analysis presented in this thesis work has been developed with a completely different framework from the one used in the pp analysis at $\sqrt{s}$ = 7 TeV. This new independent code has been introduced after having observed some dicrepancies in cross-section extraction using two different existing codes. The analysis code is based on the framework used in the EMCal jet measurements in the ALICE experiment. This enables to validate the existing analysis and, due to its structure, facilitates future photon-jet analysis in order to study the jet quenching.

A careful comparison of the results obtained with the existing pp analysis [67] and with the analysis using the new code has been performed. In the Figures 5.11 and 5.12, one can compare some relevant plots corresponding to this comparison. On the plots of the Figure 5.11 one can see the purity comparison obtained with the two analysis methods with and without the charged particle veto respectively on the left and on the right plot. This comparison comes from the beginning of the analysis. In the Figure 5.12, the ratio of the corrected isolated photon spectra, using the two methods, is plotted. These spectra have been obtained without performing any charged particle rejection.

Such comparison allowed to point out the impact of the charged particle veto cut on the cross-section. Indeed, the signal extraction method, described more in detail in chapter 8, does not cancel the discrepancy observed after the neutral cluster selection but it tends to increase it. Such behaviour is now taken into account in the isolated photon cross-section analysis as systematic errors. It validated the analysis procedure. Both methods showed consistent results. The analysis general procedure, presented in this thesis, to extract the isolated photon cross-section in p-Pb collisions with neutral and charged particle contributions is similar to the one from the p-p analysis; a signifi-

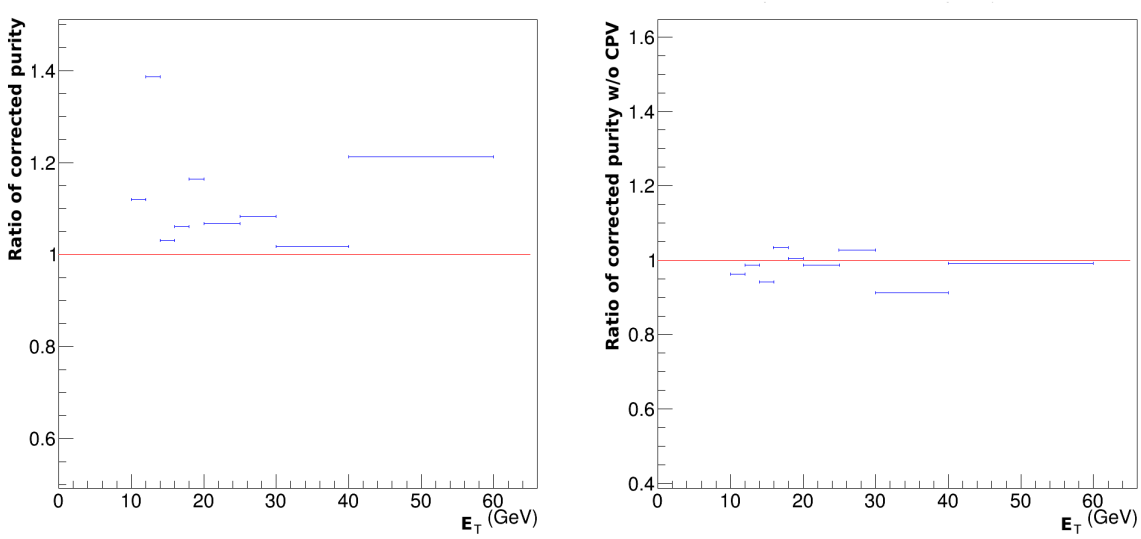

Figure 5.11: Comparison of the purity results obtained with the two analysis framework. The left plot corresponds to the beginning of the analysis. The right plot illustrates an advanced stage of comparison without applying a charged particle veto.

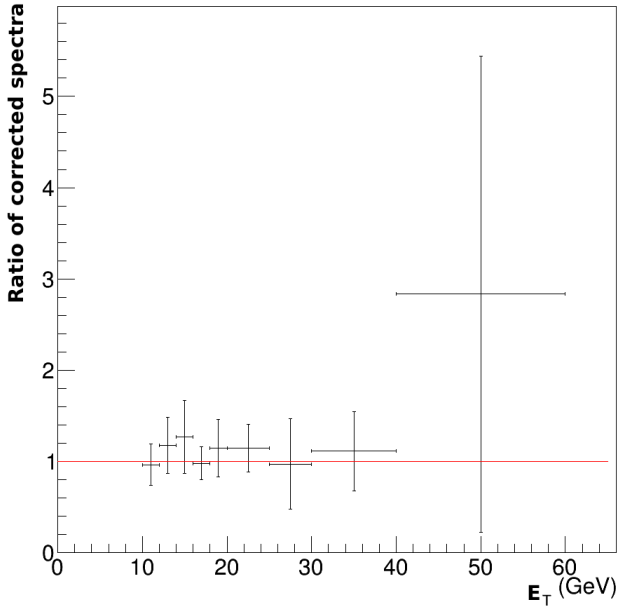

Figure 5.12: Comparison of the corrected isolated photon spectra in pp collisions at $\sqrt{s}$ = 7 TeV obtained with the two different analysis with the LHC11c data set

cant difference is the way to deal with the underlying event analysis as presented in the next chapter.

In this chapter, we have presented the method used to select the events from the p-Pb and Pb-p collision data sets. The events are selected using high trigger levels from runs of data selected via Qual-

ity Assurance analysis. The characteristics of the Monte-Carlo simulations of signal and background, necessary for the signal extraction, have been shown. The tracks, used to compute the energy from charged particles in the isolation cone, result from a combination of the ITS and the TPC tracks. The neutral clusters are selected, after applying a set of quality cuts, by rejecting the clusters from charged particles applying a charged particle veto. Among them, the candidate clusters for prompt photons are selected via the topology of the energy deposit in the calorimeter. The isolated photon analysis in p-Pb collisions has been calibrated with the pp data.

CHAPTER 6

Isolated photon spectra

Contents

In the chapter 2, we have presented the isolation analysis method which implies to reject fragmentation photon clusters surrounded by the energy deposit from hadrons. An isolation cone, as well as a discriminant energy threshold, have to be determined. In p-Pb collisions, not only a hard process is expected in parton-parton interaction. The underlying event contribution has to be quantified to allow the evaluation of the hadronic activity which would enclose the fragmentation photon. The determination of a proper isolation criteria in the analysis is the purpose of this chapter.

6.1 Underlying event contributions

In parton-parton interaction, only one hard process is expected. In collisions involving nucleons, a significant number of soft interactions should occur producing an amount of particle energy deposit in the detectors. Here one has to understand the underlying event contribution as the contribution coming from all the processes except the hard one. In order to choose the proper energy threshold in the isolation cone, one has to distinguish the hadronic energy coming from a jet of particles and the one coming from the underlying events. The production of underlying events is illustrated schematically in the Figure 6.1. A careful study of the underlying events has to be done. Different methods are used allowing the determination of the neutral, charged or joint contributions. The isolation cone radius is taken as R=0.4.

The different methods consist in evaluating the energy contribution in the detector area where no signal from a photon or a jet is expected. The hypothesis is made that the jet-jet or photon-jet

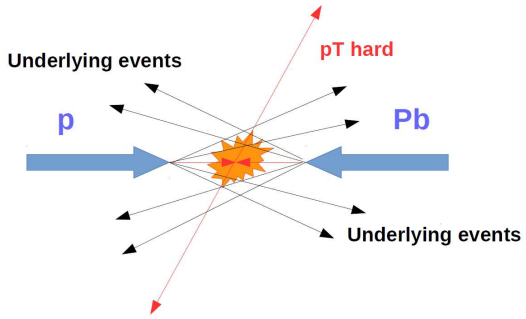

Figure 6.1: Scheme to illustrate the underlying events production in the p-Pb (Pb-p) collision

event produced in the hard process are emitted at the opposite in azimuth. The EMCal calorimeter or the TPC can be involved in the determination of the energy contribution of the underlying events. The main advantage to use the EMCal acceptance is that this enables to study neutral and charged contributions and allows to perform the isolation on neutral and charged contributions in the isolation cone. The methods consist in measuring the energy contribution in η band and φ band in the EMCal acceptance. The considered areas are illustrated by the left view of the Figure 6.2, ③ ⑤ . One can also study only the charged underlying events contribution in the TPC acceptance using four different methods, φ band and η band (similar to what has been presented in the previous paragraph) in the TPC acceptance presented in the Figure 6.3, ④ ⑥ . A method using the whole TPC acceptance, except the isolation cone and a back-to-back band, has been tested. The corresponding scheme can be seen in the Figure 6.2, ① . The fourth underlying event contribution can also be studied in two orthogonal cones with respect to the considered cluster. When a jet-jet or a photon-jet event occurs the produced prompt photons are emitted at the opposite (180°) of a jet. No signal is expected in the areas around $\varphi \sim 90°$. It makes this part of the detector an interesting zone to study the underlying events. The scheme in the Figure 6.3, ② , illustrates the considered area. This method has been used in the pp isolated photon analysis [67], where the contribution of such events was negligeable.

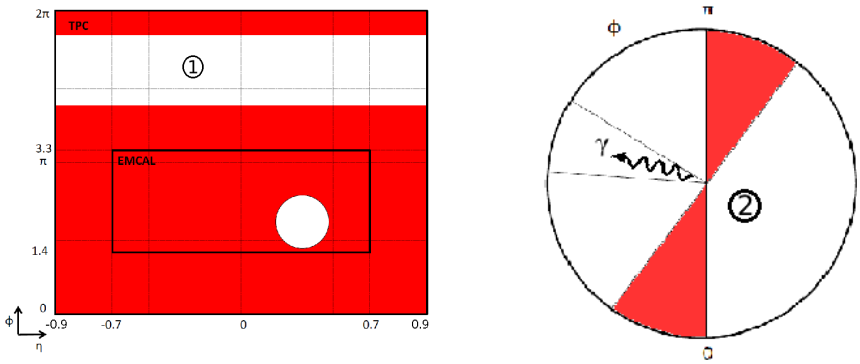

Figure 6.2: Scheme to illustrate underlying events study in the TPC acceptance except a back to back band (left). Scheme to illustrate charged underlying events in two orthogonal cones in the TPC acceptance (right).

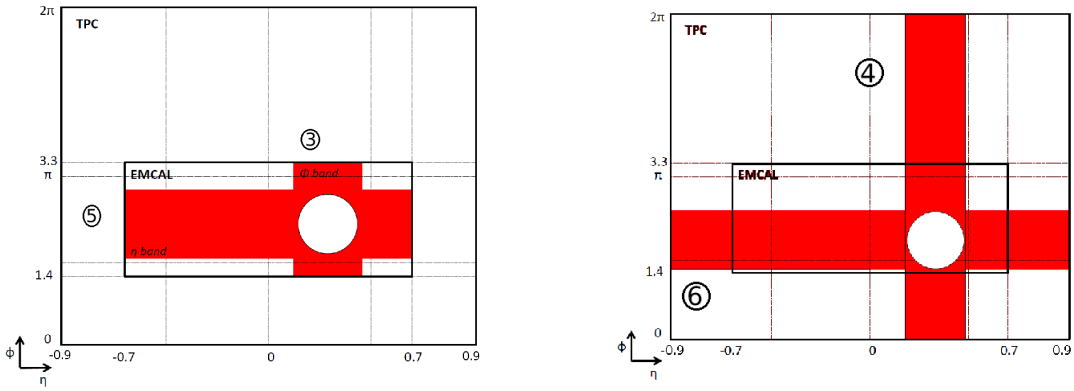

Figure 6.3: Scheme to illustrate the area where charged and neutral underlying events are studied in the EMCal acceptance (left). Scheme to illustrate charged underlying events in η band and φ band in the TPC acceptance (right).

In each case, the energy contribution from the isolation cone has been removed. The mean underlying event contributions in each E_T bin has been normalised to the considered area as:

$$< \sum p_T^{UE} >= \frac{< \sum p_T^{tracks/clusters} >}{A^{UEarea}} \tag{6.1}$$

The events selected by the two triggers, EG1 and EG2, have been used. Two overlapping points, (14-16 GeV and 16-18 GeV bins), have been used to compare the obtained results. A point color convention has been adopted, red points for events selected with EG2 trigger (7 GeV) and blue points for EG1 (11 GeV) event selection. In the next sections, the results obtained in each data set have been computed and presented in tables, the plots correspond to the LHC13d+e+f events since results from the different data sets were all consistent. As a reminder, the LHC13d and LHC13e data sets correspond to the p-Pb collisions whereas the LHC13f data set corresponds to Pb-p collisions.

6.1.1 Methods to estimate the charged underlying event contribution

TPC acceptance except a back to back band ①

In this method, we have considered all the TPC areas except a back to back band (left scheme of the Figure 6.2) in order to maximize the acceptance where underlying events are considered. A band at the opposite of the triggering cluster has been rejected in order not to be too sensitive to flow like events or to reject the hadronic activity coming from the opposite jet. The underlying events contribution is based on charged particles only and are reported in the tables.

One can, firstly, notice that the mean underlying events contribution is similar for every data set (see the Table 6.1). A large increase of the mean charged underlying event contributions with E_T is observed in the Figure 6.4 which can be due to remaining contribution coming from the jet.

LHC13d	TPC acceptance except a back to back band					
	$< \sum p_T^{UE} >$ (GeV/c)					
	Charged					
	LHC13d		*LHC13e*		*LHC13f*	
Bin (GeV)	**EG1**	**EG2**	**EG1**	**EG2**	**EG1**	**EG2**
10-12 GeV		3.50 ± 0.01		3.51 ± 0.01		3.50 ± 0.01
12-14 GeV		3.57 ± 0.01		3.57 ± 0.01		3.58 ± 0.01
14-16 GeV	3.67 ± 0.02	3.67 ± 0.02	3.64 ± 0.01	3.64 ± 0.01	3.64 ± 0.01	3.64 ± 0.01
16-18 GeV	3.71 ± 0.02	3.71 ± 0.02	3.74 ± 0.02	3.74 ± 0.02	3.71 ± 0.02	3.71 ± 0.02
18-20 GeV	3.76 ± 0.03		3.78 ± 0.02		3.81 ± 0.02	
20-25 GeV	3.90 ± 0.03		3.91 ± 0.02		3.88 ± 0.02	
25-30 GeV	4.03 ± 0.04		4.03 ± 0.03		4.05 ± 0.03	
30-40 GeV	4.19 ± 0.05		4.22 ± 0.04		4.25 ± 0.04	
40-60 GeV	4.62 ± 0.08		4.41 ± 0.07		4.52 ± 0.06	

Table 6.1: Mean charged underlying event contribution normalized per unit area in the TPC acceptance except a back to back band for LHC13d and LHC13e and LHC13f events

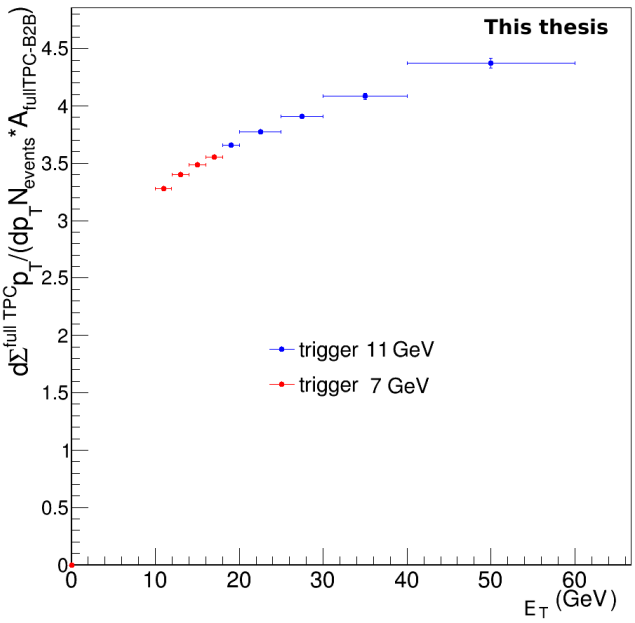

Figure 6.4: $< \sum p_T^{TPCexceptBBBand} >$ depending on E_T, mean underlying event contributions per surface area depending on the energy of the considered cluster for charged contribution using the LHC13d+e+f data set

Orthogonal cones ②

In this second method, we have considered two orthogonal cones perpendicular in the TPC

acceptance to the triggering cluster. This method has been previously used in order to determine the underlying event contribution in the isolated photon analysis in p-p collisions at $\sqrt{s}$ = 7 TeV and has the advantage to measure the underlying events in the region where no signal could be expected.

LHC13d	**Orthogonal Cones**					
	$< \sum p_T^{UE} >$ **(GeV/c)**					
	Charged					
Bin	*LHC13d*		*LHC13e*		*LHC13f*	
Bin	**EG1**	**EG2**	**EG1**	**EG2**	**EG1**	**EG2**
10-12 GeV		2.57 ± 0.02		2.57 ± 0.02		2.57 ± 0.02
12-14 GeV		2.55 ± 0.02		2.55 ± 0.02		2.55 ± 0.02
14-16 GeV	2.56 ± 0.02	2.56 ± 0.02	2.56 ± 0.02	2.56 ± 0.02	2.56 ± 0.02	2.56 ± 0.02
16-18 GeV	2.56 ± 0.03	2.56 ± 0.03	2.56 ± 0.03	2.56 ± 0.03	2.56 ± 0.03	2.56 ± 0.03
18-20 GeV	2.58 ± 0.04		2.58 ± 0.04		2.58 ± 0.04	
20-25 GeV	2.63 ± 0.04		2.63 ± 0.04		2.63 ± 0.04	
25-30 GeV	2.68 ± 0.06		2.68 ± 0.06		2.68 ± 0.06	
30-40 GeV	2.77 ± 0.07		2.77 ± 0.07		2.77 ± 0.07	
40-60 GeV	2.63 ± 0.11		2.64 ± 0.11		2.64 ± 0.11	

Table 6.2: Mean charged underlying event contribution normalized per unit area in orthogonal cones in the TPC acceptance. LHC13d, LHC13e and LHC13f data have been used.

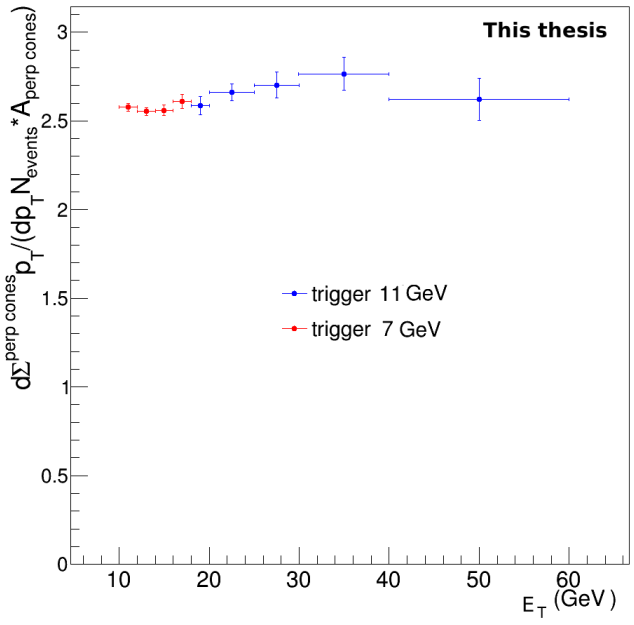

Figure 6.5: $< \sum p_T^{PerpCone} >$ depending on E_T for charged contribution using LHC13d+e+f data sets

It will quantify only charged underlying event contributions. The values obtained with the dif-

ferent data sets are presented in the Table 6.2.

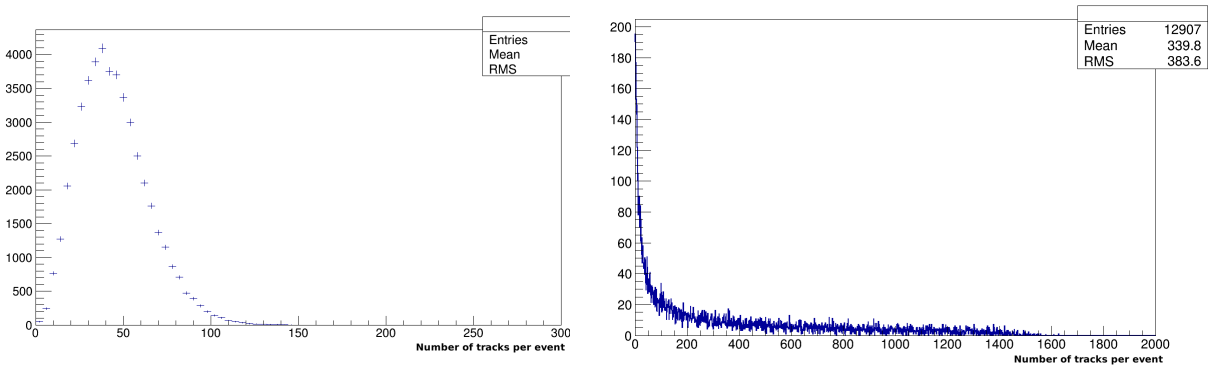

Figure 6.6: Number of tracks per event distribution in Pb-p collisions, LHC13f data set (left plot) and in Pb-Pb collisions, run 170309 of LHC11h (right plot).

Like for the previous method, the charged underlying event contribution is similar in all the considered data set (Table 6.2). Nevertheless, it is smaller than the previous ones, as one can see in the Figure 6.5. Indeed, in the case of p-Pb and Pb-p collisions, the TPC is believed not to be uniformely covered by the underlying events, contrary to what happens in Pb-Pb collisions. The tranverse region can show more empty areas what could explain the lower measured values. This is due to the much lower mean number of tracks per event in p-Pb collisions than in Pb-Pb ones. Consequently, it means that the mean track multiplicity per surface unit is also much lower in p-Pb collisions than in Pb-Pb collisions, which can be seen in the Figure 6.6 which shows the track multiplicity in p-Pb and Pb-Pb collisions. The mean value is much higher in Pb-Pb collisions for the same considered area (~340 tracks in Pb-Pb collisions in comparison with ~44 tracks in p-Pb collisions).

6.1.2 Methods to estimate the neutral and charged underlying events contribution

In the previous paragraph, we have introduced two methods to evaluate the charged underlying event contributions. In this subsection, we present two methods enabling the determination of neutral and charged underlying event contributions.

φ band ③ ④

A φ band corresponds to a η value fixed by the isolation cone defined around the triggering cluster. Charged and neutral underlying events can be studied using the φ band in the EMCal acceptance as seen in the left view of the Figure 6.2 or the right plot of the Figure 6.3. This φ acceptance are sensitive to flow-like events (see chapter 1) or to the opposite jets which are emitted in the opposite azimuthal direction to a prompt photon. Nevertheless, the mean value of the underlying events per unit area will be computed in order to caracterise its behaviour with increasing E_T. The values obtained with the different data sets are shown in the Tables 6.3, 6.4 and 6.5.

LHC13d	**φ Band**					
	Emcal acceptance $< \sum p_T^{UE} >$ **(GeV/c)**				***TPC acceptance*** $< \sum p_T^{UE} >$ **(GeV)**	
	Neutral		*Charged*			
Bin (GeV)	**EG1**	**EG2**	**EG1**	**EG2**	**EG1**	**EG2**
10-12 GeV		1.89 ± 0.02		3.20 ± 0.04		3.09 ± 0.01
12-14 GeV		1.90 ± 0.02		3.27 ± 0.04		3.12 ± 0.01
14-16 GeV	1.91 ± 0.03	1.91 ± 0.03	3.25 ± 0.05	3.24 ± 0.05	3.24 ± 0.02	3.24 ± 0.02
16-18 GeV	1.97 ± 0.04	1.97 ± 0.04	3.30 ± 0.07	3.30 ± 0.07	3.27 ± 0.03	3.27 ± 0.03
18-20 GeV	1.96 ± 0.05		3.43 ± 0.09		3.36 ± 0.04	
20-25 GeV	2.06 ± 0.05		3.47 ± 0.07		3.50 ± 0.03	
25-30 GeV	2.12 ± 0.09		3.58 ± 0.12		3.68 ± 0.06	
30-40 GeV	2.15 ± 0.11		3.65 ± 0.19		3.86 ± 0.07	
40-60 GeV	2.31 ± 0.13		3.85 ± 0.22		4.23 ± 0.11	

Table 6.3: Mean charged and neutral underlying event contributions normalized per φ band area in the EMCal and the TPC acceptance for LHC13d events

LHC13e	**φ Band**					
	Emcal acceptance $< \sum p_T^{UE} >$ **(GeV/c)**				***TPC acceptance*** $< \sum p_T^{UE} >$ **(GeV/c)**	
	Neutral		*Charged*			
Bin (GeV)	**EG1**	**EG2**	**EG1**	**EG2**	**EG1**	**EG2**
10-12 GeV		1.94 ± 0.02		3.16 ± 0.03		3.08 ± 0.01
12-14 GeV		1.95 ± 0.02		3.22 ± 0.03		3.14 ± 0.01
14-16 GeV	1.99 ± 0.03	1.99 ± 0.03	3.25 ± 0.04	3.25 ± 0.04	3.20 ± 0.02	3.20 ± 0.02
16-18 GeV	2.08 ± 0.04	2.08 ± 0.04	3.39 ± 0.06	3.39 ± 0.06	3.32 ± 0.02	3.32 ± 0.02
18-20 GeV	1.99 ± 0.04		3.37 ± 0.07		3.40 ± 0.03	
20-25 GeV	2.06 ± 0.04		3.41 ± 0.06		3.53 ± 0.03	
25-30 GeV	2.13 ± 0.07		3.45 ± 0.09		3.70 ± 0.04	
30-40 GeV	2.09 ± 0.08		3.69 ± 0.13		3.86 ± 0.06	
40-60 GeV	2.38 ± 0.15		3.55 ± 0.18		4.23 ± 0.11	

Table 6.4: Mean charged and neutral underlying event contributions normalized per φ band area in the EMCal and the TPC acceptance for LHC13e events

One can first notice that the mean underlying contribution is similar in all the considered data set, as seen in the Tables 6.3, 6.4 and 6.5, what could be expected since a φ band should not be sensitive to the asymmetry of p-Pb and Pb-p collisions. In the left plot of the Figure 6.1.2, we can notice that the mean charged and underlying event contribution increases slightly with E_T in the EMCal acceptance whereas the charged underlying event contributions in the TPC acceptance shows a clear growth in the right plot of the Figure 6.1.2. This is directly explained by the fact that we measure the signal coming from the opposite jet of a prompt photon in jet-jet or photon-jet events.

η band ⑤ ⑥

An η band corresponds to a fixed φ value defined by the isolation cone diameter around the trig-

LHC13f	φ Band					
	Emcal acceptance $< \sum p_T^{UE} >$ **(GeV/c)**				***TPC acceptance*** $< \sum p_T^{UE} >$ **(GeV/c)**	
	Neutral		*Charged*			
Bin (GeV)	**EG1**	**EG2**	**EG1**	**EG2**	**EG1**	**EG2**
10-12 GeV		1.96 ± 0.02		3.14 ± 0.04		3.08 ± 0.01
12-14 GeV		1.95 ± 0.02		3.27 ± 0.03		3.16 ± 0.01
14-16 GeV	1.98 ± 0.03	1.98 ± 0.03	3.20 ± 0.05	3.20 ± 0.05	3.23 ± 0.02	3.23 ± 0.02
16-18 GeV	1.98 ± 0.03	1.98 ± 0.03	3.31 ± 0.06	3.31 ± 0.06	3.30 ± 0.02	3.30 ± 0.02
18-20 GeV	2.03 ± 0.05		3.40 ± 0.08		3.43 ± 0.03	
20-25 GeV	2.15 ± 0.05		3.49 ± 0.07		3.49 ± 0.03	
25-30 GeV	2.13 ± 0.08		3.49 ± 0.11		3.74 ± 0.04	
30-40 GeV	2.03 ± 0.08		3.64 ± 0.13		3.92 ± 0.05	
40-60 GeV	2.60 ± 0.22		3.51 ± 0.20		4.38 ± 0.10	

Table 6.5: Mean charged and neutral underlying event contributions normalized per φ band area in the EMCal and the TPC acceptance for LHC13f events

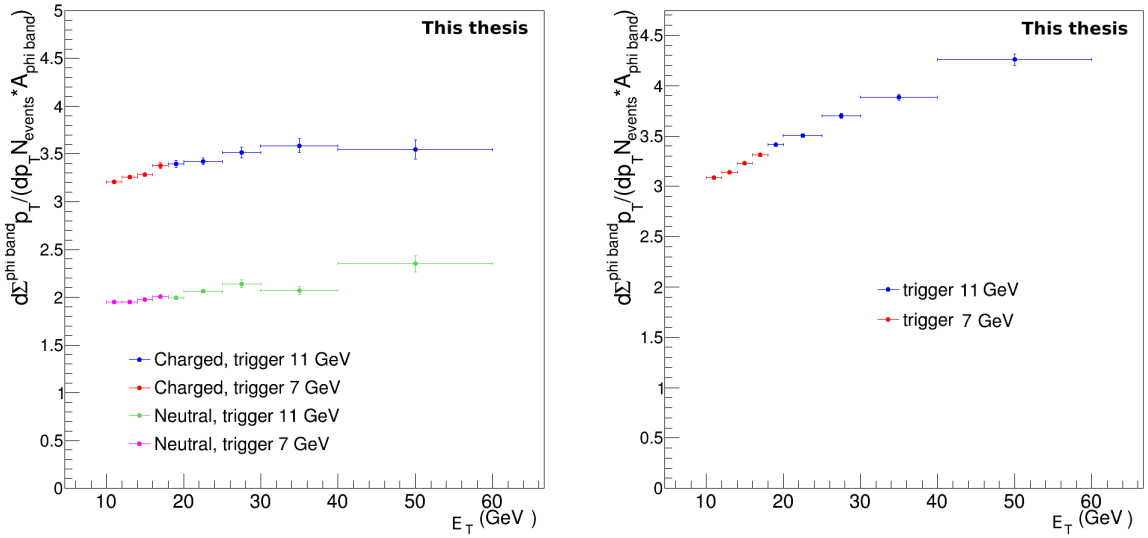

Figure 6.7: Left plot: $< \sum p_T^{Phiband} >$ depending on E_T for neutral and charged contribution in the EMCal acceptance using LHC13d+e+f data set. Right plot: $< \sum p_T^{Phiband} >$ depending on p_T for charged contribution in the TPC acceptance using LHC13d+e+f data set.

gering cluster. Charged and neutral underlying events can be studied using an η band in the EMCal acceptance, as illustrated in the left plot of the Figure 6.2. The η band values in the TPC acceptance (left plot of the Figure 6.3) have been computed in order to compare to the results obtained in the EMCal acceptance for the charged contribution. The computation of different data sets are presented in the different tables. It can be noted that no difference is measured between the LHC13d/e and LHC13f data sets.

One can remark that the behaviour and the values of the mean charged underlying events per

LHC13d	η Band					
	Emcal acceptance $< \sum p_T^{UE} >$ **(GeV/c)**				***TPC acceptance*** $< \sum p_T^{UE} >$ **(GeV/c)**	
	Neutral		*Charged*			
Bin (GeV)	**EG1**	**EG2**	**EG1**	**EG2**	**EG1**	**EG2**
10-12 GeV		1.89 ± 0.03		3.58 ± 0.05		3.20 ± 0.02
12-14 GeV		1.87 ± 0.03		3.63 ± 0.05		3.25 ± 0.02
14-16 GeV	1.91 ± 0.03	1.91 ± 0.03	3.64 ± 0.06	3.64 ± 0.06	3.34 ± 0.03	3.34 ± 0.03
16-18 GeV	1.90 ± 0.04	1.90 ± 0.04	3.63 ± 0.08	3.63 ± 0.08	3.29 ± 0.04	3.29 ± 0.04
18-20 GeV	1.90 ± 0.06		3.62 ± 0.09		3.34 ± 0.05	
20-25 GeV	1.97 ± 0.05		3.93 ± 0.09		3.44 ± 0.04	
25-30 GeV	2.00 ± 0.07		3.74 ± 0.15		3.34 ± 0.07	
30-40 GeV	2.04 ± 0.10		3.76 ± 0.18		3.49 ± 0.09	
40-60 GeV	1.93 ± 0.12		4.14 ± 0.24		3.75 ± 0.14	

Table 6.6: Mean charged and neutral underlying event contributions normalized per η band area in the EMCal and the TPC acceptance for LHC13d events

LHC13e	η Band					
	Emcal acceptance $< \sum p_T^{UE} >$ **(GeV/c)**				***TPC acceptance*** $< \sum p_T^{UE} >$ **(GeV/c)**	
	Neutral		*Charged*			
Bin (GeV)	**EG1**	**EG2**	**EG1**	**EG2**	**EG1**	**EG2**
10-12 GeV		1.89 ± 0.03		3.48 ± 0.04		3.22 ± 0.02
12-14 GeV		1.88 ± 0.02		3.62 ± 0.04		3.29 ± 0.02
14-16 GeV	1.92 ± 0.03	1.92 ± 0.03	3.60 ± 0.05	3.60 ± 0.05	3.29 ± 0.02	3.29 ± 0.02
16-18 GeV	1.97 ± 0.04	1.97 ± 0.04	3.68 ± 0.06	3.68 ± 0.06	3.34 ± 0.03	3.34 ± 0.03
18-20 GeV	2.05 ± 0.05		3.68 ± 0.08		3.39 ± 0.04	
20-25 GeV	1.97 ± 0.04		3.84 ± 0.07		3.48 ± 0.04	
25-30 GeV	1.92 ± 0.06		3.79 ± 0.11		3.51 ± 0.06	
30-40 GeV	2.02 ± 0.07		3.88 ± 0.16		3.56 ± 0.07	
40-60 GeV	2.35 ± 0.12		3.71 ± 0.20		3.30 ± 0.10	

Table 6.7: Mean charged and neutral underlying event contributions normalized per η band area in the EMCal and the TPC acceptance for LHC13e events

cluster momentum are the same computed in the EMCal (left plot of the Figure 6.1.2) and in TPC acceptance (right plot of the Figure 6.1.2), we observe a small increase with E_T values. Contrary to the case of φ band (Figure 6.1.2) we do not measure the signal due to the interaction kinematic properties. Indeed, in a jet-jet or photon-jet event producing a prompt photon. The signal is expected in an area situated at 180° from the considered cluster issued from a prompt photon.

6.1.3 Choice of the method

To summarize, we have introduced four different methods: two methods based on charged background and two based on charged and neutral underlying event contributions.

The method using the TPC acceptance, except a back to back band, cannot be used since the

LHC13f	η Band					
	Emcal acceptance $< \sum p_T^{UE} >$ **(GeV/c)**				***TPC acceptance*** $< \sum p_T^{UE} >$ **(GeV/c)**	
	Neutral		*Charged*			
Bin (GeV)	**EG1**	**EG2**	**EG1**	**EG2**	**EG1**	**EG2**
10-12 GeV		1.88 ± 0.03		3.51 ± 0.05		3.20 ± 0.02
12-14 GeV		1.88 ± 0.02		3.61 ± 0.04		3.28 ± 0.02
14-16 GeV	1.87 ± 0.03	1.87 ± 0.03	3.56 ± 0.06	3.56 ± 0.06	3.31 ± 0.02	3.31 ± 0.02
16-18 GeV	1.95 ± 0.04	1.95 ± 0.04	3.72 ± 0.08	3.72 ± 0.08	3.41 ± 0.03	3.41 ± 0.03
18-20 GeV	2.03 ± 0.05		3.84 ± 0.09		3.45 ± 0.04	
20-25 GeV	2.01 ± 0.05		3.82 ± 0.08		3.35 ± 0.03	
25-30 GeV	2.09 ± 0.09		3.82 ± 0.12		3.56 ± 0.06	
30-40 GeV	2.34 ± 0.21		4.34 ± 0.25		3.74 ± 0.07	
40-60 GeV	2.33 ± 0.19		3.87 ± 0.28		3.80 ± 0.14	

Table 6.8: Mean charged and neutral underlying event contributions normalized per η band area in the EMCal and the TPC acceptance for LHC13f events

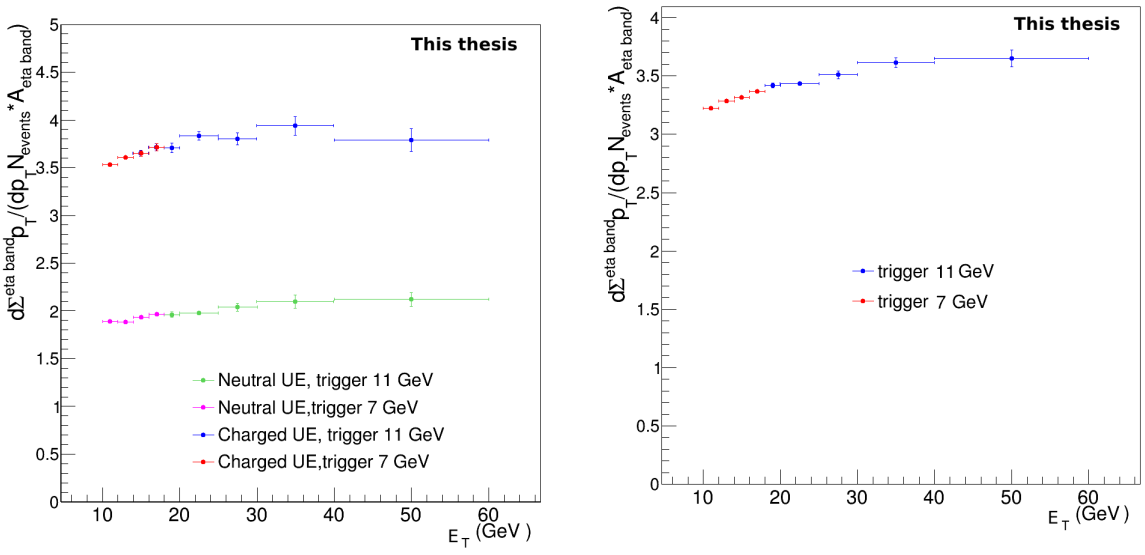

Figure 6.8: Left plot: $< \sum p_T^{EtaBand} >$ depending on E_T for neutral and charged contribution in EMCal acceptance using LHC13d+e+f data set. Right plot: $< \sum p_T^{EtaBand} >$ depending on E_T for charged contribution in TPC acceptance using LHC13d+e+f data set.

E_T dependance shows that we also measure the signal and not only the underlying events contribution. For the same reason, the φ band method is also eliminated. They have enabled to verify the consistency of the results. A pertinent choice has to be done between orthogonal cones and the η band method. First, we will discuss how the underlying event will be taken into account in the measurement.

The values of the underlying events, as one can see in the Figure 6.9, are distinctly correlated to the E_T cluster value; it decreases while E_T increases. This could be explained by the collision

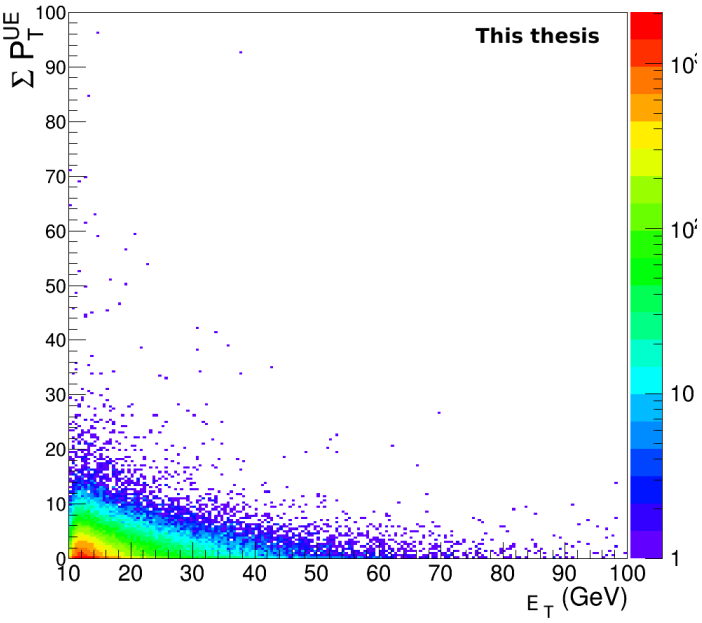

Figure 6.9: $\sum p_T^{EtaBand}$ for charged contribution depending on considered E_T cluster. LHC13d+e+f events have been used.

asymetry at a given energy leading to substract the underlying events event by event to take care of the fluctuations in the background energy contribution. Moreover, we would like to perform the isolation on both, charged and neutral, particles and charged particles only (see section 6.2). The orthogonal cone method enables to gauge solely the charged underlying event contribution. It cannot be used directly, without an extrapolation, to perform the isolation also on neutral energy. In the case where the isolation is performed only with the charged particle contribution, the relevant choice of the underlying events method would have been the orthogonal cones. In this analysis, the choice has been made to use a similar method to measure the isolated photon spectra performing isolation with charged and neutral contributions and with only charged contribution in the isolation cone, to compare the obtained results. Finally, only the η band method fits the requirements. As a further cross-check of the analysis, one could use the orthogonal cone method to quantify the systematic uncertainty associated to the choice of the method using an extrapolation to determine neutral energy contribution.

Nonetheless, in the case of p-Pb and Pb-p collisions, there is a track asymetric distribution in pseudo rapidity. Using an η band in the EMCal acceptance symetric in η ($-0.67 < |\eta| < 0.67$), should not affect the measurement. In the TPC acceptance, this could lead to an overestimation of the contribution of the charged underlying events, while we are in the less filled area, and to an underestimation in the other area. Performing a jet measurement has a direct impact on the considered jet E_T and leads to a bias in the measured spectra. In the case of the isolated photon cross section measurement, this will not have such impact on the spectra since the underlying events contribution is

measured not to correct the energy itself but to apply a discriminant energy threshold.

In the case when the underlying event is overestimated, the neutral cluster, already considered as isolated (mainly direct photons), will still be isolated since the negative energy inside the isolation will be taken into account. This leads to artificially increase the number of isolated neutral clusters by isolating fragmentation photon or π^0 clusters. The impact should be small and compensated by the case where underlying events are underestimated and the isolation criteria are not fulfilled. To further confirm the hypothesis, a study of the underlying events, depending on the considered η bin, could be realized.

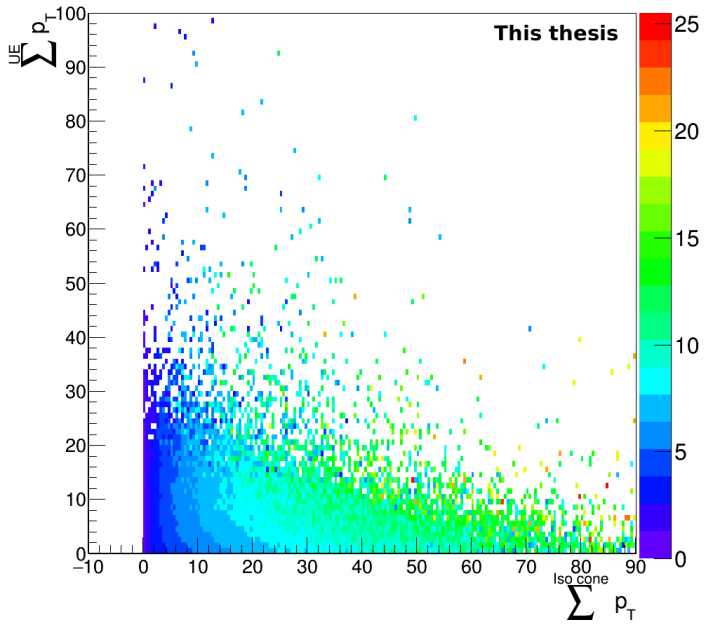

Figure 6.10: $\sum p_T^{EtaBand}$ for charged contribution depending on charged $\sum p_T^{cone}$ in the isolation cone. LHC13d+e+f data have been used.

Finally, we must ensure that we measure underlying events in the η band and not mainly the energy issued from a jet of particules. In the contribution of charged underlying events, in terms of charged energy in the isolation cone, shown in the Figure 6.10, no obvious correlations are noticed. An increasing energy inside the isolation cone does not lead to an increasing background energy. This behaviour indicates that we measure the background contribution using η bands.

In the analysis of the isolated photon, we use the η band in order to substract underlying event contribution in the isolation cone. We can compare the values obtained in the p-Pb analysis to the one obtained in the pp analysis [67] where the charged and neutral contribution was around 2 GeV per surface unit (corresponding to $\sum p_T^{cone} = 1$ GeV/c in the isolation cone). Here we have a value around 4.5 GeV per surface unit corresponding to $\sum p_T^{cone} = 2.2$ GeV/c in the isolation cone. This energy is already higher that the one used as energy threshold in the pp analysis [67]. This is another argument in favor of underlying event subtraction in the cone energy in the case of analysis with the

p-Pb (Pb-p) data of isolated photons.

6.2 Determination of the isolation criteria

In the previous section, we have seen that the underlying events are substracted from the isolation cone energy:

$$\sum_I^{cone} p_{T,i}^{clusters/tracks} - \sum_i^{UE} p_{T,i}^{clusters/tracks} \frac{A^{cone}}{A^{UE}} < p_T^{\text{iso threshold}} \tag{6.2}$$

The p_T threshold is fixed to be discriminant enough without rejecting too many interesting signals and to maximize the reachable statistics. From JetPHOX results, presented in the Table 6.11, it appears that an energy threshold at 2 GeV enables to select from 79 to 95 % of direct photons in prompt photon cross-section computation, depending on the E_T bin. Moreover, the most discriminant parameter is the energy threshold, and not the size of the isolation cone. In order to avoid the latter to be outside of the EMCal acceptance one needs to apply a fiducial cut. This is why the size of the isolation will be chosen in the purpose to minimize the fiducial cut applied and to reach better statistics, while not constraining too much the gluon radiation. A cone size with a radius at R=0.4 will be used in this analysis as in the p-p analysis [67].

The isolation criteria can be summarized as:

$$R = 0.4 \tag{6.3}$$

$$p_T^{\text{iso threshold}} = 2GeV/c \tag{6.4}$$

	Isolation criteria				
	$R < 0.4$, p_T^{max}		$p_T^{max} < 5$ GeV		$R < 0.4$
$p_T^{\gamma}(GeV)$	2 GeV	5 GeV	$R < 0.3$	$R < 0.5$	$\epsilon = 0.1$
10-12	79%	66%	66%	66%	85%
50-70	95%	89%	89%	89%	87%

Figure 6.11: Contribution from direct photons with respect to fragmentation ones in the isolation cone for different isolation criteria in pp collisions at $\sqrt{s}$ = 7 TeV. Computation has been performed with JetPHOX (pp collisions) and CTEQ6.6 parton distribution function model

In this analysis, the isolation is performed on neutral and charged contributions in the isolation cone as it has been done in the p-p analysis [67]. The EMCal acceptance is $-0.67 < |\eta| < 0.67$ and $1.4 < \varphi < 3.3$. This leads to a fiducial cut at $-0.27 < |\eta| < 0.27$ and $1.8 < \varphi < 2.9$ to take into account the photon candidates without drastically decrease the number of selected events. In order to reduce this fiducial cut, the isolation will also be achieved only on charged particles. Indeed, in this case, the reachable area in the EMCal calorimeter is now $-0.47 < |\eta| < 0.47$ and $1.4 < \varphi < 3.3$ (the

TPC acceptance is $-0.87 < |\eta| < 0.87$ and complete in azimuth). Furthermore, using this isolation method cancels the main bias in the purity estimation (discussed in the section 7.1). In the long run, it could enable to study gamma-jet events using the DCAL making the isolation on charged particles. However, it is not easily comparable with pQCD calculations in which the different sources of contribution are not taken into account separately.

The results obtained with these two methods will be compared to check their consistency.

6.3 Uncorrected isolated photon spectra

In this section the isolated photon raw spectra, obtained using the isolation on charged and neutral particles and only on charged particles, is discussed. The results for LHC13d/e (p-Pb collisions) and LHC13f (Pb-p collisions) will be computed and plotted separately, because their normalization are slightly different (see section 7.4). On the plots, the values obtained with the trigger EG2 have been renormalized to the one obtained with EG1 using the rejection factor to verify if they are consistent after normalization. In the result tables, the results of two level triggers are not renormalized.

6.3.1 Isolation using neutral and charged particles

In this subsection, the presented results have been obtained using the neutral and charged contributions in the isolation cone:

(6.5) $$R = 0.4$$

(6.6) $$\sum_I^{cone} p_{T,i}^{clusters+tracks} - \sum_i^{UE} p_{T,i}^{clusters+tracks} \frac{A^{cone}}{A^{UE}} < 2GeV/c$$

In the formula 6.6, "clusters" have to be understood as "neutral clusters".

One can notice that the two overlapping points for the two different trigger levels, EG1 and EG2, have compatible values within the statistical error bars, as seen in the Figures 6.12 wich represents the isolated photon energy spectrum in p-Pb and Pb-p collisions. It confirms that the two level triggers may be used in this analysis to recover the same E_T range ([10-60] GeV) as in the pp analysis [67].

6.3.2 Isolation using charged particles

In this paragraph, the isolation is performed using only the charged contribution in the isolation cone:

(6.7) $$R = 0.4$$

$$\sum_I^{cone} p_{T,i}^{tracks} - \sum_i^{UE} p_{T,i}^{tracks} \frac{A^{cone}}{A^{UE}} < 2GeV \tag{6.8}$$

The obtained raw isolated spectra, $\frac{dN^{\gamma iso}}{dp_T N^{events}}$, for p-Pb collisions (LHC13d and LHC13e) and Pb-p collisions (LHC13f), presented in the Figure 6.13, show a nice agreement of the overlapping points from EG1 and EG2. The values obtained with EG1 and EG2 have been normalized using their respective rejection factor. In the case of the isolation performed on charged and neutral contributions, we can reach a similar E_T range as in the pp analysis ([10-60] GeV) [67], using the two L1 gamma triggers, EG1 and EG2.

The results presented in the Figure 6.13 are not directly comparable to the ones obtained by performing the isolation on neutral clusters and tracks energy contribution in the isolation cone. Indeed, the remaining contamination from neutral meson decay is not similar. This will be more deeply discussed in the next chapter. Moreover, one has to notice that when the isolation is performed on charged particles only, the EMCal reachable acceptance is significantly higher (around three times higher).

This chapter was dedicated to the determination of the discriminant isolation criteria by evaluating the energy contribution of the underlying events. We have presented the approach which has led to the choice of the η band method. This last one has advantage to allow the evaluation of the charged and the neutral contributions. The energy from underlying events is subtracted event-by-event from the isolation cone energy threshold which is fixed at 2 GeV/c. The raw isolated spectra for the p-Pb and the Pb-p collisions have been obtained. The results with EG1 and EG2 triggers show good agreement for the two overlapping points after normalization by the corresponding rejection factor. The photon energy range reached is $[10-60]$ *GeV/c, similar to the one in the pp analysis.*

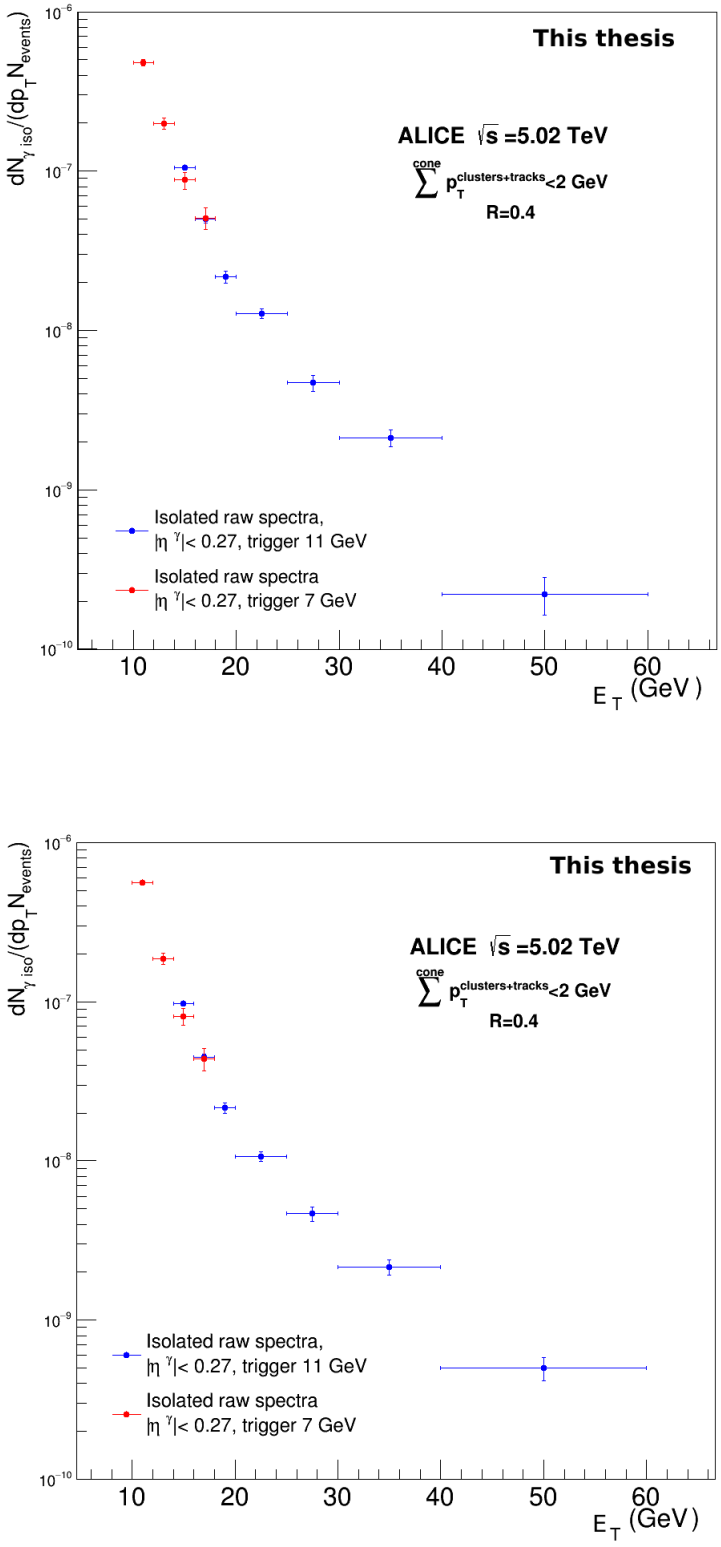

Figure 6.12: Isolated photon energy spectrum when the energy inside the isolation cone is computed with neutral clusters and tracks. In blue, the results obtained with the EG1 trigger. In red, the results obtained with the EG2 trigger. Top: LHC13d and LHC13e data have been added. Bottom: LHC13f has been used in this plot.

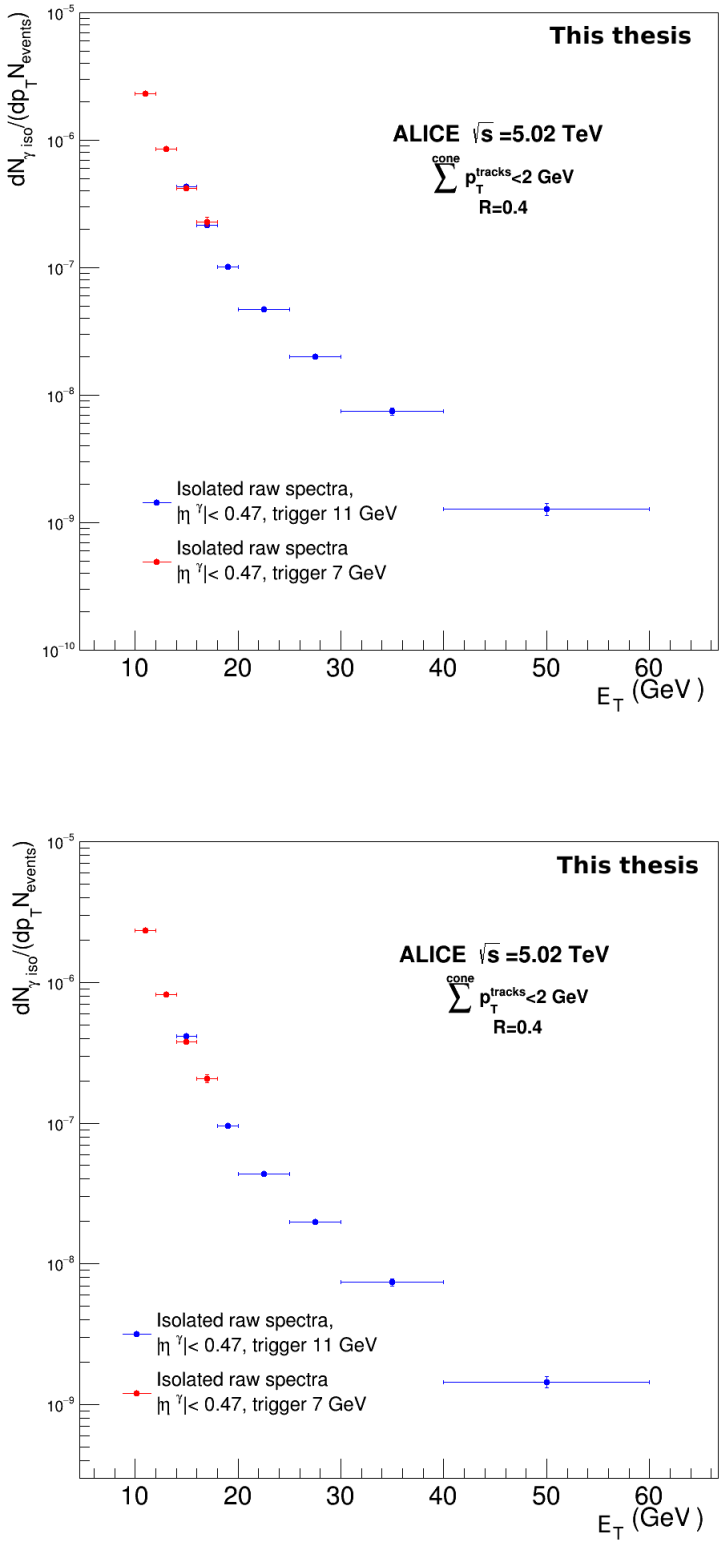

Figure 6.13: Isolated photon energy spectrum depending on the photon cluster energy when the energy inside the isolation cone is computed only on tracks. In blue, the results obtained with the EG1 trigger. In red, the results obtained with the EG2 trigger. Upper plot: LHC13d and LHC13e data,corresponding to p-Pb collisions, have been added. Bottom plot: LHC13f data set corresponding to Pb-p collisions has been used.

CHAPTER 7

Signal extraction and normalization

Contents

This chapter is devoted to the determination of the isolated photon cross-section at $\sqrt{s_{NN}} = 5.02$ TeV. The remaining contamination, essentially from the neutral meson decay, in the raw spectra has to be evaluated. The reconstruction efficiency of the detector is determined via Monte-Carlo simulation. The cross-section is obtained with the minimum bias reference cross-section. The luminosity in the measurement is calculated. Systematic uncertainties have been associated to the choice made in the analysis process.

7.1 Contamination

We have measured the raw isolated photon spectra in p-Pb and Pb-p collisions with the ALICE experiment. The isolation cut does not allow to remove all the background. There is a remaining contamination essentially from the neutral meson decay for the lower E_T values where some decay photons can be isolated. In the previous section, we have actually measured $N_{\bullet}^{\mathrm{iso}} = S_{\bullet}^{\mathrm{iso}} + B_{\bullet}^{\mathrm{iso}}$ where:

- • represents the circular shape clusters, the signal region, where , $0.1 < \lambda_0^2 < \lambda_{0,\,\mathrm{max}}^2 \in [0.3; 0.45]$, as defined in the chapter 5,

- iso indicates the region where the $\sum^{\text{cone}} p_T < p_T^{\text{threshold}}$,
- $S_{\bullet}^{\text{iso}}$ is the signal corresponding to isolated prompt photons,
- $B_{\bullet}^{\text{iso}}$ is the background contamination in the region (mainly photons from decay),
- $N_{\bullet}^{\text{iso}}$ is the total number of isolated cluster in the signal region.

We need to determine the remaining background, $B_{\bullet}^{\text{iso}}$, to estimate the associated purity,$\mathbb{P}$, and to recover $S_{\bullet}^{\text{iso}}$.

$$\mathbb{P} = \frac{S_{\bullet}^{\text{iso}}}{N_{\bullet}^{\text{iso}}} = 1 - \frac{B_{\bullet}^{\text{iso}}}{N_{\bullet}^{\text{iso}}} \tag{7.1}$$

The spectrum presented in the Figures 6.12 and 6.13 correspond to $N_{\bullet}^{\text{iso}}$. Since we cannot directly access to $S_{\bullet}^{\text{iso}}$, we need to determine $B_{\bullet}^{\text{iso}}$. These isolated clusters coming from the background do not have any kinematic or topological difference with the ones coming from direct photons (which constitute our signal). Nevertheless, we know that the clusters with an elliptic shape (high λ_0^2, note as $\neq \bullet$) mainly correspond to background particles (see section 5.3.2). Under the hypothesis that the isolation probability of such clusters is the same as our background cluster (with circular shape, $\bullet$, $0.1 < \lambda_0^2 < \lambda_{0,\,\text{max}}^2 \in [0.3; 0.45]$) in the measurement,

$$\frac{B_{\bullet}^{\text{iso}}}{B^{\neq \text{iso}}{}_{\bullet}} = \frac{B_{\neq \bullet}^{\text{iso}}}{B_{\neq \bullet}^{\neq \text{iso}}} \Longleftrightarrow B_{\bullet}^{\text{iso}} = \frac{B_{\neq \bullet}^{\text{iso}}}{B_{\neq \bullet}^{\neq \text{iso}}} \times B_{\bullet}^{\neq \text{iso}} \tag{7.2}$$

where the signal and the background regions are defined by the cluster shape, the λ_0^2 values. On the scheme 7.1, describing the $\sum^{\text{cone}} p_T$ depending on the λ_0^2 values, one can see the different considered regions. This method, the so-called ABCD method, has been described in [119]. The strong hypothesis that is made implies that the cluster shape, energy and isolation probability are totally independant. This is not true and we will discuss it in more detail in the section 7.1.2.

For the time being, we can replace the $B_{\bullet}^{\text{iso}}$ expression in the purity definition.

$$\mathbb{P} = 1 - \frac{B_{\neq \bullet}^{\text{iso}}}{B_{\neq \bullet}^{\neq \text{iso}}} \times \frac{B_{\bullet}^{\neq \text{iso}}}{N_{\bullet}^{\text{iso}}} \tag{7.3}$$

One can rationally hypothesize that direct photons are almost all isolated and with a circular cluster shape, meaning that, in the signal region, only background clusters are not isolated and in the background region there are only background clusters, thus

$$B_{\bullet}^{\neq iso} = N_{\bullet}^{\neq \text{iso}} \tag{7.4}$$

$$B_{\neq \bullet}^{\neq \text{iso}} = N_{\neq \bullet}^{\neq iso} \tag{7.5}$$

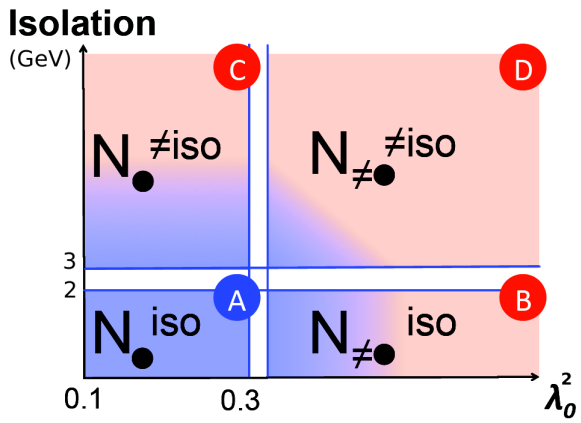

Figure 7.1: Scheme of the purity method representing the different considered regions depending on the $\sum_{cone} p_T$ and on the λ_0^2 of the considered clusters, extracted from [119]

(7.6) $$B_{\neq\bullet}^{\text{iso}} = N_{\neq\bullet}^{iso}$$

This leads to express the purity as:

(7.7) $$\mathbb{P} = 1 - \left(\frac{N_{\neq\bullet}^{\text{iso}}}{N_{\neq\bullet}^{\neq\text{iso}}}\right) \times \left(\frac{N_{\bullet}^{\neq\text{iso}}}{N_{\bullet}^{\text{iso}}}\right)$$

and the associated error as:

(7.8) $$\Delta\mathbb{P} = (1-\mathbb{P}) \times \sqrt{\left(\frac{\Delta N_{\neq\bullet}^{\text{iso}}}{N_{\neq\bullet}^{\text{iso}}}\right)^2 + \left(\frac{\Delta N_{\neq\bullet}^{\neq\text{iso}}}{N_{\neq\bullet}^{\neq\text{iso}}}\right)^2 + \left(\frac{\Delta N_{\bullet}^{\neq\text{iso}}}{N_{\bullet}^{\neq\text{iso}}}\right)^2 + \left(\frac{\Delta N_{\bullet}^{\text{iso}}}{N_{\bullet}^{\text{iso}}}\right)^2}$$

The "non isolated" criterion is posted from 2 to 3 GeV/c in order to avoid side effect between the isolated and not isolated clusters. The background region limits are presented in the Table 7.1 and depend on the signal region limits $((\lambda_0^2)_{,\,\max} + 0.1 < (\lambda_0^2)_{\neq\bullet} < (\lambda_0^2)_{,\,\max} + 1.1)$.

E_T	Signal range •	Background range, ≠ •
10-12 GeV	$0.1 < \lambda_0^2 < 0.45$	$0.55 < \lambda_0^2 < 1.55$
12-16 GeV	$0.1 < \lambda_0^2 < 0.4$	$0.50 < \lambda_0^2 < 1.50$
16-18 GeV	$0.1 < \lambda_0^2 < 0.35$	$0.45 < \lambda_0^2 < 1.45$
18-60 GeV	$0.1 < \lambda_0^2 < 0.3$	$0.40 < \lambda_0^2 < 1.40$

Table 7.1: Background range depending on the bin energy used in order to determine the purity

7.1.1 Purity with the ABCD method in the data

In this section, the purity results obtained with the formulas 7.7 and 7.8, for the isolation on charged and neutral particles and only charged particles are introduced. In each case, the results for LHC13f

(Pb-p collisions) are computed separately from the LHC13d and LHC13e (p-Pb collisions) ones to take care of the normalization differences (as in the section 6.3). Two overlapping points corresponding to the two trigger levels, EG1 and EG2 have been used like in the case of the determination of the raw isolated photon spectra.

7.1.1.1 Isolation on neutral and charged particles

The purity values associated to the isolation with charged and neutral particles have been computed using the formula 7.7.

LHC13d/e	Purity	
E_T	*EG1*	*EG2*
10-12 GeV		0.09 ± 0.07
12-14 GeV		0.30 ± 0.08
14-16 GeV	0.44 ± 0.03	0.41 ± 0.11
16-18 GeV	0.52 ± 0.04	0.64 ± 0.09
18-20 GeV	0.57 ± 0.05	
20-25 GeV	0.68 ± 0.04	
25-30 GeV	0.68 ± 0.06	
30-40 GeV	0.80 ± 0.05	
40-60 GeV	0.55 ± 0.18	

LHC13f	Purity	
E_T	*EG1*	*EG2*
10-12 GeV		0.24 ± 0.06
12-14 GeV		0.22 ± 0.09
14-16 GeV	0.38 ± 0.03	0.37 ± 0.11
16-18 GeV	0.43 ± 0.05	0.54 ± 0.11
18-20 GeV	0.52 ± 0.06	
20-25 GeV	0.66 ± 0.04	
25-30 GeV	0.77 ± 0.04	
30-40 GeV	0.79 ± 0.04	
40-60 GeV	0.88 ± 0.04	

Table 7.2: $\mathbb{P}$ (eq.7.7), the purity associated to the photons isolated on charged and neutral particles. Left table: LHC13d and LHC13e data have been added. Right table: events from LHC13f have been used.

As expected, the computed purity increases with E_T (Figure 7.2) since the number of π^0 with respect to prompt photon (see section 2.2.2 of chapter 2) and the number of isolated π^0 (see discussion section 7.1.2) decrease. The overlapping points are compatible within the statistical error bars. Due to the low statistics available in each data set, the associated errors are significant, especially in the $[40-60]$GeV bin using the LHC13d/e events.

LHC13d/e	Purity	
E_T	*EG1*	*EG2*
10-12 GeV		0.19 ± 0.04
12-14 GeV		0.35 ± 0.04
14-16 GeV	0.36 ± 0.02	0.44 ± 0.06
16-18 GeV	0.47 ± 0.02	0.59 ± 0.06
18-20 GeV	0.52 ± 0.03	
20-25 GeV	0.55 ± 0.03	
25-30 GeV	0.61 ± 0.04	
30-40 GeV	0.71 ± 0.03	
40-60 GeV	0.72 ± 0.06	

LHC13f	Purity	
E_T	*EG1*	*EG2*
10-12 GeV		0.21 ± 0.03
12-14 GeV		0.34 ± 0.04
14-16 GeV	0.36 ± 0.02	0.36 ± 0.06
16-18 GeV	0.45 ± 0.02	0.55 ± 0.05
18-20 GeV	0.48 ± 0.03	
20-25 GeV	0.54 ± 0.03	
25-30 GeV	0.68 ± 0.03	
30-40 GeV	0.68 ± 0.03	
40-60 GeV	0.78 ± 0.04	

Table 7.3: Purity, $\mathbb{P}$ (equ.7.7), as a function of E_T associated to the isolated photon measurement performing the isolation only on charged particles. Left table: the LHC13d and LHC13e events have been added. Right table: the LHC13f data has been used.

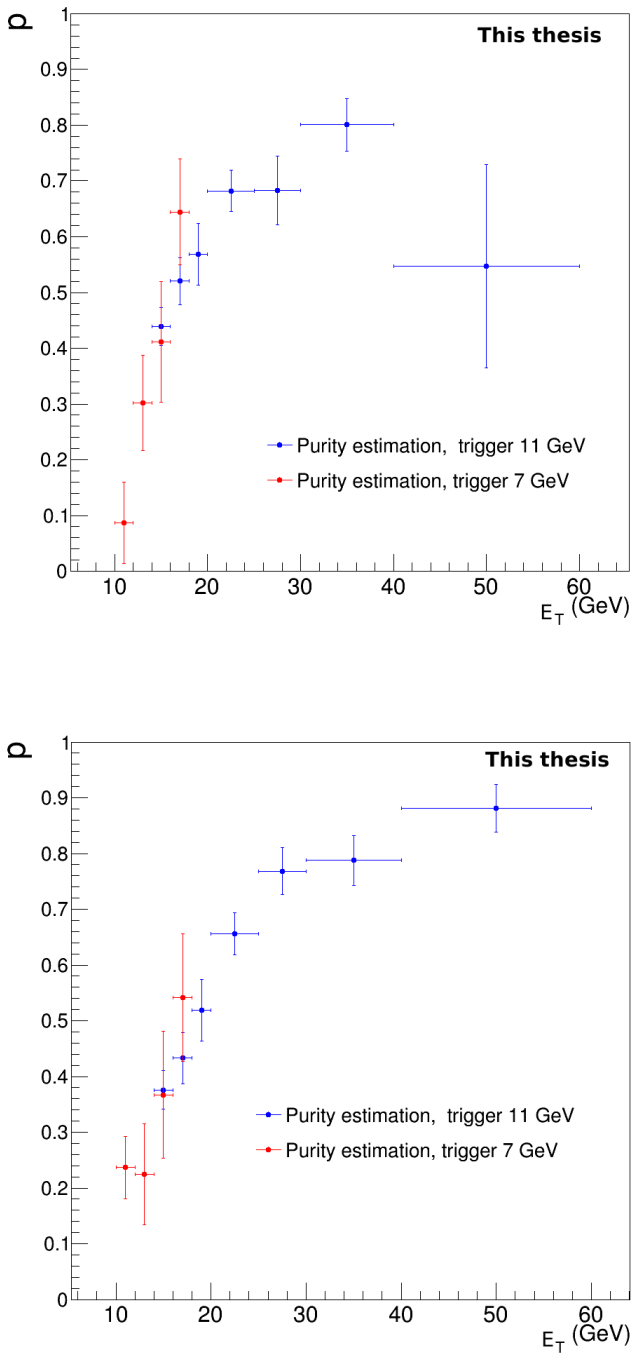

Figure 7.2: $\mathbb{P}$, purity obtained with the ABCD method and the isolation on charged and neutral particles LHC13d and LHC13e data (top plot) and using LHC13f events (bottom plot). In red: results obtained with the EG2 trigger. In blue: results obtained with the EG1 trigger.

7.1.1.2 Isolation on charged particles

The purity associated to the isolation with only charged particles has been computed using the formula 7.7 and the associated error of the formula 7.8.

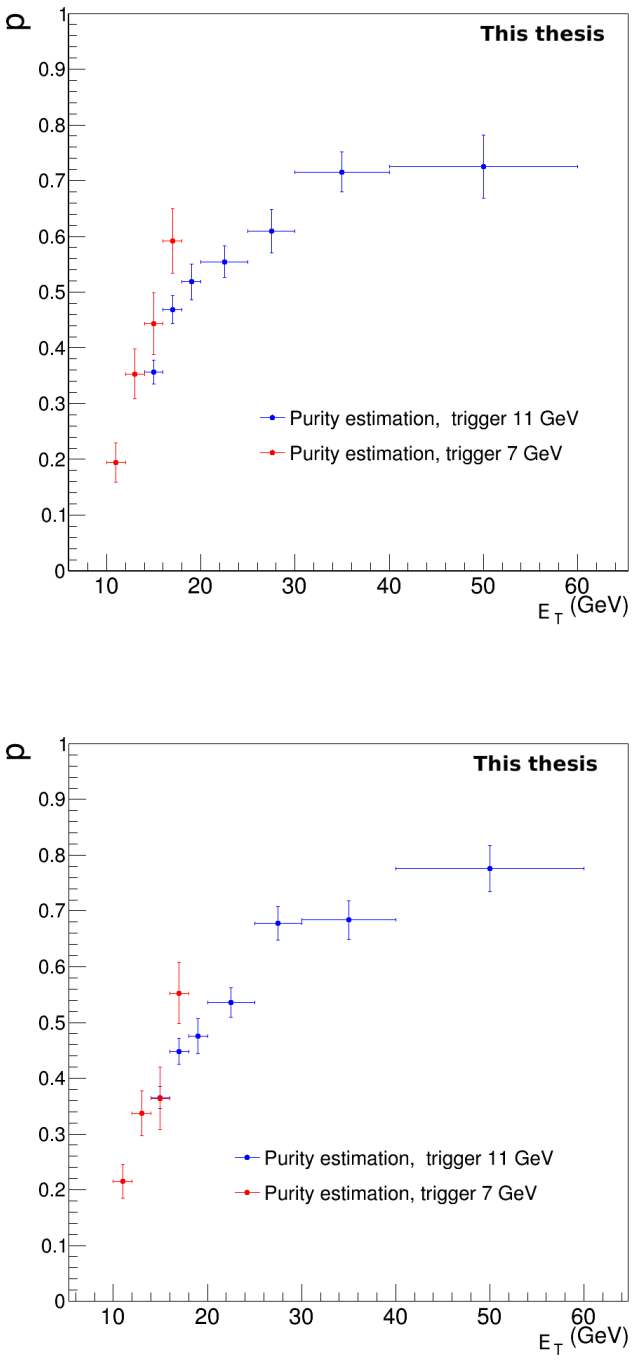

Figure 7.3: Purity, $\mathbb{P}$, as a funtion of E_T obtained with the ABCD method and the isolation with only charged particles using the LHC13d and LHC13e data (top plot) and using the LHC13f data (bottom plot). In red: results obtained with the EG2 trigger. In blue: results obtained with the EG1 trigger.

In the case of the isolation performed on charged and neutral contributions in the isolation cone, the purity increases with E_T, as can be seen in the Figures 7.3. Nevertheless, the statistical errors are lower due to higher number of clusters reachable due to the higher EMCal acceptance in this case.

The purity results are slightly higher, especially for the lower E_T values due to the less important bias introduced in the method of the contamination determination (see section 7.1.2).

7.1.2 Purity correction

We have seen in the section 7.1, that in order to determine the remaining contamination, some assumptions have to be made. Let us go back to the strongest one, introduced in the formula 7.2, that the background isolation probability is the same in the signal region (circular cluster shapes, $\bullet$), and in the background region (elliptic cluster shapes, $\neq \bullet$) which is equivalent to assume that there is no correlation between the cluster shower shape and the energy inside the isolation cone.

Actually, the shower shape reflects the merging of π^0 photon clusters. When a π^0 cluster is in the signal region, it means it has a circular shape instead of the expected elliptic one. We can split the problem depending on the cluster p_T. Indeed, for the higher energy cluster it means that the two photon π^0 showers are totally merged into one high energy cluster since the decay angle is inversely proportional to the particle energy. The isolation probability of such clusters should be similar to the elliptic one in the background region. However, when the background clusters have a low energy and a circular shape, it means that an asymmetric decay happened and the photon partner can be in the isolation cone and contribute to the isolation energy. The background cluster will be probably not isolated. This is not the case for an elliptic background cluster. To summarize, it means that the background isolation probability is lower in the signal region ($\bullet$) than in the background one ($\neq \bullet$). We are currently underestimating the purity in our measurement in the lower E_T bins. When we are performing the isolation on charged particles only we should be affected by this particular problem since we have just considered the charged contribution in the isolation cone.

For the highest cluster energy, one has to take also into account that in a collimated jet environment, an elliptic cluster shape can be due to showers from two different particles. In this case, it means that this particle energy does not contribute to the isolation. It will lead to overestimate the background isolation probability for cluster with an elliptic shape compared to the one with a circular one. The real purity is lower than the one calculated with the ABCD method. This second bias is expected to have less effects since in a collimated jet environment the energy in the isolation cone is most probably much higher than the isolation energy threshold.

These introduced biases have to be corrected with the methods presented in the next sections 7.1.2.1 and 7.1.2.2. The first one, using the invariant mass correction, is only available for the lower E_T values. The second one is based on a mixing of Monte Carlo simulations to estimate the purity bias and extract a correction factor. This last method was used in [67] [120] [119].

7.1.2.1 Invariant mass correction

In the following part, we will study a correction on the purity by determining the residual contamination in signal region from unmerged π^0 using invariant mass analysis and, to a lesser extend, η

invariant mass analysis. Such method allows to avoid a dependence on Monte-Carlo simulations in which cluster shapes are not well reproduced. A preliminary study in pp collisions showing the possibility to apply an invariant mass correction in the three first bins has motivated this analysis.

The π^0 invariant mass is computed by looping on all other neutral clusters (index 2) in the event, for each neutral cluster candidate (index 1) as:

$$M_{\gamma\gamma} = \sqrt{2E_{\gamma 1}E_{\gamma 2}(1 - cos(\theta_{\gamma 1\gamma 2}))} \tag{7.9}$$

where:

- $M_{\gamma\gamma}$ the combination of two photon masses

The result is fitted by a gaussian and a second order polynomial functions in order to reproduce the combinatorial background as:

$$\text{Fit function: } F(M_{\gamma\gamma}) = Ae^{-(M_{\gamma\gamma}-m_0)^2/(2\sigma^2)} + a \times M_{\gamma\gamma}^2 + b \times M_{\gamma\gamma} + c \tag{7.10}$$

with:

- m_0, the π^0 or η fixed masses [22]
- σ the width of the mass peak
- A the amplitude of the mass peak.

The number of π^0 is recovered using the Gauss integral divided by the bin width:

$$N_{\pi^0} = \frac{A \times \sigma \times \sqrt{2\pi}}{\text{bin width}} \tag{7.11}$$

This is done in each E_T bin in order to determine the number of π^0 or η. In practice, in this analysis, the number of π^0 is reachable only in the first energy bin as one can see in the Figure 7.4 where the invariant mass distribution in the lowest energy bin is plotted. Moreover, the statistical error associated is quite high. The huge error associated to the number of η does not allow one to use the invariant mass analysis to determine the associated contamination in the signal.

Applying a correction using an invariant mass analysis is not reliable for high p_T neutral mesons since they are all merged. Morevover, in the lower energy bins, the important error associated to the determination of the number of neutral mesons will drastically increase the already non-negligeable error associated to the isolated photon measurement. For these reasons, the choice has been made not to use this method to correct the biases in the purity measurement in the data and to use Monte-Carlo simulations.

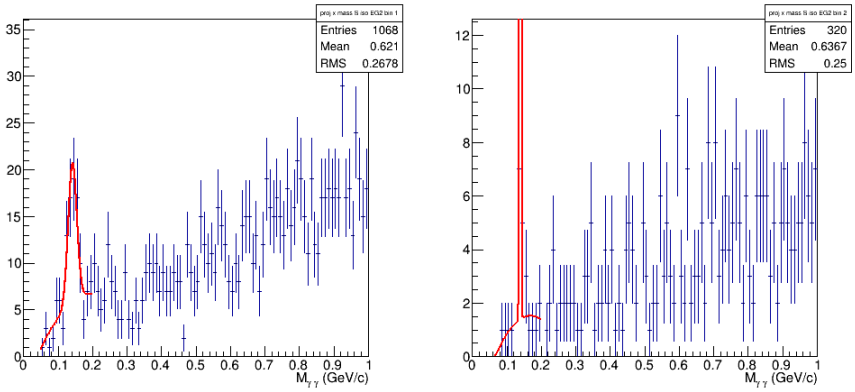

Figure 7.4: Invariant mass distribution in the [10 – 12] GeV and [12 – 14] GeV energy bins using the LHC13f data set and EG2 trigger.

7.1.2.2 Correction using Monte-Carlo simulations

We have seen, in the section 7.1.2, that the purity estimation using the "ABCD" method in the data is biased mainly on asymmetric neutral meson decays. This bias cannot be corrected using only data based analysis as an invariant mass analysis to measure the remaining contamination coming from neutral mesons.

The double ratio from the hypothesis expressed in the equation (7.2) means that the isolation probability is equivalent in the signal region, $\bullet$, to the one in the background region, $\neq \bullet$. This hypothesis is not valid due to the bias, according to the considered region, in the isolation energy induced by the possible presence of the decay photon partner. Jet-jet simulations, reproducing the background (see section 5.1.3), are used in order to evaluate this bias. Moreover, we have also seen that a second hypothesis is introduced in the purity determination in the equations (7.4), (7.5) and (7.6), implying that there is no signal, except in the region where clusters are isolated and with a circular shape. The bias introduced via this hypothesis can be determined using the gamma-jet simulation which enables to reproduce the signal in each region (A, B, C and D regions). A mix of jet-jet and gamma-jet Monte-Carlo simulations ($(N)_{MC(GJ+JJ)} = (N)_{JJ} + r \times N_{GJ}$) will be used in order to correct the existing biases assuming that the isolation fractions are the same in the data and in the Monte-Carlo mix as:

$$(B^i_j)_{data} = (k^i_j N^i_j)_{data} \text{ and } (B^i_j)_{MC(JJ)} = (k^i_j N^j_i)_{MC(GJ+JJ)} \tag{7.12}$$

when $k^i_j = 1$, only jet-jet simulation is considered. If we replace the corresponding values in the double ratio hypothesis equation 7.2:

$$\left(\frac{B^{\text{iso}}_{\bullet}}{k^{\neq \text{iso}}_{\bullet} N^{\neq \text{iso}}_{\bullet}} \times \frac{k^{\neq \text{iso}}_{\neq \bullet} N^{\neq \text{iso}}_{\neq \bullet}}{k^{\text{iso}}_{\neq \bullet} N^{\text{iso}}_{\neq \bullet}}\right)_{data} = \left(\frac{B^{\text{iso}}_{\bullet}}{k^{\neq \text{iso}}_{\bullet} N^{\neq \text{iso}}_{\bullet}} \times \frac{k^{\neq \text{iso}}_{\neq \bullet} N^{\neq \text{iso}}_{\neq \bullet}}{k^{\text{iso}}_{\neq \bullet} N^{\text{iso}}_{\neq \bullet}}\right)_{MC(GJ+JJ)} = 1 \tag{7.13}$$

if we assume that the contamination is the same in the data and in the Monte-Carlo mix, the mixing ratio r will be choosen in purpose,

then $\left(\frac{k_{\neq\bullet}^{\neq\text{iso}}}{k_{\bullet}^{\neq\text{iso}}k_{\neq\bullet}^{\text{iso}}}\right)_{data} = \left(\frac{k_{\neq\bullet}^{\neq\text{iso}}}{k_{\bullet}^{\neq\text{iso}}k_{\neq\bullet}^{\text{iso}}}\right)_{MC(GJ+JJ)}$ and the equation 7.13 becomes:

$$\left(\frac{B_{\bullet}^{\text{iso}}}{N_{\bullet}^{\neq\text{iso}}} \times \frac{N_{\neq\bullet}^{\neq\text{iso}}}{N_{\neq\bullet}^{\text{iso}}}\right)_{data} = \left(\frac{B_{\bullet}^{\text{iso}}}{N_{\bullet}^{\neq\text{iso}}} \times \frac{N_{\neq\bullet}^{\neq\text{iso}}}{N_{\neq\bullet}^{\text{iso}}}\right)_{MC(GJ+JJ)} \tag{7.14}$$

leading to the following expression:

$$\left(B^{\text{iso}}\right)_{data} = \left(\frac{N_{\neq\bullet}^{\text{iso}}N_{\bullet}^{\neq\text{iso}}}{N_{\neq\bullet}^{\neq\text{iso}}}\right)_{data} \times \left(\frac{B_{\bullet}^{\text{iso}}}{N_{\bullet}^{\neq\text{iso}}} \times \frac{N_{\neq\bullet}^{\neq\text{iso}}}{N_{\neq\bullet}^{\text{iso}}}\right)_{MC(GJ+JJ)} \tag{7.15}$$

Now we can replace the obtained $B_{\bullet}^{\text{iso}}$ expression in the purity equation 7.1:

$$\mathbb{P}_{corr} = 1 - \left(\frac{N_{\neq\bullet}^{\text{iso}}N_{\bullet}^{\neq\text{iso}}}{N_{\neq\bullet}^{\neq\text{iso}}N_{\bullet}^{\text{iso}}}\right)_{data} \times \left(\frac{B_{\bullet}^{\text{iso}}}{N_{\bullet}^{\neq\text{iso}}}\frac{N_{\neq\bullet}^{\neq\text{iso}}}{N_{\neq\bullet}^{\text{iso}}}\right)_{MC(GJ+JJ)} \tag{7.16}$$

To simplify the notation in the text and the error expression, we will call $\alpha_{MC(GJ+JJ)}$, the double ratio issued from the Monte-Carlo mix:

$$\alpha_{MC(GJ+JJ)} = \left(\frac{B_{\bullet}^{\text{iso}}}{N_{\bullet}^{\neq\text{iso}}}\frac{N_{\neq\bullet}^{\neq\text{iso}}}{N_{\neq\bullet}^{\text{iso}}}\right)_{MC(GJ+JJ)} \tag{7.17}$$

$B_{\bullet}^{\text{iso}}$ being the number of isolated clusters with a circular shape measured in the jet-jet simulation,

The associated error, from Monte-Carlo simulations, is:

$$\Delta\alpha_{MC(GJ+JJ)} = \alpha_{MC(GJ+JJ)} \times \sqrt{\left(\frac{\Delta B_{\bullet}^{iso}}{B_{\bullet}^{iso}}\right)^2 + \left(\frac{\Delta N_{\bullet}^{\neq iso}}{N_{\bullet}^{\neq iso}}\right)^2 + \left(\frac{\Delta N_{\neq\bullet}^{\neq iso}}{N_{\neq\bullet}^{\neq iso}}\right)^2 + \left(\frac{\Delta N_{\neq\bullet}^{iso}}{N_{\neq\bullet}^{iso}}\right)^2} \tag{7.18}$$

The error associated to the purity determination is

$$\Delta\mathbb{P}_{corr} = (1-\mathbb{P}_{corr}) \times \sqrt{(\frac{\Delta(1-\mathbb{P})}{(1-\mathbb{P})})^2 + (\frac{\Delta\alpha}{\alpha})^2} \tag{7.19}$$

One has to determine the mixing ratio of the gamma-jet versus jet-jet simulations in the Monte-Carlo mix. It is determined in such a manner that the isolation fractions are the same in the data and in the Monte-Carlo mix. To start, a similar value as the one used in the isolated photons pp analysis [67] has been chosen to evaluate the $\alpha_{MC(GJ+JJ)}$ double ratio. The corresponding percentage of injected gamma-jet simulation in the mixing is 44%. The obtained results for the double ratio $\alpha_{MC(GJ+JJ)}$ are presented in the Table 7.4. The values for lower energy bins are below unity. The

	p-Pb		Pb-p	
	$\alpha_{MC(GJ+JJ)}$			
Energy bin (GeV)	**EG1**	**EG2**	**EG1**	**EG2**
10-12		0.85 ± 0.02		0.76 ± 0.01
12-14		0.86 ± 0.03		0.75 ± 0.02
14-16	0.82 ± 0.04	0.80 ± 0.04	0.75 ± 0.03	0.75 ± 0.03
16-18	1.00 ± 0.06	0.97 ± 0.07	0.96 ± 0.06	0.96 ± 0.06
18-20	0.89 ± 0.08		0.86 ± 0.08	
20-25	1.09 ± 0.09		1.11 ± 0.09	
25-30	1.12 ± 0.14		1.47 ± 0.18	
30-40	1.37 ± 0.20		2.29 ± 0.30	
40-60	2.07 ± 0.42		1.40 ± 0.25	

Table 7.4: $\alpha_{MC(GJ+JJ)}$ obtained with a mixing ratio of Monte-Carlo simulation of $r = 0.78$ ($\frac{0.78}{1+0.78} =$ 44% of gamma-jet simulation) in each considered energy bin. The values have been obtained with the two level of triggers and the data from p-Pb (LHC13d+e data set) and Pb-p collisions (LHC13f data set)

equation (7.16) indicates, as expected, that the purity $\mathbb{P}$ was underestimated for these considered cluster energies. The double ratio values, $\alpha_{MC(GJ+JJ)}$, are higher than unity for the highest energies, meaning that the purity was overestimated. This tends to confirm the hypothesis on the biases on the purity determination only in the data with the ABCD method.

	p-Pb		Pb-p	
	Corrected purity			
Energy bin (GeV)	**EG1**	**EG2**	**EG1**	**EG2**
10-12		0.22 ± 0.06		0.42 ± 0.04
12-14		0.40 ± 0.08		0.42 ± 0.07
14-16	0.54 ± 0.04	0.53 ± 0.09	0.53 ± 0.03	0.53 ± 0.09
16-18	0.52 ± 0.05	0.65 ± 0.10	0.46 ± 0.05	0.56 ± 0.11
18-20	0.62 ± 0.06		0.58 ± 0.06	
20-25	0.65 ± 0.05		0.62 ± 0.05	
25-30	0.64 ± 0.08		0.66 ± 0.07	
30-40	0.73 ± 0.08		0.51 ± 0.12	
40-60	0.06 ± 0.42		0.83 ± 0.07	

Table 7.5: $\mathbb{P}_{corr}$ results depending on the considered energy bin. The results have been computed for the two levels of triggers EG1, 11 GeV, and EG2, 7 GeV. The values obtained in p-Pb collisions and Pb-p collisions are presented separately.

In the Figure 7.5, the results of $\alpha_{MC(GJ+JJ)}$ as a function of the energy bins are plotted for different Monte-Carlo mixing rates. One can notice that the chosen mixing ratio does not have a huge influence of the obtained results. In the lowest energy bins no significant differences are observed. For the highest energy values, the case where no signal is injected (marker ⧫) gives lower $\alpha_{MC(GJ+JJ)}$

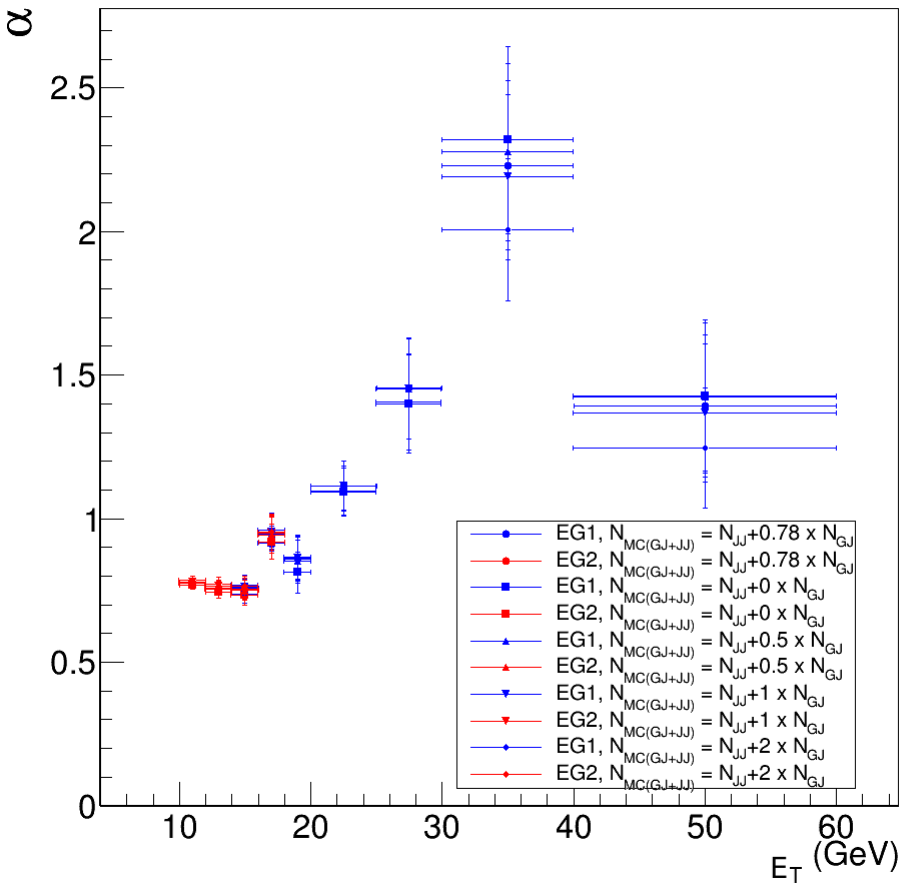

Figure 7.5: Double ratio $\alpha_{MC(GJ+JJ)}$ values obtained with different amount of signal injected in the Monte-Carlo mix. The red points are obtained with the EG2 trigger and the blue points with the trigger EG1. The style of the markers depends on the Monte-Carlo mix. The computations have been performed using the simulations anchored to the Pb-p data (see chapter 5).

values. It indicates that contamination of signal in the B, C and D regions (equation 7.4, 7.5 and 7.6), is higher for these considered energy clusters. This could be explained by the fact that for these considered energies the elliptic shape clusters mainly come from multiple particle contributions and not from neutral meson decays. The change in the choice of the mixing ratio, meaning the proportion of the signal versus background injected in the Monte-Carlo mix, will be taken into account in the systematics uncertainties.

The values of the purity obtained after the correction from the Monte-Carlo mix, $\mathbb{P}_{corr}$ are presented in the Table 7.5 for the two levels of triggers considered, as well as for p-Pb and for Pb-p collisions. The corresponding plots can be found in the Figure 7.6. In comparison with the results obtained for the purity only in the data (Table 7.2), the corrected value of the purity is, as expected (see section 7.1.2), higher for the lowest considered energy bins. This is mainly due to the bias in the

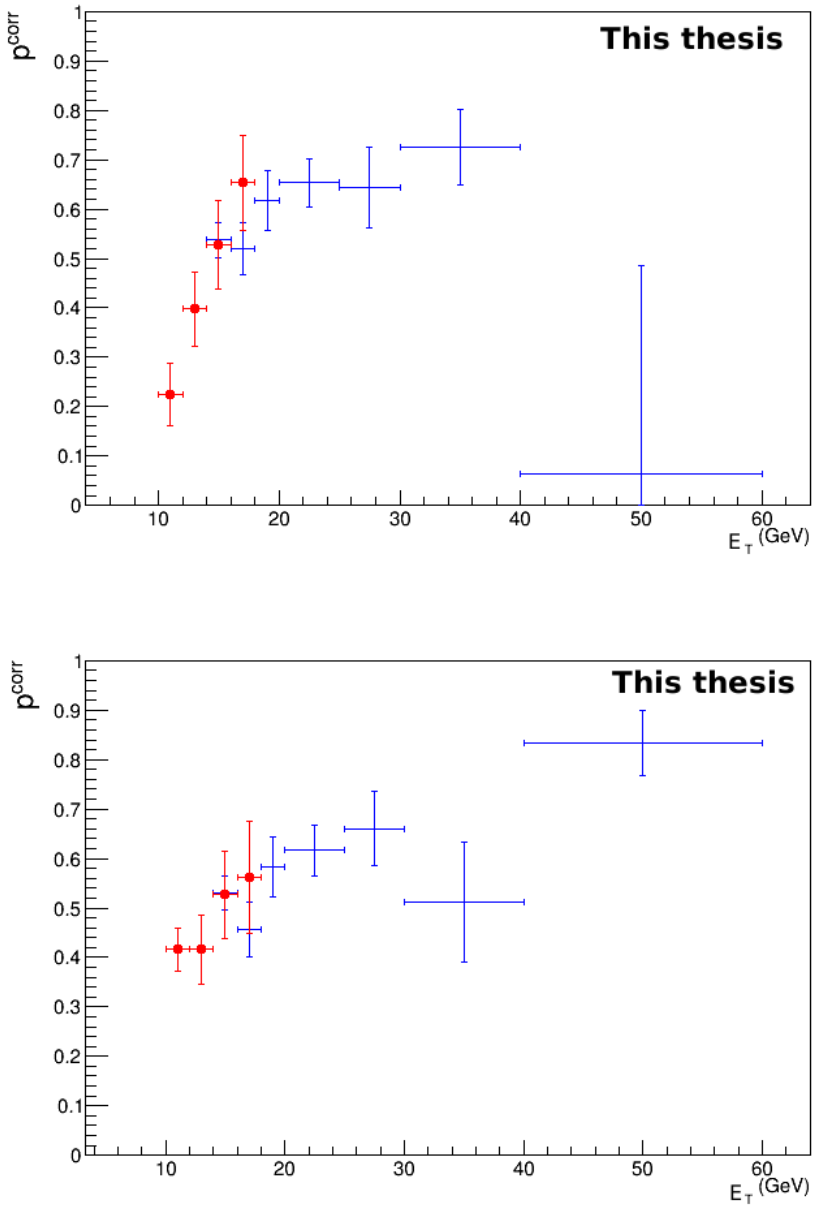

Figure 7.6: $\mathbb{P}_{corr}$ as a function of the cluster energy . The red points correspond to the results obtained with the EG2 trigger whereas the blue points are the results computed with the EG1 trigger. The top figure has been obtained performing the measurement with the p-Pb collisions data, LHC13d+e data sets. The bottom plot corresponds to the values obtained with the Pb-p collisions data, LHC13f data set.

isolation probability. The isolation probability of the background is higher in the signal region, $\bullet$, than in the background region, $\neq \bullet$. At the opposite, the corrected purity $\mathbb{P}_{corr}$ is slightly lower than $\mathbb{P}$ for the highest considered energies. This is imputed to the presence of multiple particle contribution clusters in the background region $\neq \bullet$ that tends to overestimate the isolation probability with respect to the signal region, $\bullet$.

In the Figure 7.6, one can also see that the corrected purity in the highest energy bin [40−60] GeV is extremelly low. This can be imputed to the low statistics, as reflected by the important statistical error associated to this purity value. The non corrected purity $\mathbb{P}$ was already quite low, $\mathbb{P} = 0.55$ and the associated statistical error was equal to 32%. This bin, whose result is not significant, is kept in the analysis in order to perform the merging of the results, from LHC13d/e and LHC13f events, after normalization in the next chapter.

7.1.2.3 Comparison of the isolation with charged and neutral particles and with only charged particles

In the previous section, we have seen that we expected less bias in the purity determination in the data, when the isolation is performed only on charged particles. Moreover, in that case, we expected to select more events. Indeed, the reachable detector acceptance is higher, $\Delta\eta \times \Delta\varphi = 0.94 \times 1.9$ in comparison with the acceptance, $\Delta\eta \times \Delta\varphi = 0.54 \times 1.1$, accessible when the isolation is realized with neutral and charged particles.

To test the hypothesis adopted on the purity determination with the isolation performed with charged particles, we evaluate the quantity $\frac{d^2N^{iso}}{dE_T d\eta}\mathbb{P}(E_T)$ associated to isolated photons in both cases and compare the obtained results. This quantity corresponds to the raw spectra normalized per surface area and corrected for the purity defined as:

$$\frac{d^2N^{iso}}{dE_T d\eta}\mathbb{P}(E_T) = \frac{dN^{iso}}{N^{evts}dE_T}\frac{2\pi}{d\eta d\varphi}\mathbb{P}(E_T) \tag{7.20}$$

In order to simplify the notation, we introduce d^2N^{iso} as $d^2N^{iso} = \frac{d^2N^{iso}}{dE_T d\eta}$ and $d^2N^{iso}\mathbb{P}$ as $d^2N^{iso}\mathbb{P} = \frac{d^2N^{iso}}{dE_T d\eta}\mathbb{P}(E_T)$. We can define the associated error to $N^{iso}_{2diff,\mathbb{P}}$ as:

$$\Delta d^2N^{iso}\mathbb{P} = d^2N^{iso}\mathbb{P} \times \sqrt{\left(\frac{\Delta d^2N^{iso}}{d^2N^{iso}}\right)^2 + \left(\frac{\Delta\mathbb{P}}{\mathbb{P}}\right)^2} \tag{7.21}$$

The Figure 7.7 shows the differential counting of isolated photon obtained using the charged and neutral isolation over the same using charged isolation with and without purity correction. On the lefts plots, one can see the comparison $\left(d^2N^{iso}\mathbb{P}\right)_{neutral+charged} / \left(d^2N^{iso}\mathbb{P}\right)_{charged}$ with no purity correction. We can notice that the ratio is not flat, especially at the lowest energy values where the measurement with charged particles appears to have much higher values. On the right plots, contrary to the previous case, the comparison is done with the purity correction using the Monte-Carlo mix for the measurement with neutral and charged particles. The resulting ratio, $\left(d^2N^{iso}\mathbb{P}_{corr}\right)_{\text{neutral+charged}} / \left(d^2N^{iso}\mathbb{P}\right)_{\text{charged}}$, is flatter in this case and the discrepancy observed for the lower energy values, when the purity is not corrected, appears to be cancelled. The behaviour is seen both in the case of p-Pb collisions (LHC13d+e data set) on the top plots, and in Pb-p collisions (LHC13f data set) on the bottom plots. This observation tends to confirm the hypothesis made on

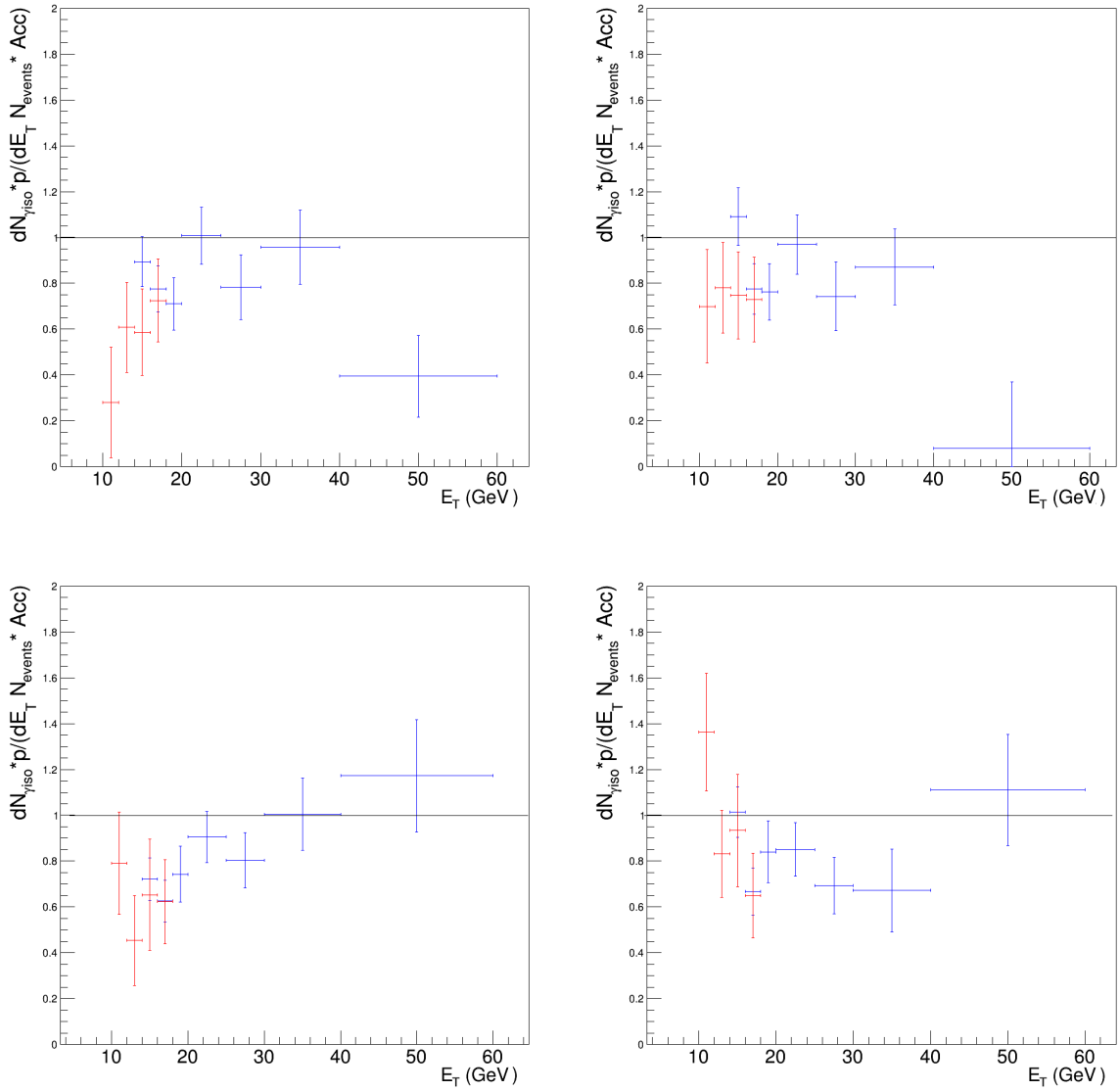

Figure 7.7: Ratio of the corrected from the purity spectra obtained with isolation performed only on charged particles or both on charged and neutral particles, as a function of the photon energy. The left plots correspond to $\left(d^2N^{iso}\mathbb{P}\right)_{neutral+charged} / \left(d^2N^{iso}\mathbb{P}\right)_{charged}$. The right plots represent $\left(d^2N^{iso}\mathbb{P}_{corr}\right)_{neutral+charged} / \left(d^2N^{iso}\mathbb{P}\right)_{charged}$. The top plots correspond to the results obtained with the p-Pb collisions data (LHC13d+e data set) whereas the bottom plots have been performed with the Pb-p collisions data (LHC13f data set).

the purity determination with the ABCD method in the data which should not be biased in the case where the isolation is performed with charged particles. To further confirm, the comparison of the fully corrected spectra of isolated photon performing the isolation with neutral and charged energy contributions and only the charged energy contribution could be done.

We can observe that the charged particle results appear, on all the plots of the Figure 7.7, to be slightly higher that the neutral and charged results. This can be explained by the choice of the isolation energy threshold. Indeed, we have chosen to apply the isolation criteria $p_T^{threshold} = 2GeV/c$,

which means, that when the isolation is performed only with charged particles, the equivalent energy isolation criterion performing the isolation with charged and neutral particles is higher. In the other way, the $p_T^{threshold} = 2GeV/c$ with isolation performed with neutral and charged particles is equivalent to a lower threshold for isolation with charged particles only. One could try to determine an equivalent isolation criteria by looking separately at the contributions from charged and neutral particles in the isolation. Regarding the ratio of the charged and neutral contributions of the underlying events extracted in the chapter 6, we could expect the proportion equal to 1/3 for the neutral and 2/3 for the charged contributions. It would be interesting to compare the obtained results with theoretical models which do not allow to discriminate the charged from the neutral energy contribution in the isolation cone. In any case the equivalent threshold is always an approximation that should be taken into account in systematic errors.

Energy bin (GeV)	$d^2N^{iso}\mathbb{P}_{corr}$ **Neutral charged**		$d^2N^{iso}\mathbb{P}$ **Charged**	
	EG1	**EG2**	**EG1**	**EG2**
10-12		±30%		±19%
12-14		±22%		±13%
14-16	±9%	±21%	±7%	±14%
16-18	±12%	±22%	±7%	±12%
18-20	±14%		±8%	
20-25	±11%		±7%	
25-30	±18%		±9%	
30-40	±17%		±9%	
40-60	±365%		±14%	

Energy bin (GeV)	$d^2N^{iso}\mathbb{P}_{corr}$ **Neutral charged**		$d^2N^{iso}\mathbb{P}$ **Charged**	
	EG1	**EG2**	**EG1**	**EG2**
10-12		±12%		±14%
12-14		±19%		±13%
14-16	±8%	±21%	±7%	±16%
16-18	±14%	±26%	±7%	±12%
18-20	±14%		±9%	
20-25	±12%		±8%	
25-30	±16%		±8%	
30-40	±25%		±9%	
40-60	±19%		±11%	

Table 7.6: Statistical relative error in the measurement of $d^2N^{iso}\mathbb{P}_{corr}$ when the isolation is performed with neutral and charged contribution in the isolation cone and the $d^2N^{iso}\mathbb{P}$ results for an isolation realized using the charged particles contribution. In the left plot, the results have been obtained with the p-Pb collisions data sets. In the right table, are presented the results of the measurement performed with Pb-p collisions.

It has been chosen, at this level of the analysis, to compare the gain in terms of statistical errors of the measurement performed only with charged particles. Indeed, the expected differences in the analysis were in the purity determination. In the Table 7.6, are presented the results obtained for the isolation on neutral and charged particles with a corrected purity, $\left(d^2N^{iso}\mathbb{P}_{corr}\right)_{neutral+charged}$, and the results obtained for the isolation only on charged particles with no correction on purity, $\left(d^2N^{iso}\mathbb{P}\right)_{charged}$. One can see that the statistical relative error is approximately twice lower for the higher cluster energy bins in the case where the isolation is performed with charged particles. This comes from the fact that no additionnal errors are introduced by any purity correction. It is also due to the increase of the reachable detector acceptance, as one can notice in the Figure 6.13, in comparison to the Figure 6.12. The uncertainties associated to the measurement in the last bin of the neutral and charged isolation analysis in p-Pb collisions is not meaningfull. The huge error is due to the low number of events in this energy bin. This point is however kept in order to perform the merging of the p-Pb and Pb-p collision results at the end of this analysis.

All this makes the method performing isolation only on charged particles an interesting solution to improve an analysis limited by the fiducial cut in the detector acceptance. The close to unity values, obtained in the comparison performed in the Figure 7.7, allow to be confident in the consistency of the results obtained with the two methods. This should be checked by changing the energy threshold to a lower and more 'equivalent' one, in the case where the isolation is performed only with charged particles. In this analysis, the choice has been made to perform the isolation with charged and neutral particles. Indeed, this makes the comparison to theoretical predictions more straightforward. Moreover, the analysis in pp collisions has been done using this method. Thus, the determination of a R_{pA} will not be biased by uncertainties introduced by a not equivalent isolation criteria.

7.2 Efficiency

In the previous section, we have estimated the contamination remaining in the measurement. To determine the isolated photon cross-section, one has to evaluate the overall of detector reconstruction efficiency taking into account the identification, acceptance and isolation efficiencies. To achieve this purpose, the number of generated isolated photons is compared to the number of reconstructed ones via photon-jet Monte-Carlo simulations which is expected to reproduce the signal. The efficiency is defined as:

$$\epsilon(E_T) = \frac{dN^{id}_{\gamma_{iso}}}{dE_T^{reco}} / \frac{dN^{gen}_{\gamma_{iso}}}{dE_T^{gen}} \tag{7.22}$$

with:

- $\frac{dN^{id}_{\gamma_{iso}}}{dE_T^{reco}}$ being the number of reconstructed photons known as isolated from the Monte-Carlo generation,
- $\frac{dN^{gen}_{\gamma_{iso}}}{dE_T^{gen}}$ being the number of isolated photons generated in the Monte-Carlo simulation.

In order to simplify the notation in this paragraph, we lighten the formula as $\frac{dN^{id}_{\gamma_{iso}}}{dE_T^{reco}} = dN^{\text{iso, reco}}$ and $\frac{dN^{gen}_{\gamma_{iso}}}{dE_T^{gen}} = dN^{\text{iso, gen}}$. The error associated to the efficency can be expressed:

$$\Delta\epsilon = \epsilon \times \sqrt{\left(\frac{\Delta dN^{\text{iso, reco}}}{dN^{\text{iso, reco}}}\right)^2 + \left(\frac{\Delta dN^{\text{iso, gen}}}{dN^{\text{iso, gen}}}\right)^2} \tag{7.23}$$

The simulation LHC16c3c has been used for the p-Pb collisions data and the simulation LHC16c3c2 for the Pb-p collisions data (see section *Monte-Carlo simulation* in chapter 5). Since the efficiency is computed for all events of the period, the isolation criteria were fixed in order not to reject the underlying events event-by-event but to increase the energy threshold in the isolation cone as:

Efficiency p-Pb		
Energy (GeV)	$\epsilon(E_T)$	
	EG1	EG2
10-12		0.718 ± 0.005
12-14		0.714 ± 0.005
14-16	0.762 ± 0.005	0.711 ± 0.005
16-18	0.740 ± 0.005	0.706 ± 0.005
18-20	0.726 ± 0.005	
20-25	0.728 ± 0.003	
25-30	0.743 ± 0.004	
30-40	0.757 ± 0.003	
40-60	0.778 ± 0.003	

Efficiency Pb-p		
Energy (GeV)	$\epsilon(E_T)$	
	EG1	EG2
10-12		0.834 ± 0.005
12-14		0.830 ± 0.005
14-16	0.875 ± 0.005	0.828 ± 0.005
16-18	0.859 ± 0.006	0.830 ± 0.005
18-20	0.831 ± 0.006	
20-25	0.843 ± 0.004	
25-30	0.852 ± 0.003	
30-40	0.866 ± 0.003	
40-60	0.882 ± 0.002	

Table 7.7: Detector efficiency $\epsilon(E_T)$ determined for the two levels of triggers EG1 and EG2, in the different cluster energy bins. Left table: efficiency results obtained for p-Pb collisions with the simulation LHC16c3c are presented. Right table: efficiency has been computed for Pb-p collisions with the simulation LHC16c3c2.

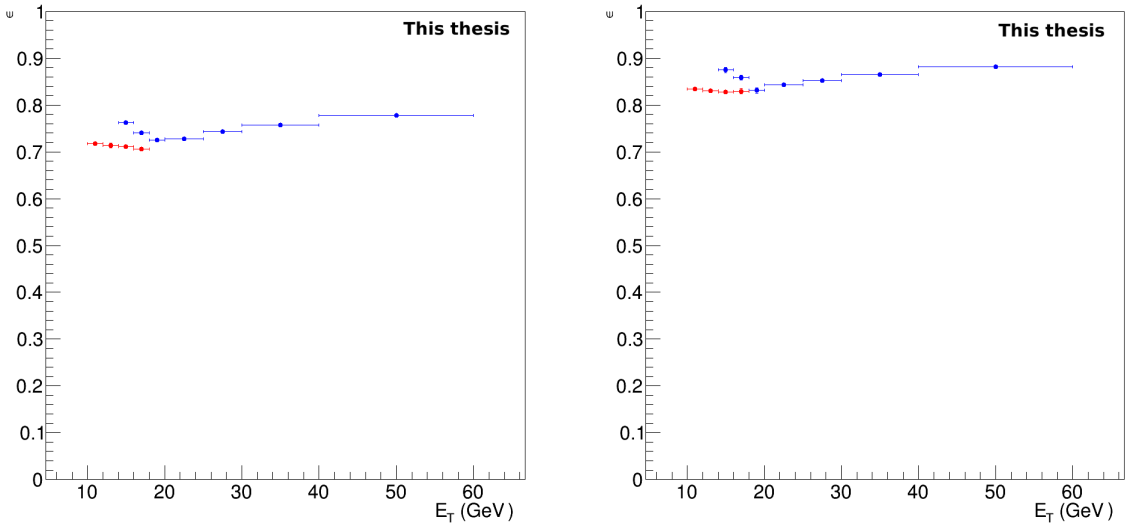

Figure 7.8: Detector efficiency $\epsilon(E_T)$ depending on the considered cluster energy bins. The red points have been obtained with the low trigger threshold EG2, at 7 GeV, whereas the blue points correspond to the high trigger threshold EG1 at 11 GeV. The left plot presents the results obtained with the p-Pb collisions data sets (LHC13d+e data set). The right plot corresponds to the detector efficiency for Pb-p collisions (LHC13f data set).

$$\sum_I^{cone} p_{T,i}^{clusters/tracks} = \sum_I^{cone} p_{T,i}^{clusters/tracks} + \sum_i^{UE} p_{T,i}^{clusters/tracks} \frac{A^{cone}}{A^{UE}} < 3.7 \text{ Gev/c} \tag{7.24}$$

Moreover, one has to point out that the detector efficiency is weakly dependent on the chosen isolation criteria. The associated uncertainties will be taken into account in the systematic errors associated to the choice of the isolation cut.

In the Table 7.7, the detector efficiency results obtained with the two levels of triggers and in p-Pb and Pb-p collisions are presented. These results have been plotted in the Figure 7.8. One can see that the detector efficiency is higher in Pb-p than in p-Pb collisions. That could come from the different mapping of the bad channels. Moreover, in both cases the two overlapping points from the two different triggers do not show any consistency. The points obtained with the high level trigger tend to be higher than the ones obtained with the low trigger threshold. Further analyses should be done to determine these discrepancy origins.

7.3 Systematic uncertainties

This section is dedicated to the determination of systematic uncertainties of the measurement. Four sources of systematics errors have been studied:

- the charged particle veto cut (track matching cut) (see section 5.3.1),
- the λ_0^2 cut (see section 5.3.2),
- the non isolation cut in the purity determination (see section *Contamination* of this chapter) and
- the mixing ratio proportion (see section *Contamination* of this chapter).

All these errors are assumed to be independent. One has to notice that the determination of the systematics errors is preliminary and should be improved for the final the final analysis.

Energy bin (GeV)	**p-Pb**		**Pb-p**	
	λ_0^2			
	EG1	**EG2**	**EG1**	**EG2**
10-12		6.6%		6.4%
12-14		7.6%		7.3%
14-16	6.7%	6.9%	7.5%	7.6%
16-18	25.7%	5.0%	25.9%	26.2%
18-20	23.1%		23.1%	
20-25	21.4%		22%	
25-30	19.8%		20.3%	
30-40	17.8%		18.3%	
40-60	40.15%		16.6%	

Table 7.8: Systematic uncertainties associated to λ_0^2 cut in p-Pb and Pb-p collisions. The two levels of trigger, EG1 and EG2, have been used.

Track matching

The systematic errors associated to the track matching cut have been determined by varying simultaneously the track matching cut of 20% around the nominal values. $\Delta\varphi < 0.024$ and $\Delta\eta < 0.016$

Energy bin (GeV)	p-Pb		Pb-p	
	Isolation probability			
	EG1	EG2	EG1	EG2
10-12		8.7%		5.7%
12-14		1.2%		3.2%
14-16	3.3%	6.7%	0.9%	2.6%
16-18	2%	0.6%	4.1%	4.3%
18-20	2.9%		1.6%	
20-25	2.5%		4.4%	
25-30	1.5%		1.4%	
30-40	3.3%		5.6 %	
40-60	11%		1.1%	

Energy bin (GeV)	p-Pb		Pb-p	
	Mixing ratio			
	EG1	EG2	EG1	EG2
10-12		1.5%		1.2%
12-14		1.1%		4.5%
14-16	1.1%	1.3%	1.5%	2%
16-18	1.1%	0.8%	4%	2.5%
18-20	1.1%		2.3%	
20-25	1.1%		0.8%	
25-30	0.2%		1.1%	
30-40	0.2%		5%	
40-60	40.5%		0.5%	

Table 7.9: Systematic uncertainties from non-isolation cut (left table) and mixing ratio choice (right table) in function of the considered energy bin in p-Pb and Pb-p collisions. The two levels of trigger have been used.

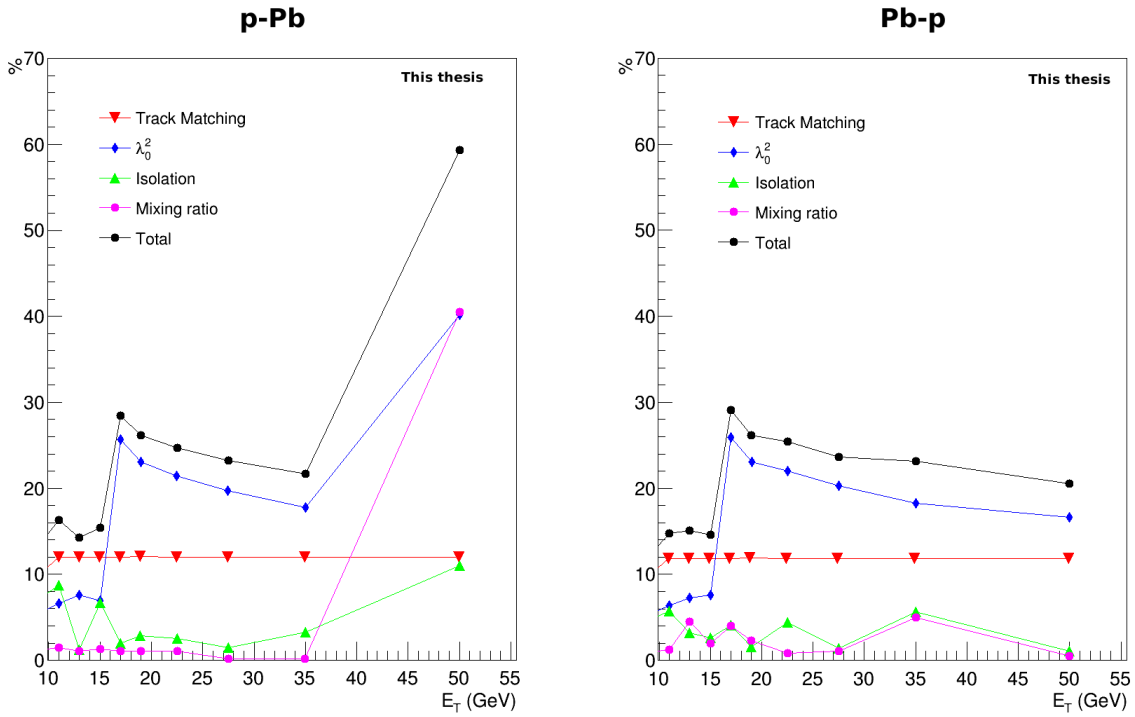

Figure 7.9: Systematic uncertainties in function of the considered energy bin associated to the measurement in p-Pb (left plot) and Pb-p (right plot) collisions.

is a stricter cut than the one used in the analysis ($\Delta\varphi < 0.030$ and $\Delta\eta < 0.020$) whereas $\Delta\varphi < 0.036$ and $\Delta\eta < 0.024$ cut rejects more clusters. They are evaluated on the fully corrected spectra. Indeed, the charged particle veto applied has an impact at each step of the analysis, an effect compensating another one as for the isolation and for the purity for example. In a preliminary study, as no differences are expected between p-Pb and Pb-p collisions as indicate the results from the other

sources of errors, these systematic errors have been studied only using the Pb-p collision data and Monte-Carlo simulations. To further confirm the hypothesis, one could evaluate this source of uncertainties in the p-Pb collisions data and in the corresponding anchored Monte-Carlo simulations. The track matching cut being based on a statistical study, a fit by a constant function of the associated errors depending on the energy bin has been performed. This procedure enabled to extract an error of 12%.

Shower shape

The variation of the λ_0^2 has been changed as shown in the Table 7.10. The elliptic cluster shape has been used for the purity determination by adding 0.1 and 1.1 to respectively the low and the upper limit of the λ_0^2 cut. The results for p-Pb and Pb-p collisions are presented in the Table 7.8. The values tend to increase with the considered energy bin.

E_T	Signal range	Signal range (tight)	Signal range (loose)
10-12 GeV	$0.1 < \lambda_0^2 < 0.45$	$0.1 < \lambda_0^2 < 0.35$	$0.1 < \lambda_0^2 < 0.55$
12-16 GeV	$0.1 < \lambda_0^2 < 0.4$	$0.1 < \lambda_0^2 < 0.3$	$0.1 < \lambda_0^2 < 0.5$
16-18 GeV	$0.1 < \lambda_0^2 < 0.35$	$0.1 < \lambda_0^2 < 0.25$	$0.1 < \lambda_0^2 < 0.45$
18-60 GeV	$0.1 < \lambda_0^2 < 0.3$	$0.1 < \lambda_0^2 < 0.25$	$0.1 < \lambda_0^2 < 0.4$

Table 7.10: Shower shape cut applied for the different energy ranges in the standard analysis (left column) and in the determination of systematic uncertainties

The two other sources of systematic errors are linked to the method used to estimate the purity of the measurement.

Non isolated cut

The first one is the non isolated cut in the purity determination. The variation of the corrected purity has been determined with the non isolated cut momentum values taken at 2 GeV/c and at 5 GeV/c. As a reminder the cut chosen in this analysis is 3 GeV/c and a 2 GeV/c cut corresponds to an absence of gap between isolated and non-isolated clusters. The results are presented in the left part of the Table 7.9. They are below 10% and the trending is almost flat.

Monte-Carlo mix

The last source of systematic errors studied here is the quantity of the signal, the photon-jet simulation, injected in the Monte-Carlo mix to correct the purity. The amount of signal has been chosen at 0% and 50%. The corresponding uncertainties in p-Pb and Pb-p collisions are seen in the right part of the Table 7.9. As we have already shown on the Figure 7.5 (see in *Contamination* section), the dependence on the signal quantity in the Monte-Carlo mix is weak.

The distribution of the systematic uncertainties as a function of the considered energy bin is shown on the Figure 7.9. As one can notice, the main sources of systematic errors are the track matching cut as well as the λ_0^2. They are added quadratically in order to determine full systematic

Energy bin (GeV)	p-Pb		Pb-p	
	Systematics			
	EG1	EG2	EG1	EG2
10-12		16.3%		14.8%
12-14		14.3%		15.1%
14-16	14.1%	15.4%	14.2%	14.6%
16-18	28.4%	13.0%	29.1%	29.2%
18-20	26.2%		26.2%	
20-25	24.7%		25.5%	
25-30	23.2%		23.6%	
30-40	21.7%		23.1%	
40-60	59.3%		20.5%	

Table 7.11: Total systematic uncertainties associated to the measurements in p-Pb and Pb-p collisions for the two levels of trigger.

errors associated to the measurement in p-Pb and Pb-p collisions. The results are presented in the Table 7.11. The value of the systematic uncertainties in the $[40-60]$ GeV bin from the p-Pb collisions data are huge. This is due to the very low number of isolated photons in this energy range. The latter bin have been kept since the p-Pb and Pb-collisions cross-section results will be merged (see chapter 8).

7.4 Cross section determination

7.4.1 Integrated luminosity in the measurement

The integrated luminosity associated to the isolated photon measurement in p-Pb collisions (and the cross-section) can be determined via the known minimum bias cross-section obtained with Van Der Meer scans (see section 3.2.2). The values of the corresponding minimum bias trigger, V0, are [110]:

$$\sigma(\text{V0}) = 2.09 \pm 0.07 \text{ b (syst) (p-Pb)} \tag{7.25}$$

$$\sigma(\text{V0}) = 2.12 \pm 0.07 \text{ b (syst) (Pb-p)} \tag{7.26}$$

The integrated luminosity associated to the measurement is defined as:

$$L_{int} = \frac{N_{evt} RF}{\sigma^{MB}} \tag{7.27}$$

$$L_{int} = \frac{N^{\text{EG1 evts}} RF^{EG1} + N^{\text{EG2 evts}} RF^{EG2}}{\sigma^{MB}} \tag{7.28}$$

with the associated statistical error:

$$\Delta L_{int} = L_{int}\left(\sqrt{\left(\frac{\Delta RF^{EG1}}{RF^{EG1}}\right)^{2}} + \sqrt{\left(\frac{\Delta RF^{EG2}}{RF^{EG2}}\right)^{2}}\right) \tag{7.29}$$

The systematic error is the one associated to the determination of the minimum bias cross-section which is expressed in the equations 7.25 and 7.26. It is similar in p-Pb and Pb-p collisions. As the minimum bias cross-sections in p-Pb and Pb-p collisions are different, the results in both systems are presented separately.

p-Pb collisions

The parameters to determine the integrated luminosity in p-Pb collisions are the following:

- trigger EG2 at 7GeV
  - $N^{\text{EG2 evts}} = 242902$
  - $RF^{EG2} = 1681 \pm 38$
- trigger EG1 at 11GeV
  - $N^{\text{EG1 evts}} = 507401$
  - $RF^{EG1} = 6082 \pm 255$

The integrated luminosity associated to the measurement performed in p-Pb collisions with the LHC13d+e data sets is:

$$\Longrightarrow L_{int} = 1.67 \pm 0.11^{stat} \pm 0.07^{syst}\ \text{nb}^{-1} \tag{7.30}$$

Pb-p collisions

The parameters to determine the integrated luminosity in Pb-p collisions are:

- trigger EG2 at 7GeV
  - $N^{\text{EG2 evts}} = 299254$
  - $RF^{EG2} = 1681 \pm 38$
- trigger EG1 at 11GeV
  - $N^{\text{EG1 evts}} = 624510$
  - $RF^{EG2} = 6082 \pm 255$

The integrated luminosity associated to the measurement performed in Pb-p collisions with LHC13f data set is:

$$\Longrightarrow L_{int} = 2.03 \pm 0.13^{stat} \pm 0.07^{syst}\ \text{nb}^{-1} \tag{7.31}$$

The integrated luminosities associated to the measurements are low.

7.4.2 Isolated photon cross-section

All the parameters have been determined to obtain the isolated photon cross-section associated to p-Pb and Pb-p collisions at $\sqrt{s}$ = 5.02 TeV through the formula:

$$\frac{d^2\sigma^{iso}}{dE_T d\eta} = \frac{dN^{iso}}{N^{evts} dE_T} \frac{2\pi}{d\eta d\varphi} \frac{\mathbb{P}_{corr}(E_T)}{\epsilon(E_T) RF} \sigma^{MB} \tag{7.32}$$

where:

- $\frac{dN^{iso}}{N^{evts} dE_T}$ is the raw spectrum, obtained in the section 6.3.1,
- $d\eta d\varphi$ is the detector acceptance reachable after the fiducial cut as $d\eta d\varphi = 0.54 \times 1.1$,
- $\mathbb{P}_{corr}(E_T)$ is the corrected purity using Monte-Carlo mix determined in the section *Purity correction - Correction using Monte-Carlo simulations* in this chapter,
- $\epsilon(E_T)$ has been determined in the section *Efficiency* of this chapter,
- σ^{MB} is the minimum bias cross-section,
- RF is the rejection factor determined in the section 5.1.2.
- with $\frac{\sigma^{MB}}{RF} = \frac{N^{evt}}{L_{int}}$ for the considered trigger in the results.

In order to simplify the notation, we define:

- $\sigma^{\text{iso}}_{2diff} = \frac{d^2\sigma^{iso}}{dE_T d\eta}$
- $N^{\text{iso}}_{diff} = \frac{dN^{iso}}{N^{evts} dE_T}$.

The statistical error associated to the determination of the differential cross-section can be written as:

$$\Delta\sigma^{\text{iso}}_{2diff} = \sigma^{\text{iso}}_{2diff} \sqrt{\left(\frac{\Delta N^{\text{iso}}_{diff}}{N^{\text{iso}}_{diff}}\right)^2 + \left(\frac{\Delta \mathbb{P}_{corr}}{\mathbb{P}_{corr}}\right)^2 + \left(\frac{\Delta\epsilon}{\epsilon}\right)^2 + \left(\frac{\Delta RF}{RF}\right)^2} \tag{7.33}$$

The systematic uncertainties have been determined in the section 7.3. The uncertainties issued from the minimum bias cross-section of reference (3%, see previous section and [110]) have been quadratically added to the ones coming from the measurement.

The Figures 7.10 and 7.11 show the differential cross-section of isolated photons at $\sqrt{s}$ = 5.02 TeV in p-Pb and Pb-p collisions respectively. The results obtained with the two different trigger levels, EG1 and EG2, show consistency. In order to perform the comparison with models and p-p results in the next chapter, results from EG2 trigger will be used to obtain the third energy bin results. The

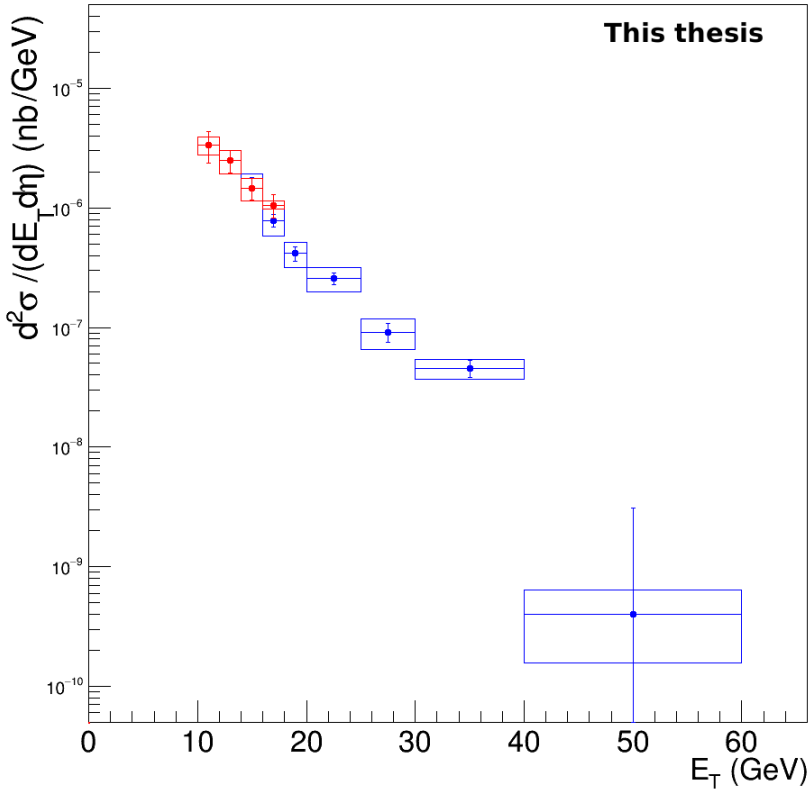

Figure 7.10: Isolated photon differential cross-section in p-Pb collisions at $\sqrt{s}$ = 5.02 TeV as a function of the considered photon transverse energy bin. Red points have been obtained with the low level trigger EG2 at 7 GeV. Blue points have been computed using the high level trigger EG1.

points are too close to the threshold to use the EG1 trigger. The differential cross-section in the fourth bin is obtained with the EG1 level trigger which select more events and have a lower statistical error associated.

For this particular analysis performed in the pseudo-rapidity region $-0.27 < |\eta| < 0.27$, no differences are expected between the analysis in p-Pb and Pb-p collisions. As a consequence, the Figures 7.10 and 7.11 show similar trends as well as similar values. The main differences between the two cases are the signal extraction and the normalization by the detector efficiency as well as the minimum bias cross-section. In the next chapter, we will present the comparison of the obtained results with the theorical pQCD (perturbative Quantum ChromoDynamics) calculations and to the isolated photon measurement performed in p-p collisions at $\sqrt{s}$ = 7 TeV.

In this chapter, we have presented the first measurement of the isolated photon cross-section at $\sqrt{s_{NN}}$ = 5.02 TeV in p-Pb and Pb-p collisions. The remaining contamination in the isolated photon spectra has been evaluated. This was performed via isolation probability in the circular cluster shape

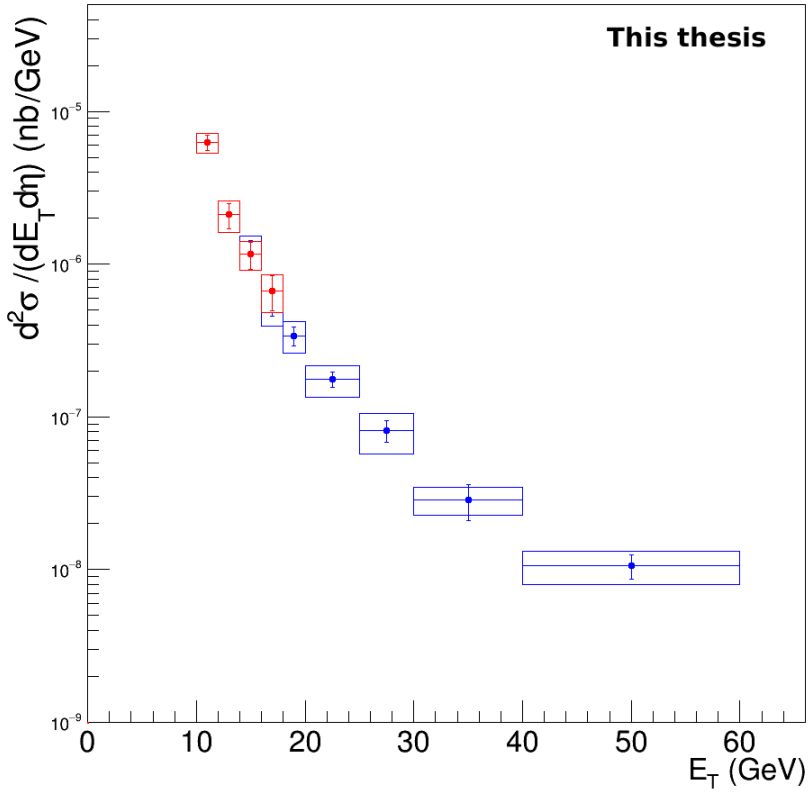

Figure 7.11: Isolated photon differential cross-section in Pb-p collisions at $\sqrt{s}$ = 5.02 TeV as a function of the considered photon transverse energy bin. Red points have been obtained with the low level trigger EG2 at 7 GeV. Blue points have been computed using the high level trigger EG1.

region where the signal is expected and in the region of the elliptic shape clusters mainly populated by the background clusters. The bias introduced by this method is corrected using Monte-Carlo simulations. The detector reconstruction efficiency has been determined with a photon-jet Monte-Carlo simulation reproducing the signal. The choices made in the analyis induce systematic uncertainties which have been estimated. The cross-section of isolated photons in p-Pb and Pb-p collisions has been obtained with the corresponding integrated luminosities of $1.67 \pm 0.11^{stat} \pm 0.07^{syst}$ nb^{-1} *and* $2.03 \pm 0.13^{stat} \pm 0.07^{syst}$ nb^{-1}.

CHAPTER 8

Comparison with theoretical models and p-p results

Contents

The last chapter is dedicated to a discussion of the previously obtained measurement of the isolated photon cross-section in p-Pb collisions. Theoretical expectations will be tested via the comparison of the experimental results with calculations performed with pQCD calculations using different nPDF (nuclear Parton Distribution Function) models. The results will also be compared to the ones obtained in the analysis of isolated photons in pp collisions with the ALICE experiment, via the nuclear modification factor which could demonstrate modification in the isolated prompt photon production in p-Pb collisions.

8.1 Comparison with theoretical models

8.1.1 Jetphox, a next-to-leading order pQCD calculation program

Jetphox is a program to compute the cross-section of high p_T photons, hadrons or jets produced in hadron+hadron$\rightarrow \gamma$/hadron + jet + X at the NLO (Next-to-Leading-Order) in pQCD [121]. It allows the isolation cuts contrary to some other models, like INCNLO [122] program used to calculate inclusive prompt photon cross-section. The calculation results with JetPHOX will be compared to the cross-section of isolated photons in p-Pb collisions with the ALICE data.

The proper use of JetPHOX has been checked by reproducing the results published by ATLAS [63] and CMS [62] on the isolated photon cross-section measurements in pp collisions [123]. We have obtained a nice agreement which makes us confident in the way JetPHOX is used for this analysis.

The computation of the isolated photon cross-section in p-Pb collisions has been performed with the isolation criteria $R = 0.4$ and $p_T^{threshold} = 2$ GeV/c. The parton distribution function in proton we use is the PDF (Parton Distribution Function) CT10 [124] which results from adjustements with the experimental data from the high energy collider Tevatron. The nuclear effects on the par-

ton distribution function induced by the proton inside a nucleus have been taken into account by using the nPDF EPS09 [41]. It is one of the most recent nPDF models constrained by the avalaible data from colliders. The chosen fragmentation function is BFGII [59] used to modelise two parton interaction and the quark and gluon fragmentation into photon.

pQCD energy scale uncertainties

The errors induced by the choice of the energy scales of the pQCD calculation have been evaluated by varying the renormalisation (μ_R), factorisation (μ_f), and fragmentation (μ_F) scales independently between 0.5 and 2

$$\mu_R = 0.5,2 \text{ et } \mu_f = \mu_F = 1$$
$$\mu_f = 0.5,2 \text{ et } \mu_R = \mu_F = 1$$
$$\mu_F = 0.5,2 \text{ et } \mu_R = \mu_f = 1$$

The associated uncertainties are calculated by the maximal and the minimal differences with the nominal values, as:

$$f_{max} = max(\frac{f_{\mu_{R=F=f}=1} - f_{\mu_R,\mu_F,\mu_f}}{f_{\mu_R,\mu_F,\mu_f}}) \tag{8.1}$$

$$f_{min} = min(\frac{f_{\mu_{R=F=f}=1} - f_{\mu_R,\mu_F,\mu_f}}{f_{\mu_R,\mu_F,\mu_f}}) \tag{8.2}$$

One could vary the energy scales separately in order to maximize the scale uncertainties as in the pp cross section calculations with the CMS experiment [62] and the ALICE experiment [67]. It has an influence mainly on the lower energy values [123] and the difference is negligeable with respect to the uncertainties linked to the data analysis.

nPDF uncertainties

The uncertainties from nPDF parametrization are modelised using a JetPHOX calculation performed with the nPDF EPS09 [41], HKN07 [125] and nDS [126] for fixed energy scales at $\mu_R = \mu_f = \mu_F = 1$. This procedure enables to take into account the different model of parton distribution in the nucleon which includes the transition between shadowing and anti-shadowing at different energy scale [54]. The error has been defined as the maximal discrepancy e_{max} obtained between two nPDFs for each energy bin.

$$e_{max} = max(\frac{f_{PDF_i} - f_{PDF_j}}{f_{PDF_i}})_{i,j=1,2,3} \tag{8.3}$$

This enables to define a range of isolated photon cross-section values allowed by the different nPDF models.

Jetphox PDF: CT10 nPDF:EPS09, FF: BFG II			
Energy bin (GeV)	$\frac{d^2\sigma^{iso}}{dE_T d\eta}$ **(nb.GeV^{-1})**	$C(E_T)$	**Corrected** $\frac{d^2\sigma^{iso}}{dE_T d\eta}$ **(nb.GeV^{-1})**
10-12	23.99	0.90	21.59
12-14	12.39	0.89	11.03
14-16	6.97	0.89	6.21
16-18	4.23	0.89	3.77
18-20	2.74	0.89	2.44
20-25	1.38	0.89	1.23
25-30	0.58	0.88	0.51
30-40	0.22	0.88	0.19
40-60	0.049	0.88	0.043

Table 8.1: Differential cross section in each energy bin, obtained with Jetphox computation, CT10 PDF, EPS09 nPDF and BFG II FF.

Furthermore, the isolation cut in JetPHOX is implemented at the partonic level whereas in the measurement we are performing the isolation at the particle level. In order to correct the cross-sections from this bias, we have determined a correction factor as it was done in the isolated photon analysis in the CMS experiment [62] and in the isolated photon measurement in the ALICE experiment with pp collisions at $\sqrt{s}$ = 7 TeV [67]. This factor has been determined via the photon-jet Pythia Monte-Carlo simulation reproducing the signal, where the identified direct photons are supposed to be isolated at the partonic level since there is an absence of background. The correction factor can be expressed as:

$$C(E_T) = \frac{\frac{dN^{id}_{\gamma_{iso}}}{dE_T^{reco}}}{\frac{dN^{id}_{\gamma}}{dE_T}} \tag{8.4}$$

where:

- $\frac{dN^{id}_{\gamma_{iso}}}{dE_T^{reco}}$ is the number of reconstructed isolated direct photons and
- $\frac{dN^{id}_{\gamma}}{dE_T}$ is the total number of direct photons generated.

The obtained values are shown in the Table 8.1. They are similar in all the considered energy bins and close to the 0.88 value that was obtained in the isolated photon p-p analysis [67]. In the Table 8.1, are also presented the raw results of JetPHOX calculations with PDF CT10 and nPDF EPS09 and the FF BFG II, as well as the corrected JetPHOX calculations using the correction factor. These results are used to perform the comparison with the measurement of the isolated photons in p-Pb collisions. One has to notice that JetPHOX values are pp equivalent cross-sections.

8.1.2 Comparison of pQCD calculations with the ALICE p-Pb results

As written in the previous chapter, the results from p-Pb collisions and Pb-p collisions are merged. The weighted average cross-section values have been computed to take into account the number

of events from each data set. JetpPHOX enables to compute the p-p equivalent cross-section. In order to obtain the last one, the differential spectrum has to be normalised via the nuclear overlap function related to the average number of nucleon-nucleon collisions (see chapter 1) as:

Energy bin (GeV)	p-Pb	Pb-p	Mean
	$\frac{d^2N_{pA}/dE_T d\eta}{<T_{pA}>}$ ± stat ± syst (nb.GeV^{-1})		
10-12	$16.30 \pm 4.76 \pm 2.72$	$29.98 \pm 3.66 \pm 4.59$	$23.85 \pm 4.15 \pm 3.80$
12-14	$12.12 \pm 2.56 \pm 2.70$	$10.09 \pm 1.92 \pm 2.30$	$11.00 \pm 2.21 \pm 2.48$
14-16	$7.11 \pm 1.51 \pm 1.54$	$5.55 \pm 1.16 \pm 1.16$	$6.25 \pm 1.32 \pm 1.33$
16-18	$3.81 \pm 0.48 \pm 0.98$	$2.55 \pm 0.37 \pm 0.68$	$3.11 \pm 0.42 \pm 0.82$
18-20	$2.02 \pm 0.28 \pm 0.47$	$1.63 \pm 0.23 \pm 0.38$	$1.80 \pm 0.25 \pm 0.42$
20-25	$1.26 \pm 0.14 \pm 0.29$	$0.84 \pm 0.10 \pm 0.20$	$1.03 \pm 0.12 \pm 0.24$
25-30	$0.44 \pm 0.08 \pm 0.13$	$0.39 \pm 0.06 \pm 0.11$	$0.41 \pm 0.07 \pm 0.12$
30-40	$0.22 \pm 0.04 \pm 0.04$	$0.14 \pm 0.04 \pm 0.03$	$0.18 \pm 0.04 \pm 0.03$
40-60	$0.002 \pm 0.013 \pm 0.001$	$0.050 \pm 0.010 \pm 0.012$	$0.028 \pm 0.011 \pm 0.012$

Table 8.2: pp equivalent cross-section depending on the considered photon energy bin. The presented results are issued from the p-Pb and Pb-p collisions data. In the last column the weighted average values are shown.

$$\left(\frac{d^2\sigma}{dE_T d\eta}\right)_{\text{p-p equi}} = \frac{d^2N_{pA}/dE_T d\eta}{<T_{pA}>} = \frac{dN^{iso}}{N^{evts}dE_T}\frac{2\pi}{d\eta d\phi}\frac{\mathbb{P}_{corr}(E_T)}{\epsilon(E_T)}\frac{1}{RF}\frac{1}{<T_{pA}>} \tag{8.5}$$

with:

- $<T_{pA}> = \frac{<N^{coll}>}{\sigma^{NN}_{inel}} = 0.0983 \pm 0.0035$ mb^{-1} [42], the nuclear overlap factor which takes into account the number of nucleon binary collisions in p-A collisions (see chapter 1).
- $d^2N_{pA}/dp_T d\eta$ is defined as the weighted average value of the measurements performed in p-Pb collisions and Pb-p collisions:

$$d^2N_{pA}/dE_T d\eta = \frac{\left(d^2N_{pA}/dE_T d\eta\right)_{\text{p-Pb}} N^{\text{evts, p-Pb}} + \left(d^2N_{pA}/dE_T d\eta\right)_{\text{Pb-p}} N^{\text{evts, Pb-p}}}{N^{\text{evts, tot}}} \tag{8.6}$$

As a reminder (see chapter 5), $N^{\text{evts, p-Pb}} = 750303$ and $N^{\text{evts, Pb-p}} = 923764$ for a total number of events $N^{\text{evts, tot}} = 1674067$.

In the Table 8.2, the $d^2N_{pA}/dE_T d\eta$ results in p-Pb collisions, $\left(d^2N_{pA}/dE_T d\eta\right)_{\text{p-Pb}}$, and Pb-p collisions, $\left(d^2N_{pA}/dE_T d\eta\right)_{\text{Pb-p}}$ are presented. In the last column, one can see the weighted average values in each photon energy bin. These last values are used in the comparison with the theoretical predictions.

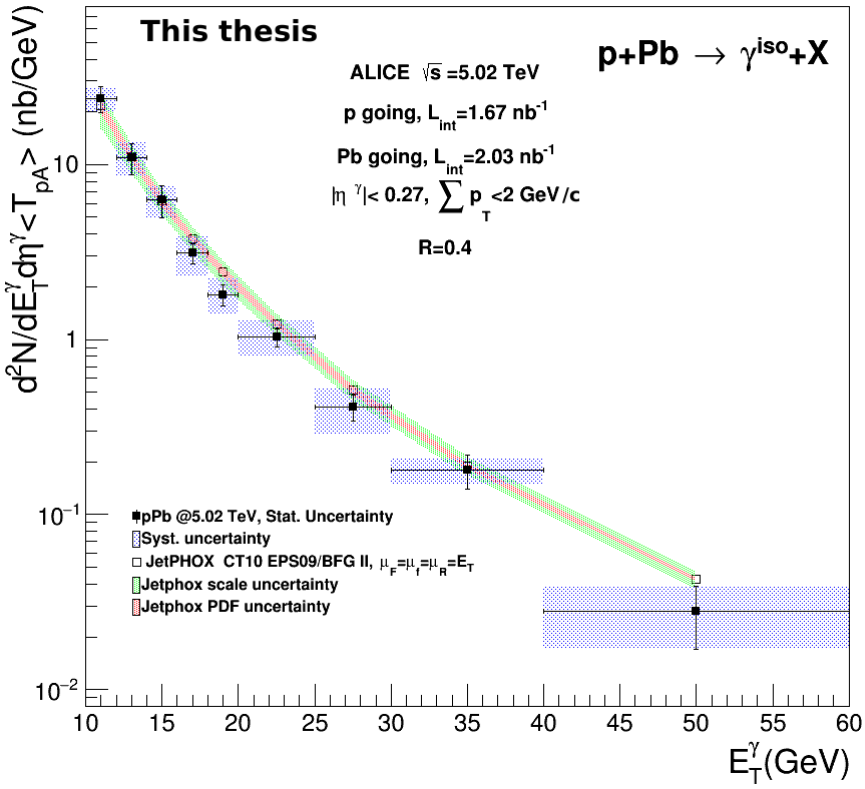

Figure 8.1: $\left(\frac{d^2\sigma}{dE_T d\eta}\right)_{\text{p-p equi}}$ as a function of the considered photon energy. The Jetphox computation has been performed with the PDF CT10 and the nPDF EPS09. The green area represents the JetPHOX calculation uncertainties associated to the energy scale. The uncertainty associated to the PDF choice corresponds to the red area.

In the Figure 8.1, one can see the p-p equivalent isolated photon cross-section in p-Pb collisions at $\sqrt{s}$ = 5.02 TeV. The JetPHOX computations and the associated uncertainties, described in the previous section are also shown. We can point out that the measured cross-section exhibits a similar trend to the pQCD calculations. The corresponding ratio has been plotted in the Figure 8.2 with the uncertainties associated to the theoretical predictions which are represented by the red dashed lines for the pQCD energy scale choice and by the green dashed lines for the nPDF choice. We can see that the results are consistent within the large errror bars. At the lower photon energy values the results are in full agreement. At higher energies ($\geq 16GeV$), the measured cross-section values appear to be on average lower that the JetPHOX calculations by about 20% even if the measurement remains compatible with the theory within uncertainties. The agreement of the theory with the isolated photon analysis results is consistent in pp and Pb-Pb collisions. Indeed, as presented in chapter 2, the measurement performed at the LHC were all compatible with the theoretical calculations. This is the case in in pp collisions analysis at $\sqrt{s}$ = 7 TeV with the ALICE experiment where the results are compatible with the pQCD calculations.

We can compare the obtained results in p-Pb collisions to the measurement of the isolated photon cross-section in pp collisions at $\sqrt{s}$ = 7 TeV via the determination of the nuclear modification factor.

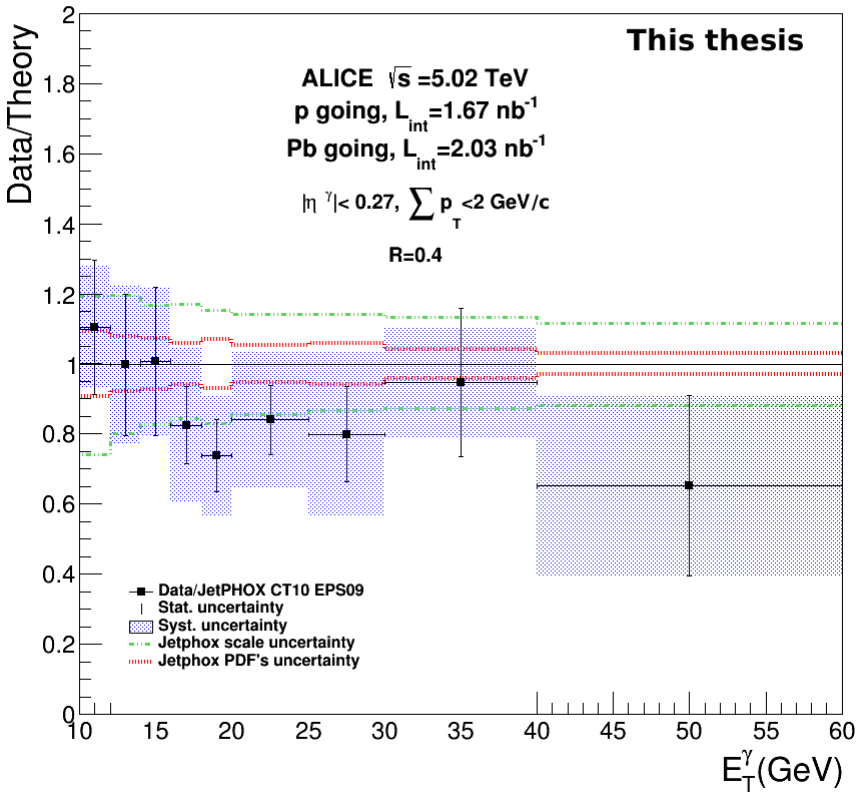

Figure 8.2: Ratio of the pp equivalent isolated photon cross-section in p-Pb collisions at $\sqrt{s}$ = 5.02 TeV with the calculation performed with JetPHOX. JetPHOX computations with the PDF CT10, the nPDF EPS09 and the FF BFG II. The uncertainty envelops associated to the energy scale choice are represented by the green dashed lines. The red dashed lines correspond to the nPDF choice uncertainty.

8.2 Comparison with pp results and R_{pA}

In order to compare isolated photons production in pp and p-Pb collisions [67], one can determine the nuclear modification factor is defined as (see chapter 1):

$$R_{pA} = \frac{d^2N_{pA}/dE_T d\eta}{< T_{pA} > d\sigma^2_{pp}/dE_T d\eta} \tag{8.7}$$

where:

$\frac{d^2N_{pA}/dE_T d\eta}{< T_{pA} >}$ is the pp equivalent cross-section of the isolated photon cross-section measured in p-Pb collisions determined in the previous section (see the Table 8.2).

In the isolated photon analysis, the determination of the nuclear modification factor is particularly interesting. Indeed, the p-Pb collisions at LHC enables to probe shadowing effects in the small-x region scanning the low energy range in high energy collisions contrary to the previously performed measurement at RHIC in d+Au collisions [53] . Such effect leads to a suppression in p-Pb collisions with respect to results in pp collisions.

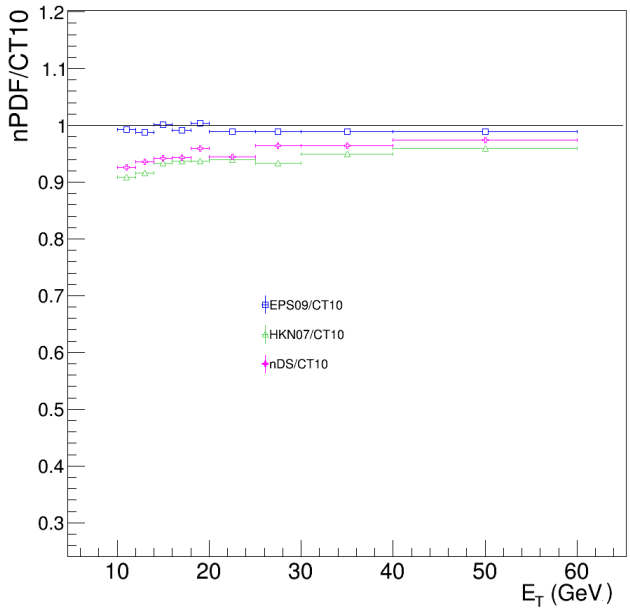

Figure 8.3: Ratio of the isolated photon cross-section as a function of the photon energy, obtained via JetPHOX calculations with only a PDF and with a nPDF. The results obtained with different nPDF are plotted. The blue points correspond to the comparison with the EPS09 nPDF, the green points to the HKN07 nPDF and the pink points to the nDS nPDF.

In the Figure 8.3 we show the isolated photon cross-section calculations at $\sqrt{s}$ = 5.02 TeV performed with JetPHOX and a CT10 PDF compared to the same calculations using different nPDF. The blue points correspond to the EPS09 nPDF, the pink points to the nDS nPDF and the green points to the HKN07 nPDF. These comparisons have been achieved in order to evaluate the nuclear effect on the cross-section measurement in the considered photon energy range $[10-60]$ GeV. When the used nPDF EPS09, no clear nuclear effects appear. At the opposite, the calculations of the ratio with the HKN07 and the nDS nPDF show a clear suppression, especially for the lower photon energy values. The considered ratios clearly show different behaviour which corresponds to a transition between shadowing and anti-shadowing effects occuring at different energy scale depending on the used nPDF model [53]. This difference is due to the gluon distribution functions which are poorly constrained in this x-regions [55]. The isolated photon R_{pA} should enable to constrain these

Energy bin (GeV)	p-p results	
	$d\sigma^2_{pp}/dp_T dy$ (nb.GeV^{-1})	Extrapolation coeff.
10-12	$31.6 \pm 2.8^{\text{stat}} \pm 4.74^{\text{syst}}$	0.77
12-14	$19.8 \pm 1.8^{\text{stat}} \pm 2.58^{\text{syst}}$	0.75
14-16	$10.7 \pm 1.1^{\text{stat}} \pm 1.4^{\text{syst}}$	0.73
16-18	$5.8 \pm 0.8^{\text{stat}} \pm 0.8^{\text{syst}}$	0.72
18-20	$4.7 \pm 0.7^{\text{stat}} \pm 0.8^{\text{syst}}$	0.71
20-25	$2.0 \pm 0.3^{\text{stat}} \pm 0.4^{\text{syst}}$	0.71
25-30	$6.6.10^{-1} \pm (2.1\dot{1}0^{-1})^{\text{stat}} \pm (1.5^{-1})^{\text{syst}}$	0.69
30-40	$3.8.10^{-1} \pm (1.0.10^{-1})^{\text{stat}} \pm (0.8.10^{-1})^{\text{syst}}$	0.68
40-60	$5.9.10^{-2} \pm (2.5.10^{-2})^{\text{stat}} \pm (1.1\dot{1}0^{-2})^{\text{syst}}$	0.66

Table 8.3: Isolated photon cross-section in p-p collisions at $\sqrt{s}$ = 7 TeV and extrapolation coefficient for the p-p reference at $\sqrt{s}$ = 5.02 TeV. The extrapolation coefficients have been determined by comparison of the isolated photon cross-section obtained with JetPHOX at a center-of-mass energy of 7 TeV and at a center-of-mass energy of 5.02 TeV. The Jetphox computation has been performed with the CT10 PDF and the BFG II FF.

gluon distributions. Indeed, a theoretical relation links the R_{pA} of the isolated photon to the parton distribution functions of the gluon at mid-rapidity [54]:

$$R_{pA} \simeq \frac{R^A_{F_2} + R^A_G}{2} \tag{8.8}$$

with:
$R^A_{F_2}$ the nuclear structure function
R^A_G the gluon nuclear distribution.

Extrapolation of the pp cross-section of reference

The cross-section results in pp collisions at $\sqrt{s}$ = 7 TeV with the ALICE experiment are shown in the Table 8.3 with its systematic and statistical uncertainties. One can notice that the order of magnitude of the systematic errors is the same in both analysis, whereas the statistical errors are slightly lower in the analysis with the pp collision data.

The pp reference measurement with the ALICE data has been performed at $\sqrt{s}$ = 7 TeV and not at $\sqrt{s}$ = 5.02 TeV. To take into account this bias, an extrapolation of the cross-section results has been done. We have compared the JetPHOX computation at $\sqrt{s}$ = 7 TeV, with the PDF CT10 and the FF BFG II, to the JetPHOX isolated photon cross-section obtained with the same PDF and FF in a center-of-mass energy of 5.02 TeV. Extrapolation coefficients have been extracted from this comparison. They are presented in the Table 8.3 and the cross-section values are reduced by about 30 %. One can remark that the values are closed to the corresponding difference in the center-of-mass energy. The coefficients will be applied on the results of the isolated photon cross-section at $\sqrt{s}$ = 7 TeV to obtain the pp reference for the R_{pA} calculation.

One has to notice that the underlying event subtraction is a specific procedure of the p-Pb analysis. In the pp analysis, the underlying event contribution is only evaluated to check the efficiency of the isolation criteria. For this reason the isolation criteria are not fully equivalent between the two analysis. The equivalent energy threshold in the pp analysis is higher than 2 GeV/c and can slightly modify the measured isolated photon cross-section.

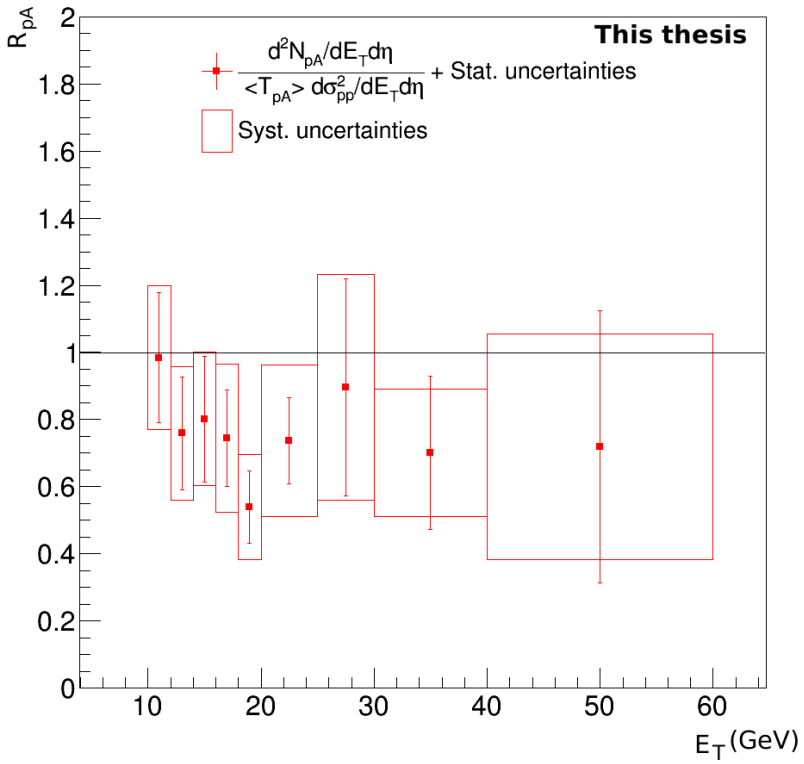

Figure 8.4: Nuclear modification factor, R_{pA}, depending on the photon energy. The p-p reference has been extrapolated from the p-p isolated photon cross-section measurement at $\sqrt{s}$ = 7 TeV in the ALICE experiment.

The nuclear modification factor, R_{pA}, results as a function of the photon energy bin are presented in the Figure 8.4. The uncertainties from the pp and the p-Pb analysis have been quadratically added. The statistical errors are represented by the error bars whereas the boxes correspond the systematic uncertainties. One can see that the values are slightly lower than unity. The measured R_{pA} seems to indicate a presence of shadowing effects even if the large uncertainties prevent to draw any definitive conclusion with such large experimental error bars.

In this chapter, we have compared the results of the isolated photon cross-section with the pQCD calculations performed with three different nPDF models, EPS09, HKN07 and nDS. The ratio tends to be lower that the expectation but are compatible with unity within the calculation uncertainties and the large experimental uncertainties. The measurement of the nuclear modification factor R_{pA} does

not clearly indicate a supression in the isolated photon production in p-Pb collisions with respect to the production in pp collisions. It is difficult to constrain the models due to very large uncertainties from the two experimental analysis. No clear modification has also been observed in the production of isolated photon in Pb-Pb collisions with respect to pp collisions at LHC [28] [68].

Conclusions

Heavy ion p-Pb collision studies, considered as a reference for Pb-Pb collisions, enable one to probe the cold nuclear matter effects to better understand the QGP formation. Direct photons produced in the initial partonic interaction are not affected by the hadronic matter. Their production is correlated to the initial parton distribution function (in proton) or nuclear parton distribution functions (in lead ions). In the measurement, photons produced in a parton fragmentation have similar kinematic properties. The experimental method of isolation is used to discriminate the direct photons from the fragmentation ones. The results from isolated photon measurements, already performed at the LHC energies in the CMS and the ATLAS experiments, are consistent with theoretical calculations. The isolated photon analysis, presented in this thesis, represents the first isolated photon measurement in p-Pb collisions performed with the data taken by the ALICE experiment. The main detector involved in the measurement is the EMCal calorimeter whose high level trigger allows the analysis of rare events such as prompt photon production. The isolated photon measurement in p-Pb collisions has been calibrated using the pp data. The development of a new independent framework enabled to validate the analysis procedure developed for the isolated photon in pp collisions with the ALICE experiment.

The isolated prompt photon cross-section in p-Pb collisions has been obtained from the raw isolated spectra by evaluating the remaining contamination from neutral meson decays. The purity has been estimated using the properties of the photon and π^0 decay shower shapes into the calorimeter. However, this method is based on assumptions which induce a bias. Thus, a purity correction is performed using Monte-Carlo simulations, reproducing the signal and the background. Monte-Carlo simulations of the signal also enable to determine the overall reconstruction efficiency of the isolated photon in the EMCal. The cross-section values have been obtained via the minimum bias equivalent spectra and with the minimum bias cross-section of reference. The use of the two high level triggers of the EMCal calorimeter with a threshold at 7 GeV and at 11 GeV has allowed to study an energy range from 10 GeV to 60 GeV, which is similar to the one of the isolated photon analysis with the ALICE experiment in pp collisions at $\sqrt{s}$ = 7 TeV.

The cross-section determination of isolated prompt photons, for which pQCD calculations are feasible, can provide constrains on nuclear PDF through the nuclear modification factor, R_{pA}. The present results have been compared to the theory via Jetphox calculations, using different models of nPDF and to the p-p ALICE results, via the R_{pA}. The results are compatible within the uncertainties

with the pQCD calculation. The computed R_{pA} is compatible with unity within the large error bars but tends to favor the nPDF HKN07 and nDS models, due to the transition between shadowing and anti-shadowing effects which occur at higher photon energy values.The main limitation of this measurement is the small number of cluster candidates and the large errors associated. Since prompt photons are rare events whose properties make them difficult to extract from the background, the method employed for the signal extraction increases the uncertainty. As a consequence, it is not easy to draw a strong conclusion with respect to the obtained results.

To reduce the bias introduced in the analysis in the purity determination, due to the bad reproduction of the shower shape in the Monte-Carlo simulations with respect to the data, it would be interesting to perform a smearing of the shower shape distribution by a Landau function as it has been introduced in the analysis of isolated photon-hadron correlations [120] and applied to the isolated photons in pp collisions [67]. Some further studies for the systematic uncertainties could also be done. To improve the analysis, one could perform centrality dependent measurements. This study would be limited taking into account the low number of cluster candidates. An analysis as a function of the pseudo-rapidity could also has been done to take into account any differences between the p-Pb and the Pb-p collision in the determination of the isolation energy. However, in the particular case of this analysis, the expected improvement should be negligeable with respect to the already associated error bars.

From the experimental point of view, we have seen that the method performing the isolation only on charged particles seemed to give consistent results, less biased by the purity correction method, and enabling to reduce statistical errors by a factor of 2. On the other side, the comparison with theoretical results is complicated in the way that the isolation criteria are not fully equivalent. This is a problem in the case of the determination of the isolated photon production cross-section to test or to constrain theoretical models. Nevertheless, this method could be applied to perform correlation analyses when isolated photons are used as references to study parton energy loss in the medium. Especially, this method could be used to perform isolated photon measurements in the DCal (Di-jet Calorimeter), installed in Run II at the LHC, avoiding any fiducial cut in the detector acceptance which made this calorimeter unusable for such an analysis.

The upcoming data taking in RunII in p-Pb collisions at $\sqrt{s_{\rm NN}}$ =5.02 TeV and $\sqrt{s_{\rm NN}}$ = 8 TeV, and the already taken data from Pb-Pb collisions at $\sqrt{s_{\rm NN}}$ =5.02 TeV and pp collisions at $\sqrt{s}$ = 13 TeV, will allow, in a near future, to complete the description of the hadronic matter by reaching some small x-regions still unexplored. Indeed, the measurement of the isolated prompt photon cross-section could be performed in Pb-Pb collisions with the ALICE experiment with the RunII data at $\sqrt{s_{\rm NN}}$ = 5.02 TeV, a similar center-of-mass energy as in the p-Pb collisions. The RunI data at $\sqrt{s_{\rm NN}}$ = 2.76 TeV contains less events to analyse and should not easily allow the measurement in different centrality regions. Such a measurement in the Pb-Pb analysis would complete, in the low energy region, the already measured cross-section distributions in the CMS and the ATLAS experiments. By measuring the isolated prompt photon cross-section, one would access the direct photon cross-section, whose production is expected to be unmodified by the medium. One could consider

to measure fragmentation photons in Pb-Pb collisions with respect to a pp reference whose production should be modified by a QGP formation. Moreover, such a measurement with the p-Pb data would bring knowledge of the CNM effects on the parton fragmentation. Some feasibility studies could be performed by measuring the inclusive prompt photon distribution at high momentum in the calorimeter in the different collision systems with the assumption that the direct photon production is unmodified. Another way could be to study the non-isolated photons and extract the signal with a similar method as the one presented in the isolated photon analysis with the ALICE experiment.

APPENDIX A

Quality Assurance of LHC13d, LHC13e and LHC13f data

A.1 EMCal

A representative overview of the EMCal quality assurance analysis for the considered periods, LHC13d, LHC13e and LHC13f, in the analysis is presented here. All plots cannot be shown but the relevant ones.

On Figure A.1, the number of events in each run of the periods LHC13d, LHC13e and LHC13f are represented. Figure A.2 represents the mean cluster energy per event per supermodule in each runs of all the considered periods.

Figure A.3 presents some extracted plots of the quality assurance analysis of the run 195827 from LHC13d data set.

The bad channel mapping for the periods considered for the analysis are the following:

- LHC13d and LHC13f: from 195344 to 196310
- LHC13f:
  - from 196433 to 196563 similar from 196608 to 196646 similar from 197302 to 197348
  - from 196563 to 196608
  - from 196646 to 197094 similar from 197099 to 197302
  - from 197094 to 197099
  - from 197348 to 197388

The considered bad channel map periods of LHC13f have been surrounded in red on bottom plot of Figure A.2.

A.2 ITS and TPC

In this section, the trending plot for each analysed period LHC13d, LHC13e and LHC13f, from some other detectors quality assurance analysis are presented in the Figures A.4, A.5, A.6, A.7, A.8 and A.9.

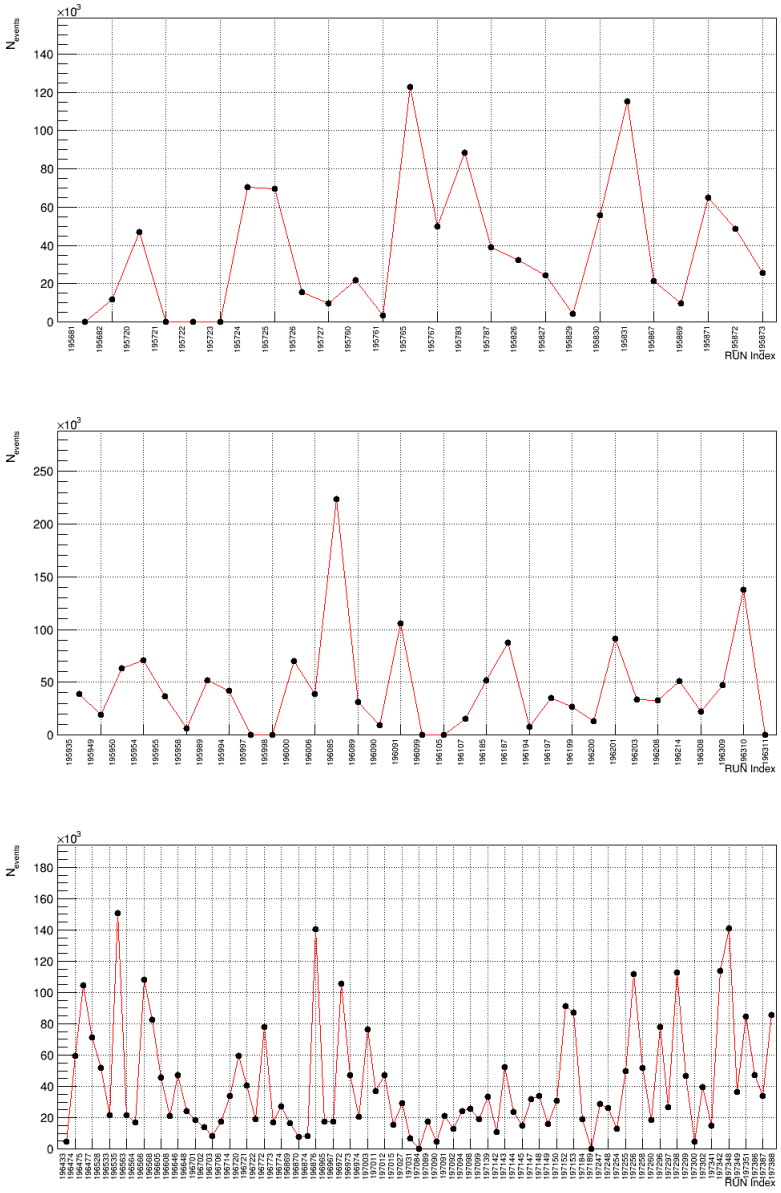

Figure A.1: Number of events per run for LHC13d (upper plot), LHC13e (middle plot) and LHC13f (bottom plot) data sets.

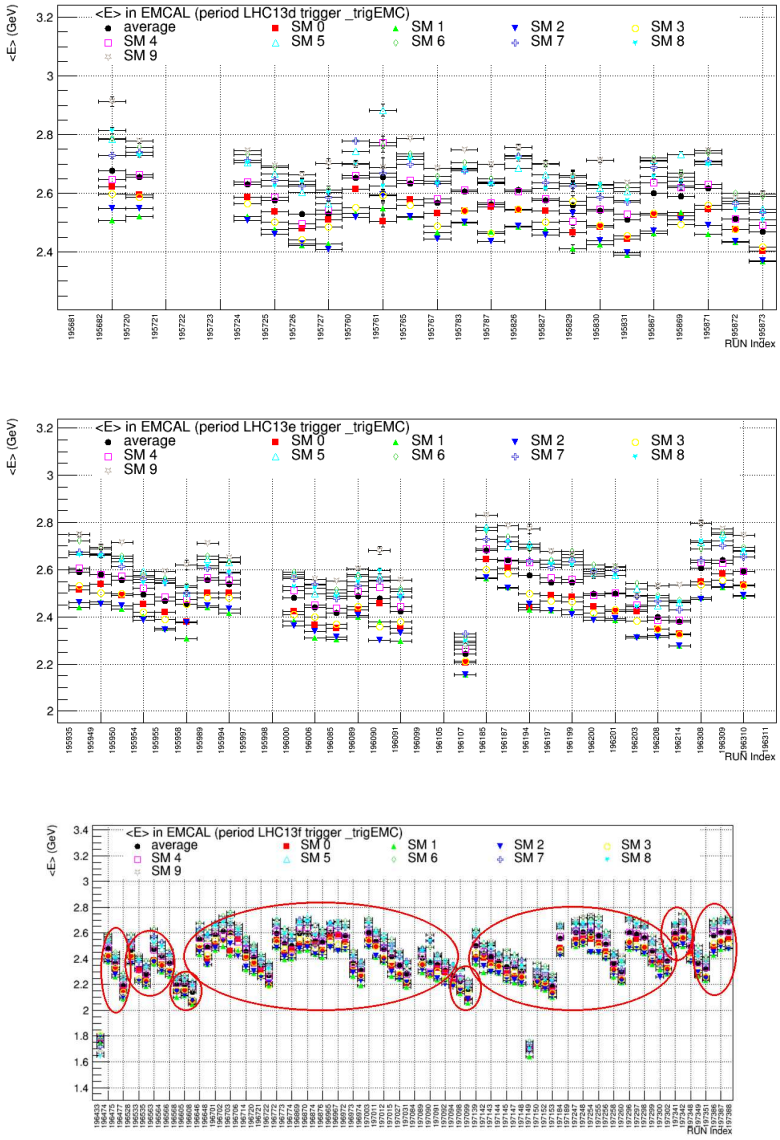

Figure A.2: Mean cluster energy per event in LHC13d (upper plot), LHC13e (middle plot) and LHC13f (bottom plot) data sets.

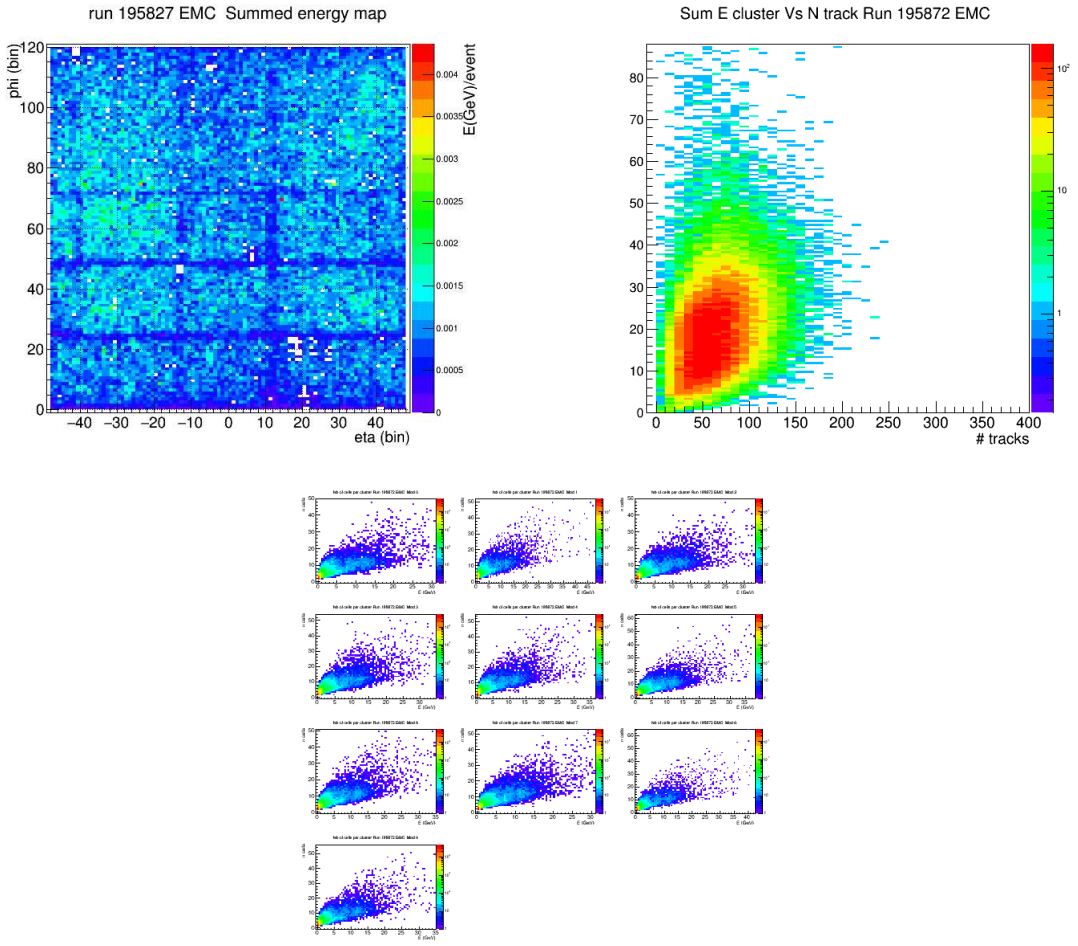

Figure A.3: Run level quality assurance analysis in EMCAL for the run 195827 of LHC13d data setTHe upper left plot is the energy map in the calorimeter. The upper right plot is the summed cluster energy depending on the track multiplicity. The bottom plot represents the number of cells per clusters depending on the cluster energy.

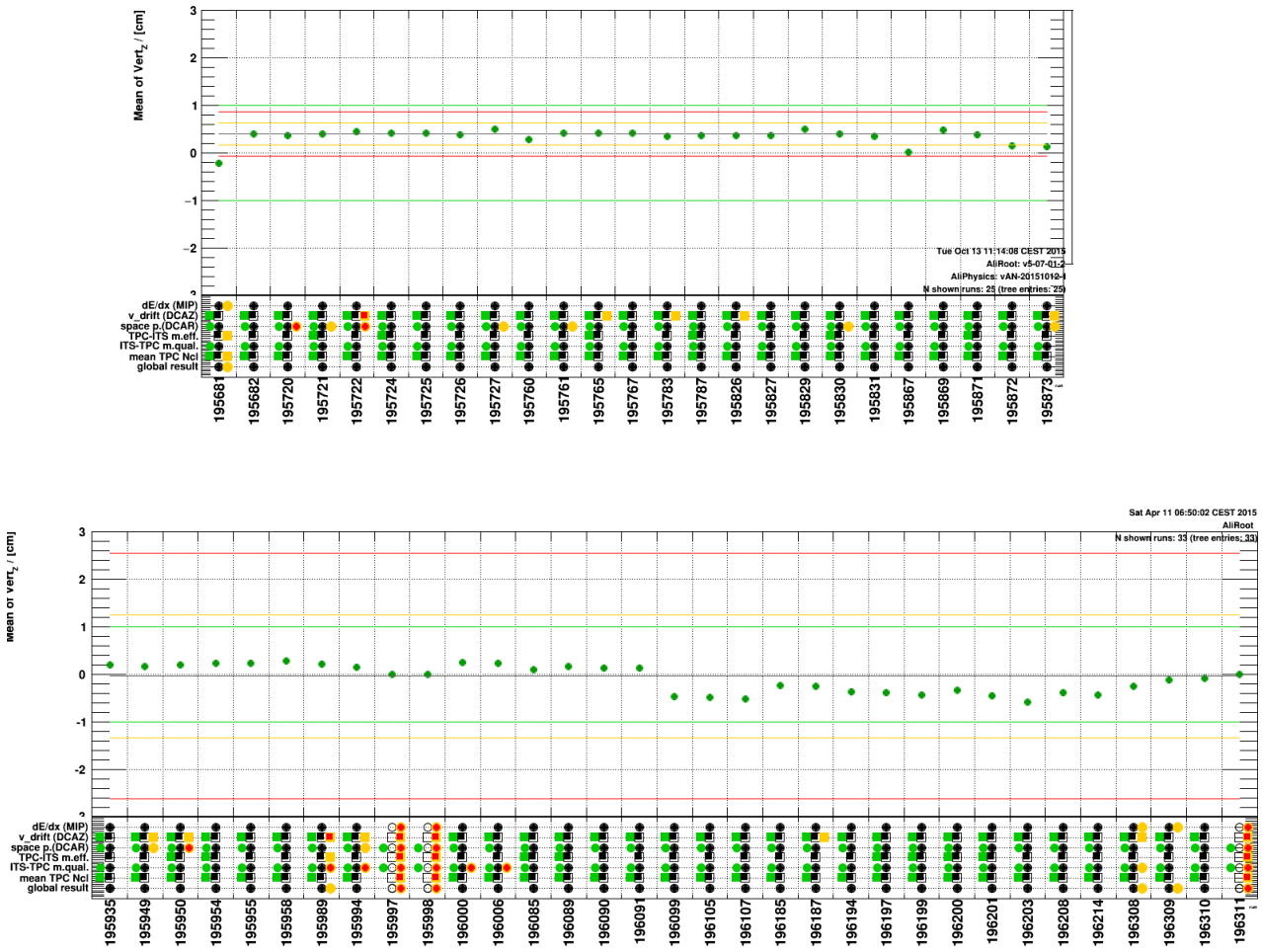

Figure A.4: Mean vertex in beam direction for tracks per run in each data sets, LHC13d (upper plot), LHC13e (middle plot).

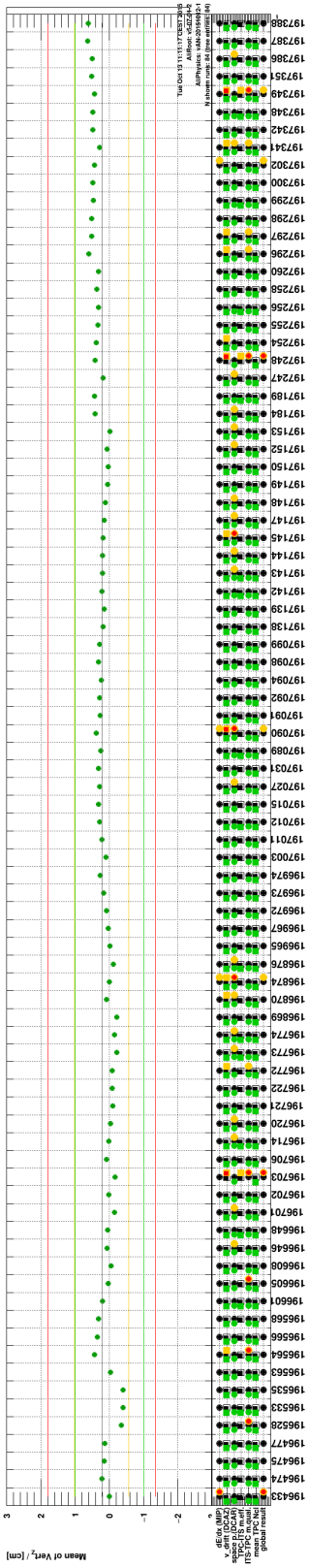

Figure A.5: Mean vertex in beam direction for tracks per run in and LHC13f data set.

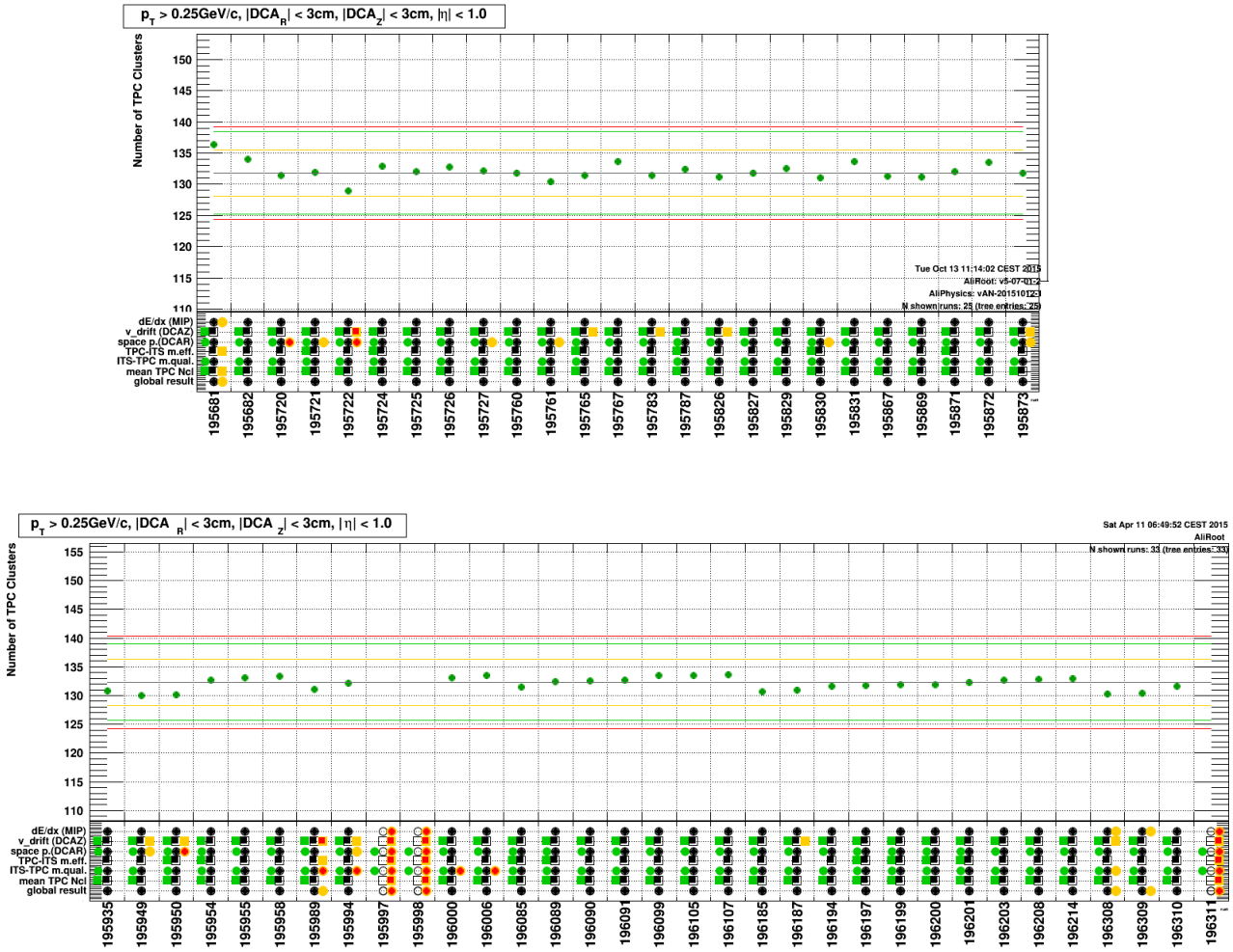

Figure A.6: Mean number of TPC clusters per event in each run of the considered periods in the analysis, LHC13d (upper plot) and LHC13e (bottom plot).

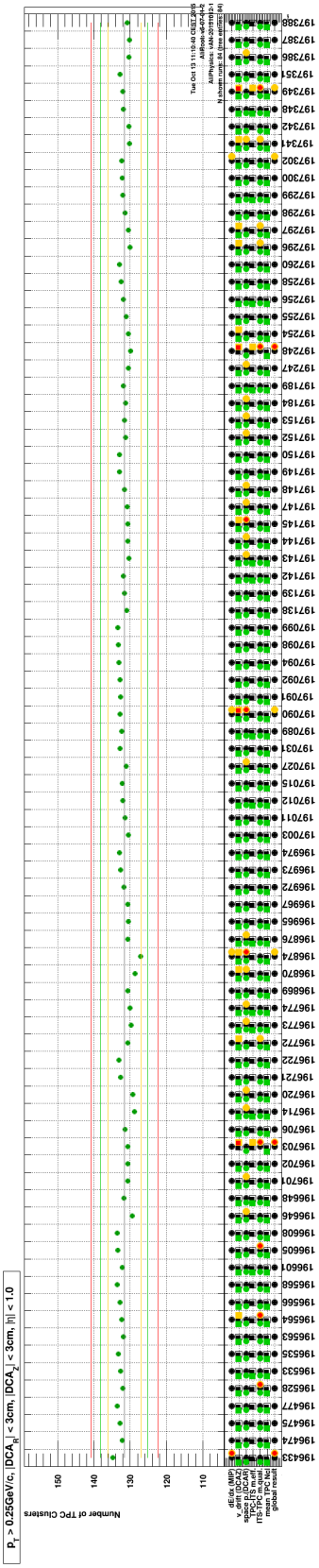

Figure A.7: Mean number of TPC clusters per event in each run of LHC13f period.

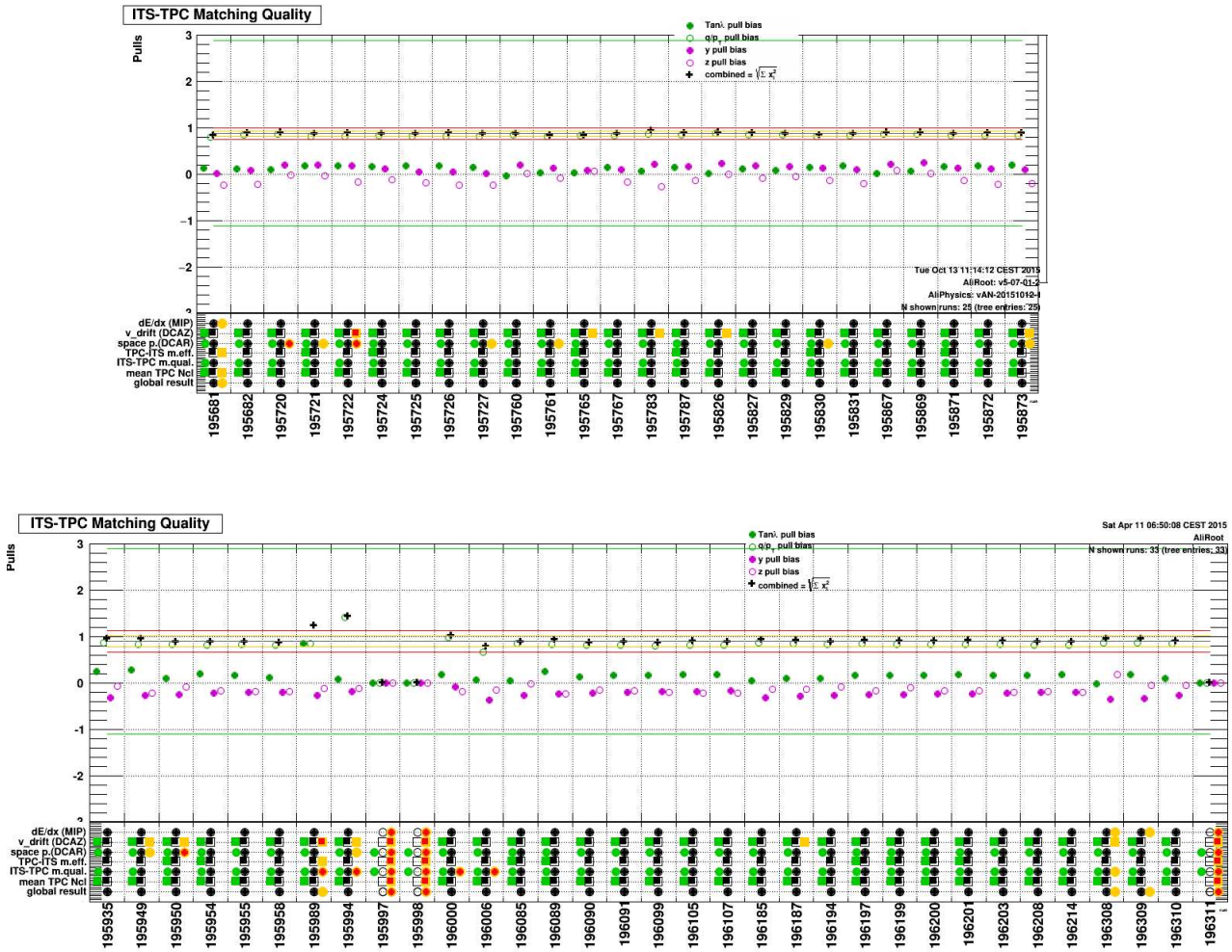

Figure A.8: TPC-ITS track matching quality in each run of LHC13d (upper plot) and LHC13e (bottom plot) data sets.

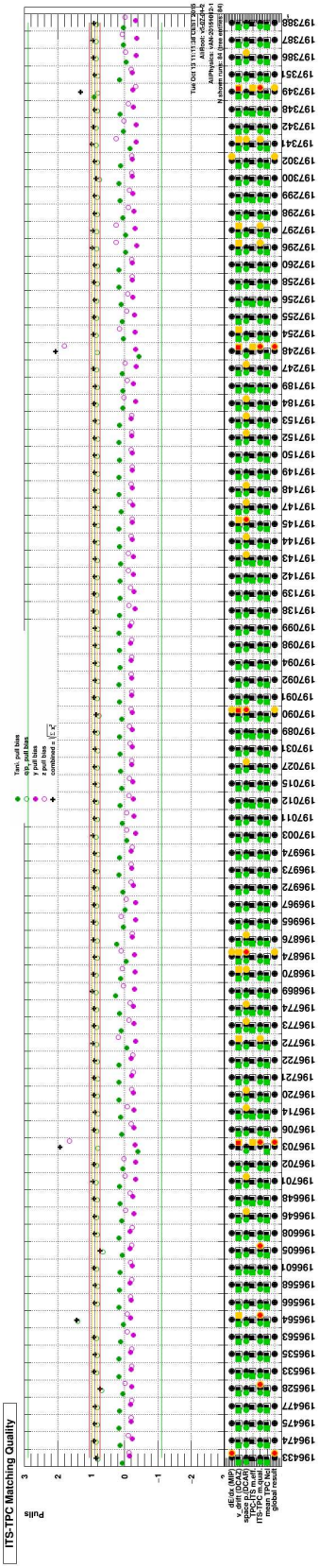

Figure A.9: TPC-ITS track matching quality in each run of LHC13f data set.

APPENDIX B

Cluster cut selectivity

The cluster momentum distribution are presented after the different cut applied at the analysis level.

In the Figure B.1, one can wee the raw spectra, the clusters distribution after the arrival time of the clusters and the one on the number of cells composing the clusters. They respectively cut 12% and 20 % with respect to the previous clusters distribution. One cannot clearly see the difference in the spectrum after the cut on the number of cells because it affects essentially the lowest momentum part of the spectrum, well below the trigger threshold.

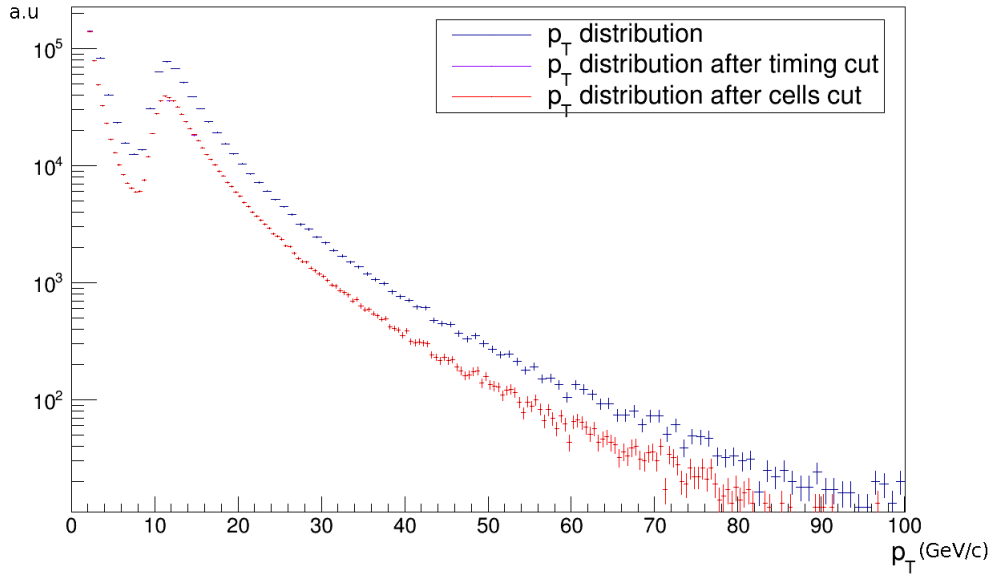

Figure B.1: Cluster momentum distribution in EMCal calorimeter after different cuts. The events have been selected with EG1 trigger from LHC13f data.

In Figure B.2, the clusters distribution are represented after the number of local maxima cuts, the track matching cut, the distance to bad channel criteria and the fiducial cut. They respectively remove 5%, 29%, 19% and 77% of the clusters with respect to the previous distribution. One can notice that the more restricitive cut is the fiducial one.

The cut selectivity is summarized in the Table B.1.

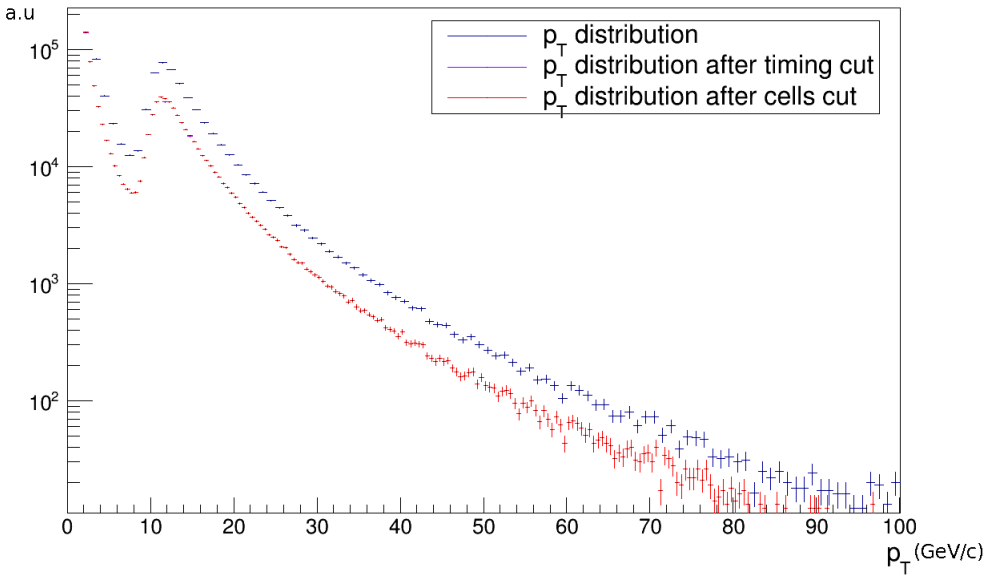

Figure B.2: Cluster momentum distribution after different cuts. Events have been selected with EG1 trigger in LHC13f data set.

Cut	**% from previous**	**% from raw spectra**
Timing cut	12%	12%
Number of cells	20%	29%
Number of local maxima	5%	32%
Track matching	29%	52%
Distance to bad channel	19%	61%
Fiducial cut	77%	91%

Table B.1: Rejection in % of the different cluster cuts applied in the analysis.

Bibliography

[1] Super-Kamiokande Collaboration, *Evidence for oscillation of atmospheric neutrinos*, Phys. Rev. Lett. **81**, 1562–1567 (1998).

[2] SNO Collaboration, *Measurement of the rate of* $\nu_e + d \rightarrow p + p + e^-$ *interactions produced by* ^8B *solar neutrinos at the Sudbury Neutrino Observatory*, Phys. Rev. Lett. **87**, 071 301 (2001).

[3] SNO Collaboration, *Direct evidence for neutrino flavor transformation from neutral-current interactions in the Sudbury Neutrino Observatory*, Phys. Rev. Lett. **89**, 011 301 (2002).

[4] T. W. B. Kibble, *Symmetry breaking in non-abelian gauge theories*, Phys. Rev. **155**, 1554–1561 (1967).

[5] F. Englert, and R. Brout, *Broken symmetry and the mass of gauge vector mesons*, Phys. Rev. Lett. **13**, 321–323 (1964).

[6] P. W. Higgs, *Broken symmetries, massless particles and gauge fields*, Physics Letters **12**, 132 – 133 (1964).

[7] P. W. Higgs, *Broken symmetries and the masses of gauge bosons*, Phys. Rev. Lett. **13**, 508–509 (1964).

[8] L. Evans, and P. Bryant, *LHC Machine* **3**, S08 001 (2008).

[9] ATLAS Collaboration, *Observation of a new particle in the search for the Standard Model Higgs boson with the ATLAS detector at the LHC*, Physics Letters B **716**, 1 – 29 (2012).

[10] CMS Collaboration, *Observation of a new boson at a mass of 125 GeV with the CMS experiment at the LHC*, Physics Letters B **716**, 30 – 61 (2012).

[11] ATLAS Collaboration, and CMS Collaboration, *Combined measurement of the Higgs boson mass in* pp *collisions at* $\sqrt{s} = 7$ *and 8 TeV with the ATLAS and CMS experiments*, Phys. Rev. Lett. **114**, 191 803 (2015).

[12] S. Weinberg, *A model of leptons*, Phys. Rev. Lett. **19**, 1264–1266 (1967).

[13] S. L. Glashow, J. Iliopoulos, and L. Maiani, *Weak interactions with lepton-hadron symmetry*, Phys. Rev. D **2**, 1285–1292 (1970).

[14] S. L. Glashow, *Partial-symmetries of weak interactions*, Nuclear Physics **22**, 579 – 588 (1961).

[15] D. J. Gross, and F. Wilczek, *Asymptotically free gauge theories. I*, Phys. Rev. D **8**, 3633–3652 (1973).

[16] K. G. Wilson, *Confinement of quarks*, Phys. Rev. D **10**, 2445–2459 (1974).

[17] R. P. Feynman, *Very high-energy collisions of hadrons*, Phys. Rev. Lett. **23**, 1415–1417 (1969).

[18] G. Sterman, J. Smith, J. C. Collins, J. Whitmore, R. Brock, J. Huston, J. Pumplin, W.-K. Tung, H. Weerts et al., *Handbook of perturbative QCD*, Rev. Mod. Phys. **67**, 157–248 (1995).

[19] Henrik B., and Nielsen H.B., *Hadron production from a boiling quark soup*, Nuclear Physics B **128**, 275 – 293 (1977).

[20] Politzer H. D., *Asymptotic freedom: An approach to strong interactions*, Physics Reports **14**, 129 – 180 (1974).

[21] S. Bethke, *The 2009 world average of α_s*, The European Physical Journal C **64**, 689–703 (2009).

[22] Particle Data Group, *Review of particle physics*, Chin. Phys. **C38**, 090 001 (2014).

[23] M. S. Aksent'eva, *On the theory of stars*, Phys. Usp. **41**, 621–623 (1998).

[24] U. W. Heinz, and M. Jacob, *Evidence for a new state of matter: An Assessment of the results from the CERN lead beam program*, arXiv:nucl-th/0002042 (2000).

[25] D. H. Rischke, and M. Gyulassy, *The maximum lifetime of the quark-gluon plasma*, Nuclear Physics A **597**, 701 – 726 (1996).

[26] J. D. Bjorken, *Highly relativistic nucleus-nucleus collisions: The central rapidity region*, Phys. Rev. D **27**, 140–151 (1983).

[27] M. L. Miller, K. Reygers, S. J. Sanders, and P. Steinberg, *Glauber Modeling in High Energy Nuclear Collisions*, Annual Review of Nuclear and Particle Science **57**, 205–243 (2007).

[28] CMS Collaboration, *Measurement of isolated photon production in pp and PbPb collisions at $\sqrt{s_{NN}}$ = 2.76 TeV*, Physics Letters B **710**, 256–277 (2012).

[29] The CMS Collaboration, *Study of high-p_T charged particle suppression in PbPb compared to pp collisions at $\sqrt{s_{NN}}$ = 2.76 TeV*, The European Physical Journal C **72**, 1–22 (2012).

[30] CMS Collaboration, *Study of Z boson production in PbPb collisions at $\sqrt{s_{NN}}$* = 2.76 TeV, Phys. Rev. Lett. **106**, 212 301 (2011).

[31] The CMS collaboration, *Study of W boson production in PbPb and pp collisions at $\sqrt{s_{NN}}$ = 2.76 TeV*, Physics Letters B **715**, 66 – 87 (2012).

[32] The CMS collaboration, *Suppression of non-prompt J/ψ, prompt J/ψ, and Υ(1S) in PbPb collisions at $\sqrt{s_{NN}}$ = 2.76 TeV*, Journal of High Energy Physics **2012**, 1–54 (2012).

[33] CMS Collaboration, *Evidence of b-Jet Quenching in PbPb Collisions at $\sqrt{s_{NN}}$* = 2.76 TeV, Phys. Rev. Lett. **113**, 132 301 (2014).

[34] J. Velkovska, *What have hard probes taught us about the quark–gluon plasma as measured in CMS?*, Nuclear Physics A **932**, 17 – 24 (2014), Hard Probes 2013 6th International Conference on Hard and Electromagnetic Probes of High-Energy Nuclear Collisions.

[35] W. A. Horowitz, and M. Gyulassy, *Quenching and tomography from the RHIC to the LHC*, Journal of Physics G: Nuclear and Particle Physics **38**, 124 114 (2011).

[36] J.-Y. Ollitrault, *Anisotropy as a signature of transverse collective flow*, Phys. Rev. D **46**, 229–245 (1992).

[37] ALICE Collaboration, *Elliptic flow of charged particles in Pb-Pb collisions at* $\sqrt{s_{NN}}$ = 2.76 *TeV*, Physical Review Letters **105**, 252 302 (2010).

[38] The ALICE Collaboration, *Anisotropic Flow of Charged Particles in Pb-Pb Collisions at* $\sqrt{s_{NN}}$ = 5.02 TeV, Phys. Rev. Lett. **116**, 132 302 (2016).

[39] K. Rith, *The EMC effect — status and perspectives*, Zeitschrift für Physik C Particles and Fields **38**, 317–324 (1988).

[40] A. Accardi, *Cronin effect in proton-nucleus collisions: a survey of theoretical models*, arXiv:hep-ph/0212148 (2002).

[41] K. J. Eskola, H. Paukkunen, and C. A. Salgado, *EPS09 – a new generation of NLO and LO nuclear parton distribution functions*, Journal of High Energy Physics **2009**, 065–065 (2009).

[42] ALICE Collaboration, *Centrality dependence of particle production in p-Pb collisions at* $\sqrt{s_{NN}}$ = *5.02 TeV* **91** (2015), arXiv: 1412.6828.

[43] The ALICE Collaboration, *Measurement of charged jet production cross sections and nuclear modification in p–Pb collisions at* $\sqrt{s_{NN}}$ = *5.02 TeV*, Physics Letters B **749**, 68 – 81 (2015).

[44] The ALICE Collaboration, *Long-range angular correlations on the near and away side in p–Pb collisions at*, Physics Letters B **719**, 29 – 41 (2013).

[45] The ALICE Collaboration, *Suppression of* ψ*(2S) production in p-Pb collisions at* $\sqrt{s_{NN}}$ = *5.02 TeV*, Journal of High Energy Physics **2014**, 1–25 (2014).

[46] P. Levai, G. Papp, G. Fai, M. Gyulassy, G. G. Barnafoldi, I. Vitev, and Y. Zhang, *Discovery of jet quenching at RHIC and the opacity of the produced gluon plasma*, Nuclear Physics A **698**, 631–634 (2002).

[47] CMS Collaboration, *Observation and studies of jet quenching in PbPb collisions at* $\sqrt{s_{NN}}$ = 2.76 *TeV* **84**, 024 906 (2011).

[48] R. P. Feynman, *The behavior of hadron collisions at extreme energies* (Springer Netherlands, Dordrecht), pp. 289–304 (1988).

[49] D. dÉnterria, and J. Rojo, *Quantitative constraints on the gluon distribution function in the proton from collider isolated-photon data*, Nuclear Physics B **860**, 311–338 (2012).

[50] J. C. Collins, D. E. Soper, and G. Sterman, *Factorization of hard processes in QCD*, arXiv:hep-ph/0409313 (2004).

[51] X.-N. Wang, Z. Huang, and I. Sarcevic, *Jet quenching in the opposite direction of a tagged photon in high-energy heavy-ion collisions*, Physical Review Letters **77**, 231–234 (1996).

[52] R. J. Fries, B. Müller, and D. K. Srivastava, *High-energy photons from passage of jets through quark-gluon plasma*, Phys. Rev. Lett. **90**, 132 301 (2003).

[53] F. Arleo, K. J. Eskola, H. Paukkunen, and C. A. Salgado, *Inclusive prompt photon production in nuclear collisions at RHIC and LHC*, Journal of High Energy Physics **2011**, 1–17 (2011).

[54] A. François, and T. Gousset, *Measuring gluon shadowing with prompt photons at RHIC and LHC*, Physics Letters B **660**, 181 – 187 (2008).

[55] C. Brenner Mariotto, and V. P. Gonçalves, *Nuclear shadowing and prompt photons in hadronic collisions at ultrarelativistic energies*, Phys. Rev. C **78**, 037 901 (2008).

[56] P. Aurenche, J. Ph. Guillet, E. Pilon, M. Werlen, and M. Fontannaz, *Recent critical study of photon production in hadronic collisions*, Phys. Rev. D **73**, 094 007 (2006).

[57] R. Ichou, and D. d'Enterria, *Sensitivity of isolated photon production at TeV hadron colliders to the gluon distribution in the proton*, Phys. Rev. D **82**, 014 015 (2010).

[58] P. M. Nadolsky, H.-L. Lai, Q.-H. Cao, J. Huston, J. Pumplin, D. Stump, W.-K. Tung, and C.-P. Yuan, *Implications of CTEQ global analysis for collider observables*, Phys. Rev. D **78**, 013 004 (2008).

[59] L. Bourhis, M. Fontannaz, and J. P. Guillet, *Quarks and gluon fragmentation functions into photons*, Eur. Phys. J. C **2**, 529–537 (1998).

[60] P. Aurenche, M. Fontannaz, J.-P. Guillet, Bernd A. Kniehl, E. Pilon, and M. Werlen, *A critical phenomenological study of inclusive photon production in hadronic collisions*, Eur. Phys. J. C **9**, 107–119 (1999).

[61] CMS Collaboration, *Measurement of the Isolated Prompt Photon Production Cross Section in pp Collisions at* $\sqrt{s} = 7$ *TeV*, Physical Review Letters **106**, 082 001 (2011).

[62] CMS Collaboration, *Measurement of the differential cross section for isolated prompt photon production in pp collisions at 7 TeV*, Physical Review D **84**, 052 011 (2011).

[63] ATLAS Collaboration, *Measurement of the inclusive isolated prompt photon cross section in pp collisions at* $\sqrt{s} = 7$ *TeV with the ATLAS detector*, Physical Review D **83**, 052 005 (2011).

[64] ATLAS Collaboration, *Measurement of the inclusive isolated prompt photon cross-section in pp collisions at using of ATLAS data*, Physics Letters B **706**, 150–167 (2011).

[65] ATLAS Collaboration, *Measurement of the inclusive isolated prompt photons cross section in pp collisions at* $\sqrt{s} = 7$ *TeV with the ATLAS detector using* $4.6 fb^{-1}$, Physical Review D **89**, 052 004 (2014).

[66] ATLAS Collaboration, *Measurement of the inclusive isolated prompt photon cross section in pp collisions at* $\sqrt{s} = 8$ *TeV with the ATLAS detector*, J. High Energ. Phys. (2016), dOI: 10.1007/JHEP08(2016)005.

[67] A. Mas, M. Germain, D. Lodato, M. Marcquard, and L. Ronflette for the ALICE Collaboration, *Isolated direct photon cross section measurement in pp collisions at* $\sqrt{s}$*= 7 TeV with the ALICE detector at LHC*, ALICE analysis note.

[68] ATLAS Collaboration, *Centrality, rapidity and transverse momentum dependence of isolated prompt photon production in lead-lead collisions at* $\sqrt{s_{NN}} = 2.76$ *TeV measured with the ATLAS detector*, arXiv:1506.08552 (2015).

[69] PHENIX Collaboration, *Measurement of direct photon production in* $p\overline{p}$ *collisions at* $\sqrt{s} =$ 200 GeV, Phys. Rev. Lett. **98**, 012 002 (2007).

[70] UA1 Collaboration, *Direct photon production at the CERN proton-antiproton collider*, Physics Letters B **209**, 385 – 396 (1988).

[71] UA2 Collaboration, *Direct photon production in $\bar{p}p$ collisions at $\sqrt{s}$ = 630 GeV*, Z. Phys. C **41**, 395 (1988).

[72] J. Alitti, G. Ambrosini, R. Ansari, D. Autiero, P. Bareyre, I.A. Bertram, G. Blaylock, P. Bonamy, K. Borer et al., *A measurement of single and double prompt photon production at the CERN pp collider*, Physics Letters B **288**, 386 – 394 (1992).

[73] CDF Collaboration, *Comparison of the isolated direct photon cross sections in $p\overline{p}$ collisions at $\sqrt{s}$ = 1.8TeV and $\sqrt{s}$ = 0.63TeV*, Phys. Rev. D **65**, 112 003 (2002).

[74] D0 Collaboration, *Isolated Photon Cross Section in the Central and Forward Rapidity Regions in $p\overline{p}$ Collisions at $\sqrt{s}$ = 1.8TeV*, Phys. Rev. Lett. **77**, 5011–5015 (1996).

[75] D0 Collaboration, *Isolated photon cross section in $p\overline{p}$ collisions at $\sqrt{s}$ = 1.8 TeV*, Phys. Rev. Lett. **84**, 2786–2791 (2000).

[76] CDF Collaboration, *Direct photon cross section with conversions at CDF*, Phys. Rev. D **70**, 074 008 (2004).

[77] D0 Collaboration, *Ratio of Isolated Photon Cross Sections in $p\overline{p}$ Collisions at $\sqrt{s}$ = 630 and 1800 GeV*, Phys. Rev. Lett. **87**, 251 805 (2001).

[78] DO collaboration, *Measurement of the isolated photon cross section in collisions at*, Physics Letters B **639**, 151 – 158 (2006).

[79] CDF Collaboration, *Measurement of the inclusive isolated prompt photon cross section in $p\overline{p}$ collisions at $\sqrt{s}$ = 1.96 TeV using the CDF detector*, Phys. Rev. D **80**, 111 106 (2009).

[80] G. Alverson, W. F. Baker, G. Ballocchi, R. Benson, D. Berg, S. Blusk, C. Bromberg, D. Brown, D. Carey et al., *Production of direct photons and neutral mesons at large transverse momenta by π^- and p beams at 500 GeV/c*, Phys. Rev. D **48**, 5–28 (1993).

[81] Fermilab E706 Collaboration, *Evidence for Parton k_T Effects in High- p_T Particle Production*, Phys. Rev. Lett. **81**, 2642–2645 (1998).

[82] Fermilab E706 Collaboration, *Measurement of direct-photon production at the Fermilab Tevatron fixed target energies*, Phys. Rev. D **70**, 092 009 (2004).

[83] H.-L. Lai, M. Guzzi, J. Huston, Z. Li, P. M. Nadolsky, J. Pumplin, and C.-P. Yuan, *New parton distributions for collider physics*, Phys. Rev. D **82**, 074 024 (2010).

[84] T. Becher, C. Lorentzen, and M. D. Schwartz, *Precision direct photon and W -boson spectra at high p_T and comparison to LHC data*, Phys. Rev. D **86**, 054 026 (2012).

[85] ALICE Collaboration, *Performance of the ALICE experiment at the CERN LHC*, Int. J. Mod. Phys. A **29**, 1430 044 (2014).

[86] The CMS Collaboration, *The CMS experiment at the CERN LHC*, Journal of Instrumentation **3**, S08 004 (2008).

[87] The ATLAS Collaboration, *The ATLAS Experiment at the CERN Large Hadron Collider*, Journal of Instrumentation **3**, S08 003 (2008).

[88] The LHCb Collaboration, *The LHCb Detector at the LHC*, Journal of Instrumentation **3**, S08 005 (2008).

[89] The ALICE Collaboration, *The ALICE experiment at the CERN LHC*, Journal of Instrumentation **3**, S08 002 (2008).

[90] The LHCf Collaboration, *The LHCf detector at the CERN Large Hadron Collider*, Journal of Instrumentation **3**, S08 006 (2008).

[91] The TOTEM Collaboration, *The TOTEM Experiment at the CERN Large Hadron Collider*, Journal of Instrumentation **3**, S08 007 (2008).

[92] CMS Collaboration, *The CMS electromagnetic calorimeter project: Technical Design Report*, Technical Design Report CMS (CERN, Geneva) (1997), CERN-LHCC-97-033.

[93] ATLAS Collaboration, *ATLAS liquid-argon calorimeter: Technical Design Report*, Technical Design Report ATLAS (CERN, Geneva) (1996), CERN-LHCC-96-041.

[94] LHCb Collaboration, *LHCb calorimeters: Technical Design Report*, Technical Design Report LHCb (CERN, Geneva) (2000), CERN-LHCC-2000-036.

[95] ALICE Collaboration, *ALICE: Physics Performance Report, Volume I*, Journal of Physics G: Nuclear and Particle Physics **30**, 1517 (2004).

[96] ALICE Collaboration, *ALICE: Physics Performance Report, Volume II*, Journal of Physics G: Nuclear and Particle Physics **32**, 1295 (2006).

[97] ALICE Collaboration, *ALICE Inner Tracking System (ITS): Technical Design Report*, Technical Design Report ALICE (CERN, Geneva) (1999), CERN-LHCC-99-012.

[98] ALICE Collaboration, *ALICE time projection chamber*, Technical Design Report ALICE (2000), CERN-LHCC-2000-001.

[99] ALICE Collaboration, *ALICE high-momentum particle identification*, Technical Report Design ALICE (1998), CERN-LHCC-99-5.

[100] ALICE Collaboration, *ALICE time-of-flight system (TOF)*, Technical Design Report (2000), CERN-LHCC-2002-016.

[101] ALICE Collaboration, *ALICE transition-radiation detector: Technical Design Report*, Technical Design Report ALICE (CERN, Geneva) (2001), CERN-LHCC-2001-021.

[102] ALICE Collaboration, *ALICE Photon Spectrometer (PHOS): Technical Design Report*, Technical Design Report ALICE (CERN, Geneva) (1999), CERN-LHCC-99-4.

[103] ALICE Collaboration, *ALICE electromagnetic calorimeter Technical Design Report*, Technical Design Report ALICE (2008), CERN-LHCC-2008-014.

[104] ALICE Collaboration, *ALICE DCal: An Addendum to the EMCal Technical Design Report Di-Jet and Hadron-Jet correlation measurements in ALICE*, Technical Design Report ALICE (2010), CERN-LHCC-2010-011.

[105] A. Fernández, E. Gámez, G. Herrera, R. López, I. León-Monzón, M.I. Martínez, C. Pagliarone, G. Paic, S. Román et al., *ACORDE a cosmic ray detector for ALICE*, Nuclear Instruments and Methods in Physics Research Section A: Accelerators, Spectrometers, Detectors and Associated Equipment **572**, 102 – 103 (2007), frontier Detectors for Frontier PhysicsProceedings of the 10th Pisa Meeting on Advanced Detectors.

[106] ALICE Collaboration, *ALICE zero-degree calorimeter (ZDC)*, Technical Design Report ALICE (1999), CERN-LHCC-99-5.

[107] The ALICE Collaboration, *ALICE photon multiplicity detector (PMD)*, Technical Design Report ALICE (1999), CERN-LHCC-2003-038.

[108] The ALICE Collaboration, *ALICE forward detectors: FMD, TO and VO*, Technical Design Report ALICE (2004), CERN-LHCC-2004-025.

[109] ALICE Collaboration, *ALICE dimuon forward spectrometer*, Technical Design Report ALICE (CERN, Geneva) (1999), CERN-LHCC-99-022.

[110] The ALICE collaboration, *Measurement of visible cross sections in proton-lead collisions at s NN = 5.02 TeV in van der Meer scans with the ALICE detector*, Journal of Instrumentation **9**, P11 003 (2014).

[111] ALICE Collaboration, *The ALICE central trigger processor*, in *Proceedidngs, 6th Workshop on Electronics for LHC experiments, Cracow, Poland, 11-15 Sep 2000* (2000), pp. 318–322.

[112] ALICE Collaboration, *ALICE trigger data-acquisition high-level trigger and control system*, Technical Design Report ALICE (2004), CERN-LHCC-2003-062.

[113] F. Carena, W. Carena, S. Chapeland, V. Chibante Barroso, F. Costa, E. Dénes, R. Divià, U. Fuchs, A. Grigore et al., *The ALICE data acquisition system*, Nuclear Instruments and Methods in Physics Research Section A: Accelerators, Spectrometers, Detectors and Associated Equipment **741**, 130 – 162 (2014).

[114] C. W. Fabjan, and F. Gianotti, *Calorimetry for particle physics*, Rev. Mod. Phys. **75**, 1243–1286. 96 p (2003).

[115] J. Allen, T. Awes, A. Badalá, S. Baumgart, R. Bellwied, L. Benhabib, C. Bernard, N. Bianchi, F. Blanco et al., *Performance of prototypes for the ALICE electromagnetic calorimeter*, Nuclear Instruments and Methods in Physics Research Section A: Accelerators, Spectrometers, Detectors and Associated Equipment **615**, 6–13 (2010).

[116] T. Sjostrand, S. Mrenna, and P. Skands, *PYTHIA 6.4 Physics and Manual*, Journal of High Energy Physics **2006**, 026 (2006).

[117] J. Pumplin, D. R. Stump, J. Huston, H. L. Lai, Pavel M. Nadolsky, and W. K. Tung, *New generation of parton distributions with uncertainties from global QCD analysis*, JHEP **07**, 012 (2002).

[118] R. Brun, F. Bruyant, M. Maire, A.C. McPherson, and P. Zanarini, *GEANT3 user's guide*, Technical report, CERN DD/EE/84-1 (1987).

[119] G. Conesa Balbastre, J. Faivre, C. Furget, M. Germain, A. Mas, L. Ronflette, C. Silvestre Tello, and A. Vauthier, *Isolated photons purity estimation*, ALICE analysis note.

[120] G. Conesa Balbastre, J. Faivre, C. Furget, C. Silvestre Tello, and A. Vauthier, *Isolated γ-hadron correlations with EMCal in pp collisions at $\sqrt{s}$ = 7 TeV in 2011 data*, ALICE analysis note.

[121] P. Aurenche, J. Ph. Guillet, E. Pilon, M. Werlen, and M. Fontannaz, *Recent critical study of photon production in hadronic collisions* **73**, 094 007 (2006).

[122] P. Aurenche, M. Fontannaz, J.-P. Guillet, B. Kniehl, E. Pilon, and M. Werlen, *A critical phenomenological study of inclusive photon production in hadronic collisions*, The European Physical Journal C - Particles and Fields **9**, 107–119 (1999).

[123] Ronflette L., *Etude de la production de photons isolés au LHC avec ALICE et comparaison aux prédictions théoriques*, Master's thesis, Université Joseph Fourier, Grenoble 1 (2013).

[124] H.-L. Lai, M. Guzzi, J. Huston, Z. Li, P. M. Nadolsky, J. Pumplin, and C.-P. Yuan, *New parton distributions for collider physics*, Phys. Rev. D **82**, 074 024 (2010).

[125] M. Hirai, S. Kumano, and T.-H. Nagai, *Determination of nuclear parton distribution functions and their uncertainties at next-to-leading order*, Phys. Rev. C **76**, 065 207 (2007).

[126] D. de Florian, and R. Sassot, *Nuclear parton distributions at next to leading order*, Phys. Rev. D **69**, 074 028 (2004).

UNIVERSITE BRETAGNE LOIRE

UNIVERSITÉ DE NANTES

Thèse de Doctorat

Lucile RONFLETTE

Isolated photon production in p-Pb collisions at $\sqrt{s_{NN}}$ = 5.02 TeV with the ALICE experiment at the LHC

Etude de la production de photons isolés dans les collisions p-Pb à $\sqrt{s_{NN}}$ = 5.02 TeV dans l'expérience ALICE au LHC

Résumé

La chromodynamique quantique est la théorie associée à l' interaction forte dans le modèle standard. Elle prédit le confinement des partons (quarks et gluons) à l' intérieur des hadrons dans des conditions thermodynamiques standards. Lorsque des hautes densités d'énergie sont mises en jeu, un état de déconfinement de la matière hadronique, le plasma de Quarks et Gluons (PQG), est prédit par la théorie. Cet état aurait existé aux premiers instants de l' Univers. L ' expérience ALICE (A Large Ion Collider Experiment) au CERN-LHC est dédiée à l' étude de la matière hadronique dans les collisions pp, p-Pb et dans les collisions Pb-Pb où la formation d'un PQG est attendue. Dans cette thèse, nous présentons l'étude des photons issus des interactions dures entre partons. Leur section efficace de production est calculable dans le cadre de la chromodynamique quantique perturbative. Une telle mesure effectuée dans les collisions p-Pb, permet d' étudier les effets nucléaires froids. Expérimentalement, les photons prompts sont mesurés en utilisant la méthode de l'isolement. La mesure de la section efficace des photons isolés dans les collisions p-Pb à $\sqrt{s_{NN}}$ = 5.02 TeV avec le calorimètre EMCal de l' expérience ALICE est présentée. Les résultats sont consistants avec les calculs théoriques effectués. La comparaison avec la section efficace mesurée dans les collisions pp a été réalisée via la détermination du facteur de modification nucléaire, R_{pA}. Ce dernier est compatible avec l'unité et n'indique aucune modification claire, due à des effets nucléaires, de la production de photons prompts dans les collisions p-Pb.

Mots clés
photons isolés, photons directs, pQCD, collisions p-Pb, calorimètre électromagnétique, ALICE, LHC, PQG

Abstract

Quantum ChromoDynamics is the theory associated to the strong interaction in the standard model. It predicts that partons (quarks and gluons) are confined into hadrons at standard thermodynamic conditions. A state of deconfined hadronic matter, the Quark-Gluon Plasma (QGP), is predicted for a high energy density and would have existed in the early state of the Universe. ALICE (A Large Ion Collider Experiment) at CERN-LHC (Large Hadron Collider) is dedicated to hadronic matter study in p-p, p-Pb (Pb-p) and in Pb-Pb collisions where QGP formation is expected.
In this thesis, we will present the study of photons coming directly from parton-parton hard scatterings, the prompt photons. Their production cross-section is calculable in perturbative Quantum ChromoDynamics theory. Such a measurement in p-Pb collisions enables the study of cold nuclear matter effects whose knowledge is crucial to distinguish key signatures of the QGP from nuclear effects in Pb-Pb collisions.
Experimentally, the prompt photon can be discriminated using the isolation analysis method. In this thesis, the measurement of the isolated photon cross-section in p-Pb collisions at $\sqrt{s_{NN}}$ = 5.02 TeV with the EMCal calorimeter of the ALICE experiment, is presented. The results are consistent, within the uncertainties, with theoretical calculations. The comparison with the measured cross-section in p-p analysis is performed via the determination of the nuclear modification factor R_{pA}. The last one is compatible with the unity and does not clearly indicate modification of the prompt photon production due to nuclear effects in p-Pb collisions.

Key Words
isolated photons, direct photons, pQCD, p-Pb collisions, electromagnetic calorimeter, ALICE, LHC, QGP

L'Université Bretagne Loire